

Nuclear Magnetic Resonance

Studies of Ion Adsorption in

Supercapacitor Electrodes



Alexander Charles Forse

Trinity Hall

University of Cambridge

This dissertation is submitted for the degree of

Doctor of Philosophy

August 2015

Declaration

This dissertation is the result of my own work and includes nothing which is the outcome of work done in collaboration except as declared in the Preface and specified in the text.

It is not substantially the same as any that I have submitted, or, is being concurrently submitted for a degree or diploma or other qualification at the University of Cambridge or any other University or similar institution except as declared in the Preface and specified in the text. I further state that no substantial part of my dissertation has already been submitted, or, is being concurrently submitted for any such degree, diploma or other qualification at the University of Cambridge or any other University or similar institution except as declared in the Preface and specified in the text

It does not exceed the prescribed word limit for the Degree Committee for the Faculty of Physics & Chemistry.

Abstract

Supercapacitors (or electric double-layer capacitors) are high power energy storage devices that store charge by the non-faradaic adsorption of ions at the interface between porous carbon electrodes and an electrolyte solution. The development of new electrode materials and electrolytes with improved performances is an active area of research today, yet there are relatively few studies of the molecular mechanisms of the charge storage process. In this work, nuclear magnetic resonance (NMR) spectroscopy is developed for the study of the charge storage mechanisms of supercapacitors.

Importantly, NMR experiments show that electrolyte ions adsorbed inside the pores of the carbon electrodes can be resolved from those in bulk electrolyte for a range of supercapacitor electrode materials. Chemical shift calculations show that the adsorbed species are subject to ring current effects, whereby the delocalised electrons in the carbon shield the nearby nuclei. The calculated effects depend on the local carbon structure, helping to rationalise the variations observed when different porous carbons are studied experimentally, and allowing structural information to be extracted from the spectra.

NMR experiments performed on electrodes extracted from ionic liquid-based supercapacitors with different applied voltages allow the numbers of adsorbed ions to be measured upon charging. It is shown that supercapacitor charging involves the migration of both anions and cations in and out of the carbon pores in each electrode, with the anions dominating the charge storage process. When combined with lineshape measurements, which offer information about the diffusion of adsorbed ions, the power performances of supercapacitor devices with different electrolytes are rationalised.

In situ NMR methods are then developed to allow mechanistic studies of working supercapacitors as they are charged and discharged inside the NMR magnet. The experiments reveal that the charge storage mechanism depends on both the electrolyte and the electrode material studied. During charging, reversible chemical shift changes are also observed, arising from the introduction of paratropic ring currents. Finally, cross polarisation experiments allow the selective observation of the adsorbed electrolyte species, and show that their motion slows down during supercapacitor charging. Overall, the NMR approach offers unique insights into the molecular mechanisms of the supercapacitance phenomenon.

Acknowledgements

First and foremost, I would like to thank my fantastic supervisor Professor Clare Grey for providing endless support, ideas and inspiration. It has been a privilege to work with such a brilliant scientist and group leader. I would also like to thank Dr. John Griffin for being an incredible mentor and teacher over the course of my studies, and for always being willing to discuss ideas or help with experiments, forever in good humour. Dr. Hao Wang and Dr. Céline Merlet have also offered a great deal of support and cheer over the course of my studies for which I am very thankful. Grey group members in general have been great colleagues over the last three years, and in particular I would like to thank Dr Nicole Trease, Dr Andrew Ilott, Dr Phoebe Allan, Elizabeth Humphreys and Dr. Paul Bayley for their contributions to this work, as well as Kent Griffith and Michael Hope from whom I have learned a lot.

Beyond the Grey group, collaborators Professor Yury Gogotsi, Professor Patrice Simon and Professor Volker Presser have all played an important part in this work, and I am very grateful for all the scientific discussions we have shared and all the work they have put into this project. I would also like to express my gratitude to Dr. Nick Bampas who has been an incredible source of wisdom and support throughout my time in Cambridge. He has gone out of his way on countless occasions to ensure my time here has been a happy and productive one. I also greatly acknowledge the Sims Scholarship for providing the funding for my studies.

My time in Cambridge has been a thoroughly enjoyable one, and for this I thank my friends and family. I thank the magnificent James Horscroft and Dan Bean who have always been there for me, both to celebrate the highs and to pick me up during the lows. Friends from the lab, T.H.M.C.R.F.C., The Missionaries, and the Wulfhaus have also been great throughout. I would like to thank my amazing partner Helen for her endless love and support during the last three years. Finally, I thank my parents Kay and Peter, and my sister Amy. I could not have asked for a more loving and supportive family.

Table of Contents

Declaration	ii
Abstract	iii
Acknowledgements	iv
List of Abbreviations	ix
List of Publications	x
Chapter 1: Introduction	1
Chapter 2: Supercapacitors	4
2.1 Basic Principles of Energy Storage	4
2.2 Electrochemical Characterisation of Supercapacitors.....	6
2.2.1 Cyclic voltammetry	6
2.2.2 Galvanostatic charge-discharge experiments	7
2.2.3 Chronoamperometry.....	8
2.3 Materials for Supercapacitors.....	9
2.3.1 Electrolytes.....	9
2.3.2 Carbon electrodes	10
2.4 The Effects of Carbon Porosity on Capacitance.....	15
2.5 Molecular Modelling of Supercapacitors	16
2.6 New Experimental Methods to Study Supercapacitance.....	19
2.7 Aims of This Thesis.....	21
Chapter 3: Nuclear Magnetic Resonance Spectroscopy.....	22
3.1 The Zeeman Interaction.....	22
3.2 Interactions in NMR.....	22
3.2.1 Chemical shielding	22
3.2.2 Inter-nuclear couplings.....	27
3.2.3 Bulk magnetic susceptibility effects	28
3.3 The Vector Model	29
3.4 Techniques in NMR.....	31
3.4.1 Spin echo experiments	31
3.4.2 Relaxation time measurements.....	32
3.4.3 Cross polarisation	33
3.4.4 Two-dimensional NMR.....	36
3.5 Chemical Exchange in NMR	38
3.6 Ring Current Effects	40
3.7 Electronic Structure Calculations	42
Chapter 4: NMR Studies of Electrolyte Adsorption in Porous Carbons.....	46

4.1 Context and Scope	46
4.2 Experimental Details	47
4.2.1 Carbon materials	47
4.2.2 NMR experiments	48
4.2.3 Scanning Electron Microscopy experiments.....	49
4.3 Results and Discussion	49
4.3.1 NMR spectra for an activated carbon soaked with electrolyte.....	49
4.3.2 Investigating carbide-derived carbons	52
4.3.3 Chemical exchange of ions between in- and ex-pore environments	55
4.3.4 Experimental considerations for studying adsorption in porous carbons	58
4.4 Summary and Outlook.....	61
Chapter 5: The Relationship Between Carbon Structures and Ring Current Shifts	63
5.1 Context and Scope	63
5.2 Experimental Details	65
5.2.1 Nucleus-independent chemical shift calculations	65
5.2.2 Carbon materials	65
5.2.3 NMR experiments	66
5.2.4 Determination of pore size distributions	66
5.2.5 Raman spectroscopy.....	67
5.2.6 Powder X-ray diffraction	67
5.3 Results and Discussion	67
5.3.1 Effect of carbon domain size.....	67
5.3.2 Effect of carbon pore size on the NICS.....	69
5.3.3 Effects of carbon curvature	71
5.3.4 Additional considerations for NICS calculations	72
5.3.5 Revisiting the NMR spectra of electrolyte-soaked TiC-CDCs	75
5.3.6 Experimental observation of carbon pore size effects	77
5.3.7 Experimental observation of carbon ordering effects	79
5.3.8 Characterising structural order in porous carbons.....	80
5.4 Summary and Outlook.....	83
Chapter 6: NMR Studies of the Charging Mechanisms of Ionic Liquid-based Supercapacitors	86
6.1 Context and Scope	86
6.2 Experimental Details	88
6.2.1 Carbon materials	88
6.2.2 Ionic liquids.....	88

6.2.3 NMR sample preparation for carbons soaked with ionic liquid.....	88
6.2.4 NMR experiments	89
6.2.5 Preparation of coin cells	89
6.2.6 Ex situ NMR experiments	89
6.2.7 Electrochemical characterisations	90
6.2.8 Nucleus-independent chemical shift calculations	90
6.3 Results and Discussion	90
6.3.1 Wetting of activated carbon by ionic liquids	90
6.3.2 Experimental considerations for charging studies	92
6.3.3 Ex situ NMR studies of Pyr ₁₃ TFSI/YP50F supercapacitors	94
6.3.4 Chemical shift changes observed during charging.....	99
6.3.5 Studies of ionic liquids and CDCs	103
6.4 Summary and Outlook.....	106
Chapter 7: Dynamics of Ions Confined in Carbon Pores.....	108
7.1 Context and Scope	108
7.2 Experimental Details	109
7.2.1 Materials.....	109
7.2.2 Sample preparation for NMR experiments	109
7.2.3 NMR experiments	110
7.2.4 Lineshape simulations	110
7.2.5 Electrochemical characterisations	110
7.3 Results and Discussion	111
7.3.1 Variable temperature NMR measurements	111
7.3.2 Effects of addition of acetonitrile solvent	117
7.3.3 Rationalising the rate performance of supercapacitors	120
7.3.4 Effects of carbon porosity on dynamics	121
7.4 Summary and Outlook.....	124
Chapter 8: <i>In situ</i> NMR Studies of Supercapacitors	126
8.1 Context and Scope	126
8.2 Experimental Details	127
8.2.1 Materials.....	127
8.2.2 Sample preparation.....	128
8.2.3 Electrochemistry.....	128
8.2.4 NMR details	128
8.2.5 In situ NMR experiments	129
8.3 Results and Discussion	130
8.3.1 Cell designs for in situ NMR.....	130

8.3.2 Effects of sample orientation and supercapacitor components on spectral resolution	131
8.3.3 NMR spectrum of a supercapacitor at 0 V	135
8.3.4 In situ ^{19}F NMR spectroscopy at fixed voltages.....	136
8.3.5 In situ NMR spectroscopy with dynamic cycling	140
8.3.6 Further studies of the charging mechanism.....	143
8.3.7 The application of in situ NMR methods to other carbon materials	144
8.4 Summary and Outlook.....	147
Chapter 9: Selecting Adsorbed Species with Cross Polarisation.....	149
9.1 Context and Scope	149
9.2 Experimental Details	150
9.2.1 Materials.....	150
9.2.2 NMR details	150
9.2.3 Ex situ NMR experiments	151
9.3 Results and Discussion	151
9.3.1 Selecting the in-pore ions with cross polarisation.....	151
9.3.2 CP kinetics for Ti ^{13}C -CDC-1000 soaked with Pyr $_{13}\text{TFSI}$	155
9.3.3 CP measurements on charged electrodes	157
9.4 Summary and Outlook.....	160
Chapter 10: Conclusions and Further Work	161
Bibliography	164

List of Abbreviations

- ACN – Acetonitrile
BET – Brunauer-Emmett-Teller
BMS – Bulk Magnetic Susceptibility
CDC – Carbide-derived Carbon
CP – Cross Polarisation
DFT – Density Functional Theory
EDLC – Electric Double-layer Capacitor
EMITFSI – 1-Ethyl-3-methylimidazolium Bis(trifluoromethanesulfonyl)imide
EPR – Electron Paramagnetic Resonance
EQCM – Electrochemical Quartz Crystal Microbalance
EXSY – Exchange Spectroscopy
FID – Free Induction Decay
FWHM – Full Width at Half Maximum
HETCOR – Heteronuclear Correlation
HF – Hartree-Fock
IR – Infrared
MAS – Magic Angle Spinning
MD – Molecular Dynamics
NICS – Nucleus-independent Chemical Shift
NMR – Nuclear Magnetic Resonance
PDF – Pair Distribution Function
PFG – Pulsed Field Gradient
PTFE – Polytetrafluoroethylene
 $\text{Pyr}_{13}\text{TFSI}$ – 1-Methyl-1-propylpyrrolidinium Bis(trifluoromethanesulfonyl)imide
SEM – Scanning Electron Microscopy
TEM – Transmission Electron Microscopy

List of Publications

Below is a list of publications to which the author has contributed during this project:

1. Nuclear Magnetic Resonance Study of Ion Adsorption on Microporous Carbide-derived Carbon
Forse, A. C.; Griffin, J. M.; Wang, H.; Trease, N. M.; Presser, V.; Gogotsi, Y.; Simon, P.; Grey, C. P.
Phys. Chem. Chem. Phys., **2013**, 15, 7722-7730
2. In Situ NMR Spectroscopy of Supercapacitors: Insight into the Charge Storage Mechanism
Wang, H.;* Forse, A. C.;* Griffin, J. M.; Trease, N.M.; Trognko, L.; Taberna, P.-L.; Simon, P.; Grey, C. P.
J. Am. Chem. Soc., **2013**, 135, 18968-18980
**authors contributed equally*
3. Ring Current Effects: Factors Affecting the NMR Chemical Shift of Molecules Adsorbed on Porous Carbons
Forse, A. C.; Griffin, J. M.; Presser, V.; Gogotsi, Y.; Grey, C. P.
J. Phys. Chem. C., **2014**, 118, 7508-7514
4. Ion Counting in Supercapacitor Electrodes using NMR Spectroscopy
Griffin, J. M.; Forse, A. C.; Wang, H.; Trease, N. M.; Taberna, P.-L.; Simon, P.; Grey, C. P.
Faraday Discuss., **2014**, 176, 49-68
5. Lattice Simulation Method to Model Diffusion and NMR Spectra in Porous Materials
Merlet, C.; Forse, A. C.; Griffin, J. M.; Frenkel, D.; Grey, C. P.
J. Chem. Phys., **2015**, 142, 094701

6. NMR Study of Ion Dynamics and Charge Storage in Ionic Liquid Supercapacitors
Forse, A. C.; Griffin, J. M.; Merlet, C.; Bayley, P. M.; Wang, H.; Simon, P.; Grey, C. P. *J. Am. Chem. Soc.*, **2015**, 137, 7231-7242
7. In Situ NMR and Electrochemical Quartz Crystal Microbalance Techniques Reveal the Structure of the Electrical Double-layer in Supercapacitors
Griffin, J. M.; Forse, A. C.; Tsai, W-Y.; Taberna, P.-L.; Simon, P.; Grey, C. P. *Nature Mater.*, **2015**, 14, 812-819
8. New Insights into the Structure of Nanoporous Carbons from NMR, Raman, and Pair Distribution Function Analysis
Forse, A. C.; Merlet, C.; Allan, P. K.; Humphreys, E. K.; Griffin, J. M.; Aslan, M.; Zeiger, M.; Presser, V.; Gogotsi, Y.; Grey, C. P. *submitted*

Chapter 1

Introduction

Climate change and the dwindling supplies of fossil fuels require mankind to move towards renewable energy production. The intermittency of solar, wave and wind power brings the challenge of how to store and release energy more efficiently, such that the electricity grid can meet demand. At the same time, the electrification of vehicles requires compact and lightweight energy storage devices with the power to accelerate and the energy to cover long distances. Electric vehicles may even serve to level the load of the electricity grid when they are not in use.¹

New electrical energy storage devices are being developed to meet our energy storage needs.² Rechargeable batteries store energy by reversible chemical reactions and are widely used in portable electronic devices as well as in the first generation of electric cars.³ First steps are now being taken to integrate batteries into the grid, with Tesla Motors recently unveiling a new lithium-ion battery for homeowners to store energy generated by solar panels, as well as off-peak electricity.⁴

Supercapacitors, another class of energy storage devices, are emerging for high power applications.⁵ While they store less energy than batteries for a given size or volume, they can charge and discharge much more quickly (from within seconds to a few minutes) and have essentially unlimited cycle lifetimes (see Table 1.1).⁶ These attractive properties arise from their physical charge storage mechanism, whereby electrolyte ions are adsorbed at the surfaces of porous carbon electrodes.⁷ Supercapacitors are particularly well suited to “start-stop” applications requiring large currents, such as electric buses and metro trains.⁸ There are now buses in over 100 cities in China that are powered solely by supercapacitors, which recharge during stops and can also recover energy normally lost during braking.⁹ Supercapacitors are also being used for backup power supplies for the emergency doors on the Airbus A380 aeroplane, and the reorientation mechanism used in windmill turbine blades.⁵ The more widespread

application of supercapacitors will no doubt be facilitated by the development of new devices that can store more energy per unit cost without sacrificing their distinctive power capabilities.¹⁰

Table 1.1 Key properties of typical lithium-ion batteries and supercapacitors.^{5,6}

	Lithium-ion batteries	Supercapacitors
Storage mechanism	Chemical reactions	Physical ion adsorption
Charge/discharge Time	Minutes to hours	Seconds to minutes
Energy storage	$20 - 100 \text{ Wh}\cdot\text{kg}^{-1}$	$1 - 5 \text{ Wh}\cdot\text{kg}^{-1}$
Power density	$0.5 - 1 \text{ kW}\cdot\text{kg}^{-1}$	$5 - 10 \text{ kW}\cdot\text{kg}^{-1}$
Cost per unit energy	$\$ 1 - 2 \text{ Wh}^{-1}$	$\$ 10 - 20 \text{ Wh}^{-1}$
Cost per unit power	$\$ 75-150 \text{ kW}^{-1}$	$\$ 25-50 \text{ kW}^{-1}$
Cycle life	< 5,000 cycles	> 500,000 cycles

Supercapacitor research today largely focuses on the development of new electrode materials and electrolytes that allow the storage of more energy. Despite progress with this materials-driven approach,^{11,12} an attractive alternative is to develop a fundamental understanding of how existing technologies work, such that improved devices can be rationally designed. To this end, molecular modelling studies have greatly enhanced our understanding of the charge storage processes that take place in the nanometre-sized pores of the carbon electrodes.^{13,14} Meanwhile, advanced characterisation methods are being developed to offer a complementary probe of the charging mechanisms. Nuclear magnetic resonance (NMR) spectroscopy is one such method that is a powerful tool for the study of energy storage systems. Following a number of successful studies of the chemistry of lithium-ion batteries,^{15,16} the NMR approach has recently been applied to study supercapacitors.^{17,18}

This thesis aims to develop and apply the NMR approach in a comprehensive investigation of the charge storage mechanisms of supercapacitors. A brief overview of this work is given below.

Chapter 2 presents the background theory of how supercapacitors work and how they are tested, and also reviews recent literature in the field.

Chapter 3 introduces the essential concepts and methodology of NMR spectroscopy, the main experimental technique used in this work.

Chapter 4 introduces NMR as a probe of electrolyte adsorption in porous carbons and explains the main approaches and observations for a range of model systems.

Chapter 5 uses a combined computational and experimental approach to rationalise the form of the NMR spectra observed for electrolyte-soaked porous carbons. The effects of differences in the carbon structures are discussed, and the NMR approach is presented as a new tool for the characterisation of porous carbons.

Chapter 6 presents the application of NMR spectroscopy to ionic liquid-based supercapacitors. Experiments on electrodes extracted from charged supercapacitor cells allow an elucidation of the charging mechanism.

Chapter 7 investigates the effects of electrolyte ion dynamics on the NMR spectra and seeks to rationalise the differing power performances of supercapacitors using different electrolytes.

Chapter 8 presents the development and the application of the NMR method for studying working supercapacitor devices, allowing *in situ* quantification of the charging mechanisms.

Chapter 9 demonstrates a new strategy for the selective study of the charge storing species in NMR studies of supercapacitors.

Chapter 10 presents the main conclusions of this work and suggests new research directions.

Chapter 2

Supercapacitors

2.1 Basic Principles of Energy Storage

A simple supercapacitor can be constructed by placing two conducting electrodes in an aqueous solution of sodium chloride (Figure 2.1a).⁸ When a potential difference is applied between the electrodes, the chloride anions in the electrolyte are attracted to the positively charged electrode, while the sodium cations are attracted to the negatively charged electrode (Figure 2.1b). This results in the formation of a so-called double-layer of charge at each electrode, a concept first introduced by Helmholtz in 1853,¹⁹ with the charge developed in each electrode balanced by an equal and opposite excess ionic charge in the solution. When the applied potential is removed, charge remains stored by the electrosorption of the ions. If the capacitor is then connected across a load, electrons flow around the circuit as the electrolyte ions desorb from the electrode surface.

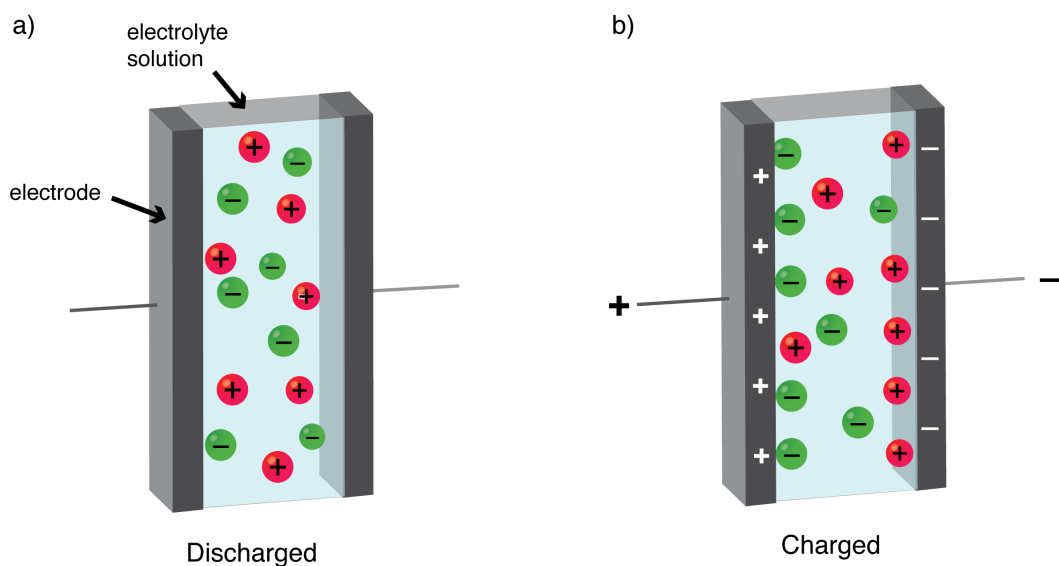


Figure 2.1 Schematic illustrating the basic operation of a supercapacitor and double-layer formation. (a) Discharged state, (b) charged state.

Since charge separation occurs at both electrodes, a supercapacitor can be considered as two capacitors in series,⁷ with the total cell capacitance, C_T , related to the capacitances of each electrode, C_1 and C_2 , by:

$$\frac{1}{C_T} = \frac{1}{C_1} + \frac{1}{C_2} \quad [2.1]$$

Note that capacitances are measured in farads. If identical electrodes are used, then it may be approximated that, $C_1 = C_2 = C$, and:

$$C = 2C_T \quad [2.2]$$

For parallel-plate electrodes, the capacitance, C , of an electrode is given by:

$$C = \frac{\epsilon_0 \epsilon_r A}{d} \quad [2.3]$$

Where ϵ_r is the dielectric constant of the electrolyte, ϵ_0 is the dielectric constant of free space, A is the electrode surface area, and d is charge separation distance at the electrode-electrolyte interface.⁵ Depending on the desired application of a device, capacitance values are typically normalised either by the electrode mass or volume, to give either specific or volumetric capacitances, respectively. While Equation 2.3 does not strictly apply to porous carbon electrodes, it still offers some insight into the key factors that determine capacitance. For modern supercapacitor devices, the combination of high surface area porous carbon electrodes (large A , 1000s of $\text{m}^2 \cdot \text{g}^{-1}$) and the atomic scale separation of charges at the electrode-electrolyte interface (small d , a few ångstroms) gives rise to very large capacitances (see Equation 2.3). Indeed, they typically exhibit capacitances many orders of magnitude greater than conventional dielectric capacitors.⁸ This is why these devices are referred to as supercapacitors.

Strictly, supercapacitors may be divided into two main categories: electric double-layer capacitors (EDLCs), which store charge as described above with no faradaic reactions and purely physical charge storage, and pseudo-capacitors which benefit from additional charge storage from fast reversible redox reactions occurring at the electrode surface.²⁰ The focus of this thesis is on EDLCs, which are more generally referred to as supercapacitors throughout.

2.2 Electrochemical Characterisation of Supercapacitors

2.2.1 Cyclic voltammetry

Cyclic voltammetry is the most common method for the electrochemical characterisation of supercapacitors. Here, the cell voltage, V , is varied linearly with time at a sweep rate given by dV/dt and the current response, i , is measured (Figure 2.2). Once the cell voltage reaches some maximum value, V_{max} , (normally chosen to avoid decomposition of the electrolyte), the sweep direction is reversed, and the voltage is varied at a rate of $-dV/dt$ until a cell voltage of zero is reached. At this point, the sweep direction is again reversed, and the experiment is typically repeated many times.

The charge stored, q , by a capacitor is given by:

$$q = C_T V \quad [2.4]$$

Assuming that the capacitance is constant over the applied voltage range, differentiation with respect to time yields:

$$i = C_T \frac{dV}{dt} \quad [2.5]$$

Thus in the cyclic voltammetry experiment, for scan rates of dV/dt a positive current given by $C \cdot dV/dt$ is expected. When the scan rate is reversed, Equation 2.5 then gives a current of $-C \cdot dV/dt$. This behaviour is shown in Figure 2.2b, with the data commonly plotted as current against voltage, giving rise to a characteristic rectangular-shaped cyclic voltammogram (Figure 2.2c). However, this only applies for an ideal system in which there is zero resistance. In practice there are a number of resistances including the ionic resistance of the electrolyte and electronic resistances of the electrode, the current collector and their interface. Modelling the supercapacitor as a series circuit with resistance, R , and capacitance, C_T (Figure 2.2d),²¹ the voltage of the system is given by:

$$V = V_R + V_C \quad [2.6]$$

Where V_R is the voltage across the resistor, and V_C is the voltage across the capacitor. The voltage is given by the product of the sweep rate and the time elapsed, V_R is given by Ohm's law, and V_C is given by Equation 2.4, giving:

$$\frac{dV}{dt} t = \frac{dq}{dt} R + \frac{q}{C_T} \quad [2.7]$$

The solution of this equation is:¹⁹

$$i = C_T \frac{dV}{dt} \left[1 - \exp\left(\frac{-t}{RC_T}\right) \right] \quad [2.8]$$

Which gives rise to the current response shown in Figure 2.2e, and the voltammogram shown in Figure 2.2f. In practice, cyclic voltammograms of supercapacitors typically resemble something much closer to Figure 2.2f than Figure 2.2c. The capacitance can be estimated by measuring the current in the plateau region, for which Equation 2.5 applies. The advantage of the cyclic voltammetry experiment is that capacitive behaviour can be readily observed, while the presence of any undesired faradaic processes (such as electrolyte decomposition) can also be identified as peaks in the voltammograms.

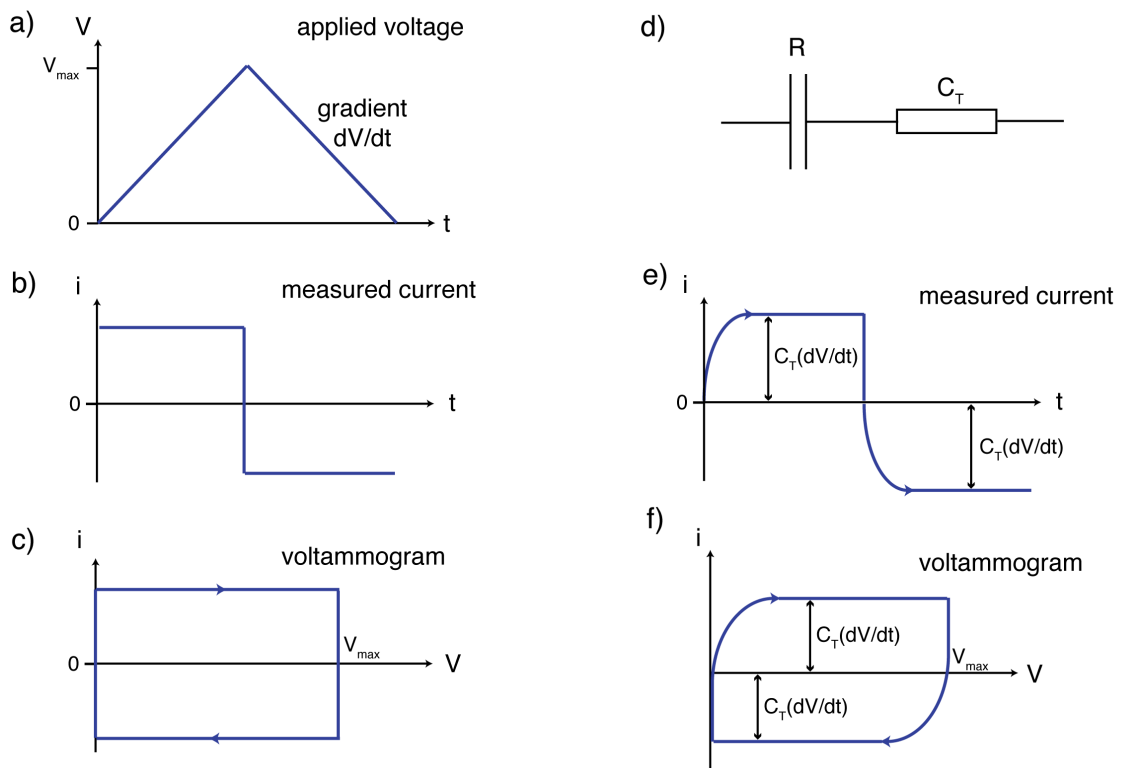


Figure 2.2 Cyclic voltammetry. (a) Applied voltage, (b) current response and (c) voltammogram for an ideal capacitor with no resistance. (d) Simple RC circuit to model a non-ideal capacitor, (e) current response and (f) voltammogram.

2.2.2 Galvanostatic charge-discharge experiments

If accurate measurements of the capacitance are required, galvanostatic (constant current) charge-discharge experiments are normally performed.²² Here, a constant current is applied to the capacitor and the voltage response is recorded (Figure 2.3). Once the voltage reaches the chosen maximum value, the current is reversed, and the

experiment is continued until V reaches zero, at which point the experiment is repeated. For a constant current, I , and for initial conditions of $V = 0$ and $t = 0$, Equation 2.6 can be written:

$$V = I \left(R + \frac{t}{C_T} \right) \quad [2.9]$$

With differentiation with respect to time yielding:

$$\frac{dV}{dt} = \frac{I}{C_T} \quad [2.10]$$

The capacitance can then be readily obtained from the gradient of the voltage against time response, while the resistance can also be measured (Figure 2.3b). It is typically recommended that several charge-discharge cycles are performed prior to the capacitance measurement, and that the capacitance is determined from the gradient of the discharge current.²²

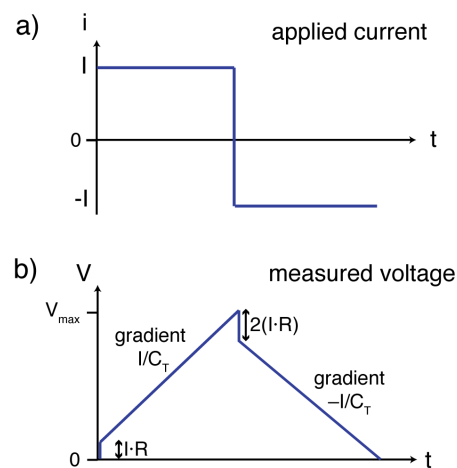


Figure 2.3 Galvanostatic charge-discharge measurements. (a) Applied current and (b) measured voltage response. The cell capacitance and resistance can be determined.

2.2.3 Chronoamperometry

In chronoamperometry experiments, constant voltages are applied to the cell and the resulting current is measured. This technique is useful if equilibrium states at a given voltage are to be studied with spectroscopic techniques. Here a fixed voltage, V_{step} , is applied to the cell and the current response is recorded as it decays towards zero (Figure 2.4). Here the current obtained from Equation 2.6 is given by:¹⁹

$$i = \frac{V_{step}}{R} \exp\left(\frac{-t}{RC_T}\right) \quad [2.11]$$

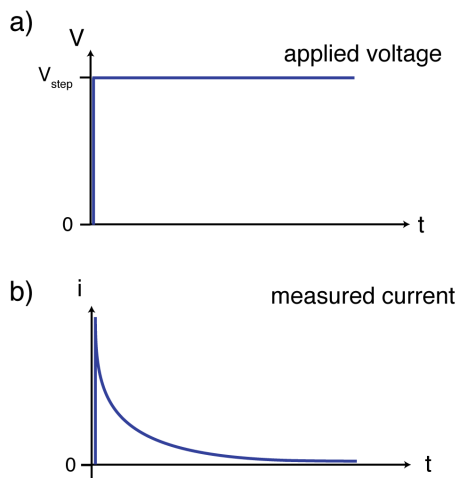


Figure 2.4 Voltage step experiment. (a) Applied voltage and (b) current response.

A final technique that is often used to characterise supercapacitors is impedance spectroscopy. Here an alternating voltage (or current) is applied to the cell and the current (or voltage) response is measured. By varying the frequency of the applied voltage, the frequency dependence of the complex impedance can be determined, allowing impedances associated with different components of the supercapacitor to be separated (*e.g.*, electric contact resistances, ionic transport resistances *etc.*).²¹

2.3 Materials for Supercapacitors

Supercapacitors typically consist of two porous carbon electrodes (attached to metal current collectors) that are separated by a porous polymer separator to prevent a short circuit. The entire assembly is soaked with electrolyte and hermetically sealed. Here, electrolytes and carbon electrode materials are discussed in detail.

2.3.1 Electrolytes

Two key parameters that define the suitability of an electrolyte for application in supercapacitors are: the maximum operating voltage before electrolyte decomposition occurs, and the ionic conductivity. The energy stored by a supercapacitor, E , with operating voltage, V , is given by:

$$E = \frac{1}{2} C_T V^2 \quad [2.12]$$

The amount of energy stored depends strongly on the maximum operating voltage, which is typically limited by the electrolyte. Aqueous electrolytes (such as sodium

chloride dissolved in water) are limited to \sim 1.0 V before water decomposes.¹² While this voltage range is relatively limited, aqueous electrolytes generally have high ionic conductivities approaching $1 \text{ S}\cdot\text{cm}^{-1}$, giving rise to very good device power performances.²³ They also have the added advantage of being relatively environmentally-friendly and cheap, and devices can also be assembled in air, avoiding the costly electrode drying process used for devices with organic electrolytes.

Organic electrolytes (such as tetraethylammonium tetrafluoroborate, NEt_4BF_4 , in acetonitrile) are typically preferred, largely due to the high operating voltages of up to 2.7 V, which allow the storage of more energy by Equation 2.12.¹⁰ Acetonitrile and propylene carbonate are the most commonly used organic solvents; the former is often preferred since it displays higher ionic conductivity (*e.g.*, \sim 60 $\text{mS}\cdot\text{cm}^{-1}$, compared to \sim 15 $\text{mS}\cdot\text{cm}^{-1}$, for 1 M NEt_4BF_4).²³ However, some concerns remain about the safety of acetonitrile, due to its flammability and toxicity.⁵ The lower ionic conductivities of organic electrolytes compared to aqueous systems can be detrimental to the power performances of devices,²³ but organic electrolytes tend to be used commercially as they offer a good balance of power and energy.

Recently, efforts have been directed towards developing ionic liquids as supercapacitor electrolytes. These solvent-free electrolytes are essentially low temperature molten salts. Since there is no solvent, the operating voltage of ionic liquids is limited only by the electrochemical stability of the ions, allowing device operating voltages above 3 V and the storage of more energy by Equation 2.12.²⁴ Ionic liquids are also safe since they have extremely low vapour pressures and are non-flammable. Their low ionic conductivities (typically $1\text{--}10 \text{ mS}\cdot\text{cm}^{-1}$)²³ compared to organic electrolytes limits their power performances and has hampered their widespread application in supercapacitors. The power performances of ionic liquid devices can be improved by using non-porous electrodes, while the operating temperature range can be extended to as wide as -50 to 100°C by employing eutectic mixtures of ionic liquids.^{25,26} This represents an improvement over the temperature range in which typical organic electrolytes can operate (\sim 30 $^\circ\text{C}$ to 80 $^\circ\text{C}$).

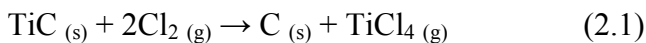
2.3.2 Carbon electrodes

2.3.2.1 Synthesis and porosity

Supercapacitors typically employ porous carbon electrodes as they have large surface areas for ion adsorption, good electronic conductivities and relatively low production

cost.²⁷ In particular, activated carbons, derived from carbon-rich organic precursors, such as coconut-shells or wood, are the materials of choice in commercial devices.¹⁰ These carbons are prepared by first carbonising the precursor organic material at high temperature (typically > 800 °C) in an inert atmosphere (N₂ or Ar). A subsequent high temperature activation step is then carried out, normally with potassium hydroxide, phosphoric acid, carbon dioxide or steam, which is thought to develop the porosity of the carbon.²⁸ The resulting activated carbons exhibit pores with different diameters, often ranging from micropores (diameters less than 2 nm), and mesopores (diameters between 2 and 50 nm), to macropores (diameters greater than 50 nm), according to the IUPAC classification.²⁹

In addition to organic precursors, inorganic precursors such as metal carbides can be used to synthesise porous carbons. Such carbide-derived carbons (CDCs), have recently gained attention due to their tuneable pore sizes.^{30–32} CDCs are typically produced by heating a metal carbide precursor in a halogen gas,³² with selective extraction of the metal leaving an amorphous carbon with high specific surface area (surface area per unit mass). For example, chlorine-treatment of titanium carbide forms titanium carbide-derived carbon (TiC-CDC) according to Chemical Equation 2.1.



TiC-CDC is predominantly microporous and has a narrow pore size distribution since the TiC rock-salt lattice (with uniform first neighbour carbon separation) acts a template for the forming carbon.³² Moreover, the average pore size can be tuned with sub-ångstrom accuracy. Increasing the chlorine-treatment temperature increases the average pore size and broadens the pore size distribution.³³ The specific surface area typically increases with chlorine-treatment temperatures up to 1000 °C, but decreases for higher temperatures.

Beyond activated carbons and CDCs, a wide range of carbon materials have recently been developed for supercapacitor application.^{11,12,27} These range from carbon nanotubes, to carbon onions and graphene-based materials. Despite the promising performance of these new materials, activated carbons produced from organic materials remain the materials of choice in commercial supercapacitors.

2.3.2.2 Structure

The structures of carbon materials^{34,35} have been actively researched since the X-ray diffraction studies of Franklin.^{36,37} She distinguished between graphitizing and non-

graphitizing carbons, the former transforming into graphite upon heating to high temperatures, and the latter showing no such transformation at temperatures as high as 3000 °C.³⁷ For porous carbons, analysis of the broad Bragg peaks is generally of limited use due to the long-range disordered structures of these materials. However, inclusion of the diffuse scattering in the analysis allows the extraction of a pair distribution function (PDF), which is a weighted histogram of atom-atom distances showing the likelihood of finding an atom pair separated by a certain distance.³⁸ PDF studies show that porous carbons often exhibit a high degree of local ordering, with a propensity for hexagonal carbon rings in which the carbons are sp^2 hybridised.^{39–41} Correlations in the PDFs typically extend over tens of ångstroms, suggesting that there is local order on this length scale.⁴⁰ Transmission electron microscopy (TEM) images corroborate these ideas and generally show curved carbon sheets arranged in a disordered fashion.^{33,39,42} The sheet curvature is thought to arise from the presence of non-hexagonal carbon rings, observed in experimental⁴² and modelling studies.^{43–45} One model structure consistent with all these observations consists of fullerene-like fragments arranged in a highly disordered fashion.³⁵

Computation modelling has offered new insights into the structures of porous carbons, with two main approaches carried out so far. The *reconstructive* approach involves performing hybrid Monte Carlo simulations, where the positions of the carbon atoms are randomly adjusted in a series of moves. The probability of each move being accepted depends on changes of the agreement of the model structure with experimental data (typically a PDF) and changes of the energy of the system calculated using a classical force field.^{44,45} This approach has been used to model the structures of TiC-CDCs and saccharose-based activated carbons, with the model structures showing structural heterogeneity with a range of non-hexagonal carbon rings detected in defective and curved carbon sheets. The second, *mimetic*, approach seeks to mimic the conditions of the carbon synthesis, and is more predictive than the reconstructive approach as the only input from experiment is the density. Here, monatomic carbon at high temperature (resembling a fluid) is cooled (quenched) in a molecular dynamics (MD) simulation to generate porous carbon structures.⁴⁶ In the simulations of Palmer *et al.*, different quench-rates gave rise to model structures ascribed to TiC-CDCs with different chlorine-treatment temperatures, qualitatively reproducing trends in specific surface area and porosity.⁴⁷ Simulated TEM images also showed some agreement with the experimental data. The model structures suggest that for a chlorine-treatment temperature of 800 °C, the carbon is highly disordered with few connected carbon rings,

while at 1200 °C, the structure consists of large curved carbon sheets (Figure 2.5). It should be kept in mind that these simulations do not take into account any functional groups in the carbon (*e.g.*, ketones, epoxides, alcohols *etc.*), which are known to exist in small amounts.²⁸

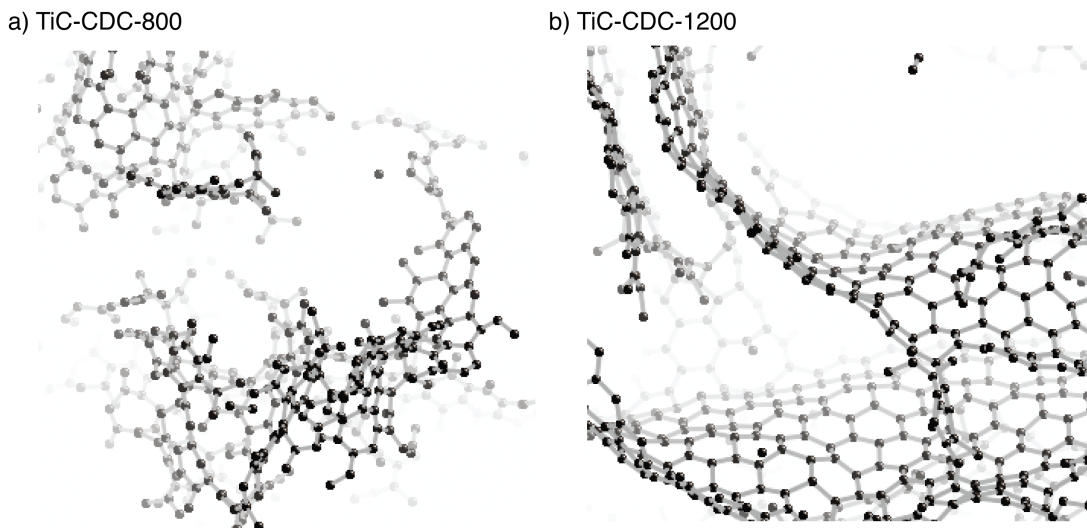


Figure 2.5 Model TiC-CDC structures generated by quenched molecular dynamics structures by Palmer *et al.*⁴⁷ The simulated structure for TiC-CDC-1200 consists of curved carbon sheets (b), while the structure of TiC-CDC-800 is more disordered with smaller carbon fragments observed (a).

One of the most common experimental techniques used to probe the structures of porous carbons is Raman spectroscopy. Raman spectra of porous carbons typically exhibit two main bands, the D-band ($\sim 1350 \text{ cm}^{-1}$) and the G-band ($\sim 1580 \text{ cm}^{-1}$),²⁸ see an example in Figure 2.6. When graphite is studied, only the G-band is observed,⁴⁸ and so this band has been associated with ordered graphene sheets. The D-band, on the other hand, is associated with defects or disorder in the carbon sheets, with the full-width at half-maximum (FWHM) of this peak giving a measure of disorder in the carbon-carbon bonding. Dash *et al.* showed that as the chlorine-treatment temperature of TiC-CDCs was increased, the D-band (and G-band) FWHMs decreased, consistent with an increase in ordering in the carbon-carbon bonding.³³ The intensity ratio of the D- and G-bands can give a measure of the crystallite size (in the in-plane direction) for nano-crystalline graphite,^{48,49} though caution has to be applied when extending this interpretation to porous carbons, as these do not consist of graphitic nano-crystals.²⁸

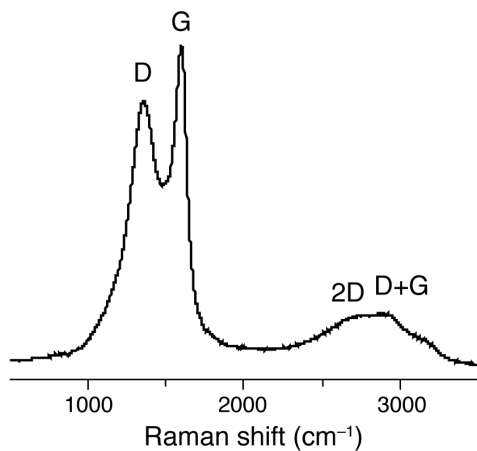


Figure 2.6 Raman spectrum of TiC-CDC-600, with the D and G bands clearly visible.

The porosity of the carbon is an important characteristic in determining its performance as a supercapacitor electrode material. Pore size distributions are typically extracted from gas sorption isotherms. Samples are first outgassed by heating in a vacuum, before being cooled to 77 K. A small amount of gas (typically N₂ or Ar) is then introduced into the system, with the amount of adsorbate (mass or volume) measured after equilibration. After many more measurements with the gradual addition of gas, the adsorption isotherm is obtained, which is the build-up of the amount of adsorbed gas against the relative pressure (p/p_0). The reverse process is then carried out with slow reductions in gas pressure to obtain the desorption isotherm. A schematic gas sorption isotherm is shown in Figure 2.7a for a purely microporous carbon material (a type I isotherm according to the IUPAC classification).⁵⁰

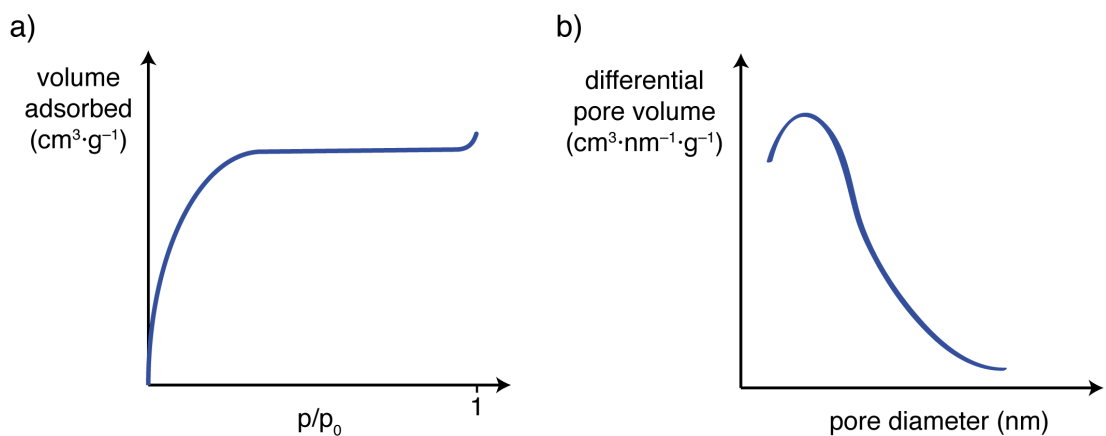


Figure 2.7 (a) Schematic adsorption isotherm for a purely microporous carbon. (b) Schematic pore size distribution.

The adsorption isotherm is then converted to a pore size distribution (Figure 2.8b), which corresponds to solving:

$$\Gamma(P) = \int_{H_{\min}}^{H_{\max}} \Gamma(H, P) f(H) dH \quad [2.13]$$

Where $\Gamma(P)$ is the adsorption isotherm, $\Gamma(H, P)$ is the model adsorption isotherm for a pore of size H , $f(H)$ is the pore size distribution, and the limits H_{\max} and H_{\min} are the maximum and minimum pore sizes considered in the analysis.^{51,52} In the classical density functional theory (DFT) approach developed by Lastoskie *et al.*, and later Neimark *et al.*,^{51,53} it is assumed that the carbon consists of non-interconnected slit-shaped pores, with chemically homogeneous graphitic surfaces. The model isotherms $\Gamma(H, P)$ are obtained using a classical density functional theory approach, whereby the density profile of the adsorbed gas inside a pore is calculated at different pressures by minimising a potential function. The assumptions underlying this method should be kept in mind when interpreting the pore size distributions. One particularly interesting point, noted by Dombrowski *et al.*, is that different carbon pore size distributions may be obtained when using N₂ and Ar sorption isotherms measured on the same material.⁵² This may be due to chemical interactions of N₂ with functional groups in the carbon.

2.4 The Effects of Carbon Porosity on Capacitance

Much of supercapacitor research today involves the development of new electrode materials with improved capacitance, to increase the amount of energy that can be stored by devices (Equation 2.12). Initial research efforts focused on increasing the specific surface area of carbon electrode materials to increase their capacitance (Equation 2.3).⁵⁴ In 2006, the importance of the carbon pore size was highlighted in the seminal work of Chmiola *et al.*³¹ A large increase in the capacitance of TiC-CDC was reported as the pore size was decreased below 1 nanometre, using the electrolyte NEt₄BF₄ in acetonitrile (1.5 M). As illustrated by Figure 2.8, the specific capacitance increased as the chlorine-treatment temperature (and thus average pore size) was decreased. This was despite decreases in the specific surface area. Capacitances normalised by the carbon surface area (determined using Brunauer–Emmett–Teller (BET) theory) were also reported, whereby the capacitance increase at small pore sizes appeared more marked.

These results showed the importance of carbon pore size, and challenged the previous view that pores smaller than the solvated electrolyte ions do not contribute significantly to the capacitance. Indeed, the average pore sizes studied were all smaller than the solvated cation and anion sizes (1.30 and 1.16 nm respectively).⁵⁵ It was hypothesised

that ion desolvation allows a closer approach of charge centres at the electrode-electrolyte interface, reducing the charge separation distance and increasing the capacitance (Equation 2.3).⁵⁶ To probe the relationship between ion size and pore size in the absence of a solvent, the capacitance of TiC-CDC was measured using an ionic liquid electrolyte.⁵⁷ The pore size that resulted in the largest capacitance was very similar to the largest dimension of the anions and cations (which were of similar size), again illustrating the importance of pore size effects.

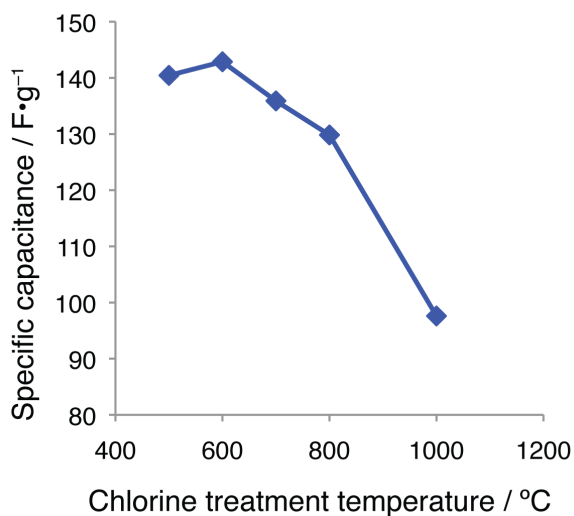


Figure 2.8 Specific capacitances of TiC-CDCs (NEt_4BF_4 1.5 M in acetonitrile electrolyte) with different chlorine-treatment temperatures and pore sizes. As the pore size is decreased, an anomalous increase in capacitance is observed.

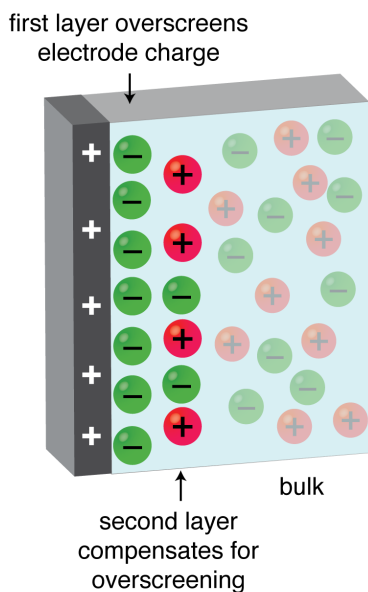
While other work on activated carbons has measured similar increases in capacitance as the carbon pore size was decreased,⁵⁸ Centeno *et al.* have reported that there is no correlation between pore size and capacitance.^{59,60} They stressed that surface areas determined using BET theory are inaccurate for microporous carbons, and capacitances should not be normalised by this quantity. However, in the work of Chmiola *et al.*, the anomalous capacitance increase was also observed in the absence of any surface area normalisation, and the cause of the conflicting findings on pore size effects therefore remains unclear. Clearly further experiments and theoretical work could help understand the different findings of these studies.

2.5 Molecular Modelling of Supercapacitors

Molecular modelling studies have greatly progressed the understanding of charge storage in supercapacitors. MD studies of planar electrodes with ionic liquid electrolytes have revealed that the first adsorbed layer of counter-ions carries a greater charge than

the electrode surface.^{61,62} A second layer of ions of opposite polarity (co-ions) then counter-balances the excess charge in the first layer. This so-called “overscreening” effect may extend over several layers of ions. Figure 2.9a schematically illustrates overscreening effects away from a charged planar carbon surface. A MD study of an organic electrolyte at a charged graphite surface revealed that the presence of acetonitrile solvent decreases the extent of layering away from the surface.⁶³ These recent pictures of ionic layering differ from Stern’s classical theory of dilute electrolytes (Figure 2.9b). Stern combined the theory of a well-defined layer of ions at the surface (introduced by Helmholtz) with the theory of a diffuse layer (of Gouy and Chapman) in which the excess ionic charge in the solution decreases exponentially away from the surface.¹⁹

a) Overscreening effects



b) Stern model

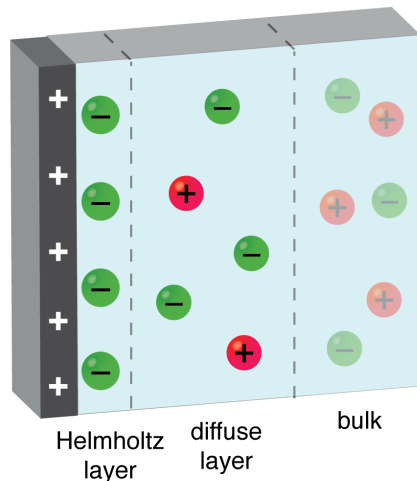


Figure 2.9 (a) Schematic illustrating overscreening effects away from a charged planar surface. The first layer of ions in the electrolyte overcompensates for the charge stored in the electrode. A subsequent layer (or layers) then counter-balances the excess charge in the first layer before reaching bulk behaviour. (b) The classical Stern model of the electric double-layer.

Theories for planar electrodes cannot readily be applied to porous carbon materials, where the pore size is often on the order of the ion size. Advanced theoretical studies have therefore been carried out on slit-pore systems. Two separate studies (one based on MD simulations and the other on classical density functional theory calculations) showed that the capacitance varies in an oscillatory manner as the pore size is varied.^{64,65} This oscillatory behaviour was explained by considering the overlap of the electric double-layers arising from the two pore walls, resulting in high (or low)

capacitance when the overlap of regions of cations and anions is constructive (or destructive). This work showed good agreement with some experiments,^{31,57} and suggested that the lack of correlation between capacitance and average pore size in other studies might be related to the broad pore size distributions of the studied carbons.

A further study of slit-pores introduced the concept of a superionic state to explain the increase in capacitance observed with decreasing pore size in TiC-CDC.⁶⁶ It was proposed that packing of ions of like charge within the pores is facilitated by image forces arising from the pore walls. As the pore size is decreased, such image forces allow denser ion packing and more efficient capacitive charge storage.⁶⁷ Not only did this work help to explain the anomalous increases in capacitance observed experimentally, but it also predicted an interesting voltage-induced phase transition, with a sudden expulsion of ions of the incorrect charge (for storing energy) from the pores.

More advanced molecular simulation methods have recently been developed to model charge storage in porous nano-structured carbons.^{68–72} In one study, MD simulations were carried out to probe capacitive charge storage in simulated CDC structures with an ionic liquid electrolyte.⁶⁸ The simulations displayed high specific capacitances for the model CDCs, with charge storage taking place via the exchange of anions and cations in and out of the carbon pores. For example in the positive electrode, counter-ions (anions) were adsorbed into the carbon pores, while co-ions (cations) were ejected. The absence of overscreening effects inside the nano-sized carbon pores was proposed to explain the high capacitances calculated for porous carbons, compared to graphite. These simulations have also shown how ions can occupy a range of different adsorption sites in porous carbons, with the most confined ions storing charge more efficiently.⁷³

More recent work has introduced the idea of ionophilic and ionophobic carbon pores.^{74–76} The former are filled with electrolyte ions in the absence of an applied potential, while the latter are not. The charging dynamics of slit-pores were shown to depend on their ionophilicity/ionophobicity, with charging of ionophobic pores proceeding in a front-like manner, leading to faster charging than for ionophilic pores, where charge storage was found to proceed via a diffusive ion exchange process.⁷⁶

Despite recent experimental and theoretical developments, more work is required to understand the ion environments and the molecular mechanisms of charge storage in

porous carbons. In particular, experimental techniques must be developed to test the interesting predictions from theoretical studies.

2.6 New Experimental Methods to Study Supercapacitance

Currently, there are relatively few experimental methods available to study the molecular mechanisms of charge storage in supercapacitors. Atomic force microscopy and surface force balance methods have been used to probe layering effects at charged planar surfaces,^{77–80} and show agreement with the results from molecular simulations described above. These techniques, however, are not able to probe adsorption processes in porous materials.

Infrared (IR) spectroscopy has recently been demonstrated as a new tool to probe supercapacitor charging.^{81,82} Here, changes in intensity of the absorbances from bond vibrations in the electrolyte anions and cations are monitored during charging, allowing the behaviour of the two ions to be tracked separately. For experiments on TiC-CDC supercapacitors with ionic liquid electrolytes, losses of intensity were observed for both the anion and cation absorbances during charging, suggesting that both ions penetrated deeper into the carbon particles, beyond the depth to which the IR photons were able to penetrate.⁸¹ Further experiments on carbon nanofibres revealed an ion exchange mechanism, whereby counter-ions penetrated into the carbon particles, while co-ions were ejected.⁸² While this method has offered new insights, precise information about the local environments of the detected ions cannot easily be obtained.

Electrochemical quartz crystal microbalance (EQCM) studies have also recently been applied to study supercapacitors.⁸³ In these experiments, supercapacitor electrodes are cast onto quartz crystals with resonance frequencies that are sensitive to changes of the loaded mass. Changes of the quartz crystal frequency during supercapacitor charging can be correlated to mass changes, and therefore ion adsorption processes in the electrodes. These experiments have revealed that the charge storage mechanism can vary depending on the studied voltage range.^{84,85} For low charge densities, the observed mass changes were smaller than those calculated for a pure adsorptive processes, and were therefore interpreted as arising from ion exchange processes. On the other hand, for higher applied potentials, the measured mass changes were in agreement with a purely counter-ion adsorption-driven charging mechanism.^{84,85} Experiments also revealed that the range of potentials that these mechanisms operate in can be sensitive to the electrolyte studied.⁸⁴ Moreover, mass changes have been used to infer average ion-

solvation numbers,^{85,86} though this procedure assumes that only counter-ions are adsorbed during charging, and that the co-ions do not play any role in the charge storage process. Despite the successes of the EQCM approach, it is difficult to unambiguously separate processes from the adsorption/desorption of the anions, cations and solvent with a single measured parameter (the electrode mass).

Beyond EQCM and IR spectroscopy, diffraction-based methods have also shown promise for the study of supercapacitors. Small angle neutron scattering experiments by Boukhalfa *et al.* have suggested that an ion exchange charging mechanism operates for both aqueous and organic electrolytes in activated carbon electrodes.^{87,88} An interesting feature of these measurements is that adsorption/desorption processes can be monitored as a function of the pore size, with the largest changes observed for the smallest pores. A more recent study by Prehal *et al.* using small angle x-ray scattering revealed similar effects.⁸⁹

NMR spectroscopy is a further powerful tool for the investigation of the local structure and dynamics of electrode–electrolyte interfaces in a non-invasive and element-selective way. This latter feature allows the separate observation of different species (such as cations, anions and solvent) in electrochemical systems. NMR spectroscopy has found many uses in understanding the chemistries of lithium-ion batteries, monitoring processes such as dendrite formation in symmetrical lithium-lithium cells, intercalation in graphitic electrodes, and conversion reactions in silicon electrodes^{15,16,90–92} More recently, some of the first NMR studies of supercapacitors have been carried out.^{17,18,93} These measurements have demonstrated that species adsorbed inside the carbon pores can be observed separately from those in bulk electrolyte. Charging experiments carried out on disassembled supercapacitor cells (*ex situ* measurements) suggested that ion exchange processes take place during charging.¹⁸ In addition, the first *in situ* studies on working supercapacitors have recently been carried out.¹⁷ While these first studies are very promising, there is considerable scope for further development and application of the NMR approach for studying supercapacitors. So far only a few activated carbons have been studied, with little systematic variation of the properties of the electrode, and with only organic electrolytes studied.

2.7 Aims of This Thesis

The main aim of this thesis is to develop and apply the NMR approach for studying supercapacitors, both to quantify the effects of the electrode and the electrolyte on the charge storage mechanisms. Specifically, the aims are to:

- Study electrolyte adsorption by NMR in a range of model carbon materials including TiC-CDCs and activated carbons.
- Understand how the carbon structure influences the form of the NMR spectra for electrolyte-soaked carbons.
- Carry out charging experiments using NMR spectroscopy on new electrolytes such as ionic liquids.
- Investigate ion dynamics using NMR and relate these to the charging rates of supercapacitors.
- Develop the *in situ* NMR approach for the quantitative study of the charging mechanisms of working supercapacitors.
- Develop new NMR methods for the selective observation of the charge storing ions in supercapacitors.

Chapter 3

Nuclear Magnetic Resonance Spectroscopy

Nuclear Magnetic Resonance (NMR) spectroscopy is the main technique used in this thesis. This section begins by reviewing some of the basic theory, before exploring some of the theory more pertinent to NMR studies of ion adsorption on carbon.

3.1 The Zeeman Interaction

Nuclei possess a nuclear spin, specified by the quantum number, I . There are $2I + 1$ different energy levels, specified by the quantum number, m_I , which is integer or half integer and may be negative or positive. In the presence of an applied magnetic field, these energy levels become non-degenerate due to the nuclear Zeeman interaction. For the simplest case of $I = \frac{1}{2}$, as for ^1H and ^{13}C , there are two energy levels, with $m_I = \frac{1}{2}$ and $m_I = -\frac{1}{2}$. In NMR spectroscopy, the transitions between these energy levels are observed as the Larmor frequency, ω_0 ($\text{rad}\cdot\text{s}^{-1}$), which is given by:

$$\omega_0 = -\gamma B_0 \quad [3.1]$$

for a nuclear spin with gyromagnetic ratio γ (measured in units of $\text{rad}\cdot\text{s}^{-1}\cdot\text{T}^{-1}$) in an applied magnetic field B_0 (T).

3.2 Interactions in NMR

3.2.1 Chemical shielding

By Equation 3.1, all nuclei of a particular isotope will give rise to the same Larmor frequency; however, NMR spectra often exhibit several resonances at different frequencies. This is because the nuclear spins do not interact with the applied magnetic field alone. Spins may also interact with: the magnetic fields arising from the circulation of nearby electrons (chemical shielding), other nearby nuclear spins (via J couplings

through bonds, and dipolar couplings through space), and, for nuclei with $I > \frac{1}{2}$, electric field gradients (via quadrupolar coupling).

Chemical shielding arises from the circulation of electrons around the nucleus in the presence of the applied magnetic field. This circulation induces a local magnetic field, specified as, B_{ind}^i , for a nucleus i , given by:

$$B_{ind}^i = -\sigma^i B_0 \quad [3.2]$$

Where σ^i is the chemical shielding for nucleus i (strictly a second-rank tensor).⁹⁴ The effective magnetic field experienced by the nucleus, B_{eff}^i , is then the sum of the applied magnetic field and the induced magnetic field at that nucleus:

$$B_{eff}^i = B_0 + B_{ind}^i = B_0(1 - \sigma^i) \quad [3.3]$$

Thus nuclei in different local environments experience different local magnetic fields and therefore exhibit different resonance frequencies. Consider for example the ¹H NMR spectrum of ethanol (CH₃CH₂OH), where a separate resonance is observed for each of the three chemically distinct types of hydrogen. For a nucleus i , the observed resonance frequency, ω_{obs}^i , is given by:

$$\omega_{obs}^i = -\gamma B_{eff}^i = -\gamma B_0(1 - \sigma^i) \quad [3.4]$$

To remove the field dependency of NMR frequencies and to obtain more manageable numbers, frequencies are normally expressed as the chemical shift, δ_{ppm}^i , defined as:

$$\delta_{ppm}^i = 10^6 \times \frac{\omega_{obs}^i - \omega_{ref}}{\omega_{ref}} \quad [3.5]$$

Where ω_{ref} is the observed frequency of a reference molecule, typically tetramethylsilane for ¹³C and ¹H NMR.

The chemical shielding interaction is in general anisotropic with respect to the direction of the applied magnetic field. The chemical shielding for a nucleus i , σ^i , can be described by a second-rank tensor of the form:

$$\sigma^i = \begin{pmatrix} \sigma_{xx}^i & \sigma_{xy}^i & \sigma_{xz}^i \\ \sigma_{yx}^i & \sigma_{yy}^i & \sigma_{yz}^i \\ \sigma_{zx}^i & \sigma_{zy}^i & \sigma_{zz}^i \end{pmatrix} \quad [3.6]$$

Expanding Equation 3.2, with the magnetic field along the laboratory z -axis, the result is:

$$\begin{pmatrix} B_{ind,x}^i \\ B_{ind,y}^i \\ B_{ind,z}^i \end{pmatrix} = - \begin{pmatrix} \sigma_{xx}^i & \sigma_{xy}^i & \sigma_{xz}^i \\ \sigma_{yx}^i & \sigma_{yy}^i & \sigma_{yz}^i \\ \sigma_{zx}^i & \sigma_{zy}^i & \sigma_{zz}^i \end{pmatrix} \cdot \begin{pmatrix} 0 \\ 0 \\ B_0 \end{pmatrix} = \begin{pmatrix} -\sigma_{xz}^i B_0 \\ -\sigma_{yz}^i B_0 \\ -\sigma_{zz}^i B_0 \end{pmatrix} \quad [3.7]$$

This equation shows that the induced magnetic field at a nucleus may be in any given direction relative to the applied magnetic field. Consider the example of benzene (Figure 3.1). The electrons readily circulate around the π orbitals, giving rise to induced magnetic fields that vary depending on the position of the studied nucleus and the orientation of the molecule relative to the applied magnetic field.

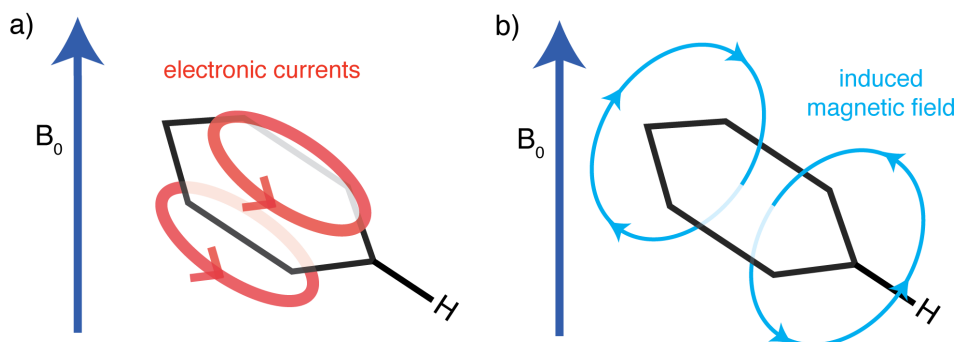


Figure 3.1 (a) Schematic showing the circulation of π electrons induced in a benzene molecule by a magnetic field, and (b) the resulting induced magnetic field. In general the induced magnetic field is in a different direction from the applied field and depends on the relative orientations of the molecule and the magnetic applied field.

A different chemical shielding tensor is needed for each nucleus in a molecule in general. For each nucleus, there exists a principal axis system (X, Y, Z), such that if the applied magnetic field is aligned along any of the three principal axes, the resulting induced field at the nucleus is parallel to the applied magnetic field.⁹⁴ For example, in the case that the applied magnetic field is aligned along the X principal axis, the induced field is given by:

$$B_{ind}^i = -\sigma_{XX}^i B_0 \quad [3.8]$$

If the applied magnetic field is applied along Y:

$$B_{ind}^i = -\sigma_{YY}^i B_0 \quad [3.9]$$

And if it is aligned along the Z-axis:

$$B_{ind}^i = -\sigma_{ZZ}^i B_0 \quad [3.10]$$

The elements σ_{XX}^i , σ_{YY}^i and σ_{ZZ}^i are known as the principal components of the chemical shielding tensor. All other elements of this tensor are zero in the principal axis system. For an isotropic liquid with rapid molecular tumbling, the isotropic chemical shielding (and therefore chemical shift) is observed:⁹⁴

$$\sigma_{iso}^i = \frac{1}{3}(\sigma_{XX}^i + \sigma_{YY}^i + \sigma_{ZZ}^i) \quad [3.11]$$

The resonance frequency is then given by:

$$\omega_{iso}^i = -\gamma B_0 (1 - \sigma_{iso}^i) \quad [3.12]$$

However, in solids (or anisotropic liquids, such as liquid crystals) the situation is more complex. For a single crystal of a molecular solid, the molecules occupy lattice sites, and in the simplest case all molecules have the same orientation with respect to the applied magnetic field. A single chemical shielding (and therefore chemical shift) is then observed for a given chemical environment, which depends on the orientation of the crystal (strictly the principal axis system of the studied nuclear spin) relative to the applied magnetic field direction, and the chemical shielding tensor of that site (Figure 3.2a). For a powdered crystalline material, the observed spectrum is the superposition of the resonances arising from each crystallite (Figure 3.2b), with the resulting spectrum referred to as a powder pattern. The form of the powder pattern depends on the form of the chemical shift tensor, with the sharp corners of the lineshape coinciding with the principal values of the tensor. The chemical shift anisotropy, δ_{aniso}^i , and the asymmetry, η^i , for a nucleus i , are useful parameters which relate to the form of the tensor, and are given by:

$$\delta_{aniso}^i = \delta_{ZZ}^i - \delta_{iso}^i \quad [3.13]$$

$$\eta^i = \frac{\delta_{YY}^i - \delta_{XX}^i}{\delta_{aniso}^i} \quad [3.14]$$

Where δ_{iso}^i is the isotropic chemical shift, and δ_{ZZ}^i , δ_{YY}^i , and δ_{XX}^i , are the principal components of the chemical shift tensor, with their order defined as:

$$|\delta_{ZZ}^i - \delta_{iso}^i| \geq |\delta_{XX}^i - \delta_{iso}^i| \geq |\delta_{YY}^i - \delta_{iso}^i| \quad [3.15]$$

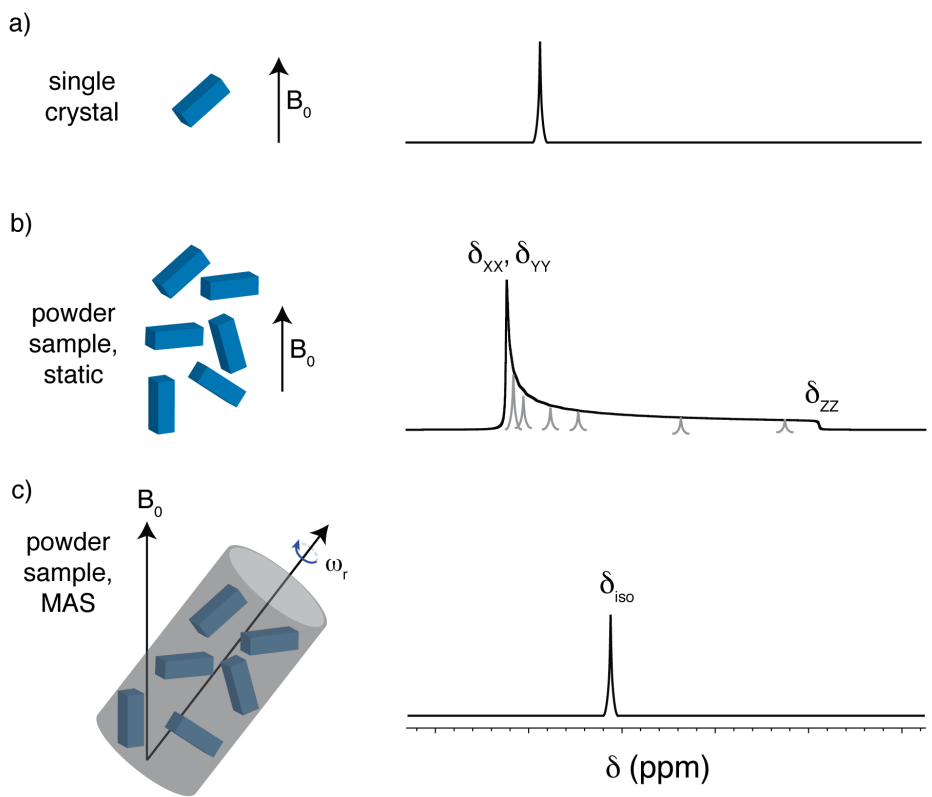


Figure 3.2 (a) Schematic static NMR spectrum of a single crystal. (b) Static NMR spectrum of a powdered crystalline material for a chemical environment where a powder pattern is observed (note, here $\eta^i = 0$). Grey lines show contributions from individual crystallites. (c) Schematic showing the effects of MAS, which solely reveals a resonance at the isotropic chemical shift for a sufficiently fast spinning frequency.

In general, the effects of the chemical shift anisotropy lead to complicated NMR spectra with many overlapping broad resonances. To improve spectral resolution, experiments on solids are normally carried out with magic angle spinning (MAS), whereby the sample is physically rotated around an axis at an angle of 54.74° to the applied magnetic field direction. This mimics the effects of isotopic tumbling present in the solution state and averages out the anisotropic part of the chemical shift.⁹⁵ For sample spinning frequencies much larger than δ_{aniso}^i , a single sharp resonance is observed at the isotropic chemical shift (Figure 3.2c). For lower spinning frequencies however, a series of “spinning sidebands” are observed at frequencies given by $\omega_{iso}^i + k\omega_r$, where ω_r is the sample spinning speed and k is an integer.

3.2.2 Inter-nuclear couplings

In addition to the interactions of the nuclei with the surrounding electrons, the nuclei may also interact with each other. The nuclear spins act as small magnetic dipoles that can interact either *directly* (dipolar coupling) or *indirectly* in a way that is mediated by electrons in bonds (J coupling). Here, the focus is on the dipolar coupling, which is analogous to the classical interaction between two bar magnets.

It can be shown that the dipole-dipole coupling interaction (in $\text{rad}\cdot\text{s}^{-1}$) between two nuclear spins, j and k , depends on the following parameter:⁹⁴

$$d_{jk} = -\frac{1}{2} \frac{\mu_0}{4\pi} \frac{\gamma_j \gamma_k \hbar}{r_{jk}^3} (3\cos^2 \Theta_{jk} - 1) \quad [3.16]$$

Where γ_j and γ_k are the gyromagnetic ratios of the two spins, μ_0 is a magnetic constant, \hbar is the reduced Planck constant, r_{jk} is the distance between the spins and Θ_{jk} is the angle between the vector joining the spins and the applied magnetic field direction (see Figure 3.3).

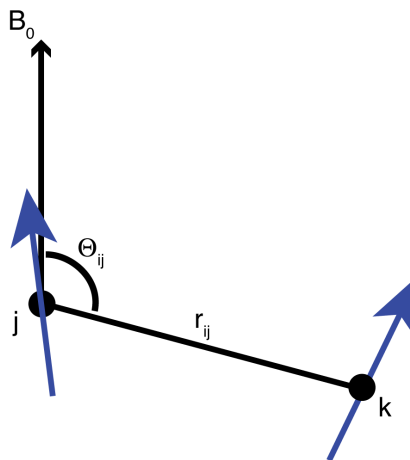


Figure 3.3 Schematic showing the key parameters that determine the dipole-dipole interaction between two nuclear spins, j and k .

Equation 3.16 demonstrates a number of the key features of the dipole-dipole coupling interaction. First, the interaction is strongest for spins that are close in space, and decays rapidly as the distance between the spins is increased. Second, dipole-dipole couplings are strongest when both nuclei have large γ values. Third, the interaction depends on the angle between the vector joining the nuclear spins and the applied magnetic field direction, such that motion affects its strength. This causes the dipole-dipole coupling interaction to average to zero for isotropic liquids,⁹⁴ but couplings are generally retained

in the solid state. Here, the presence of homonuclear dipolar couplings tends to broaden the NMR spectra of abundant high γ nuclei such that it is very difficult to resolve the different sites in static NMR experiments. Magic angle spinning (see above) however, averages the $(3\cos^2 \Theta_{jk} - 1)$ term to zero, and provided the spinning rate is fast compared to the magnitude of the dipole-dipole couplings, relatively narrow spectral lines can be obtained.

3.2.3 Bulk magnetic susceptibility effects

A further internal interaction can arise from the magnetic susceptibility of the NMR sample, depending on its bulk (macroscopic) shape. When a sample is placed inside a magnetic field, a magnetisation develops inside it. The developed magnetisation depends on the sample's magnetic susceptibility (χ), which arises primarily from the magnetic properties of the electrons, and the strength of the applied magnetic field.⁹⁶ For diamagnetic materials (negative χ) the magnetisation develops in a direction opposite to the applied magnetic field, while for paramagnetic materials (positive χ) the developed magnetisation is in the same direction as the applied field. The developed magnetisation itself has a magnetic field associated with it that affects the magnetic field in the sample, giving rise to a so-called demagnetising field.⁹⁴

For a homogeneous spherical sample, the demagnetising field is homogeneous and does not depend on the orientation of the magnetic field with respect to the sphere. For an ellipsoid sample, the demagnetising field is again homogeneous, but now depends on the orientation of the field relative to the sample.⁹⁷ As a result, there is a so-called bulk magnetic susceptibility (BMS) shift, but there is no line broadening. For a homogeneous sample of arbitrary shape, there is generally both a BMS shift and a broadening, which both depend on the shape of the sample, and its orientation relative to the applied magnetic field.^{97,98} This arises from variations in the demagnetising field in different regions of the sample. BMS effects are generally treated by considering a sphere within the sample, inside which there is no BMS effect, and separately the rest of the sample (minus the spherical hole) that gives rise to BMS effects. Long-range contributions are then considered (and summed) from all other volume elements in the rest of the sample (which act as point dipoles) to compute the BMS shift and broadening.^{97,98} For sample geometries where exact solutions of the classical magnetostatic equations are not available, the approach of Salomir *et al.* allows the rapid estimation of the magnetic

field inhomogeneity arising from a sample of arbitrary shape and magnetic susceptibility.⁹⁹

For solution-state NMR experiments the effects of magnetic susceptibility are typically very small (< 1 Hz) but this may be the factor that limits resolution. In solids, on the other hand, the susceptibility broadening is typically insignificant compared to other sources of linewidth such as the chemical shift anisotropy and dipolar coupling. However, when static liquid samples contained within solids with irregular geometries are studied, significant BMS shifts and broadenings can be observed, as in studies of liquid crystal films¹⁰⁰ and biomembranes confined between glass plates.^{98,101}

3.3 The Vector Model

Here a brief introduction is given to the vector model of NMR; a helpful construct for understanding how pulsed NMR experiments work.¹⁰²

Real samples have many nuclear spins. Since the thermal energy is typically large compared to the energy separation of the m_I levels, there exists only a small excess of spins in the lower energy m_I level. The excess is larger for nuclei with larger gyromagnetic ratios, or when stronger magnetic fields are used. This excess manifests itself as a magnetisation, M , along the laboratory z-axis, and it is this that is manipulated in pulsed NMR experiments (Figure 3.4a). If this magnetisation is manipulated such that it lies in the laboratory xy plane (then referred to as transverse magnetisation), it tends to precess about the z -axis at a frequency given by Equation 3.4.

Rotation of the magnetisation away from its equilibrium position along the z -axis is achieved by the application of a radio frequency pulse along the x (or y) axis, with a frequency very similar to the Larmor frequency of the nucleus under study. Consider the application of a linearly oscillating magnetic field along the x -axis, with frequency, ω_1 , and strength, B_1 . This field may be decomposed into two counter-rotating fields with frequencies $+\omega_1$, and $-\omega_1$. Only the component rotating in the same sense as the Larmor precession has any significant effect,¹⁰² and so only this is considered the following discussion.

The complex behaviour of the magnetisation in the presence of the applied magnetic field and the radio frequency pulse may be simplified by moving to a frame rotating at a frequency ω_1 , with axes x' , y' and z' . The positively rotating component of the radio frequency field now appears to be static along the x' -axis (Figure 3.4b). Moreover, the

applied magnetic field, B_0 , appears as a reduced field, B_{red} , along the z' -axis in this rotating frame (Figure 3.4b). The corresponding frequency is given by the offset, Ω^i :

$$\Omega^i = \omega_{obs}^i - \omega_1 \quad [3.17]$$

Provided that ω_1 is sufficiently similar to ω_{obs}^i , then B_{red} is small compared to B_1 and has a negligible effect during the application of a pulse. The application of the pulse can now be seen to rotate the magnetisation away from the z' -axis towards the $-y'$ -axis (Figure 3.4b). If the pulse is applied for the right amount of time, the magnetisation will reside along the $-y'$ -axis after the application of the pulse, a so-called 90° pulse. Following the application of this pulse, the magnetisation then precesses in the $x'y'$ plane due to the reduced field at the offset frequency (Figure 3.4c).

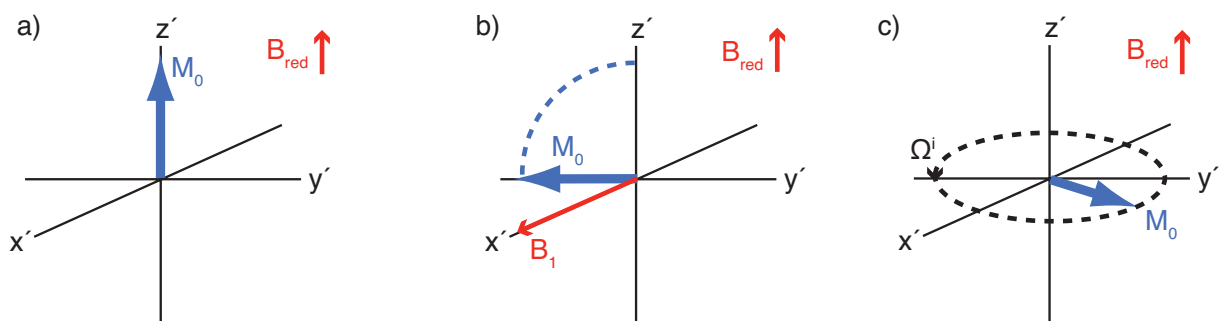


Figure 3.4 The vector model of NMR spectroscopy, viewed in the rotating frame. (a) Equilibrium magnetisation, (b) effect of a 90° pulse, and (c) precession of the magnetisation vector at the offset frequency.

The frequency of this precession is measured as the free induction decay (FID), and Fourier transformation yields the NMR spectrum. Different nuclear environments then appear as peaks with different chemical shifts. The experiment outlined here is referred to as a pulse-acquire experiment, or a one-pulse experiment. In practice, many scans are recorded to increase the signal to an acceptable level above the background noise.

The rate at which scans can be repeated depends on the time taken for the magnetisation to return to the equilibrium state shown in Figure 3.4a. The process by which this takes place is referred to as longitudinal (or spin-lattice) relaxation, and is characterised by the longitudinal relaxation time constant, T_1 . For quantitative spectra to be acquired, the time between successive scans in the NMR experiment must be greater than $5T_1$.¹⁰²

3.4 Techniques in NMR

3.4.1 Spin echo experiments

Beyond the pulse-acquire experiment described above, one of the most common pulse sequences in NMR is the spin echo experiment (Figure 3.5). Here a 90° pulse is first applied to generate transverse magnetisation. During a delay time, τ , the magnetisation vectors precess according to their offset frequencies, generating phase differences given by $\Omega_i\tau$ (see time-point 2, Figure 3.5). A 180° pulse then changes the phase of the spins to $(2\pi - \Omega_i\tau)$ (time-point 3). Finally, a further period of free precession for a time τ leaves the phases of all the spins as 2π , equivalent to 0. The spin echo pulse sequence is therefore said to “refocus” the magnetisation. Simple pulse-acquire experiments suffer from a practical problem whereby a certain dead time must be left between the 90° -excitation pulse and the start of signal detection (to allow the coil through which radio frequency pulses are delivered and in which signals are detected to “ring down”). This can lead to baseline distortions in the NMR spectra and loss of intensity for signals broadened by inhomogeneities in the magnetic field. With the spin echo experiment, these problems are avoided because the dead time is indirectly incorporated in the second τ delay.¹⁰³ Spin echo experiments have a further advantage that background signals arising from the NMR probe are suppressed. This is because these components are external to the NMR coil and experience weaker radio frequency pulses. This means that the 90° and 180° pulse lengths are significantly lengthened, and the refocusing effect described in Figure 3.5 is not achieved. A modified spin echo experiment, the “depth” experiment, essentially uses two spin echoes back-to-back to further reduce the intensity of probe background signals.¹⁰⁴

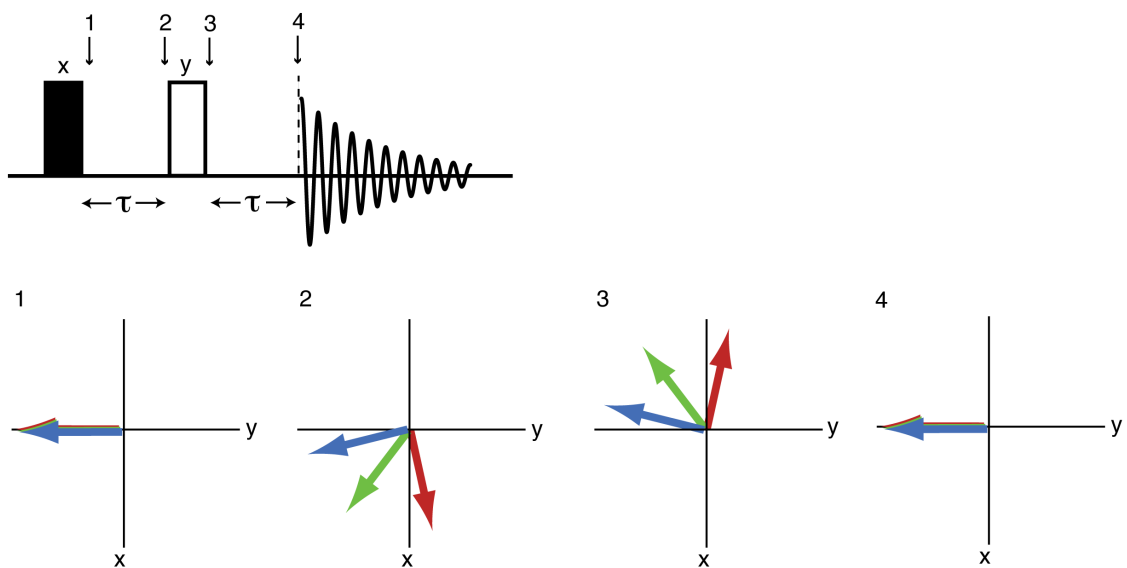


Figure 3.5 Pulse sequence for the spin echo experiment. Solid pulses represent 90° pulses, whereas unfilled pulses represent 180° pulses. The relative phases of the pulses are given (x , y etc.). Schematics show the positions of the magnetisation vectors in the rotating frame (with dashes on the axis labels now dropped for convenience) for three sites with different offset frequencies at different time points of the pulse sequence.

3.4.2 Relaxation time measurements

Another important NMR experiment is the measurement of the longitudinal relaxation time, T_1 . This may be done using the saturation recovery method (Figure 3.6). First a “saturation train” of 90° pulses separated by delays, d , (on the order of ms) is used to destroy the equilibrium magnetisation (see time-point 2, Figure 3.6). The magnetisation then begins to recover towards its equilibrium value during a delay time, τ , before being converted to transverse magnetisation by a 90° pulse and measured. Many experiments are carried out with different τ times, and the resulting signal, $I(\tau)$, is fitted to obtain the T_1 value according to:

$$I(\tau) = I_0 \left[1 - \exp\left(\frac{-\tau}{T_1}\right) \right] \quad [3.18]$$

Where I_0 is the signal obtained in the limit of complete longitudinal relaxation.

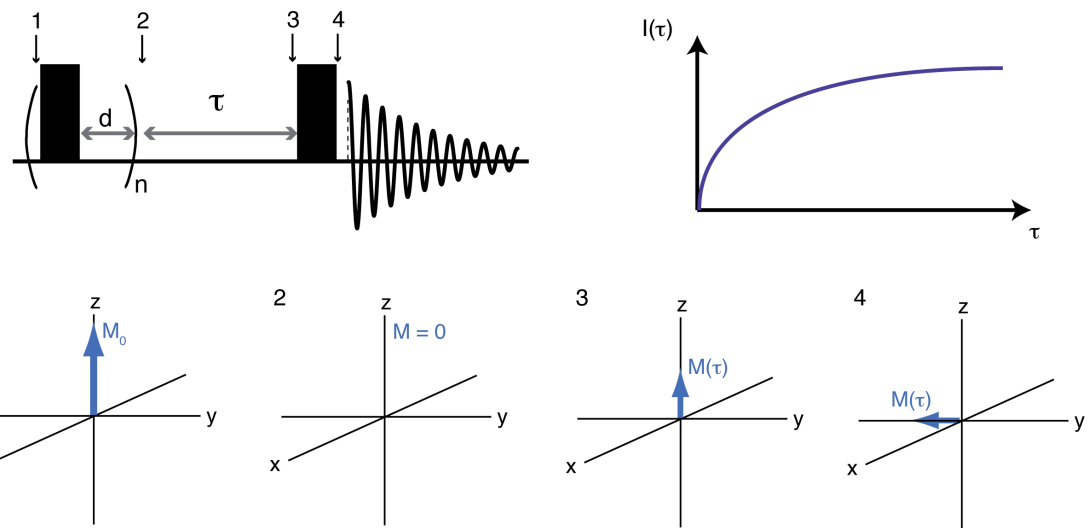


Figure 3.6 Saturation recovery pulse sequence for measuring T_1 . Schematics showing the form of the magnetisation vector for a single chemical environment are shown, as well as a schematic of the build-up of signal intensity as the time τ is varied.

3.4.3 Cross polarisation

Cross polarisation (CP) is typically used to boost the sensitivity of nuclei with low gyromagnetic ratios. Magnetisation is normally transferred from an abundant high γ nucleus, I, (such as ^1H or ^{19}F) to a low γ nucleus, S, (such as ^{13}C or ^{15}N) that is then detected. This results in a signal enhancement, the maximum value being given by γ_I/γ_S in theory.⁹⁵ Furthermore, it is often possible to repeat the scans more quickly in CP experiments (compared to direct excitation experiments on the low γ nucleus), as the T_1 relaxation times are typically much shorter for the more abundant high γ nucleus.⁹⁵

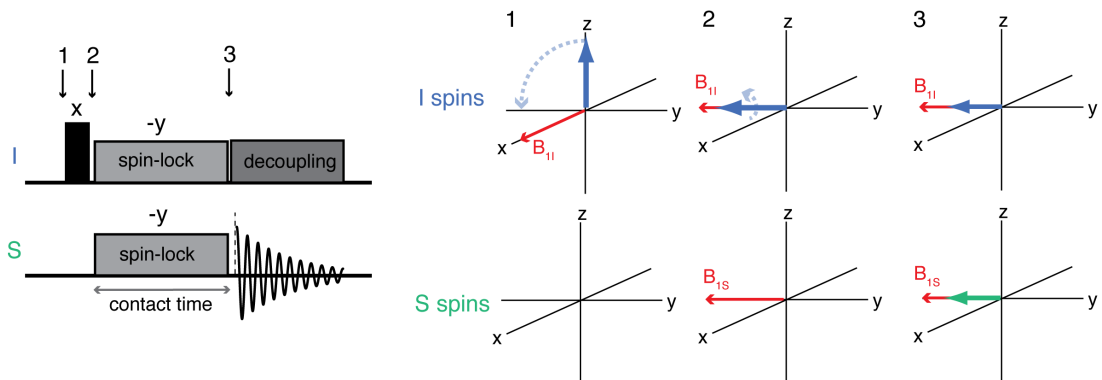


Figure 3.7 Pulse sequence for the CP experiment. Schematics show how the magnetisation is transferred from the I spins to the S spins (here the equilibrium magnetisation on the S spins is not shown for simplicity).

The standard pulse sequence for CP is shown in Figure 3.7. Following excitation of the I nuclei, “spin-locking pulses” are applied to both nuclei along the same axis on which

magnetisation was generated. These pulses suppress the free evolution of the I transverse magnetisation, and “lock” it on-axis in the rotating frame of reference. During the contact time (the time for which the spin-locking pulses are applied) it is possible for magnetisation to transfer from the I spins to the S spins via a heteronuclear dipole-dipole coupling mechanism, provided that the nutation frequencies, ω , under the contact pulses are equal for the two nuclei:

$$\omega_{1I} = \omega_{1S} \quad [3.19]$$

Which is the case when:

$$\gamma_I B_{1I} = \gamma_S B_{1S} \quad [3.20]$$

Which is the Hartman-Hahn matching condition.¹⁰³ Details regarding the quantum physics of the dipole-dipole coupling mediated transfer can be found in the review of Burum.¹⁰⁵ Following the magnetisation transfer, the NMR signal is detected on the S spins (note: a decoupling pulse is typically applied to the I spins during detection to suppress line broadening associated with heteronuclear dipole-dipole couplings). Under the conditions of magic angle spinning at a rate, ω_r , the Hartmann-Hahn matching condition is modified to:

$$\gamma_I B_{1I} = \gamma_S B_{1S} + n\omega_r \quad [3.21]$$

where n is an integer, normally 1 or 2.⁹⁵

The dipolar coupling mechanism of CP makes it a spatially selective experiment. S spins that are close to I spins have larger dipole-dipole couplings (Equation 3.16), and so experience a greater magnetisation transfer than more remote S spins. This makes CP a powerful source of structural information, and experiments are frequently used to aid with spectral assignments, or to perform spectral filtering.^{106,107} The signal obtained in CP experiments also depends on the dynamic motion of the I and S spins, given the orientation dependence of the dipolar coupling mechanism (Equation 3.16).

These effects make the quantification of different sites in CP spectra non-trivial and the signal must be measured in a series of experiments carried out with different contact times to study the CP kinetics. For transfer from abundant to dilute nuclei, the variation of the signal intensity with the contact time can generally be fitted by:¹⁰⁸

$$I(t) = A \left[\exp\left(\frac{-t}{T_{1\rho}(I)}\right) - \exp\left(-t\left(\frac{1}{T_{CP}} + \frac{1}{T_{1\rho}(S)}\right)\right) \right] \quad [3.22]$$

where t is the contact time, T_{CP} is a time constant associated with the magnetisation transfer from the I spins to the S spins, $T_{1\rho}(I)$ and $T_{1\rho}(S)$ are longitudinal relaxation time constants in the rotating frame, and A is a constant given by:

$$A = I_0 \left(1 + \frac{T_{CP}}{T_{1\rho}(S)} - \frac{T_{CP}}{T_{1\rho}(I)} \right)^{-1} \quad [3.23]$$

where I_0 is a constant that is proportional to the intensity that would be obtained in a direct excitation experiment for the species that undergo cross polarisation. By fitting these equations, the quantities of nuclei in different chemical environments undergoing cross polarisation can be determined. Moreover, the T_{CP} values give information about the dipolar coupling interactions.

To aid with the fitting of Equation 3.22, the relaxation constants $T_{1\rho}(I)$ and $T_{1\rho}(S)$ are normally measured in independent experiments. Here, magnetisation is generated by either direct excitation (Figure 3.8a) or CP (Figure 3.8b), and then a spin-locking pulse is applied for a time τ before recording the magnetisation via a 90° pulse. In general it is preferable to use the pulse sequence in Figure 3.8b, such that the $T_{1\rho}$ value is measured only for the nuclei that take part in the cross polarisation process. The delay time τ is varied and the exponential decay of the signal can then be fitted by:

$$I(\tau) = I_0' \left(\exp \frac{-\tau}{T_{1\rho}} \right) \quad [3.24]$$

where I_0' is the signal obtained with a spin-lock time of zero (Figure 3.8c).

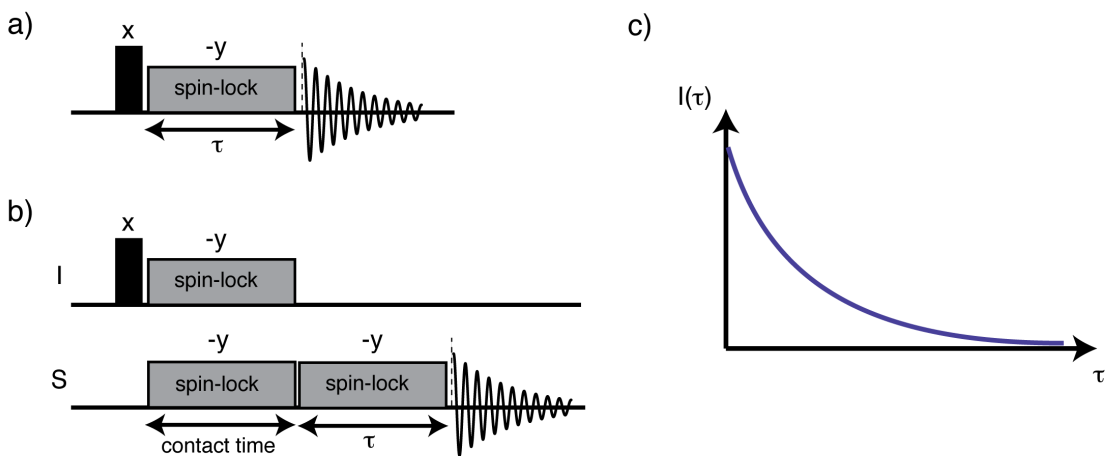


Figure 3.8 Pulse sequences for measuring $T_{1\rho}$; in each case measurements are made with different spin-lock times, τ . In (a) the signal is obtained by direct excitation, whereas in (b) signal is obtained by cross polarisation. (c) Typical exponential decay of the signal that allows a $T_{1\rho}$ value to be measured.

3.4.4 Two-dimensional NMR

In conventional one-dimensional (1D) NMR experiments, radio frequency pulses are used to prepare observable magnetisation that is then detected (Figure 3.9a). Fourier transformation gives a one-dimensional frequency spectrum, where the x-axis is frequency, f_2 , (or chemical shift) and the y-axis is intensity. In two-dimensional (2D) NMR experiments, the spectra have two frequency dimensions (f_1 and f_2), and the intensity is typically represented by a contour plot. (Figure 3.9b) In this case, experiments take the following general form: preparation of some magnetisation using radio frequency pulses and delays, evolution of magnetisation in the first time dimension (t_1), mixing of the magnetisation by some further pulses and delays, and finally, detection of the signal in the second time dimension (t_2) (Figure 3.9b). Importantly, detection of the signal occurs only in the t_2 dimension. The evolution of the signal in t_1 is measured indirectly by carrying out a series of experiments in which the t_1 time is incrementally increased (see Figure 3.9c). For example, in the first experiment, the t_1 time is set to 0, and the FID is recorded and stored. A second experiment is then carried out with the t_1 time set to Δ , with the FID again recorded and stored. Further experiments with a t_1 time of 2Δ , 3Δ and so on are recorded to produce an array of FIDs. Two-dimensional Fourier transformation then gives the 2D NMR spectrum.

The information that can be obtained from such experiments is best illustrated by an example. Consider a system whereby mobile nuclear spins may occupy two different chemical environments, A and B. In the 2D exchange spectroscopy (EXSY) NMR experiment,¹⁰⁹ a 90° pulse first generates transverse magnetisation that precesses at the

offset frequency during t_1 . Then, a further 90° pulse returns the transverse magnetisation back to the z -axis. During the delay that follows, the nuclear spins may swap from the A to the B environment, or vice-versa, or they may remain in the same environment. Finally, a further 90° pulse generates transverse magnetisation which is detected in t_2 .

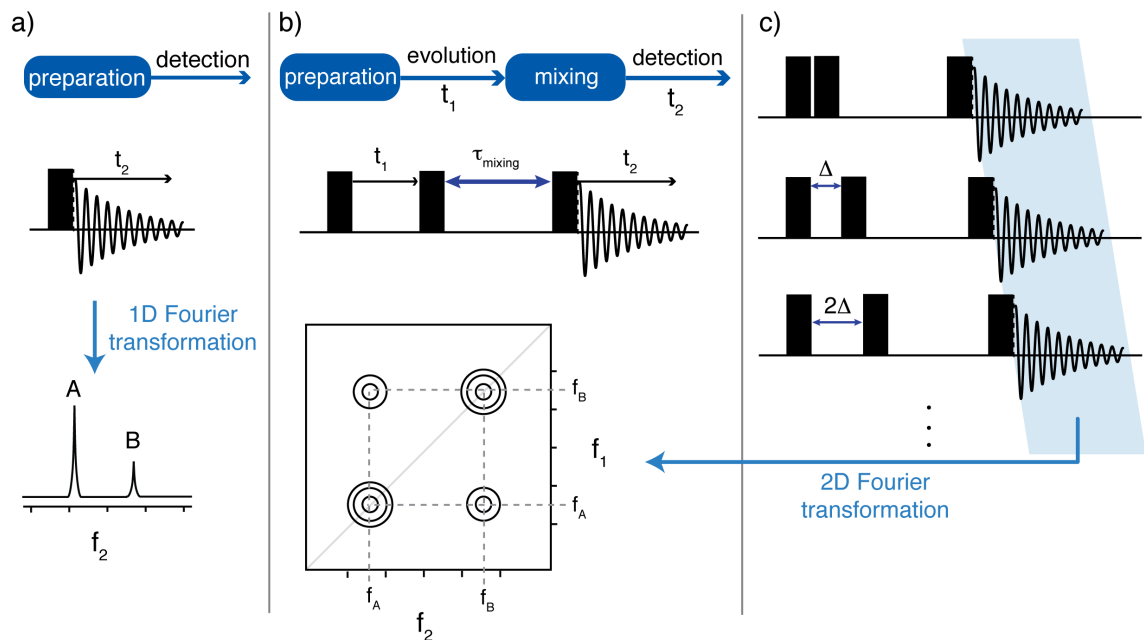


Figure 3.9 Schematic highlighting the differences between 1D and 2D NMR experiments. (a) General form of 1D NMR experiments, with an example given for a pulse-acquire sequence and spectrum shown. (b) General form of 2D NMR experiments. An example pulse sequence and spectrum is given for the 2D EXSY experiment. (c) Schematic showing how 2D NMR experiments are acquired in practice.

Resonances in the 2D EXSY NMR spectrum with identical frequency in the f_1 and f_2 dimensions correspond to nuclear spins that did not exchange from one site to the other during the mixing time. On the other hand, resonances with different frequencies in the two dimensions correspond to nuclear spins that underwent a hop from one site to the other during the mixing time. This experiment can be a powerful probe of dynamic processes, provided the resonances of the exchanging sites can be resolved in the spectrum.⁹⁴

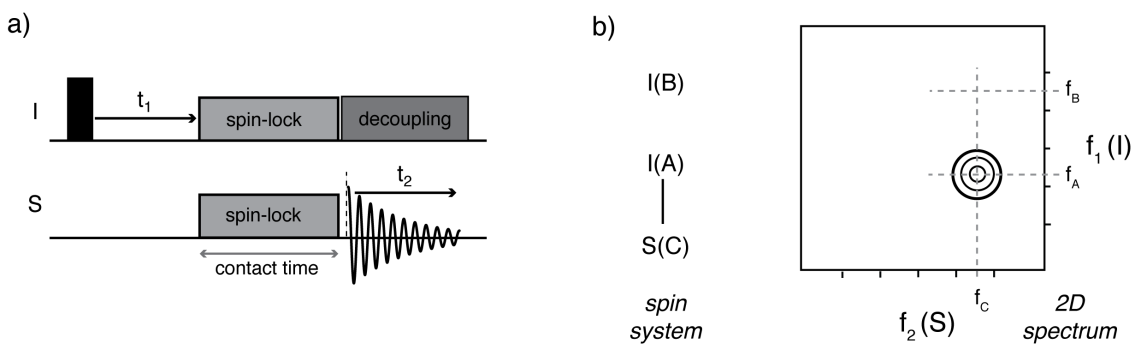


Figure 3.10 (a) Pulse sequence for 2D HETCOR experiment. (b) Schematic HETCOR spectrum for a simple spin system in which $I(A)$ is close to $S(C)$, but $I(B)$ is not.

2D NMR experiments may also be multinuclear whereby information about two (or more) different NMR active isotopes is obtained simultaneously. A good example of this is the 2D heteronuclear correlation (HETCOR) experiment that shows correlations for nuclei that undergo magnetisation transfer by CP (Figure 3.10). For the example spin system illustrated in Figure 3.10b, where only the A and the C spins couple, an A-C correlation is observed, but no correlation is observed for B and C.

3.5 Chemical Exchange in NMR

For nuclear spin systems with considerable mobility, chemical exchange can lead to significant lineshape perturbations. Consider the simple case of two-site exchange, whereby nuclear spins may exchange (hop) between two chemical environments, A and B, with their resonance frequencies separated by $\Delta\nu$ (in Hz), and with an exchange rate k_{ex} for hops in either direction. When $k_{ex} \ll \Delta\nu$ the two individual resonances can be clearly observed, and exchange is said to be in the “slow” regime. This can be seen in the spectral simulations shown in Figure 3.11a. As k_{ex} is increased and approaches $\Delta\nu$, the resonances broaden slightly, until they coalesce into a single broad resonance at the average position of the resonances from sites A and B. This coalescence occurs when $k_{ex,coalesc.} = 2.22\Delta\nu$.¹⁰² For faster exchange rates, this broad single resonance narrows; an effect referred to as “motional narrowing”. For rates $k_{ex} \gg \Delta\nu$, exchange is said to be in the “fast” regime, with a single narrow resonance observed. Importantly, the lineshape changes are most significant for exchange rates close to the value at the coalescence point, with this regime referred to as the “intermediate exchange regime”. The terms “slow intermediate exchange” and “fast intermediate exchange” are used to refer to the regimes where $k_{ex} < k_{ex,coalesc.}$, and $k_{ex} > k_{ex,coalesc.}$, respectively.

The behaviour observed here can be understood by visualising the behaviour of the individual spins (Figure 3.11b). In the slow regime, the spins spend a considerable amount of time in a given environment before hopping to the other environment. The resulting FID from an ensemble of spins (Figure 3.11c) is then composed of two different frequency components from spins A and B. The FID decays due to the dephasing of the signals from the different spins. As the exchange rate is increased, this dephasing occurs more quickly, leading to a broadening of the resonances. At the coalescence point, the time between hops is on the order of the time period of the two resonance frequencies, such that the individual spins go out of phase with each other very rapidly. The resulting short FID gives rise to a very broad resonance. For fast exchange rates, the spins hop many times during one wave period and an average frequency is observed. This averaging becomes more complete for faster exchange rates, keeping the individual spins in phase with each other for longer, and giving rise to a narrower resonance.

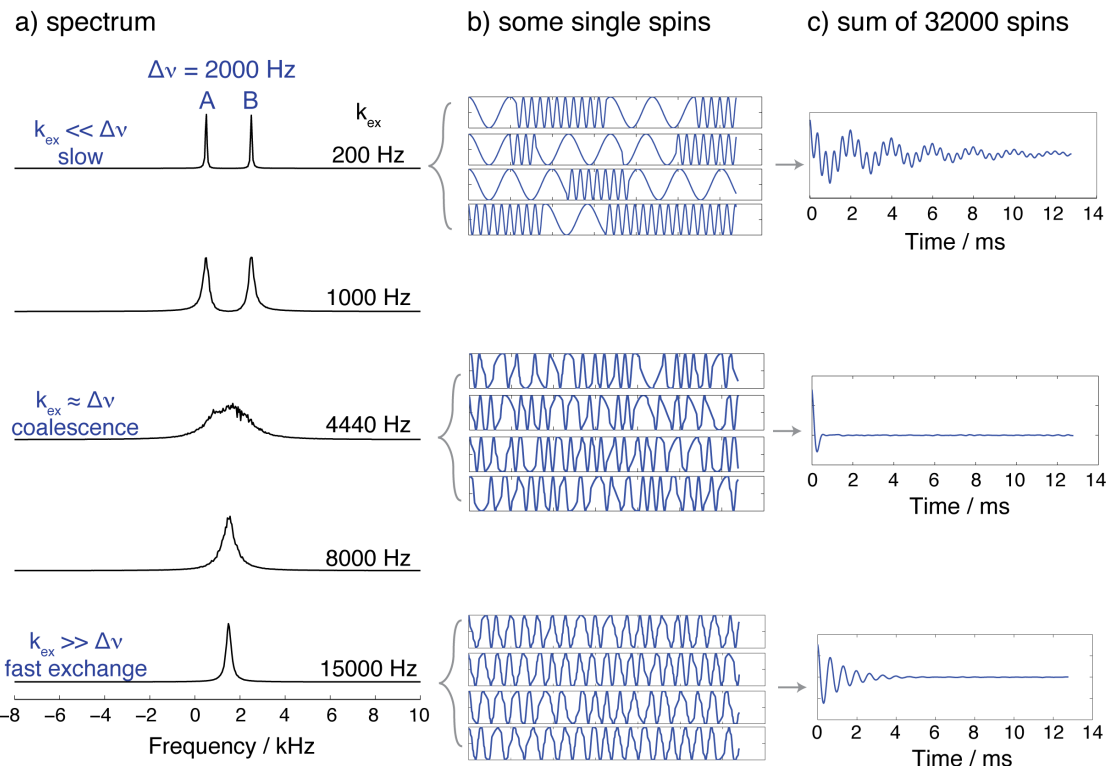


Figure 3.11 (a) Spectral simulations of a two site exchange process. Simulations were carried out in Matlab software as detailed in Section 7.2.4. (b) Sample contributions from the individual spins undergoing random hops at the exchange rate, k_{ex} . (c) The FID resulting from the summation of the signals from an ensemble of 32000 spins. Noise in the spectra arises from a lack of spin statistics.

In real systems with disorder the nuclear spins may not just occupy two different sites, but rather a distribution of different sites with different resonance frequencies. For slow

exchange rates the sum of the individual resonances will then be observed in the spectrum.¹⁰² However, as the exchange rate exceeds the frequency width of the distribution of sites, motional narrowing effects are observed. An example for a system with a rectangular profile of accessible sites with a width of 6 kHz is shown in Figure 3.12a. As the exchange rate is increased from 8 kHz to 20 kHz, the observed resonance narrows considerably (Figure 3.12b). Such lineshape variations can be a useful source of dynamic information.

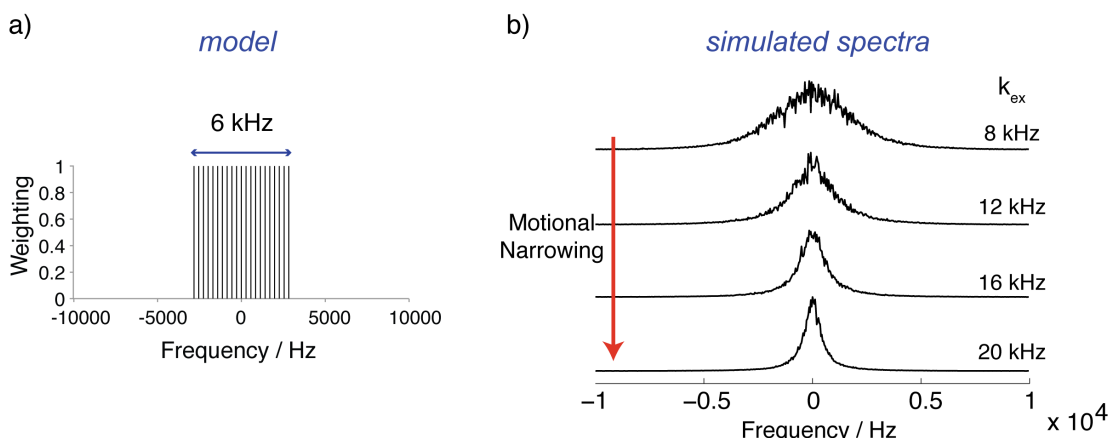


Figure 3.12 Spectral simulations for a model system with many accessible sites with different resonance frequencies. (a) Rectangular distribution of accessible sites. (b) Simulated spectra for spins undergoing random hops between the different sites in (a) at a range of exchange rates. Noise in the spectra arises from a lack of spin statistics.

3.6 Ring Current Effects

Since the aim of this thesis is to use NMR spectroscopy to study ions at the interface between an electrolyte and a carbon electrode, it is important to consider what effect the carbon surface will have on the resonance frequencies observed for the nearby nuclear spins in the electrolyte. As discussed in the previous chapter, porous carbons consist predominantly of sp^2 -hybridised carbon, and while they have no long-range order, they exhibit local order with a prevalence of hexagonal carbon rings. In the presence of an applied magnetic field, these are thought to give rise to “ring current effects”, whereby the circulation of the carbon π electrons brings about significant chemical shifts for nearby nuclear spins.¹¹⁰

Ring current effects are often significant in determining chemical shifts in organic molecules. The hydrogen atoms in benzene show a shift to high frequencies in ${}^1\text{H}$ NMR, compared to the alkene hydrogens in cyclohexene (Figure 3.13a).¹¹¹ The

phenomenological picture (Figure 3.13b) developed by Pople is commonly used to rationalise these differences.¹¹²

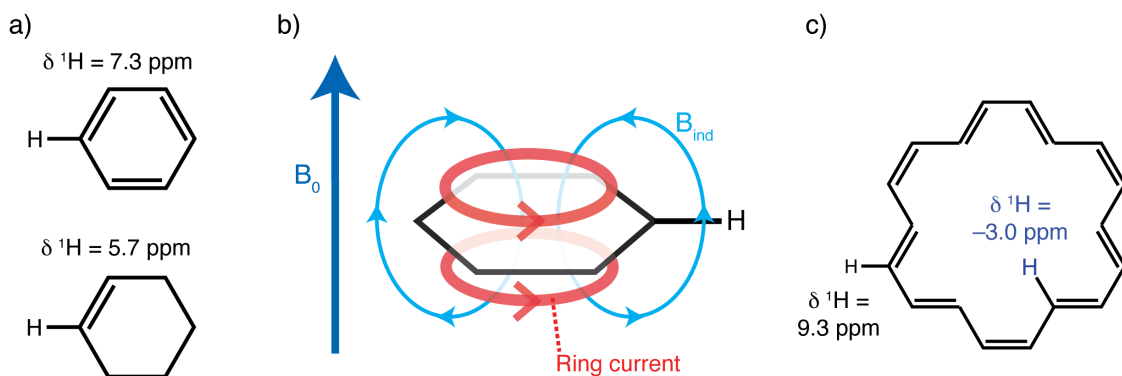


Figure 3.13 (a) ^1H chemical shifts in benzene and cyclohexene. (b) Pople’s description of aromatic ring current effects. The applied magnetic field, B_0 , causes circulation of the six π electrons in benzene, inducing a local magnetic field, B_{ind} . (c) ^1H chemical shifts in [18]annulene. Only one of the 12 outer protons and one of the 6 inner protons are shown for clarity.

The six π electrons in benzene are highly delocalised and circulate in the presence of a magnetic field, producing a ring current. This induces a local magnetic field in the proximity of the benzene ring, and the hydrogen atoms bonded to the carbon ring experience a deshielding field (Figure 3.13b). By the same model, a molecule or atom situated above or inside an aromatic ring should experience a shielding field. This effect can be seen in [18]-annulene (Figure 3.13c), where the protons on the exterior of the aromatic ring are deshielded (9.3 ppm) and those in the interior are highly shielded (-3.0 ppm).¹¹³

In 1996, Schleyer introduced the concept of a nucleus-independent chemical shift (NICS) as a measure of aromaticity.¹¹⁴ In NICS calculations, ghost atoms with no electrons or nuclear charge are positioned at various points around the structure. Calculated shielding tensors then arise purely from the shielding fields of the studied molecule.¹¹⁵ The sign of the absolute shielding is reversed to give the NICS (such that a greater NICS results in a greater chemical shift). NICS values are readily calculated using quantum mechanics programs such as Gaussian (see below).

Ring currents may be subdivided into two main classes, diamagnetic (or diatropic) and paramagnetic (or paratropic),¹¹⁶ associated with paired and unpaired electrons respectively. While diamagnetic ring currents cause a shielding field above the centre of the ring, as seen for benzene, paramagnetic ring currents cause a deshielding field, as seen for cyclobutadiene (C_4H_4).¹¹⁵ These two effects were observed in the work of Oth

et al.,¹¹³ where two electron reduction of [18]-annulene caused the resonance frequency of the interior protons to change from –3.0 to 28.1 ppm, attributed to the introduction of paramagnetic ring currents.

3.7 Electronic Structure Calculations

It is often useful to calculate NMR parameters for a structural model and compare the results to experimental values. The calculation of NMR parameters for a given molecule requires the electronic structure and the energy to be calculated. The theory of quantum mechanics shows that this problem corresponds to solving the Schrödinger equation. For a single particle this equation takes the general form:

$$\hat{H}\psi(\vec{r},t) = (\hat{T} + \hat{V})\psi(\vec{r},t) = i\hbar \frac{\partial\psi(\vec{r},t)}{\partial t} \quad [3.25]$$

where \hat{H} is the Hamiltonian operator, the sum of \hat{T} and \hat{V} , the kinetic and potential energy operators, respectively, and $\psi(\vec{r},t)$ is the wavefunction. For cases where the potential is time-independent, the time-independent Schrödinger equation applies:

$$\hat{H}\psi(\vec{r}) = E\psi(\vec{r}) \quad [3.26]$$

Where E is the energy of a particular stationary state, $\psi(\vec{r})$, of the system. For atoms, the Hamiltonian in Equation 3.26 features terms corresponding to the kinetic energy of the electrons and the nucleus, and the potential energy of the interactions between them. However the form of the Hamiltonian can be simplified using the Born-Oppenheimer approximation, which states that the positions of the nuclei appear fixed relative to the electrons. In practice this is a very good approximation as the electrons react instantaneously to motion of the nuclei, which are thousands of times more massive. Considering the simplest case of the hydrogen atom, Equation 3.26 takes the form:

$$\left(\frac{-\hbar^2}{2m_e} \nabla^2 - \frac{1}{4\pi\epsilon_0} \frac{e^2}{r} \right) \psi(\vec{r}) = E\psi(\vec{r}) \quad [3.27]$$

where m_e is the mass of the electron, ∇ is the Laplace operator, e is the electronic charge and r is the distance between the electron and the nucleus. This equation can be solved to obtain the atomic orbitals of hydrogen and their energies.

For more complicated systems the Schrödinger equation quickly becomes impossible to solve directly. Consider the helium atom. Here Equation 3.26 takes the form:

$$\left(\frac{-\hbar^2}{2m_e} \nabla_1^2 - \frac{\hbar^2}{2m_e} \nabla_2^2 - \frac{1}{4\pi\epsilon_0} \frac{2e^2}{r_1} - \frac{1}{4\pi\epsilon_0} \frac{2e^2}{r_2} + \frac{1}{4\pi\epsilon_0} \frac{e^2}{r_{12}} \right) \psi(\vec{r}) = E\psi(\vec{r}) \quad [3.28]$$

where r_1 and r_2 are the positions of electrons 1 and 2 (relative to the nucleus) and r_{12} is the distance separating the two electrons. The first two terms on the left-hand side correspond to the kinetic energy of the electrons, the third and fourth terms correspond to the attractive coulombic interactions between the electrons and the nucleus, and the fifth term relates to the repulsive interaction between the electrons. This last term proves to be particularly troublesome and prevents the solution of this equation. This is because the behaviour of each electron now depends on the other, such that Equation 3.28 cannot be separated into two solvable one-electron equations. One approach here is to write down approximate one-electron equations of the form:

$$\left(\frac{-\hbar^2}{2m_e} \nabla^2 - \frac{1}{4\pi\epsilon_0} \frac{2e^2}{r} + \hat{V}_{\text{average}} \right) \psi(\vec{r}) = E\psi(\vec{r}) \quad [3.29]$$

where \hat{V}_{average} is an approximation to the average potential of the other electron. However, this average potential depends on the position of the other electron, and therefore its wavefunction. The solution to this problem in practice is to carry out self-consistent field (SCF) calculations, whereby initial guesses for the one electron wavefunctions are used to evaluate \hat{V}_{average} , and this is used to solve Equation 3.29 and find new wavefunctions. This process is repeated until the calculated wavefunctions agree with the old ones, *i.e.*, until they are self-consistent. These ideas form the basis of Hartree-Fock (HF) methods in computational chemistry. These methods can be applied to molecules and solids with the implementation of the HF method described in detail in the book of Atkins and Friedman.¹¹⁷

An alternative approach is density functional theory (DFT), which has the advantages of being relatively inexpensive computationally, while taking into account electron-electron correlation. The central concept in DFT is that the electronic energy of the system can be written in terms of the electron density, $\rho(r)$.¹¹⁸ More specifically, the energy is given by a functional of the electron density, such that for a given electron density, there is a single corresponding energy. Hohenberg and Kohn showed that the ground state energy (and all other ground state properties) are uniquely defined by the ground state electron density.¹¹⁸ Kohn and Sham then showed that the electronic energy can be written as:¹¹⁹

$$E(\rho) = E^T(\rho) + E^V(\rho) + E^J(\rho) + E^{XC}(\rho) \quad [3.30]$$

Where $E^T(\rho)$ is the energy associated with the kinetic energy of the electrons, $E^V(\rho)$ is the potential energy associated with electron-nuclei and nuclei-nuclei interactions, $E^J(\rho)$ is the electron-electron repulsion term and $E^{XC}(\rho)$ is the exchange-correlation term which describes the non-classical interactions of the electrons (such as the effects of the Pauli exclusion principle, which reduces the probability of two electrons of like-spin approaching each other, but enhances the probability of electrons of opposite-spin approaching each other).¹¹⁷ Each of the energy terms on the right-hand side of Equation 3.30 is a functional of the electron density, all of which are precisely known except for E^{XC} , which must be approximated.

Kohn and Sham demonstrated how to carry out DFT calculations in practice,¹¹⁹ whereby a set of one-electron equations (the Kohn-Sham equations) are solved to obtain the form of the one-electron wavefunctions (or Kohn-Sham orbitals). These are solved in a self-consistent manner whereby a guess is first made for the electron density, which enables the one-electron orbitals to be obtained. With these a new electron density is calculated, and the process is repeated until the density is self-consistent. The electronic energy is then calculated using Equation 3.30.

For these methods to be successful, an accurate exchange-correlation functional must be used. This term is typically broken down into two parts that must both be approximated:

$$E^{XC}(\rho) = E^X(\rho) + E^C(\rho) \quad [3.31]$$

Where the exchange functional, $E^X(\rho)$ describes interactions between electrons with the same spin and $E^C(\rho)$ describes interactions between electrons with opposite spin. In the simplest case, these terms are assumed to depend simply on the electron density ρ (the so-called local class of functionals) but in most cases more accurate results are obtained using functionals that also depend on the gradient of the electron density (gradient-corrected functionals).¹²⁰ Considerable effort goes into constructing these functionals, with a wide variety of different options on offer. It is stressed that these are parameterised to some extent such that the results of DFT calculations agree with experimental observations, such as atomization and ionisation energies.¹²⁰ In many cases hybrid functionals are used, where a linear combination of a DFT functional and a HF term is used to describe exchange.¹²⁰ Hybrid functionals such as Becke's B3LYP¹²¹

are commonly used in NMR calculations and give a good compromise of accuracy and speed.¹²²

Programs such as Gaussian readily allow DFT calculations to be carried out on molecules. Here the one-electron wavefunctions are comprised of basis functions, which are in turn composed of sums of Gaussian functions.¹²⁰ When carrying out calculations on a molecule, the geometry is first optimised in a procedure whereby a minimum on the energy landscape is located by displacing the atoms in a series of steps. This process is complete when both the forces on the atoms and the atomic displacements (and their root-mean-square values) decrease below a certain tolerance value.¹²⁰ With the geometry-optimised structure, NMR calculations may then be carried out to determine shielding tensors.¹²² These shielding tensors are generally calculated for all the atoms in a molecule, and may also be calculated for fictitious ghost atoms at arbitrary positions in space (see above). NMR calculations are very useful when assigning NMR spectra,⁹⁵ and can also be used to understand the shifts that occur during adsorption processes.¹²³

Chapter 4

NMR Studies of Electrolyte

Adsorption in Porous Carbons

4.1 Context and Scope

Porous carbons are the most commonly used electrode materials for supercapacitors, as they have high surface areas for ion adsorption and good electronic conductivities, while being relatively cheap.²⁹ Activated carbons prepared from organic materials such as coconut-shells and wood are commonly used in commercial devices, while carbons derived from inorganic precursors such as metal carbides have recently attracted significant attention as model systems for mechanistic studies of capacitance.^{31,56,68} Great efforts have been made to tailor electrode materials to improve their capacitive performance, with the importance of the relative sizes of the pores and the electrolyte ions highlighted in a number of publications.^{31,57,65–67,124} Despite great progress, both with experimental and theoretical studies of supercapacitors,¹¹ relatively few spectroscopic techniques have been developed to directly study the local environments of the electrolyte ions in supercapacitor electrodes.

NMR spectroscopy is well-suited for studies of electrode-electrolyte interfaces, as both structure and dynamics can be investigated in a non-invasive and element-selective way.¹²⁵ This latter feature allows the separate observation of cations, anions and solvents in electrochemical systems, provided that each species contains NMR active nuclei. Harris *et al.* carried out the first NMR studies on the adsorption of molecules on activated carbons.^{110,126–130} Separate resonances could be identified for molecules inside the carbon micropores, and those residing in larger pores and spaces in the carbon. The adsorption of various molecules on a range of nutshell and coal-derived carbons was studied. Regardless of the molecule or nuclear spin studied, the resonances from

molecules in the carbon micropores appeared shielded by 6–8 ppm relative to the resonances arising from species in the larger pores and voids. This shielding was attributed to a ring current effect arising from the circulation of the delocalised carbon π electrons in the applied magnetic field. Importantly, this ring current effect provides chemical shift resolution that allows, for example, NMR studies of adsorption isotherms,¹²⁶ and studies of competitive adsorption between different molecules.^{128,129} The NMR approach has now been extended to study adsorption of molecules in carbon nanotubes, with characteristic ring current shifts again observed.^{131–134} More recent NMR studies have examined the storage of gases in porous carbons,^{135,136} as well as electrolyte adsorption in supercapacitor electrode materials at different states of charge.^{17,18,93} Here, the ring current shifts and populations of ions in the carbon pores have been found to vary with charge, though these effects are still not fully understood.

The main aim of this chapter is to introduce NMR as a probe of electrolyte adsorption in porous carbons and to demonstrate and explain the key approaches and observations for a range of model systems. Electrode materials derived from coconut-shells, as well as carbide-derived carbons are studied, with the electrolyte species inside the carbon micropores distinguishable from those in bulk electrolyte in each case. The NMR experiments show that the local environments of the adsorbed ions are sensitive to the carbon structure, and in principle offer information about these structures. 2D EXSY NMR experiments show that the electrolyte is highly dynamic, with the ions diffusing in and out of the carbon pores on a millisecond timescale. Finally, the effects of magic angle spinning are considered.

4.2 Experimental Details

4.2.1 Carbon materials

TiC-CDC powder was synthesised by chlorine-treatment of titanium carbide³³ by collaborators in the laboratory of Prof. Yury Gogotsi at Drexel University. TiC (Alfa Aesar) with an average particle size of ~2 μm was heated to the desired temperature (600, 800, and 1000 °C) in argon gas, and the gas was switched to dry chlorine for 3 h. After chlorine-treatment, the gas was switched back to argon, and then hydrogen, with the sample held at 600 °C for 2 h to remove chlorine and chloride residues. Samples treated in chlorine gas at a temperature X °C (e.g., 600 °C) are referred to as TiC-CDC-X (e.g., TiC-CDC-600).

Freestanding carbon films were fabricated as follows. Carbon powder (95 wt. %) and polytetrafluoroethylene (PTFE) binder (5 wt. %) were mixed in ethanol for at least 20 minutes. The resulting slurry was kneaded and then rolled with a doctor blade into a freestanding film of approximately 250 μm thickness.

4.2.2 NMR experiments

NMR experiments were performed using Bruker Avance spectrometers operating at magnetic field strengths of 7.1 and 9.4 T, corresponding to respective ^1H Larmor frequencies of 300.2 MHz and 400.4 MHz. Bruker 2.5 mm double resonance probes were used. NMR experiments were performed at 5 kHz MAS using a spin-echo pulse sequence ($90^\circ-\tau-180^\circ-\tau-\text{acquire}$) to avoid baseline distortions and to remove background signals associated with the probe. A spin-echo τ delay of 200 μs (a single rotor period) was typically used. For neat electrolyte samples, pulse-acquire sequences were used. ^{19}F NMR spectra were referenced relative to neat hexafluorobenzene (C_6F_6) at -164.9 ppm, while ^1H NMR spectra were referenced relative to tetramethylsilane using the CH_3 resonance of liquid ethanol at 1.2 ppm as a secondary reference. Recycle delays were adjusted to give quantitative spectra for all nuclei. Radio-frequency strengths of between 100 and 135 kHz were used for all nuclei studied, with the exception of ^2H experiments where a strength of 66 kHz was used. Chemical shifts were generally determined by inspection of the spectra, though a two peak fit in dmfit software¹³⁷ was necessary to extract $\Delta\delta$ values from the ^2H spectra.

Samples for NMR experiments were prepared for studying ion adsorption as follows. A carbon film piece (6.0 mg) was cut and heated for at least 15 h at 200 °C *in vacuo* before being transferred to an argon glovebox. The film piece was cut into small pieces and approximately half of these were packed into a 2.5 mm outer diameter zirconia MAS rotor, before adding ~ 4 μL of tetraethylammonium tetrafluoroborate, NEt_4BF_4 (≥ 99.0 %, Sigma-Aldrich), 1.5 M, in deuterated acetonitrile, D_3CCN (99.80 %, Eurisotop), electrolyte by microsyringe. The remaining carbon was then packed before capping the rotor (Vespel cap). For one experiment a different electrolyte, 1-methyl-1-propylpyrrolidinium bis(trifluoromethanesulfonyl)imide (>98 % Tokyo Chemical Industry UK) 1.8 M in deuterated acetonitrile (referred to as Pyr₁₃TFSI/dACN (1.8 M)) was used.

4.2.3 Scanning Electron Microscopy experiments

Scanning electron microscopy (SEM) experiments were carried out with the assistance of Dr. Pritesh Hiralal (Department of Engineering, University of Cambridge) using a Sigma VP microscope (Zeiss). All images were collected on carbon film samples.

4.3 Results and Discussion

4.3.1 NMR spectra for an activated carbon soaked with electrolyte

In this chapter, all NMR experiments are carried out on carbons that have had no potential applied to them, such that adsorption effects can be investigated without the additional complexity that arises from charging. For a first study, the adsorption of a typical supercapacitor electrolyte (tetraethylammonium tetrafluoroborate 1.5 M in deuterated acetonitrile; $\text{NEt}_4\text{BF}_4/\text{dACN}$) on a commercial activated carbon derived from coconut-shell (YP50F) was investigated by MAS NMR. The carbon powder was prepared as a freestanding film by mixing it with polytetrafluoroethylene (PTFE) polymer binder, a small piece of which was soaked with electrolyte and packed into a MAS rotor. Figure 4.1 shows the ^{19}F MAS NMR spectrum of the electrolyte-soaked carbon, as well as the static NMR spectrum of the neat liquid electrolyte for comparison. These ^{19}F NMR experiments allow the local environments of the BF_4^- anions to be studied. For the neat electrolyte, a single resonance is observed for BF_4^- at a chemical shift of -149.4 ppm as expected. The electrolyte-soaked carbon, however, gives an MAS NMR spectrum with two distinct resonances. The left-hand resonance has a very similar chemical shift to that of the neat electrolyte at -149.8 ppm, while the other resonance appears shielded at a chemical shift of -155.1 ppm.

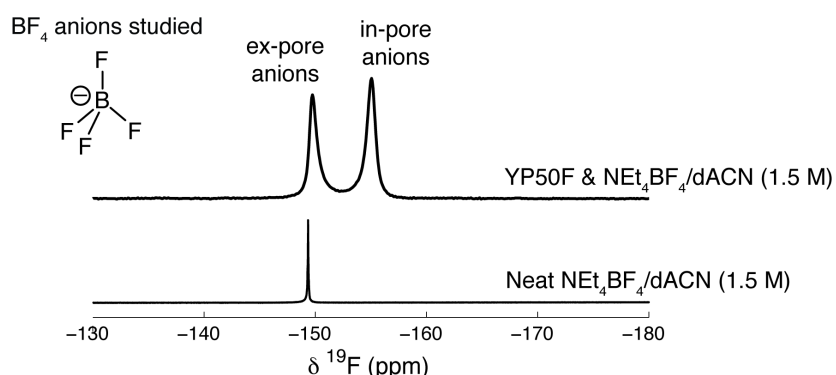


Figure 4.1 ^{19}F MAS NMR (9.4 T) spectrum of YP50F carbon film soaked with $\text{NEt}_4\text{BF}_4/\text{dACN}$ (1.5 M). A spin echo experiment with a τ delay of $200 \mu\text{s}$ was used, with an MAS rate of 5 kHz. A static pulse-acquire spectrum of the neat electrolyte is shown for comparison. In- and ex-pore BF_4^- resonances can be resolved.

The resonance at -149.8 ppm corresponds to BF_4^- in a chemical environment that is very similar to bulk electrolyte, and is referred to as “ex-pore”. The resonance at -155.1 ppm, on the other hand, is assigned to anions that are inside nanometre-sized carbon pores. Our observations in Figure 4.1 are very similar to those in the early work of Harris *et al.* highlighted above in Section 4.1,^{110,126–130} with the spectral assignments here following directly from that work. The in-pore resonance is shielded relative to the ex-pore by a ring current effect that arises from circulation of the delocalised π electrons in the carbon sheets. Such ring current effects are short-range phenomena, extending over distances on the ångstrom scale.^{138,139} The ex-pore electrolyte ions, which are remote from carbon surfaces, do not experience a ring current shift.

It is useful to define the parameter $\Delta\delta$ here:

$$\Delta\delta = \delta_{\text{in-pore}} - \delta_{\text{neat-electrolyte}} \quad [4.1]$$

which is the difference between the chemical shift of the in-pore resonance ($\delta_{\text{in-pore}}$) and that of the neat electrolyte ($\delta_{\text{neat-electrolyte}}$). The $\Delta\delta$ value gives a measure of the magnitude of the ring current shift. Here, a $\Delta\delta$ value of -5.7 ppm is measured for ^{19}F NMR measurements of the BF_4^- anions in YP50F activated carbon.

Further NMR experiments were carried out to study the other species in the electrolyte (Figure 4.2). ^1H NMR experiments allow the study of the NEt_4^+ cations (Figure 4.2a). Here, spectra are complicated slightly by the presence of two chemically distinct ^1H containing groups in each cation, the CH_2 and CH_3 groups (at 3.3 and 1.3 ppm in the neat electrolyte, respectively). In- and ex-pore resonances can be observed for both the CH_2 and the CH_3 groups. The ex-pore resonances appear at 2.9 and 0.9 ppm, with similar shifts to the neat electrolyte, while the in-pore resonances appear at -3.9 and -5.9 ppm. The $\Delta\delta$ values for the CH_2 and CH_3 groups are identical at -7.2 ppm, suggesting that the CH_2 and CH_3 groups experience very similar ring current effects. This value is of a comparable magnitude to that measured for the BF_4^- anions in the ^{19}F NMR measurements above (-5.7 ppm).

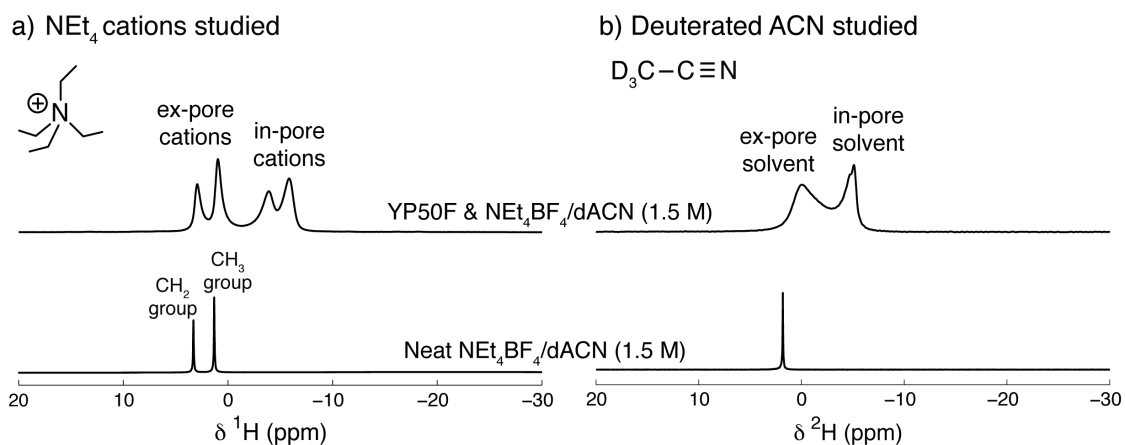


Figure 4.2 (a) ^1H and (b) ^2H MAS NMR (9.4 T) spectra of YP50F carbon film soaked with $\text{NEt}_4\text{BF}_4/\text{dACN}$ (1.5 M). A spin echo experiment with a τ delay of 200 μs was used, with an MAS rate of 5 kHz. Static pulse-acquire spectra of the neat electrolyte are shown for comparison. In- and ex-pore resonances can be observed for both the cations and the solvent molecules.

^2H NMR measurements allow the study of the deuterated acetonitrile solvent with in- and ex-pore resonances again observed (Figure 4.2b). Here, the $\Delta\delta$ value is measured as -6.9 ppm, similar in magnitude to the values measured in the ^{19}F and ^1H measurements on the anions and cations. The finding of similar $\Delta\delta$ values for the three different NMR nuclei (and three different molecules) studied here is consistent with the ring current shift mechanism, whereby any nucleus nearby a carbon surface experiences a similar shielding effect. Harris *et al.* observed similar effects, where for a given activated carbon, the $\Delta\delta$ values for different adsorbed molecules were very similar.¹¹⁰ Close inspection of the ^2H spectra reveals that the ex-pore resonance (-0.1 ppm) is significantly shifted relative to the neat electrolyte resonance (1.8 ppm). Small ex-pore/neat electrolyte shift differences were also observed in the ^1H and ^{19}F experiments above, though the magnitude of the difference is considerably greater for the ^2H spectra. The shift of the ex-pore resonance likely arises from a chemical exchange effect, which is more significant for the more rapidly diffusing solvent molecules, than the ions. It is also noted that lineshape of the ^2H ex-pore resonance appears elongated towards the in-pore resonance, again likely due to the presence of chemical exchange between these environments. The in-pore feature also appears to have two components here, possibly due to the presence of solvent in small pores that the ions are unable to access.

To interpret the NMR spectra, one must first have an idea of the structure of the carbon on a range of different length scales (Figure 4.3). Macroscopically, the carbon film is a black flexible material that can be prepared in any desired shape and size, with the film thickness approximately 0.25 mm here (Figure 4.3a). SEM images of the carbon film

(Figure 4.3b,c) show that there are a range of carbon particle sizes on the order of 1 to 10 μm . These particles are bound together by PTFE polymer, which can be seen in Figure 4.3c. A number of voids of varying sizes can be seen between the carbon particles, offering spaces which electrolyte can occupy. Electrolyte-filled voids are postulated to be the main source of the ex-pore resonance observed in the NMR experiments, while electrolyte entirely external to the carbon film piece may also contribute to the intensity of this resonance. On the nanometre scale, the carbon particles consist of predominantly sp^2 hybridised defective carbon sheets, with no long-range order (see Chapter 2).^{34,35} These sheets are arranged in such a way to give a highly porous structure, with most of the pores smaller than 2 nm for YP50F.¹⁴⁰ Figure 4.3d schematically shows nanometre sized pores, which the in-pore ions are thought to occupy. Here the local magnetic field arising from the carbon ring currents shields the in-pore nuclei.

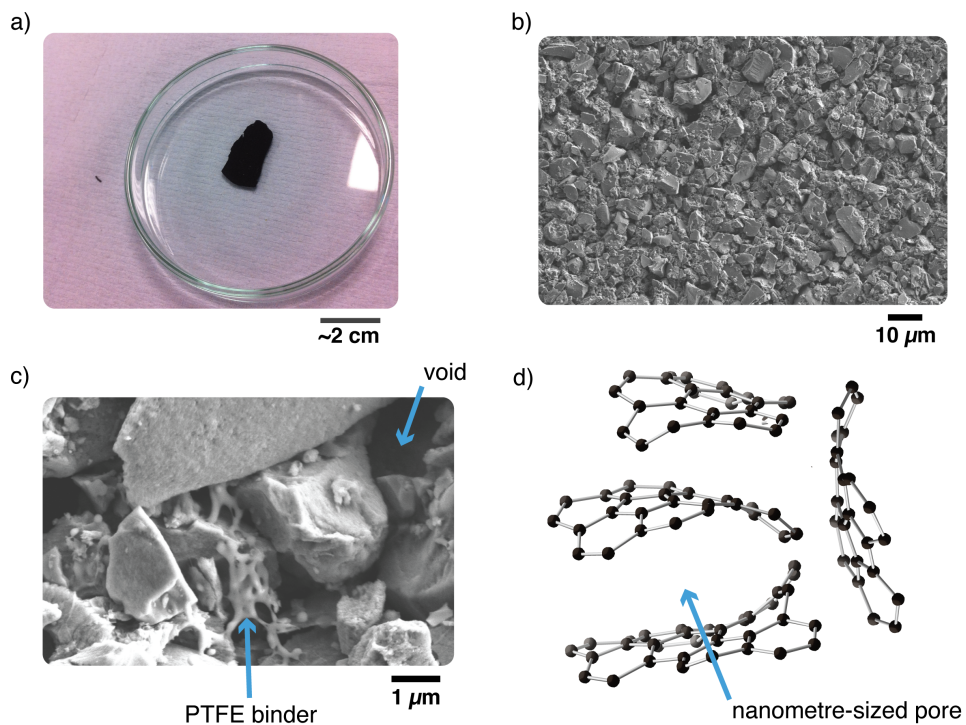


Figure 4.3 Length scales of YP50F activated carbon. (a) Macroscale structure of a carbon film. (b) and (c) SEM images showing the microscale structure of the carbon film. (d) Schematic showing a possible structure of the carbon on the nanoscale.

4.3.2 Investigating carbide-derived carbons

MAS NMR experiments were carried out on a range of electrolyte-soaked titanium carbide-derived carbons (TiC-CDCs) to investigate the relationship between the carbon structure and the resulting NMR spectra of the confined $\text{NEt}_4\text{BF}_4/\text{dACN}$ (1.5 M)

electrolyte (Figure 4.4). A series of TiC-CDCs with different chlorine-treatment temperatures were studied, with a sample chlorine treated at X °C referred to as TiC-CDC-X. In- and ex-pore anion resonances are observed for all TiC-CDC samples studied here, with the chemical shift and lineshape of the in-pore resonance sensitive to the chlorine-treatment temperature of the TiC-CDC (Figure 4.4). As the chlorine-treatment temperature is increased from 600, to 800, to 1000 °C, the $\Delta\delta$ value increases in magnitude from -2.6, to -4.0, to -5.4 ppm. For TiC-CDC-1000, the chemical shift for the in-pore anions is comparable to that for YP50F. The in-pore linewidth on the other hand is significantly larger for TiC-CDC-1000.

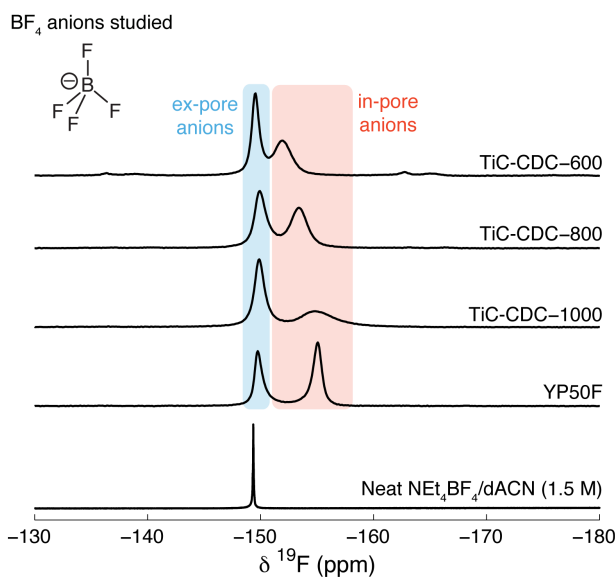


Figure 4.4 ^{19}F MAS NMR (9.4 T) spectra of TiC-CDC samples soaked with $\text{NEt}_4\text{BF}_4/\text{dACN}$ (1.5 M). Spectra are shown for electrolyte-soaked YP50F and neat electrolyte for comparison. Some small spinning sidebands can be observed for the TiC-CDC-600 sample. The chemical shift and lineshape of the in-pore anion resonance are found to vary for different carbons.

^1H and ^2H MAS NMR spectra of the electrolyte-soaked carbons are shown in Figure 4.5, with in- and ex-pore resonances again observed in all spectra. The general trends here are qualitatively very similar to those seen in the ^{19}F spectra above. As the chlorine-treatment temperature of the TiC-CDC is increased, the $\Delta\delta$ values increase in magnitude. The lineshape changes seen in the ^1H NMR spectra (Figure 4.5a) are similar to those seen in the ^{19}F spectra, with the in-pore broadening for TiC-CDC-1000 leading to considerable overlap of the in-pore CH_2 and CH_3 resonances, such that they are not resolved. The ^2H linewidths (Figure 4.5b) are consistently broader than those observed for ^{19}F and ^1H . This may arise from the chemical exchange of the in-pore and ex-pore solvent, which can lead to considerable broadening in the so-called slow-intermediate

regime.⁹⁴ There may also be a contribution to the line broadening from quadrupolar relaxation (²H has I=1), as was seen in ¹⁷O NMR studies of H₂¹⁷O in activated carbons.¹³⁰

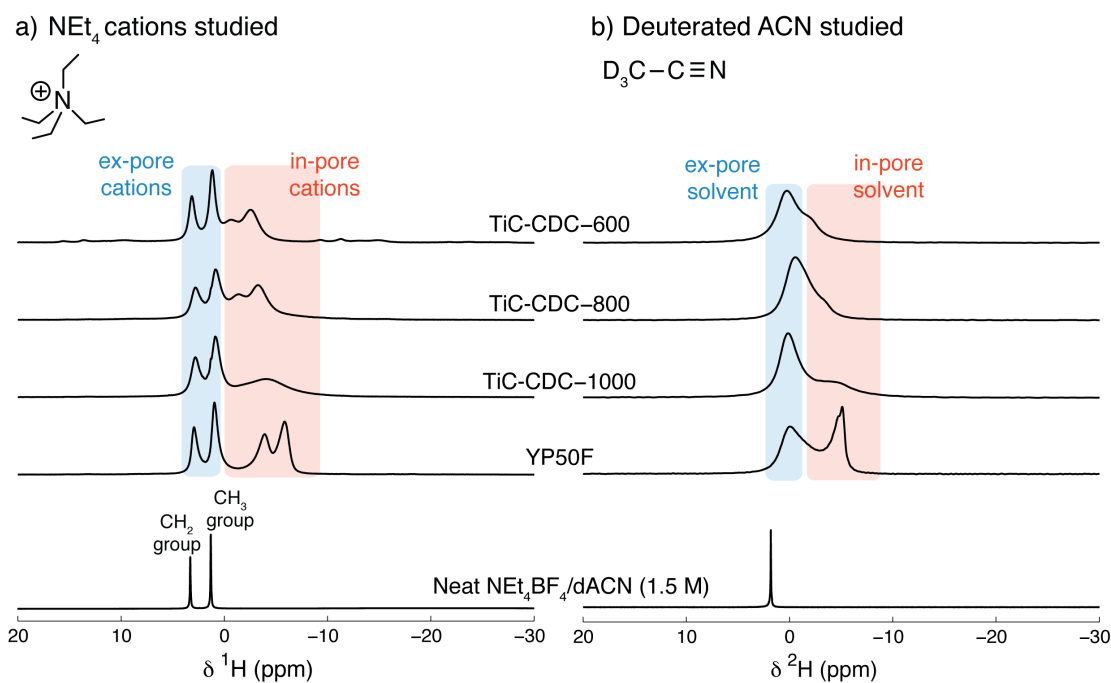


Figure 4.5 ¹H (a) and ²H (b) MAS NMR (9.4 T) spectra of TiC-CDC samples soaked with $\text{NEt}_4\text{BF}_4/\text{dACN}$ (1.5 M). Spectra are shown for electrolyte-soaked YP50F and neat electrolyte for comparison. The in-pore chemical shifts and lineshapes of the in-pore cation and solvent resonances vary in a similar way to that seen for the anions.

Extracted $\Delta\delta$ values for the spectra in Figure 4.4 and Figure 4.5 are shown in Table 4.1. For a given carbon, the $\Delta\delta$ values for the studied species and nuclei fall within a 1.5 ppm range. As the chlorine-treatment temperature of the TiC-CDCs is increased, there is a general increase in magnitude of the $\Delta\delta$ values for all nuclei studied. This variation further supports the idea that the in-pore chemical shift arises from a ring current mechanism, with differences in the local carbon structures giving rise to ring current effects of differing magnitude. Similar effects were reported by Harris *et al.* where the adsorption of organic molecules on a range of activated carbons was studied by ³¹P NMR.¹¹⁰ In that study, the $\Delta\delta$ value and in-pore linewidth were both found to vary for a given adsorbate when the carbon adsorbent was varied. Anderson *et al.*, and later Borchardt *et al.*, highlighted the effect of the carbon pore size on the ring current shifts, and showed that smaller carbon pores give rise to larger ring current shifts.^{135,141} However, local ordering in the carbon sheets may also have an effect on the in-pore chemical shift, with more ordered carbons giving rise to larger ring current shifts.¹⁴²

Table 4.1 $\Delta\delta$ values for anion, cation and solvent NMR resonances for the different carbons studied in this chapter. Values were in general determined by inspection of the spectra. For ^2H NMR spectra, values were determined from a two peak fit. Values for the ^1H spectrum of TiC-CDC-1000 were extracted from a 2D EXSY NMR experiment (see later).

Carbon	$\Delta\delta$ ^{19}F (ppm) BF_4^-	$\Delta\delta$ ^1H (ppm) $\text{NEt}_4^+ - \text{CH}_2$	$\Delta\delta$ ^1H (ppm) $\text{NEt}_4^+ - \text{CH}_3$	$\Delta\delta$ ^2H (ppm) D_3CCN
TiC-CDC-600	-2.6	-4.0	-3.9	-3.4
TiC-CDC-800	-4.0	-4.7	-4.6	-3.6
TiC-CDC-1000	-5.4	-5.8	-5.7	-5.5
YP50F	-5.7	-7.2	-7.2	-6.9

For TiC-CDCs, it is known that the average pore size tends to increase slightly as the chlorine-treatment temperature is increased.³³ However, changes in pore size are also accompanied by structural changes, such as the formation of larger ordered domains with less defective carbon sheets.^{33,47,143} Given that $\Delta\delta$ values of larger magnitude are observed as the chlorine-treatment temperature is increased here, the ordering effect appears to dominate over the pore size effect. Clearly, more work needs to be done to study the molecular level mechanism of the ring current shift mechanism here to explain the observed NMR spectra. This is the focus of Chapter 5. Moreover, the results here show that the linewidth of the in-pore resonance is also sensitive to the carbon structure. Previous studies have indicated that in-pore linewidths may arise from a distribution of different adsorption sites inside the carbon porosity.^{110,144} The origin of this linewidth warrants further study, and is discussed in Chapter 7.

4.3.3 Chemical exchange of ions between in- and ex-pore environments

^{19}F 2D EXSY experiments¹⁰⁹ were performed on electrolyte-soaked TiC-CDC-600 and TiC-CDC-1000 samples to probe the chemical exchange of ions in the in- and ex-pore environments (Figure 4.6). For a mixing time (τ_{mixing}) of 0.5 ms, only diagonal peaks are observed, with identical resonance frequencies in the two spectral dimensions. These resonances arise from anions that occupy the same chemical environment before and after the mixing time. The absence of cross peaks for this relatively short mixing time indicates that there is not a significant amount of chemical exchange between the in- and ex-pore environments on this timescale. Interestingly, the shape of the in-pore diagonal resonances suggests there is chemical exchange between different sites in the in-pore environment. For a considerably longer mixing time of 50 ms, cross peaks are observed for both samples. These arise from BF_4^- anions that are in different chemical environments before and after the mixing time (e.g., in-pore before the mixing time and ex-pore after). The observation of diagonal peaks shows that on this timescale, the BF_4^- anions undergo chemical exchange between the in- and ex-pore environments.

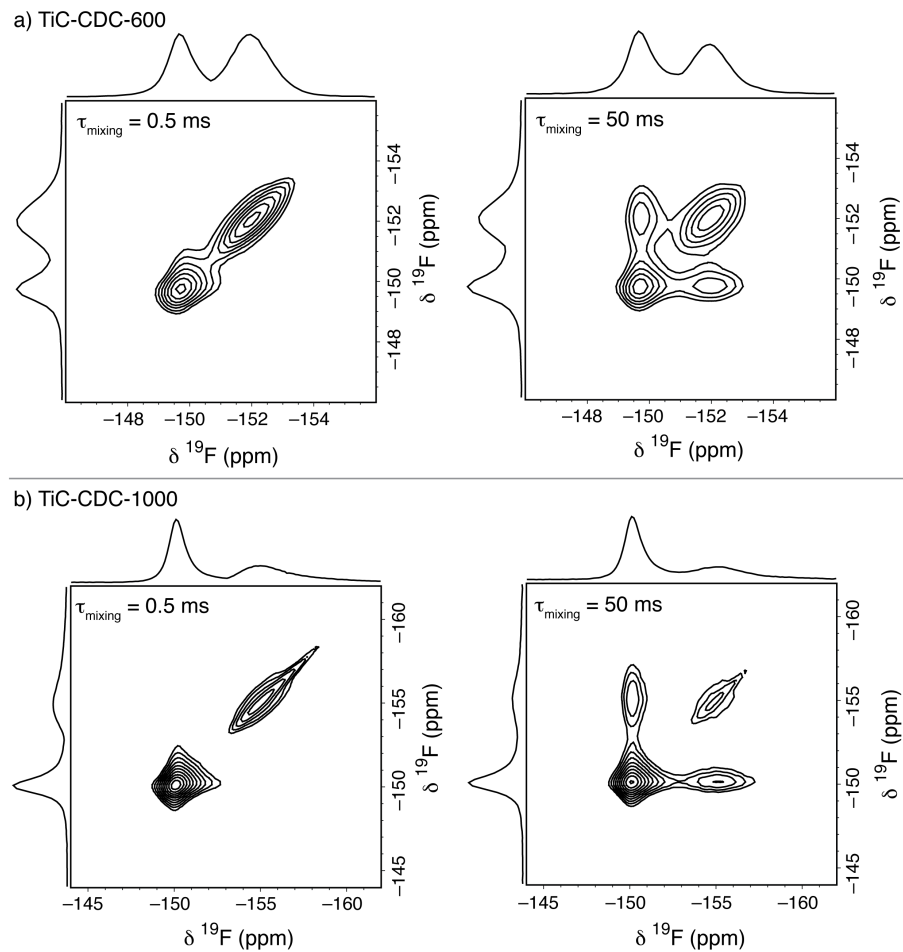


Figure 4.6 ^{19}F 2D EXSY MAS NMR (9.4 T) spectra for electrolyte-soaked TiC-CDC-600 (a) and TiC-CDC-1000 (b) samples. The mixing times used in the experiments are indicated on each spectrum. For a mixing time of 50 ms, considerable in-pore – ex-pore exchange was detected for both samples.

By performing 2D EXSY experiments with a range of mixing times it is possible to estimate an exchange rate by:⁹⁴

$$\frac{I_{cross}}{I_{diagonal}} = A \cdot \tanh(k\tau_{mixing}) \quad [4.2]$$

Where I_{cross} and $I_{diagonal}$ are the integrated intensities of the cross and diagonal peaks, k is the exchange rate, and A is a constant which represents the proportion of species that are able to undergo chemical exchange.⁹⁴ The variation of $I_{cross}/I_{diagonal}$ with τ_{mixing} is shown in Figure 4.7 for TiC-CDC-600 and TiC-CDC-1000. The similar build-up of the data with mixing time for the two samples suggest that differences in the carbon structure do not significantly affect the in-pore – ex-pore exchange rates here. Also shown are fits to Equation 4.2. The extracted exchange rates are 470 and 380 Hz for TiC-CDC-600 and TiC-CDC-1000, which are similar within the large error of the fit. However, it is noted that the fits to the data are poor, with only the points at short

mixing times well-fitted. To further investigate this behaviour, and to try to model the data points at longer mixing times, a second fit was made with two components according to:

$$\frac{I_{cross}}{I_{diagonal}} = A \cdot \tanh(k_A \tau_{mixing}) + B \cdot \tanh(k_B \tau_{mixing}) \quad [4.3]$$

Adding more parameters improves the fit as expected, especially for longer mixing times. The two component fits reveal a fast exchange rate (similar to the one component fit) and a slower exchange rate, however the fit is still poor. The findings here indicate that a wide range of exchange timescales exist for the in-pore – ex-pore exchange process. This can be rationalised by noting that in-pore ions that are close to the surface of the carbon particles will exchange more rapidly than those that are located in the centre of the carbon particles. More sophisticated modelling approaches that take these factors into account would thus be required to model the experimental data well here. The particle size, or particle size distribution, may be an important factor in determining the in-pore – ex-pore exchange rate here, though differences in the carbon pore size distribution could also have an effect.

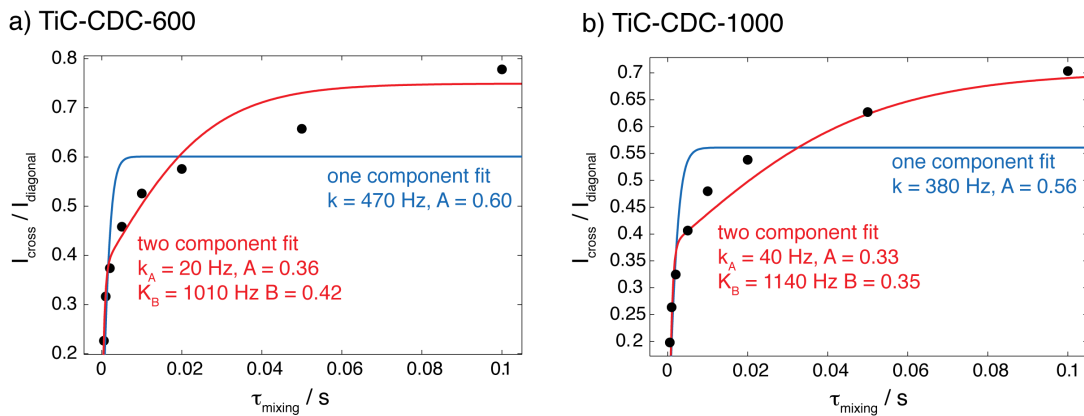


Figure 4.7 Variation of the ratio of the cross peak intensity to the diagonal peak intensity as a function of mixing time in ^{19}F EXSY experiments for electrolyte-soaked TiC-CDC-600 (a) and TiC-CDC-1000 (b). Fits to Equations 4.2 and 4.3 are shown. The data cannot be well fitted in either case suggesting that a range of exchange timescales exist for in-pore – ex-pore exchange.

Figure 4.8 shows a ^1H 2D EXSY spectrum for the electrolyte-soaked TiC-CDC-1000 sample. For a mixing time of 20 ms, cross peaks are observed, indicating that the NEt_4^+ cations are exchanging on this timescale. Interestingly, this experiment allows the

extraction of the CH_2 and CH_3 in-pore chemical shifts (-2.5 and -4.4 ppm, respectively) that were not resolved in the 1D NMR experiment. This further shows the utility of EXSY experiments as a method for enhancing spectral resolution. Finally, it is noted that while EXSY is well suited to probing exchange between spectrally resolved chemical environments (in the slow exchange regime), it offers less information about dynamics between unresolved sites, such as sites within the in-pore environment here. Such in-pore dynamics are discussed later in Chapter 7.

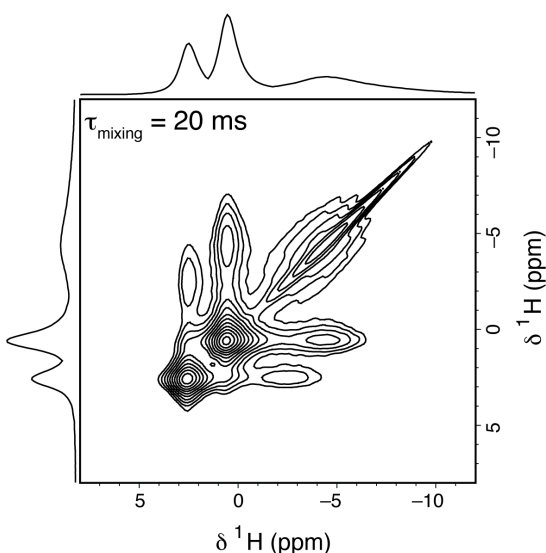


Figure 4.8 ^1H 2D exchange spectroscopy (EXSY) MAS NMR (9.4 T) spectrum for electrolyte-soaked TiC-CDC-1000. As well as revealing the presence of chemical exchange on a 20 ms timescale, this experiment allows the in-pore CH_2 and CH_3 resonance frequencies to be measured.

4.3.4 Experimental considerations for studying adsorption in porous carbons

All of the NMR experiments in this chapter so far were carried out under magic angle spinning conditions, with a sample-spinning rate of 5 kHz used in all cases. One NMR study of the adsorption of water on a nutshell-derived activated carbon showed that magic angle spinning can influence in- and ex-pore water populations.¹³⁰ This was rationalised by suggesting that centrifugation effects can occur, causing a small amount of water to exit the pores. A more recent study of $\text{NEt}_4\text{BF}_4/\text{ACN}$ adsorption in activated carbons suggested that at an MAS rate of 5 kHz, no centrifugation effects were observed, with no loss of in-pore species.¹⁸ In that study, the centrifugal forces at the edge of the rotor were estimated to be four orders of magnitude smaller than typical adsorption forces for ions. A further study examined electrolyte-soaked activated carbon fibre samples with an MAS rate of 14 kHz used.¹⁴⁵ For this relatively fast spinning speed, both in- and ex-pore intensity loss was observed on the timescale of the NMR

experiment. Clearly, these effects should be carefully monitored to check that any centrifugation effects are not significant.

During the studies of electrolyte adsorption on YP50F and TiC-CDCs presented here, prolonged sample spinning at 5 kHz did not generally cause changes to the form of the spectrum. However, in some cases, a loss of intensity from the ex-pore resonance was observed after prolonged spinning. Figure 4.9 shows such an effect in the ^{19}F NMR spectra of electrolyte-soaked TiC-CDC-600. These findings suggest that ex-pore electrolyte may escape from the rotor body into the NMR probe. There may also be a contribution from the slow evaporation of acetonitrile from the rotor, resulting in the solidification of some NEt_4BF_4 salt, which is not detected in the spin echo experiment carried out here. Either way, care must be taken to ensure rotors are well sealed to avoid electrolyte and solvent loss. Importantly, the in-pore resonance does not appear to show significant intensity changes after 14 hours of sample spinning at 5 kHz MAS rate. It is noted that the timescale of a single ^{19}F acquisition is on the order of one or two minutes, which is insignificant compared to the 14-hour timescale probed in Figure 4.9.

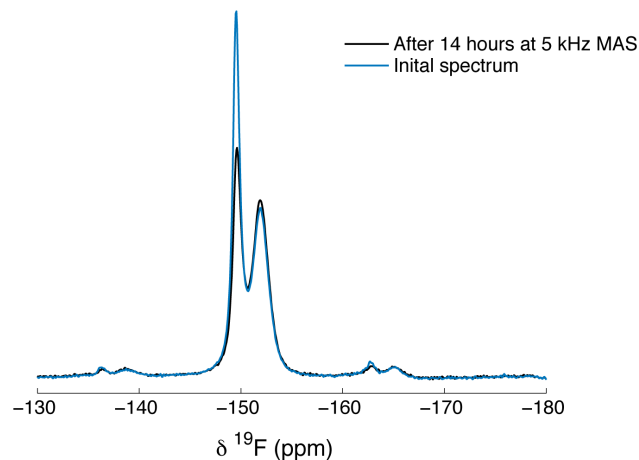


Figure 4.9 ^{19}F MAS NMR (9.4 T) experiments for electrolyte-soaked TiC-CDC-600, before and after a period of 14 hours of continuous magic angle spinning. Some ex-pore signal intensity was lost after prolonged spinning.

The sample spinning may also cause some frictional heating that could affect the mobility of the electrolyte. ^{207}Pb NMR experiments on lead nitrate, however, suggested that the frictional heating is less than 1 °C at 5 kHz MAS (see Section 7.2.3). At higher MAS speeds, sample spinning may cause more significant heating effects.

When carrying out *in situ* NMR measurements on supercapacitors, the sample (a working supercapacitor) cannot easily be spun without disrupting the electrical

connections. Static NMR experiments were carried out and compared to 5 kHz MAS NMR experiments to investigate the effects of MAS (Figure 4.10). For YP50F soaked with 1-methyl-1-propylpyrrolidinium bis(trifluoromethanesulfonyl)-imide 1.8 M in acetonitrile, referred to as Pyr₁₃TFSI/dACN (1.8 M), the in- and ex-pore resonances can be resolved in the static NMR experiment, though these are broadened compared to the MAS experiment (Figure 4.10a). For a second sample, in this case TiC-CDC-600 soaked with NEt₄BF₄/dACN (1.5 M), a single broad resonance is observed in the static experiment (Figure 4.10b). This is in stark contrast to the MAS experiment, whereby in- and ex-pore resonances may be resolved. While static experiments on YP50F may yield chemical shift and intensity information, similar experiments on TiC-CDC-600 are of limited use. This makes YP50F a much more suitable material for carrying out *in situ* NMR measurements of supercapacitors.

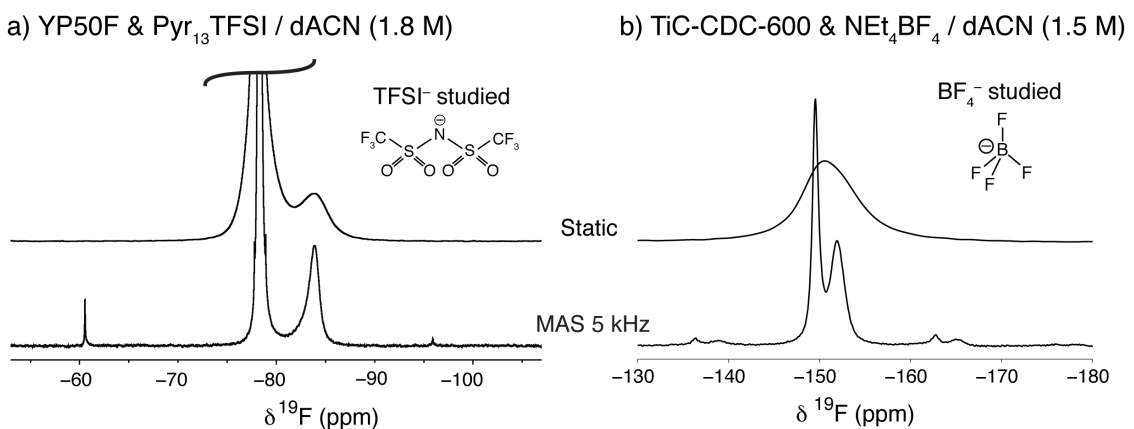


Figure 4.10 ¹⁹F MAS and static NMR experiments for electrolyte-soaked samples. (a) YP50F soaked with Pyr₁₃TFSI/dACN (1.8 M) performed at 7.1 T. (b) TiC-CDC-600 soaked with NEt₄BF₄/dACN (1.5 M) performed at 9.4 T. Magic angle spinning results in an averaging of the BMS effects and a narrowing of the spectra.

The source of the broadening in the static NMR experiments here is hypothesised to be a bulk magnetic susceptibility (BMS) effect (see Chapter 3). Given the cylindrical shape of the carbon sample in the MAS rotor and the marked diamagnetism of porous carbons (for TiC-CDCs the diamagnetic volume susceptibility is on the order of -10 ppm)¹⁴³ significant BMS effects are expected. Nuclei in different macroscopic regions of the cylindrical sample will experience different demagnetising fields, and therefore different resonance frequencies, resulting in inhomogeneous broadening of the NMR spectra. A calculation of the inhomogeneous broadening for a homogeneous cylindrical sample with a diamagnetic susceptibility of -2 ppm, orientated at the magic angle, was carried out by Dr. Andrew Ilott (New York University) using the approach of Salomir *et al.*

al. (Figure 4.11).⁹⁹ Here the variations of the BMS shift are clearly seen, which are most significant in the corners of the sample, and lead to line broadening. Interestingly, the calculations show that an overall BMS shift is not predicted for a cylindrical sample orientated at the magic angle. MAS will average out the field inhomogeneity, narrowing the resonances as observed above in Figure 4.10. Beyond the macroscopic level, there may also be BMS effects that arise from the shapes and packing of the individual carbon particles on the micron-scale.^{146,147} Provided the particles have random shapes and orientations, this will not lead to a BMS shift, though it may lead to additional broadening, again removed by MAS. The poorer resolution for the TiC-CDC-600 static sample, compared to the YP50F sample, in Figure 4.10 in part arises from the small $\Delta\delta$ value for TiC-CDC-600. However, there may also be a contribution from different BMS effects for these samples.

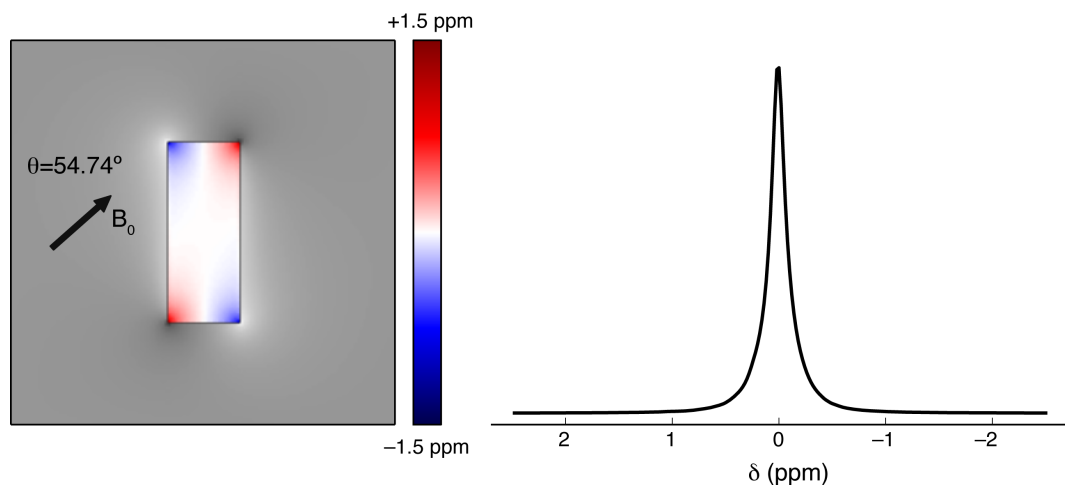


Figure 4.11 Calculation of the magnetic field inhomogeneity arising from BMS effects for a homogeneous cylinder with a diamagnetic susceptibility of -2 ppm (corresponding to a SI volume susceptibility of $-2 \cdot 10^{-6}$). The ratio of the rotor radius to the length was $1:5$. Clear variations of the local field inhomogeneity can be observed (left) which give rise to a BMS line broadening (right).

4.4 Summary and Outlook

This chapter has highlighted the power of NMR spectroscopy for the study of electrolyte adsorption in porous carbon materials. Ions and solvent molecules adsorbed inside the carbon micropores (in-pore) can be distinguished from bulk electrolyte residing in various void spaces in the sample (ex-pore) for a range of microporous carbon materials. The in-pore chemical shift has been shown to be sensitive to the carbon structure, with larger chemical shieldings seen for electrolyte-soaked TiC-CDC materials prepared at higher temperatures, regardless of the choice of the studied nuclear spin. These findings support the idea that the in-pore resonance is shielded by a

ring current effect, arising from the circulation of the carbon π electrons in the applied magnetic field. However, further work must be done to study the origin of these ring current effects, and to explain the variations seen for different carbons (Chapter 5). This is an important step towards carrying out *in situ* NMR measurements on supercapacitors (Chapter 8), where a range of carbon electrode materials would ideally be investigated.

2D EXSY NMR experiments have revealed that the electrolyte is highly dynamic, with chemical exchange occurring between the in- and ex-pore environments on a millisecond timescale. This shows that the in-pore ions should not be considered as being strongly bound to the carbon surface, as they are in fact highly mobile. Indeed, this rapid motion is vital for the fast charging and discharging of supercapacitor devices, though motion of the ions inside the carbon particles within the nano-sized pores may ultimately limit the charging rate (Chapter 7).

The use of magic angle spinning has allowed the in- and ex-pore resonances to be resolved for a range of materials here. However, for *in situ* NMR measurements on static supercapacitor samples, spectra will be broadened by bulk magnetic susceptibility effects, which may impede resolution. These effects must be carefully understood when carrying out static NMR measurements on supercapacitor devices comprising strongly diamagnetic carbon materials (Chapter 8).

Chapter 5

The Relationship Between Carbon Structures and Ring Current Shifts

5.1 Context and Scope

As discussed in the previous chapter, it is well established that separate resonances are observed for adsorbed and free species in the NMR spectra of electrolyte-soaked porous carbons. Regardless of the nuclear spin studied, resonances arising from adsorbed molecules are shifted to lower frequencies relative to their free counterparts due to ring current effects, which are nucleus-independent to a first approximation. However, if the carbon adsorbent is varied, differences in chemical shielding are observed for a given adsorbate, implying that different carbon structures give rise to different ring current effects.

For a known chemical structure, first-principles calculations can be performed to determine chemical shielding tensors and their isotropic values at arbitrary positions above and around the structure.¹¹⁵ The isotropic nucleus-independent chemical (NICS) shift at a given position, $\delta_{iso}^{NICS}(x, y, z)$, generally referred to as the NICS, is given by:

$$NICS = -(\sigma_{iso} - \sigma_{ref}) \quad [5.1]$$

Where σ_{ref} is zero in this case, yielding:

$$NICS = -\sigma_{iso} \quad [5.2]$$

While the NICS was first introduced as a measure of aromaticity,¹¹⁴ it may also be interpreted as a measure of the change in chemical shift that may be expected for adsorbates due to the influence of the carbon ring currents. Such calculations have been performed on idealised carbon systems such as graphene sheets, nanotubes, and

fullerenes.^{123,148–150} More generally, the gauge including magnetically induced current (GIMIC) method allows computation of the current density induced by a magnetic field,^{151,152} an approach which has been used to understand the aromaticity of fullerenes.¹⁵³

As discussed in Chapter 2, porous carbons exhibit extremely complicated structures, thought to consist of curved graphene-like sheets and fullerene-like units arranged in a highly disordered fashion. Given this complexity, carrying out NMR calculations on the basic building blocks that make up the carbon structures offers a convenient starting point. This ‘cluster’ approach is not only computationally straightforward, but it also precludes the need for accurate structural models for carbon structures, of which there are few.^{44,45,47} Inspiration was taken from a number of studies in the literature. For example, Moran *et al.* performed NICS calculations on a series of polybenzenoid hydrocarbons of increasing size, though they did not consider distances from the carbon relevant to molecular adsorption.¹⁵⁴ Similarly, Facelli *et al.* calculated NICSs values near model carbon fragments to rationalise inter-molecular shielding effects which are often significant in crystalline organic materials.¹³⁹ The validity of using finite molecular units to model structural and magnetic properties of graphene has also recently been demonstrated.¹⁵⁵

The main aim of this chapter is to develop an understanding of how different porous carbon structures give rise to different ring current shifts for adsorbates. This represents an important step in the development of NMR methods to study supercapacitors, where ultimately a range of different electrode materials will be studied. In the first part of the chapter, NICS calculations are carried out to probe the ring current shifts nearby a range of model carbon fragments. This allows the identification of a number of key structural factors that determine what is observed experimentally for molecules and ions adsorbed in porous carbons. Experimental spectra for TiC-CDCs from Chapter 4 are revisited, and spectra for additional carbons are presented, with the observed chemical shifts rationalised by the results of the calculations. Finally, NMR spectroscopy is proposed as a new method for the characterisation of local order in porous carbons, allowing an estimation of the sizes of the carbon domains in which ring currents are present.

5.2 Experimental Details

5.2.1 Nucleus-independent chemical shift calculations

All geometry optimisations and NMR calculations were performed using Gaussian software.¹⁵⁶ Molecular geometries were first optimised using the B3LYP exchange-correlation functional with the 6-31G(d) basis set, following the approach of Moran *et al.*¹⁵⁴ Previous work showed that NICS values calculated near aromatic hydrocarbons do not vary significantly when different basis sets are used.¹³⁹ For the case of slit-pores, the optimised structure of circumcoronene ($C_{54}H_{18}$) was used for each pore wall, separated by a distance, d . NMR calculations were performed at the B3LYP level of theory and with the 6-31G(d) basis set to evaluate the chemical shielding tensors for each atom as well as for several ghost atoms introduced around the structure. These ghost atoms have no electrons or nuclear charge and simply serve to act as probes of the local magnetic field at their position. The calculations generate the isotropic chemical shielding, σ_{iso} , with the NICS given by Equation 5.2.

5.2.2 Carbon materials

The preparation of TiC-CDC samples studied in this chapter is described in Section 4.2.1.

^{13}C enriched TiC-CDC samples were prepared by collaborators in the laboratory of Prof. Yury Gogotsi at Drexel University. Ti^{13}C was first prepared by heating a stoichiometric mixture of ^{13}C powder (0.4 g, 99 at. %, Sigma-Aldrich) and crystalline titanium (1.7 g, \geq 99.99 at. %, Sigma-Aldrich; particle size: 5–10 μm) at 1550 °C for 12 h. Ti ^{13}C -CDC samples were then prepared by chlorine-treatment as described in Section 4.2.1 for TiC-CDC.

TiC-CDC samples with an additional vacuum-annealing step were prepared by collaborators in the laboratory of Prof. Volker Presser at the Leibniz Institute for New Materials. TiC-CDC material was first held at 200 °C for 2 h to remove adsorbed water, with a final high-temperature vacuum (10^{-4} to 10^{-5} mbar) annealing step carried out at 1400 °C for 1 h. Heating and cooling rates were 10 °C min $^{-1}$.

Before preparing NMR samples, freestanding carbon films were prepared, as described in Section 4.2.1.

5.2.3 NMR experiments

NMR experiments were performed using Bruker Avance spectrometers operating at magnetic field strengths of 7.1 and 9.4 T, corresponding to respective ^1H Larmor frequencies of 300.2 MHz and 400.4 MHz. Bruker 2.5 mm double resonance probes were used. Experiments studying electrolyte ions were performed at 5 kHz MAS using a spin-echo pulse sequence ($90^\circ - \tau - 180^\circ - \tau - \text{acquire}$) to avoid baseline distortions and to remove background signals associated with the probe. For both ^{19}F and ^1H experiments, spin-echo τ delays of 200 μs (a single rotor period) were used. For ^{13}C NMR experiments on Ti ^{13}C -CDC films, a simple pulse-acquire experiment was used, with an MAS rate of 15 kHz. ^{19}F NMR spectra were referenced relative to neat hexafluorobenzene (C_6F_6) at -164.9 ppm, while ^1H NMR spectra were referenced relative to tetramethylsilane using the CH_3 resonance of liquid ethanol at 1.2 ppm as a secondary reference. ^{13}C NMR spectra were referenced to the tertiary carbon atom in adamantane at 38.5 ppm. For both ^{19}F and ^1H NMR experiments recycle delays were adjusted to give quantitative spectra. For ^{13}C NMR experiments a recycle delay of 5 s was used. Radio-frequency strengths of between 100 and 135 kHz were used for all nuclei studied, except for experiments carried out on vacuum-annealed carbons where radio frequency strengths of 98 and 82 kHz were used for ^1H and ^{19}F experiments, respectively. Chemical shifts were determined by inspection of the spectra, while peak linewidths were obtained from a two peak fits in dmfit software¹³⁷ with a single peak used to fit each in-pore and ex-pore resonance.

Samples were prepared for studying ion-adsorption as described in Section 4.2.2.

5.2.4 Determination of pore size distributions

Gas sorption experiments and analysis were carried out by collaborators in the laboratory of Prof. Volker Presser at the Leibniz Institute for New Materials. Nitrogen sorption analysis was carried out using Quantachrome Instruments (USA) Autosorb system at -196 °C. Pore size distributions were determined using quenched solid density functional theory methods⁵³ on the desorption branch of the isotherms. All samples are predominantly microporous with a small volume fraction of the total pore volume associated with pores larger than 2 nm. The cut-off of the nitrogen gas sorption analysis is around 30 nm so that no inter-particle pores between the CDC grains are considered.

5.2.5 Raman spectroscopy

Raman spectra were recorded and analysed by collaborators in the laboratory of Prof. Volker Presser. Spectra were measured using a Renishaw inVia Raman system equipped with an Nd-YAG laser and an excitation wavelength of 532 nm with power of 0.2 mW at the focal point focused on a spot of approximately 2 μm diameter. A grating with 2400 lines mm^{-1} and a 50x objective (numeric aperture: 0.9) were used, yielding a spectral resolution of 1.2 cm^{-1} . Raman peak fitting was done using two Lorentzian peaks, one for the D-band and one for the G-band.

5.2.6 Powder X-ray diffraction

Powder X-ray diffraction patterns were collected on a Panalytical Empyrean diffractometer using Cu K α radiation. 10 minute scans were recorded measuring 2θ angles from 5 to 80 degrees.

5.3 Results and Discussion

5.3.1 Effect of carbon domain size

Amorphous carbons are known to be predominantly sp² hybridised with six-membered hexagonal carbon rings.³⁵ Benzene was therefore chosen as a starting point for NICS calculations. The structure of benzene was geometry optimised in Gaussian, and NICS values were then calculated at positions at different heights, z , above the ring centre (Figure 5.1a). Positions less than 3 Å away from the carbon plane were not considered, as it is unlikely that adsorbate molecules will be able to probe these distances due to the van der Waals radii of the carbon and the probe molecule.¹⁵⁷ Negative NICS values were calculated at all positions considered here, meaning that a probe nucleus would be shielded by the carbon ring currents at all of the considered positions. This result suggests that a porous carbon comprised predominantly of benzene-like moieties should give rise to a shielding effect for nearby adsorbed ions, in qualitative agreement with the experimental data in Chapter 4 and studies in the literature.

In reality porous carbons are likely composed of somewhat larger carbon fragments than benzene.⁴⁰ For carbons derived from both organic and inorganic precursors, it is thought that the size of the graphene-like domains tends to increase for higher synthesis temperatures.^{33,143,158} To explore the effect of the carbon domain size on the NICS, further calculations were performed on a series of coronenes. Figure 5.1b shows NICS values calculated at different heights, z , above the ring plane of coronene, with three different positions in the x - y plane being considered. For all positions studied, negative

NICS values were calculated. The magnitude of the calculated NICS is greatest for small distances above the centre of coronene, and at large distances the NICS tends toward zero (Figure 5.1b). Moreover, as positions more remote from the coronene centre (in the x - y plane) are considered (see position A to B to C), the magnitudes of the NICSs tend to decrease. For example, the calculated value at 3 Å above the centre of the external 6-membered ring (position C) is -3.6 ppm, compared to -4.4 ppm at 3 Å above the central ring (position A).

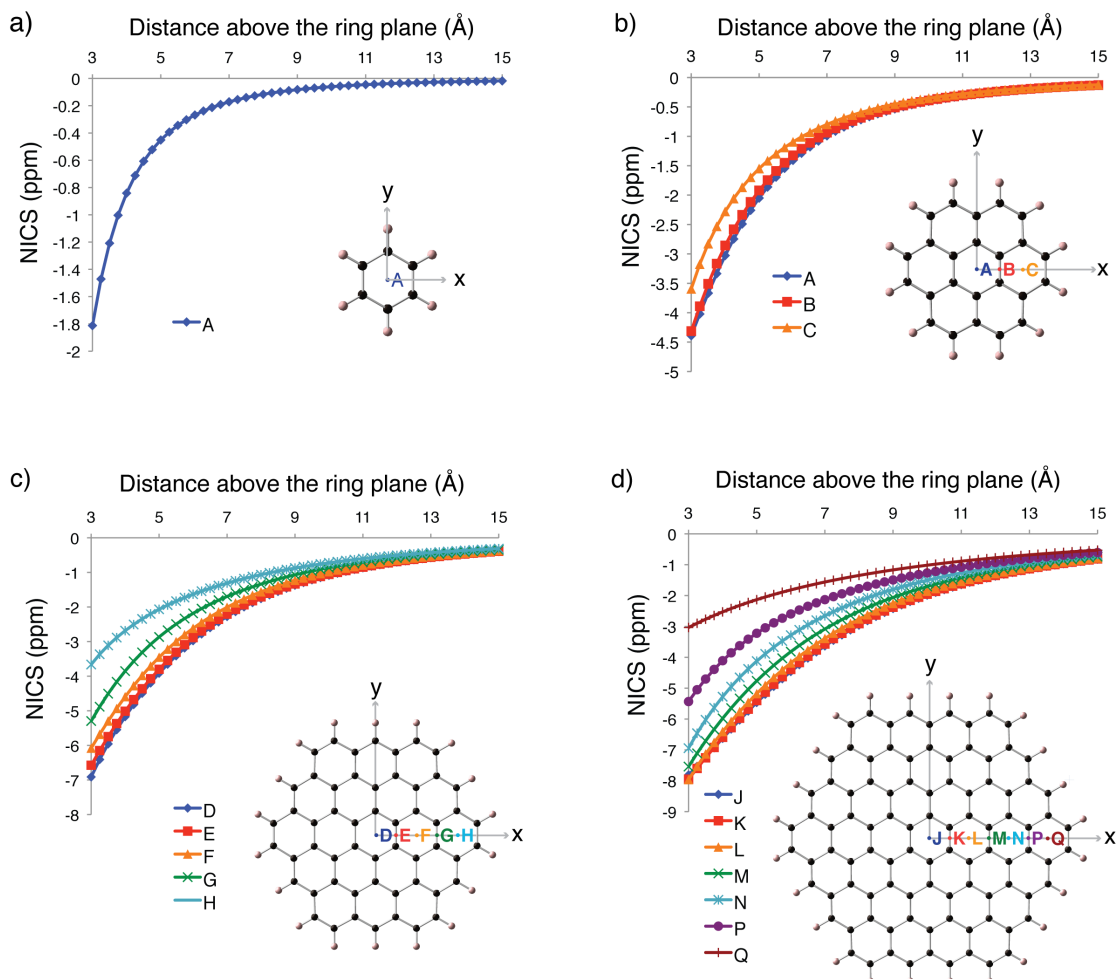


Figure 5.1 NICS calculations on (a) benzene, (b) coronene, (c) circumcoronene, and (d) dicircumcoronene. Insets show the optimised structures as well as positions in the x - y plane where values were calculated. NICS values tend to increase in magnitude as larger carbon fragments are studied.

Calculated NICS values for circumcoronene and dicircumcoronene (Figure 5.1c,d) show similar trends to coronene, with the magnitude of the shielding values largest above the centre of the molecules and smaller towards the edges. Importantly, the NICSs above the molecular centres are found to increase with the size of the carbon fragment. This trend is in agreement with previous NICS calculations used to interpret intermolecular shielding effects in the solid state structures of aromatic molecules.^{139,159}

Here, the maximum calculated NICS varies from -1.8 to -4.4 to -6.9 to -7.8 ppm as the carbon fragment diameter is increased from 2.8 to 7.5 to 12.4 to 17.3 Å, respectively. These calculations suggest that a porous carbon with more ordered hexagonal bonding and larger graphene-like domains should bring about greater shielding effects for adsorbate molecules. More disordered carbons with smaller graphene-like domains will result in smaller shielding effects. In real porous carbon particles, a liquid or gaseous adsorbate will experience a range of carbon structures on the NMR time scale. Indeed, the 2D EXSY NMR experiments presented in Chapter 4 showed that electrolyte ions undergo chemical exchange in and out of the carbon micropores on a millisecond time scale. Thus, experimentally observed in-pore chemical shifts will likely arise from a dynamic averaging of chemical shifts associated with many different adsorption sites. The effects of dynamics are discussed in more detail in Chapter 7.

5.3.2 Effect of carbon pore size on the NICS

In a real porous carbon, molecules will experience ring current effects from multiple carbon surfaces within the carbon pores. To probe the effect of well-defined carbon pore sizes on the chemical shifts of adsorbates, NICS calculations were performed on model slit-pores consisting of two individually optimised circumcoronene ($C_{54}H_{18}$) molecules (sheets) separated by a distance, d (see Figure 5.2a). In each case, NICS values were calculated at positions within the pore along the z -axis, which coincides with the C_6 symmetry axis, and positions less than 3 Å from the carbon sheets were again not considered.

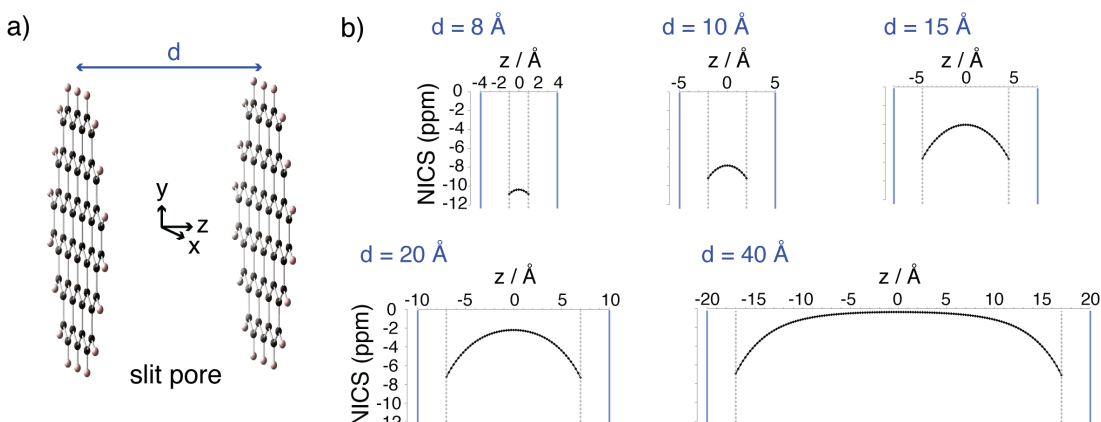


Figure 5.2 (a) Geometry of model slit-pores comprising two circumcoronene molecules. (b) NICS calculations for slit-pores with different sizes. Blue solid lines represent the positions of the pore walls, with NICS values calculated between the positions indicated by the dotted grey lines. Overlap of the ring current effects from the pore walls tend to increase NICS values as the pore size is decreased.

NICS values are shown in Figure 5.2b for a range of different pore widths, with negative NICSs calculated for all positions considered. This shows that the NMR resonance from a nucleus in a molecule within a carbon pore should again appear at a lower frequency than the resonance from the free molecule. For small pores (*e.g.*, $d = 8$ Å), considerable overlap of the shielding effects from the pore walls brings about NICS values with a large magnitude and only small variations across the pore. As the pore size is increased, this overlap becomes less significant, and for a large pore (*e.g.*, $d = 40$ Å) the overlap is negligible. Importantly, as the pore size is decreased, larger absolute NICS values are calculated. The findings here are similar to those from a previous study which employed a classical treatment of magnetic susceptibility effects from two pore walls.¹³⁵ Comparison of the values calculated for the slit-pores with those calculated above a single circumcoronene molecule (Figure 5.1c) show that the effects of the two circumcoronenes (*i.e.*, the pore walls) are additive to a very good approximation (Table 5.1). Knowing this, NICS values may readily be generated for a range of different pore sizes, if NICS values are known for a given single carbon fragment.

Again, the effects of dynamics must be considered as fast exchange between different adsorption sites will result in an averaging of the observed chemical shift. Indeed, a single NMR resonance was observed experimentally for species adsorbed in a porous carbon with a bimodal pore size distribution, suggesting there can be fast exchange within the porous network in that carbon.¹⁴¹ As such, it is very reasonable to expect fast exchange between the different positions within a pore. Averaging of the NICSs calculated here yields values of -10.6 , -8.3 , -5.2 , -3.7 , and -1.7 ppm for slit (circumcoronene) pores of width 8, 10, 15, 20, and 40 Å, respectively. While it may be more appropriate to perform a weighted average taking into account the effect of the adsorption thermodynamics (see later), the general trend of greater chemical shielding with decreasing pore size will remain unchanged. This qualitative trend agrees well with recent experimental work by Borchardt *et al.*,¹⁴¹ where ^{11}B MAS NMR spectra of the electrolyte NEt_4BF_4 in acetonitrile (1 M) adsorbed in a series of carbons with well-controlled pore sizes showed a general increase of in-pore chemical shielding as the average pore size was decreased. ^1H NMR studies of hydrogen gas adsorbed on a series of activated carbons revealed similar trends.^{135,136}

Table 5.1 Calculated NICS values for a slit-pore with $d = 10 \text{ \AA}$, as well as values calculated by summing NICSSs for individual circumcoronene molecules situated at $z = \pm 5 \text{ \AA}$. The values for the slit-pore calculations can be obtained by summing contributions from the individual pore walls.

z position (\text{\AA})	additive NICS (ppm)	slit-pore NICS (ppm)	difference (ppm)
-2.00	-9.19	-9.19	0.00
-1.75	-8.84	-8.85	-0.01
-1.50	-8.56	-8.57	-0.01
-1.25	-8.33	-8.34	-0.01
-1.00	-8.14	-8.16	-0.02
-0.75	-8.01	-8.02	-0.02
-0.50	-7.91	-7.93	-0.02
-0.25	-7.85	-7.87	-0.02
0.00	-7.83	-7.85	-0.02
0.25	-7.85	-7.87	-0.03
0.50	-7.91	-7.93	-0.03
0.75	-8.01	-8.03	-0.03
1.00	-8.14	-8.17	-0.03
1.25	-8.33	-8.36	-0.03
1.50	-8.56	-8.59	-0.03
1.75	-8.84	-8.87	-0.03
2.00	-9.19	-9.22	-0.03

5.3.3 Effects of carbon curvature

So far NICS values have only been calculated for planar carbon structures with hexagonal carbon rings. However, it has been suggested that non-hexagonal rings may be present in porous carbons, and that these give rise to the sheet curvature, resulting in disordered and porous carbon structures.³⁵ Figure 5.3a shows the geometry-optimised structures of carbon fragments with non-hexagonal rings at the centre. C₂₀H₁₀ (corannulene) is essentially a fragment of a fullerene, with a 5-membered ring at the centre and a bowl-like structure. On the other hand, C₂₈H₁₄ has a saddle shaped structure with a 7-membered ring at the centre. 5-membered carbon rings have recently been detected by TEM of an activated carbon,⁴² while 7-membered rings are also thought to be present in a range of carbon materials.¹⁶⁰ In this case, molecular species adsorbed inside porous carbons may experience a range of different curved carbon structures as well as planar ones.

To probe the effect of curvature on the NICS values, calculations were performed on C₂₀H₁₀ (Figure 5.3b). NICSSs were calculated along the C₅ symmetry axis on both the convex and concave faces. On both faces negative NICSSs were calculated, though the magnitude of the NICSSs are considerably greater on the concave face. While a maximum NICS of -1.0 ppm is calculated on the convex face (at 3 \text{\AA} from the central ring plane), the maximum NICS on the concave face is -5.5 ppm. The corresponding value for planar coronene is -4.4 ppm, intermediate between the maximum values

calculated for the two faces of $C_{20}H_{10}$. This suggests that porous carbons exhibiting different amounts of concave, convex, and planar surfaces will bring about different chemical shifts for adsorbed molecules, though the effect of dynamic averaging should again be considered. Deschamps *et al.* recently observed two different chemical environments for adsorbed ions inside activated carbons.¹⁸ In addition to resonances arising from “type I” ions adsorbed between graphene-like sheets, a less shielded resonance arising from “type II” adsorption sites was observed and was postulated to arise from ions near 5- or 7-membered carbon rings. Given the results presented here, it is possible that such a type II resonance arises from ions inside regions of the carbon exhibiting a relatively large number of convex carbon surfaces. However, based on the calculations in Figure 5.1, type II resonances may also arise from ions inside regions of the carbon with smaller carbon domains. It is also possible that the difference between type I and type II resonances is an effect from chemical exchange, whereby ions in the type II environment are undergoing fast exchange with ex-pore ions, giving rise to the smaller (average) chemical shielding of this resonance.

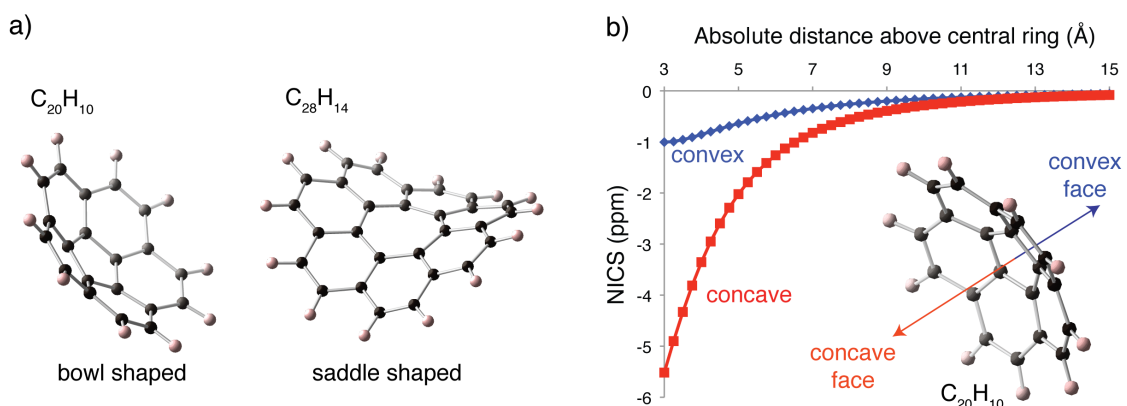


Figure 5.3 (a) Optimised structures of $C_{20}H_{10}$ and $C_{28}H_{14}$ showing how the presence of non-hexagonal carbon rings brings about curvature. (b) NICS calculations for $C_{20}H_{10}$, with values calculated along the C_5 symmetry axis on both sides of the molecule. Curvature can have a pronounced effect on the NICS values.

5.3.4 Additional considerations for NICS calculations

In the NICS calculations presented so far, only positions above the carbon planes have been considered. In principle, adsorbate molecules may also be located at the edge of the carbon sheets. Calculated NICS values along the x -axis of coronene are shown in Figure 5.4. Contrary to the rest of results presented so far, positive NICS values are calculated here, with a maximum value of 1.1 ppm (at a distance of 3 \AA from the hydrogen atoms). Thus, an adsorbate molecule located at a sheet edge would be

expected to give rise to a deshielded in-pore resonance. In practice, the chemical shift observed for in-pore ions arises from exchange of the ions between a range of sites (see Chapter 7). The observation of net shielding effects experimentally suggests that edge sites do not dominate the observed shift. This is presumably because: (i) positive NICS values calculated at the sheet edge are smaller in magnitude than those calculated above the carbon surfaces, and (ii) there are far fewer accessible sites at sheet edges than there are above planar surfaces.

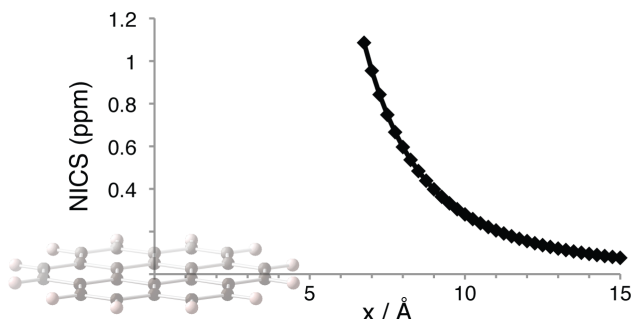


Figure 5.4 NICS values calculated in the ring plane of coronene. Values are calculated along the x -axis at positions greater than 3 Å from the hydrogen atoms. Positive NICS values are calculated for all positions considered here.

So far, only isotropic NICS values have been presented. However, the calculated shielding tensors (and therefore chemical shift tensors) are anisotropic. To illustrate this, powder patterns were simulated for positions at different distances above the ring centre of coronene (Figure 5.5). For the positions considered, the chemical shift tensors are axially symmetric. When the magnetic field coincides with the z -axis of the molecule, electrons circulate around the applied field in the π orbitals, with a large ring current established around the molecule. This leads to the large chemical shielding for the probe nucleus situated above the ring plane. However, when the magnetic field coincides with x or y molecular axes, the electrons may no longer circulate freely around the coronene π -system, and smaller electronic currents are established perpendicular to the ring plane. This has the effect of slightly deshielding the probe nucleus. The simulated spectra in Figure 5.5a correspond to an imaginary “powder” of coronene molecules with random orientations and with fixed probe nuclei above the ring centres (Figure 5.5b).

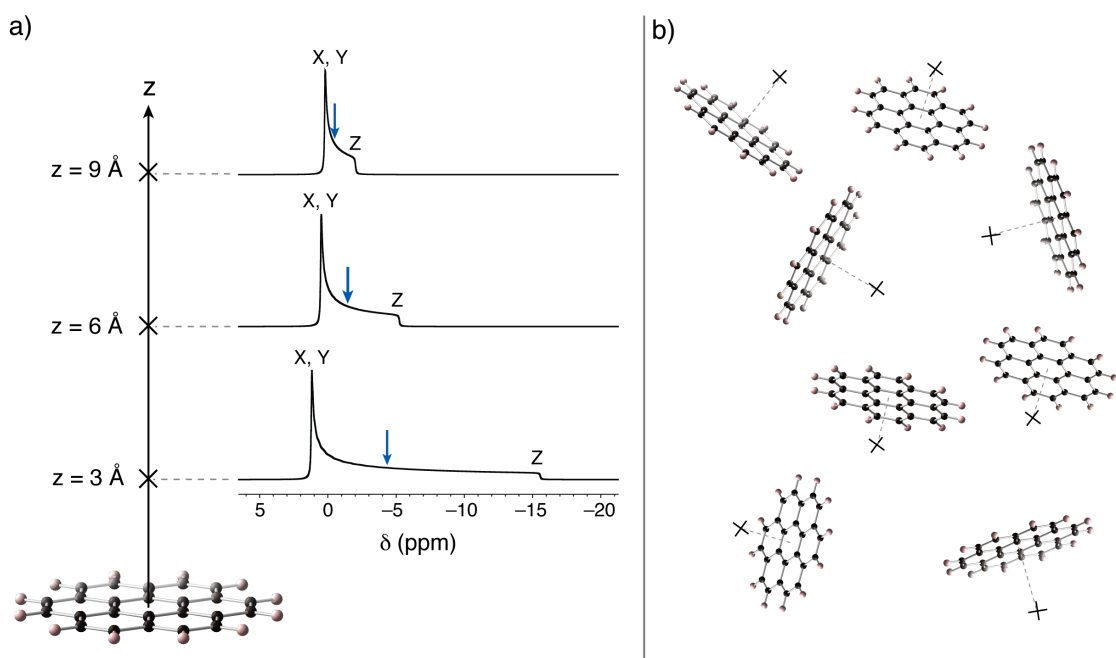


Figure 5.5 (a) Powder patterns for the NICS at different positions above the centre of coronene. The positions of the isotropic NICS values are marked with blue arrows. The spectra in (a) correspond to static NMR experiments on systems as depicted in (b), whereby fixed probe spins (marked by \times) are located above coronene molecules that are randomly distributed in space.

For the fictitious system depicted in Figure 5.5b, magic angle spinning would break the simulated powder patterns up into spinning sidebands, and in the limit of fast spinning a single narrow resonance would be observed at the isotropic chemical shift. In practice, for a liquid electrolyte there will also be considerable motion of the adsorbate nuclear spins between different sites inside the carbon pores. This will have the effect of averaging the powder patterns into narrower spectral features centred at a weighted average of the isotropic NICS values of the sites. In the limit of very fast motion of the adsorbates, the effects of anisotropy will be entirely averaged out. In general the isotropic NICS value is sufficient for comparing the ring current effects nearby different carbon structures, however, the effects of anisotropy could be important when simulating spectra or carrying out very low temperature NMR experiments.

A final complexity arises from the fact that NICS calculations do not model any differences that may be observed when different adsorbates are studied experimentally. Since no adsorbate is included in the calculation, adsorbent-adsorbate interactions are not taken into account. Changes in the carbon electronic structure may occur upon adsorption, which may be different for different ions. DFT calculations on molecules confined inside carbon nanotubes have shown that adsorbent-adsorbate interactions can lead to differences between the calculated chemical shifts and the NICS values, though

this is generally a minor effect.^{123,149} There may also be effects from differences in the shapes and sizes of adsorbates, which may affect the carbon-adsorbate distances. Experimentally, similar $\Delta\delta$ values were observed in the ^{19}F spectra of BF_4^- anions, the ^1H spectra of NEt_4^+ cations, and in the ^2H spectra of solvent molecules in Chapter 4, though there were some small differences. Therefore it is generally more appropriate to compare shifts from the same adsorbate, when studying adsorption on different carbons.

5.3.5 Revisiting the NMR spectra of electrolyte-soaked TiC-CDCs

In Chapter 4, NMR spectra were presented for a series of electrolyte-soaked TiC-CDCs. As the carbon chlorine-treatment temperature was increased, the in-pore resonances were increasingly shielded for all nuclei studied (The data is summarised in Table 5.2). There are some differences on the order of 1 ppm observed for the different molecules and nuclei, suggesting that there are small differences in the carbon-adsorbate interactions or distances, as discussed above.

Table 5.2 $\Delta\delta$ values for TiC-CDCs studied in this work. Values are reproduced from Chapter 4 for convenience. The $\Delta\delta$ values increase in magnitude at the chlorine-treatment temperature is increased.

Carbon	$\Delta\delta$ ^{19}F (ppm) BF_4^-	$\Delta\delta$ ^1H (ppm) $\text{NEt}_4^+ - \text{CH}_2$	$\Delta\delta$ ^1H (ppm) $\text{NEt}_4^+ - \text{CH}_3$	$\Delta\delta$ ^2H (ppm) D_3CCN
TiC-CDC-600	-2.6	-4.0	-3.9	-3.4
TiC-CDC-800	-4.0	-4.7	-4.6	-3.6
TiC-CDC-1000	-5.4	-5.8	-5.7	-5.5

The general variation of the $\Delta\delta$ values with chlorine-treatment temperature may be explained by considering the structures of these carbons and the results from the NICS calculations. As the chlorine-treatment temperature of the TiC-CDC sample is increased, there are a number of structural changes.³³ Pore size distributions were measured by N_2 sorption measurements, with experiments and data analysis carried out by collaborators in the laboratory of Prof. Volker Presser at the Leibniz Institute for New Materials. The average pore size of the carbons increases from 8.2 to 9.1 to 9.3 Å as the chlorine-treatment temperature is increased from 600 to 800 to 1000 °C, respectively, while the pore size distribution also broadens as the temperature is increased, with a greater number of pores with diameters > 1 nm (Figure 5.6a). On the basis of the changes of pore size and the NICS calculations in Figure 5.2, one would expect the $\Delta\delta$ value to increase with chlorine-treatment temperature, contrary to what is observed experimentally. However, increases in pore size are accompanied by increases in carbon ordering as the chlorine-treatment temperature is increased. Raman spectra of these carbons (again recorded by collaborators at the Leibniz Institute for New

Materials) reveal decreases in the full-width at half-maximum intensity (FWHM) of the D band as the chlorine-treatment temperature is increased, suggesting the carbon-carbon bonding becomes more ordered (Figure 5.6b).^{28,33} Moreover, magnetic susceptibility measurements,¹⁴³ and structural simulations using quenched MD simulations⁴⁷ also suggest that as the chlorine-treatment temperature is increased, the carbon structure becomes more ordered on a local scale with larger graphene-like domains. On the basis of the NICS calculations, increases in the size of the graphene-like domains are expected to lead to decreases of the $\Delta\delta$ values (values become more negative), as observed. Overall these findings then suggest that for these TiC-CDCs, the carbon domain size dominates over any pore-size effects. Clearly, a more definitive understanding of the interplay between carbon structures and chemical shifts could be obtained by studying a series of carbons where one of either pore size or local ordering are fixed, and the other parameter is varied.

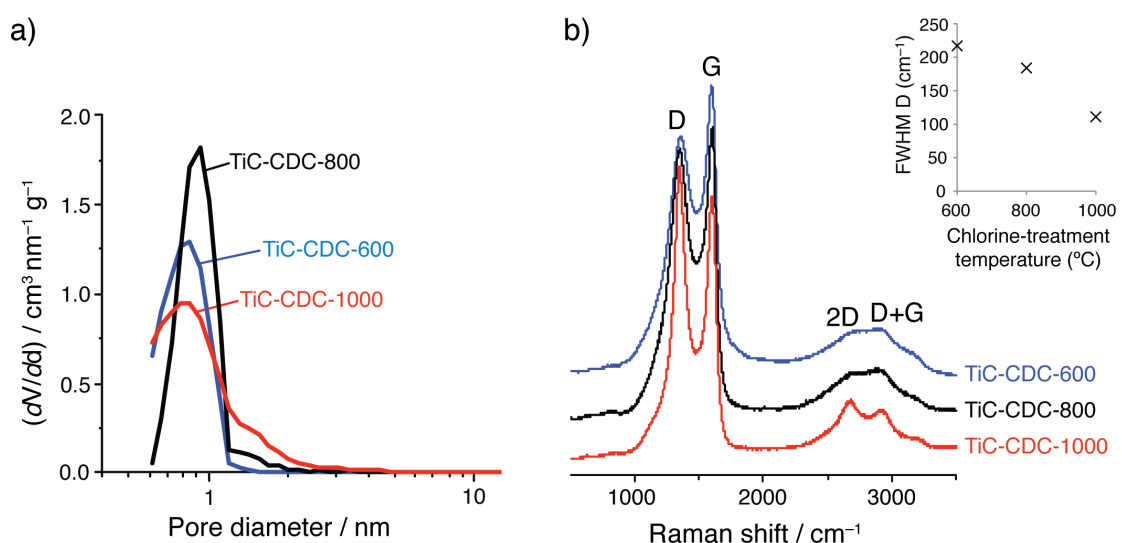


Figure 5.6 (a) Pore size distributions of TiC-CDCs extracted from N_2 sorption isotherms. (b) Raman spectra of TiC-CDCs, with the fitted D band FWHMs shown as an inset. The pore size distribution tends to broaden and shift to higher average values as the chlorine-treatment temperature is increased, while the Raman spectra also indicate that ordering in the carbon sheets increases.

The findings here agree with recent work where ^{11}B MAS NMR showed that resonances from in-pore BF_4^- anions in TiC-CDC-1000 were more shielded than those in TiC-CDC-600.¹⁴¹ This was rationalised by noting that TiC-CDC-600, with a lower synthesis temperature, is a more disordered carbon with more sp^3 -hybridized carbon. Here, however, ^{13}C NMR experiments on Ti^{13}C -CDCs do not show any peaks indicative of sp^3 -hybridized carbon (~40 ppm),¹⁶¹ and show only a single broad resonance at ~125

ppm due to sp^2 -hybridized carbon (Figure 5.7). The effect is therefore ascribed to the different carbon domain sizes in which the ring currents are present.

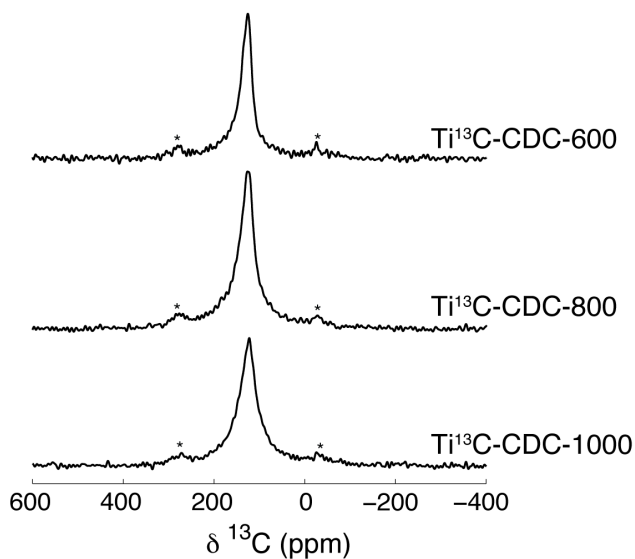


Figure 5.7 ^{13}C MAS (15 kHz) NMR of different Ti^{13}C -CDC film pieces. Spectra are normalised by the carbon film masses. Asterisks mark spinning sidebands. Each spectrum shows a single resonance consistent with sp^2 hybridised carbon.

5.3.6 Experimental observation of carbon pore size effects

To further investigate the interplay between carbon structures and the chemical shifts observed for in-pore ions, CDCs that had been synthesised with an additional vacuum-annealing step for one hour at 1400 °C at the end of the synthesis were studied (samples are then referred to as TiC-CDC-X-VAC ; *e.g.*, TiC-CDC-600-VAC for a sample chlorine treated at 600 °C). Such high temperature vacuum-annealing is thought to increase structural order in the carbon, with the formation of larger ordered hexagonal carbon domains, the removal of oxygen containing functional groups, and in some cases increased stacking of the defective carbon sheets.^{162,163} Importantly, vacuum annealing does not lead to a significant loss in carbon porosity and only leads to small changes in the carbon pore size distributions, with the resulting porosity largely dependent on the chlorine-treatment temperature used. The pore size distributions of vacuum-annealed carbons, extracted from N_2 sorption isotherms (again measured by collaborators at the Leibniz Institute for New Materials) show significant differences (Figure 5.8a). In contrast, Raman spectra (Figure 5.8b, Leibniz Institute for New Materials) of these carbons are almost identical, suggesting that the local carbon-carbon bonding of these carbons is very similar. This is presumably a result of the exposure to one common high temperature significantly above the chlorine-treatment temperatures used. It is noted

that the X-ray diffraction patterns of the vacuum-annealed carbons are also very similar to those of the normal TiC-CDCs (Figure 5.8c), suggesting that long-range graphitisation has still not occurred after vacuum annealing at 1400 °C.

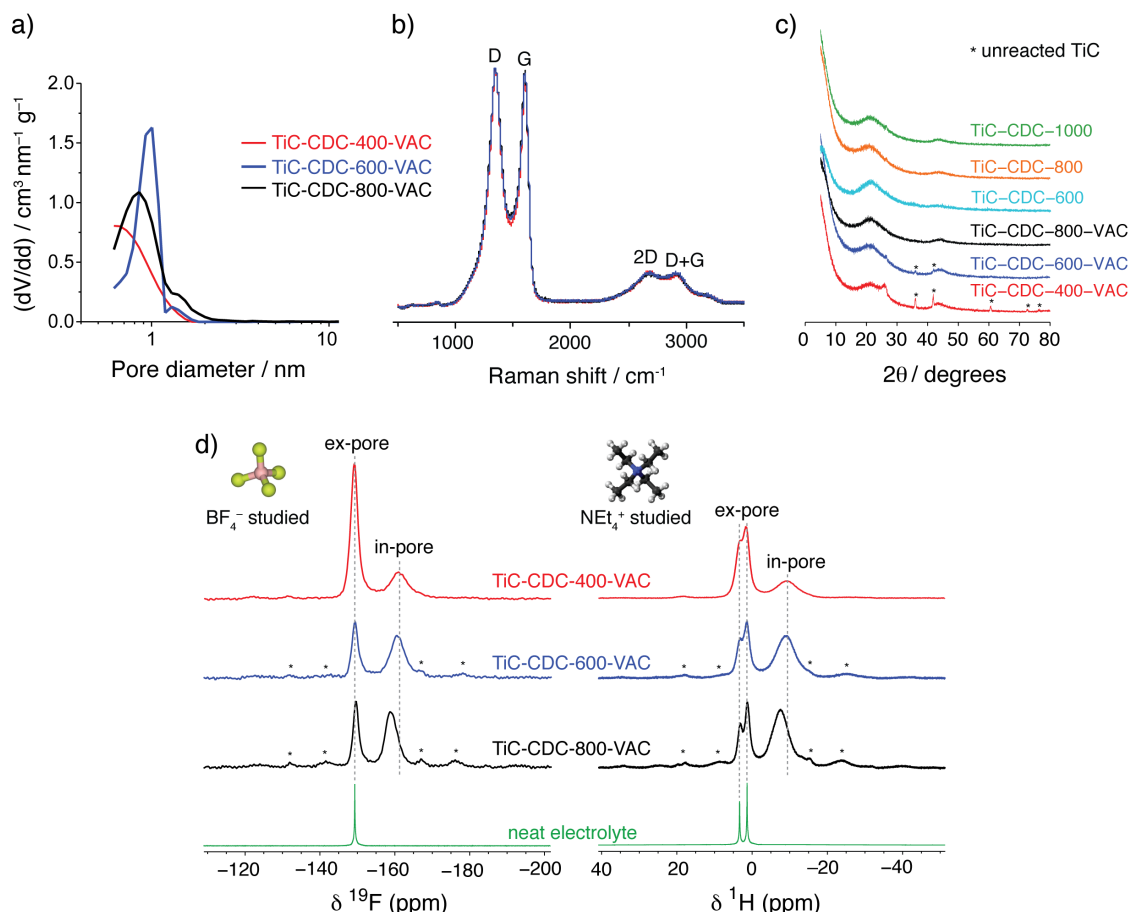


Figure 5.8 Structural characterisation of vacuum-annealed carbide-derived carbons; (a) pore size distributions measured by N₂ sorption, (b) Raman spectra and (c) X-ray diffraction patterns. In (d) ¹⁹F and ¹H MAS NMR (7.1 T) spectra are shown for electrolyte-soaked carbon samples. Here dashed lines show the positions of the in-pore resonance for TiC-CDC-400-VAC, and the positions of the neat electrolyte resonances. Asterisks mark spinning sidebands.

Figure 5.8d shows the ¹⁹F and ¹H magic angle spinning (MAS) NMR spectra of the vacuum-annealed carbons soaked with NEt₄BF₄/dACN (1.5 M). As with normal TiC-CDCs in- and ex-pore resonances can be observed in all cases, with the extracted $\Delta\delta$ values given in Table 5.3. The differences between the in-pore and neat electrolyte chemical shifts ($\Delta\delta$) are again similar for ¹⁹F and ¹H spectra for a given carbon (confirming the first-order nucleus-independence of the ring current chemical shift) but depend on the carbon chlorine-treatment temperature (Table 5.3). This can be rationalised by considering the pore size distributions of the carbons (Figure 5.8a). As the temperature of the chlorine-treatment step is increased, larger pores are formed, and

the pore size distribution also broadens. This then gives rise to $\Delta\delta$ values of smaller magnitude, in agreement with the NICS calculations above. It is noted at this point that the in-pore linewidths also vary with the chlorine-treatment temperature. This will be discussed in Chapter 7.

Table 5.3 $\Delta\delta$ values and in-pore linewidths for electrolyte-soaked vacuum-annealed carbide-derived carbons. The $\Delta\delta$ values and in-pore linewidths show decreases in magnitude as the chlorine-treatment temperature of the carbon increases.

Carbon	$\Delta\delta$ ^{19}F (ppm)	$\Delta\delta$ ^1H (ppm)	^{19}F FWHM in-pore (Hz)	^1H FWHM in-pore (Hz)
TiC-CDC-400-VAC	-11.6	-11.4	1590	2090
TiC-CDC-600-VAC	-11.1	-11.1	1230	1760
TiC-CDC-800-VAC	-9.7	-9.1	1050	1510

5.3.7 Experimental observation of carbon ordering effects

To study the effects of vacuum annealing, NMR spectra of electrolyte-soaked TiC-CDC-800 and TiC-CDC-600-VAC were compared. The NMR spectra are remarkably different, despite the similar pore size distributions of the two carbons (Figure 5.9a). The $\Delta\delta$ values are significantly larger for the vacuum-annealed carbon, while increases of the in-pore linewidth are also observed (Table 5.4). Given the similar pore size distributions of these carbons, the increases of the magnitude of the $\Delta\delta$ values must arise from increases in the sizes of the carbon domains in which ring currents are present. This could arise from the annealing of defects and the removal of functional groups. Consistent with this, Raman spectra of the carbons indicate that TiC-CDC-600-VAC has more ordered carbon-carbon bonding than TiC-CDC-800. (Figure 5.9a). Meanwhile, broader in-pore linewidths are also observed for the vacuum-annealed carbon.

In Figure 5.9b, a similar comparison is made for TiC-CDC-1000 and TiC-CDC-800-VAC, which again have similar pore size distributions. The magnitude of the $\Delta\delta$ values and in-pore linewidths are again larger for the vacuum-annealed carbon. Table 5.4 shows that for these carbons the structural differences are smaller than those in Figure 5.9a. This is as TiC-CDC-1000 is more ordered than TiC-CDC-800. It is also noted that Raman spectra of TiC-CDC-1000 and TiC-CDC-800-VAC are very similar, suggesting that the NMR method is potentially a more sensitive probe of differences in the carbon structures here. Recently, Xu *et al.* conducted a ^1H NMR study of the adsorption of water in two mesoporous carbons with similar pore size distributions.¹⁴² Their similar

observations of larger ring current shifts for the carbon prepared at higher temperature highlight the generality of the effects reported here for microporous TiC-CDCs.

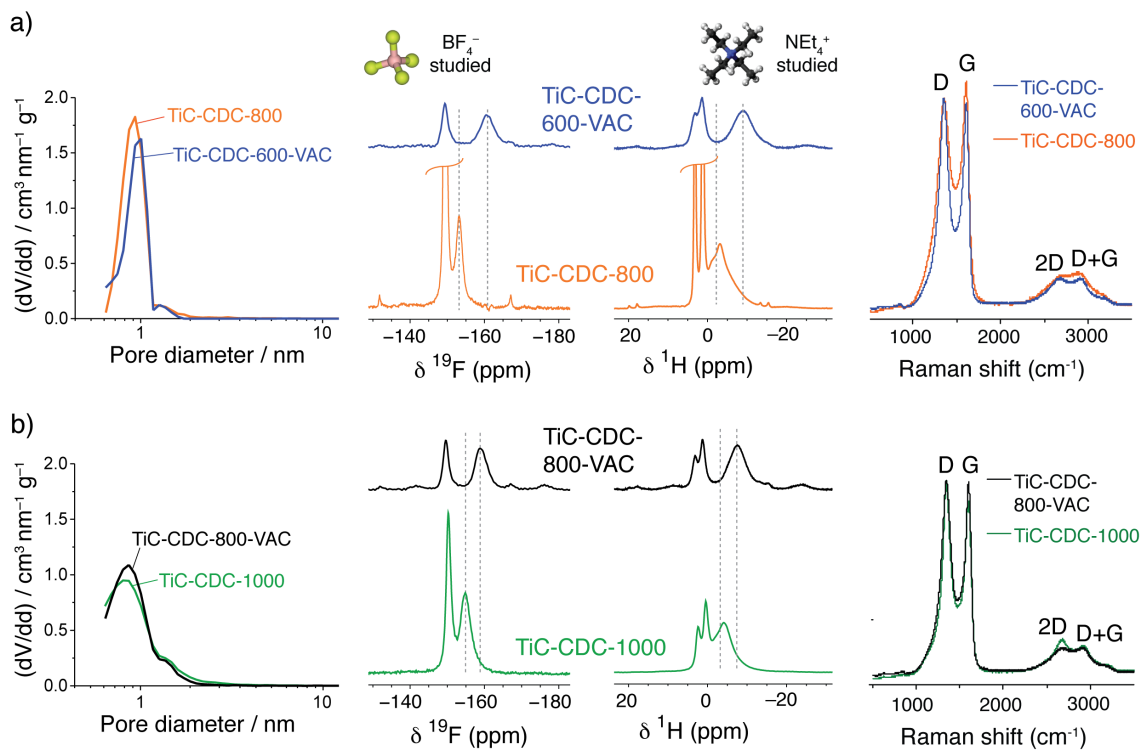


Figure 5.9 Comparison of (a) TiC-CDC-800 and TiC-CDC-600-VAC, and (b) TiC-CDC-1000 and TiC-CDC-800-VAC. Pore size distributions, ^{19}F and ^1H MAS NMR (7.1 T) spectra of electrolyte-soaked carbons, and Raman spectra are shown in each case. Vacuum annealing increases the carbon domain sizes.

Table 5.4 Comparison of ^{19}F $\Delta\delta$ values and in-pore linewidths for the carbons investigated in Figure 5.9. For the vacuum-annealed carbons, increases in the magnitude of the $\Delta\delta$ value and the linewidth are observed.

Carbon	$\Delta\delta^{19}\text{F}$ (ppm)	^{19}F FWHM in-pore (Hz)
TiC-CDC-800	-3.9	600
TiC-CDC-600-VAC	-11.1	1230
TiC-CDC-1000	-5.5	950
TiC-CDC-800-VAC	-9.7	1050

5.3.8 Characterising structural order in porous carbons

To explore the relationship between the measured $\Delta\delta$ values and carbon structure, all values measured for TiC-CDC and TiC-CDC-VAC samples are plotted against the maximum heat treatment temperature used in the synthesis of each sample in Figure 5.10a. As this temperature is increased, there is a general increase in the magnitude of the $\Delta\delta$ value, reflecting increases in the sizes of the carbon domains in which ring currents are present. For the vacuum-annealed carbons (1400 °C), the pore size effect is

clearly seen, though this is a minor effect compared to the domain size effect for the range of carbons studied here.

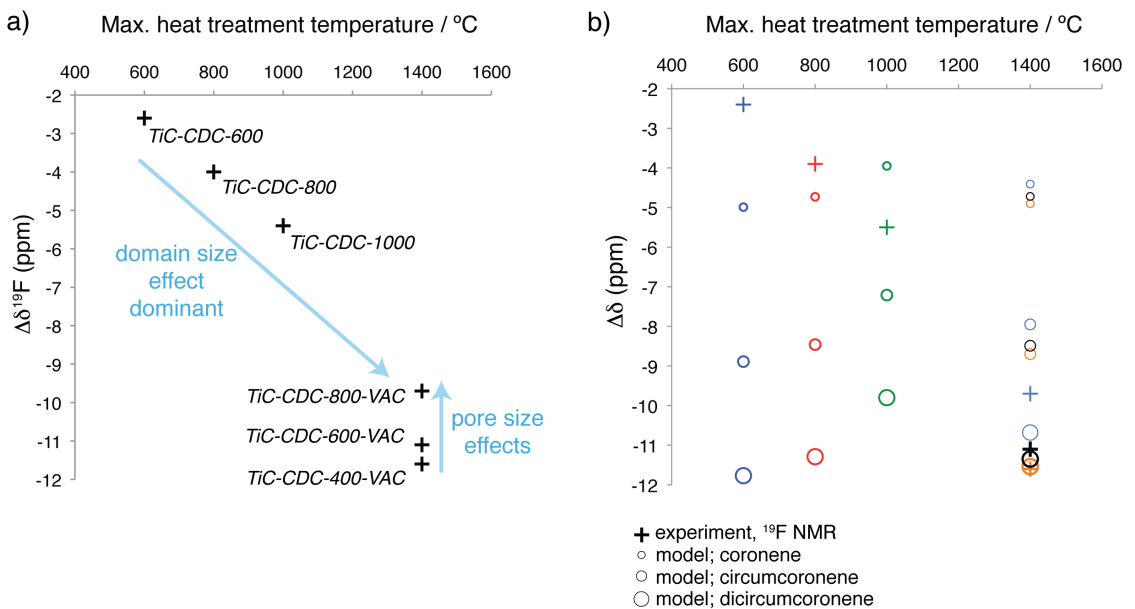


Figure 5.10 (a) Summary of $\Delta\delta$ ^{19}F values measured for carbide-derived carbons in this chapter, with values plotted against the maximum heat treatment temperature that each carbon sample was subjected to in the synthesis. (b) Simulated and experimental $\Delta\delta$ values. For each carbon, three different simulated $\Delta\delta$ values are shown, corresponding to values computed with models employing coronenes of different sizes. This plot allows structural domain sizes in which ring currents are present to be estimated for the different carbons.

Given the sensitivity of the $\Delta\delta$ value to the ring current domain sizes, it should be possible to extract structural information from the NMR spectra. The evolution of the carbon domain size with maximum heat treatment temperature was studied by simulating $\Delta\delta$ values for different model carbon structures. Simulations were carried out by Dr. Céline Merlet (University of Cambridge). In the simulations, an array of slit-pores (with coronenes used as the pore walls, as above) is studied with the distribution of pore sizes chosen to match the experimentally measured distributions, and the variations of chemical shift obtained from NICS calculations as above. This carbon model has the benefits of being computationally easy to handle, while satisfying the key requirement of consisting of sp^2 -hybridised carbon with a porous structure. Here, the adsorption thermodynamics of the in-pore molecules were also taken into account using free energy profiles obtained from MD simulations on a graphitic surface,⁶³ where simulations were carried out on a similar electrolyte (butylmethyimidazolium tetrafluoroborate, BMIBF₄, 1.5 M in acetonitrile) to that studied here. Overall, the simulation then gives the average NICS value for the system, weighted by the

distribution of the different pore sizes, and the different positions inside the individual pores (with a Boltzmann distribution of occupancies according to the free energies of the different sites). More details regarding the computational approach used here can be found in the paper of Merlet *et al.*¹⁶⁴

$\Delta\delta$ values were simulated for each carbon material (with its measured pore size distribution), with three separate simulations carried out for coronenes with different sizes, representing different characteristic domain sizes in which ring currents are present in the carbon (Figure 5.10b). The experimental $\Delta\delta$ values may then be compared to the different simulated values to assess the domain size of each carbon (with the pore size effects already accounted for in the simulations). According to the model, the domain size of TiC-CDC-600 is somewhat less than that of coronene (7.5 Å diameter). For TiC-CDC-800, the domain size is similar to that of coronene, while for TiC-CDC-1000 the domain size is intermediate between that of coronene (7.5 Å diameter) and circumcoronene (12.4 Å diameter). Following vacuum annealing, the $\Delta\delta$ values are best modelled by the dicircumcoronene (17.3 Å diameter) slit-pores (Figure 5.10b), with all carbons having a very similar characteristic domain size. For the vacuum-annealed carbons, the simulations also reproduce the variation of the $\Delta\delta$ values observed experimentally. For the dicircumcoronene model, the simulated $\Delta\delta$ values are –11.5, –11.4 and –10.7 ppm, for TiC-CDC-400-VAC, 600-VAC and 800 VAC, respectively, comparing reasonably well to the experimental values of –11.6, –11.1 and –9.7 ppm. This supports the idea that the domain sizes in these carbons are similar and that the variations of the $\Delta\delta$ values are dominated by pore size effects.

The domain sizes extracted here may be compared to the lengths to which pair distribution functions (obtained by diffraction methods) showed carbon-carbon correlations for activated carbons prepared at different temperatures.⁴⁰ Correlations between the sp² hybridised carbon atoms extended to approximately 10 and 20 Å for porous carbons prepared at 800 °C and 1200 °C, respectively, showing some qualitative agreements with the variations extracted here from the NMR simulations. In principle the NMR and pair distribution function approaches offer complementary information on the structural coherence lengths in the carbon sheets, though the NMR approach may be more sensitive to defects or functional groups that disrupt the carbon ring currents.

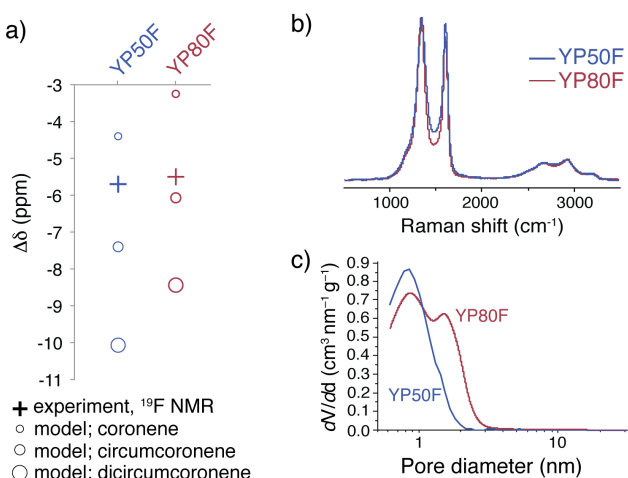


Figure 5.11 (a) Simulated and experimental $\Delta\delta$ values for YP50F and YP80F activated carbons. The simulated values take into account the measured pore size distributions of the carbons (as above for CDCs). For each carbon, three different simulated $\Delta\delta$ values are shown, corresponding to values computed with models employing coronenes of different sizes. (b) Raman spectra and (c) pore size distributions of the carbons. The NMR approach can be used to assess the carbon domain sizes.

The NMR approach developed here can be used to characterise the structures of other porous carbon materials beyond CDCs. To demonstrate this, simulated and calculated $\Delta\delta$ values for two commercial coconut-derived activated carbons, YP50F and YP80F (Kuraray, Japan) are shown in Figure 5.11a. Comparison of the experimental and simulated values indicates that the structural ordering in these carbons is similar, with a domain size intermediate between that of coronene (12.4 Å) and circumcoronene (17.8 Å), similar to that of TiC-CDC-1000. For YP80F, the experimental data point lies closer to the value simulated in the circumcoronene model than for YP50F, suggesting that YP80F has slightly larger domains. Consistent with this idea, the Raman spectra show slightly narrower features for YP80F, indicating that it has slightly more ordered carbon-carbon bonding (Figure 5.11b). It is interesting that the characteristic domain sizes of these carbons are similar despite significant differences in the pore size distributions (Figure 5.11c). Overall, the findings in Figures 5.10 and 5.11 highlight how the NMR approach offers a new way to probe structural order in porous carbons, and can provide information that is complementary to Raman spectroscopy.

5.4 Summary and Outlook

Progress has been made with the understanding of the chemical shifts observed for molecules and ions inside porous carbon materials. The combined theoretical and experimental NMR approach has allowed an exploration of the relationship between different types of carbon structures and the chemical shifts observed for adsorbed ions.

Specifically, NICS calculations on a series of model carbon fragments have shown that:

1. The ring current shifts are sensitive to the size of the graphene-like carbon domains. For more ordered carbons with larger domains, the magnitude of the calculated NICS values increases. Therefore, porous carbons with larger graphene-like domains should give rise to more shielded in-pore resonances.
2. For model slit-pores, the smaller the pore, the larger the magnitude of the calculated NICS values. This arises as the calculated NICS values of the two pore walls are additive. Thus, species adsorbed in porous carbons with smaller pores should give rise to more shielded in-pore resonances.
3. Curvature also affects the calculated NICS values, with values of larger magnitude calculated above convex surfaces than concave surfaces.

The calculations have allowed a rationalisation of the experimentally observed chemical shifts for in-pore ions and solvent molecules for a series of carbide-derived carbons, as well as for two commercial activated carbons. For the range of predominantly microporous carbons studied here, the effects of the carbon domain size were found to be dominant over the pore-size effects in determining the in-pore chemical shifts.

While NICS calculations on model fragments have allowed progress here, ideally calculations would be carried out on more realistic carbon models, such as those generated by quenched MD or hybrid Monte Carlo methods.^{44,45,47} However, these present a significant computational challenge as the number of atoms in typical unit cells are on the order of 1000. To study such structures, faster methods should be developed for the computation of NICS values. It is also important to note that the shifts observed for in-pore ions are only nucleus-independent to first order, with differences in $\Delta\delta$ values on the order of 1 ppm observed for different in-pore molecules and ions. Further NMR calculations that model adsorption effects should be carried out in future work, to properly understand the variations in the $\Delta\delta$ values.

In spite of these complexities, the NMR study of adsorbates has been identified as a promising new method to characterise structural order in porous carbons. Spectral simulations on model slit-pores that take into account the distribution of pore sizes allow domain sizes to be estimated for porous carbons, which are typically found to be below 20 Å. The NMR approach allows the domain sizes of the carbons studied in this chapter to be ordered as TiC-CDC-600 < TiC-CDC-800 < TiC-CDC-1000 ≈ YP50F < YP80F < TiC-CDC-X-VAC. However, more work must be done on more realistic

carbon structures that take into account defects such as the curvature of the carbon sheets, and the presence of functional groups.

Interestingly, the in-pore linewidths also show variations when different carbon structures are studied, motivating further study of the ion dynamics (Chapter 7). This chapter also paves the way for charging studies of supercapacitors (Chapters 6 and 8), where knowledge of the in-pore peak positions for different carbons will be important. Going beyond studies of supercapacitors the findings presented here are generally applicable to NMR studies of porous carbon materials for applications in gas storage, catalysis and water treatment.

Chapter 6

NMR Studies of the Charging Mechanisms of Ionic Liquid-based Supercapacitors

6.1 Context and Scope

Recently, ionic liquids have emerged as alternatives to conventional organic electrolytes to extend the maximum operating voltage of supercapacitors and increase the amount of energy that can be stored.^{12,24} While they have a number of attractive properties including low vapour pressure, non-flammability, and good chemical and thermal stabilities, they suffer from low ionic conductivities and high viscosities, which are detrimental to the power performance of devices.¹⁶⁵ Despite a number of promising studies utilising ionic liquids in supercapacitors,^{23,26,57,166} their power performances still cannot compete with those of organic electrolytes, and the exact mechanism of charge storage is unclear.

Theoretical studies have led the way in developing our understanding of the structure and dynamics of the interface between carbon surfaces and ionic liquids (see Section 2.5). In microporous carbons, MD simulations have suggested that charging occurs via exchange of anions and cations between the carbon pores and the bulk.^{68,69,73} More recent work has also highlighted the importance of pore ionophobicity/ionophilicity,^{74–76,167} where ionophilic pores are wetted by the ionic liquid in the absence of an applied potential, while ionophobic pores are not. Ionophobic pores were shown to exhibit faster charging dynamics than ionophilic pores, avoiding the initial overfilling of the latter with ions during charging.⁷⁶ New experimental methods must be developed to

probe the wetting of carbon micropores by ionic liquids, to study ion dynamics inside the pores, and to test the various theoretical models for the charging mechanism.

Currently, there are few experimental methods available to characterise the interface of porous carbon electrodes and ionic liquids. IR spectroscopy and EQCM studies have recently been applied to ionic liquid supercapacitors,^{81,82,85} and these techniques have allowed different supercapacitor charging mechanisms to be observed during *in situ* studies (see Section 2.6). However, in these studies it is difficult to quantify the charging processes and it is unclear exactly which electrolyte ions are detected. In principle, NMR spectroscopy is a further powerful method for studying supercapacitors, as in-pore ions can be distinguished from ex-pore ions, while anions and cations can also be studied separately. Previous NMR studies have focused on devices with organic electrolytes. A first study by Lee *et al.* used ¹¹B NMR to study the behaviour of the BF₄⁻ anions in supercapacitor electrodes extracted from disassembled charged devices.⁹³ Using this *ex situ* approach, some changes of the in-pore anion intensity could be observed during charging. A later, more comprehensive, *ex situ* NMR study by Deschamps *et al.* revealed charging to take place by a swapping of anions and cations in and out of the carbon pores.¹⁸ Recently, the first NMR measurements were made on working supercapacitor devices (*in situ* NMR),¹⁷ where ¹¹B NMR showed changes in intensity and chemical shift of the in-pore BF₄⁻ anion resonance during charging.

The main aim of this chapter is to extend the NMR methodology to study supercapacitors with ionic liquid electrolytes. The first section focuses on YP50F activated carbon and two ionic liquids that share a common anion. NMR spectra of YP50F carbon soaked with 1-methyl-1-propylpyrrolidinium bis(trifluoromethanesulfonyl)imide (Pyr₁₃TFSI) and 1-ethyl-3-methylimidazolium bis(trifluoromethanesulfonyl)imide (EMITFSI) ionic liquids show that the anions and cations wet the carbon micropores in the absence of an applied potential. The broad in-pore resonances are difficult to resolve in static NMR experiments, and therefore *ex situ* experiments with magic angle spinning are carried out to study supercapacitor charging. These measurements reveal changes of in-pore intensity and chemical shift during charging. The changes of in-pore intensity show that supercapacitor charging occurs via adsorption of counter-ions and desorption of co-ions, with adsorption and desorption of the anions playing a more dominant role than that of the cations. This unexpected mechanism is compared to previous work in the literature, and a range of possible charging mechanisms are reviewed. The in-pore chemical shift variations are shown to

arise from changes of the ring current effects that arise from the changes of the carbon electronic structure upon charging. Here, the chemical shift of in-pore ions is modulated by the amount of charge stored in the electrodes in a nucleus-independent fashion. Finally, the adsorption of Pyr₁₃TFSI in different CDCs is investigated. Here, the pore wetting in the absence of an applied potential is shown to have a significant effect on the capacitances that can be achieved in ionic liquid supercapacitors.

6.2 Experimental Details

6.2.1 Carbon materials

The main carbon studied here is YP50F activated carbon (Kuraray, Japan) of coconut-shell origin. Freestanding carbon films were prepared as described in Section 4.2.1.

TiC-CDCs were synthesised by collaborators in the laboratory of Prof. Volker Presser at the Leibniz Institute for New Materials. The synthesis method was identical to that described in Section 4.2.1, with that exception that the chlorine-treatment step was carried out for 6 h, and the following hydrogen-treatment step was carried out for 3 h. The TiC-CDC samples studied in this chapter are from a different batch than those studied in Chapters 4 and 5, and so the results should not be directly compared. Pore size distributions were obtained as described in Section 5.2.4.

6.2.2 Ionic liquids

1-Methyl-1-propylpyrrolidinium bis(trifluoromethanesulfonyl)imide (Pyr₁₃TFSI) and 1-ethyl-3-methylimidazolium bis(trifluoromethanesulfonyl)imide (EMITFSI) ionic liquids (both >98 % purity, Tokyo Chemical Industry UK), were dried *in vacuo* for at least 48 h before preparing samples.

6.2.3 NMR sample preparation for carbons soaked with ionic liquid

Pieces of carbon film (~3 mg) were cut out and dried for at least 15 h at 200 °C *in vacuo* before being transferred to an argon glovebox. These were packed into 2.5 mm outer diameter zirconia magic angle spinning (MAS) rotors, to which ~5 µL of ionic liquid was added using a microsyringe. Having allowed 10 min for the ionic liquid to soak into the carbon, any excess ionic liquid (external to the carbon film piece in the top of the rotor) was then carefully removed by inserting a small piece of tissue paper into the top of the rotor for 1 or 2 s before removing it. This was done because excess ionic liquid could cause rotor instability under MAS conditions. The masses of carbon and

ionic liquid added to each sample were determined by weighing the rotor before and after their addition.

6.2.4 NMR experiments

NMR experiments were performed using a Bruker Avance spectrometer operating at a magnetic field strength of 7.1 T, corresponding to a ^1H Larmor frequencies of 300.2 MHz. A Bruker 2.5 mm double-resonance MAS probe was used. All NMR experiments used simple pulse-acquire sequences with an MAS rate of 5 kHz, unless otherwise specified. For ^1H spectra, a probe background spectrum was recorded and subtracted. ^{19}F NMR spectra were referenced relative to neat hexafluorobenzene (C_6F_6) at -164.9 ppm, while ^1H NMR spectra were referenced relative to tetramethylsilane using the CH_3 resonance of liquid ethanol at 1.2 ppm as a secondary reference. Radio frequency strengths of between 98 and 122 KHz, and between 96 and 105 kHz were used for ^{19}F and ^1H , respectively. Recycle delays were adjusted to ensure all spectra are quantitative. Between 8 and 64 transients were coadded for each NMR experiment. Spectral deconvolutions were performed using dmfit software¹³⁷ and the SOLA package in Topspin software. A single peak was used to fit in-pore resonances, while either one or two peaks were used to fit each ex-pore resonance. For accurate determination of spectral intensities, spinning sidebands were taken into account using a chemical shift anisotropy model in the SOLA package in Topspin software. For *ex situ* NMR experiments, these intensities were then normalised to account for electrode mass differences between different coin cells.

6.2.5 Preparation of coin cells

All supercapacitor cells were fabricated using coin cell designs. First, YP50F carbon films were prepared as described above. Disc-shaped electrodes were then cut out and dried at 100 °C in vacuum for at least 15 h. Symmetric coin cells were then fabricated inside an argon glovebox, with glass fibre (Whatman) used as the separator. Electrode masses ranged from 2.7 to 4.3 mg, with the two electrode masses in each cell equal to within 0.1 mg.

6.2.6 Ex situ NMR experiments

First, coin cells were cycled by cyclic voltammetry for 5 cycles with a sweep rate of 5 $\text{mV}\cdot\text{s}^{-1}$ between limits of 0 and 3 V. A constant applied voltage of 0 V was then applied to the cells for 1 h (chronoamperometry), before applying the desired cell voltage for at least a further hour. Voltages of 0.0, 0.5, 1.0, 1.5, 2.0, and 2.5 V were studied, with two

individual cells studied for each voltage, giving a total of 12 coin cells. Having removed the cells from the cycler, they were quickly transferred to an argon glovebox ($\text{H}_2\text{O} < 0.1$ ppm, $\text{O}_2 < 0.1$ ppm), where the final cell voltage was measured using a multimeter before disassembling the cell. The time between the removal of coin cells from the cycler and cell disassembly was approximately 5 min. Only for the highest cell voltage of 2.5 V was any significant self-discharge measured prior to cell disassembly. In this case, for both cells studied, the voltage had dropped to 2.48 V before disassembly. The positive and negative carbon electrodes were then individually packed into 2.5 mm outer diameter zirconia MAS rotors.

6.2.7 Electrochemical characterisations

All electrochemical measurements were carried out in a two-electrode configuration using a Bio-Logic cycler. Cyclic voltammograms were obtained by sweeping the cell voltage from 0 to 3 V at a constant rate of $2.5 \text{ mV}\cdot\text{s}^{-1}$.

Capacitances were measured using galvanostatic charge-discharge measurements. For charging, a constant current, I , was applied until the cell voltage reached its maximum value (3 V for ionic liquids and 2 V for solvated ionic liquids). The current was then reversed to discharge the cell to a cell voltage of 0 V. Ten cycles were recorded for each different current value studied. The cell capacitance was then extracted using Equation 2.10, with the capacitance determined from the tenth discharge curve. Assuming the capacitance of the two electrodes to be equal, the gravimetric capacitance, C/m , of a single electrode was extracted using Equation 2.2. Current densities were calculated as I/m .

6.2.8 Nucleus-independent chemical shift calculations

Nucleus-independent chemical shift calculations were carried out as described in Section 5.2.1. Geometries were first optimised with the charge specified as either $+1e$ or $-1e$ and NMR calculations were performed on the resulting structures.

6.3 Results and Discussion

6.3.1 Wetting of activated carbon by ionic liquids

Figure 6.1a shows the ^{19}F MAS NMR spectrum of a piece of commercial activated carbon (YP50F) film soaked with $\text{Pyr}_{13}\text{TFSI}$ ionic liquid. In-pore and ex-pore features are clearly visible for the TFSI anions, with the spectrum showing some similarities to that obtained with the organic electrolyte $\text{NEt}_4\text{BF}_4/\text{dACN}$ (1.5 M) (Section 4.3.1). In the

¹H NMR spectrum of the Pyr₁₃ cations, in- and ex-pore resonances are again observed (Figure 6.1b). Here the spectrum is complicated by the six chemically distinct ¹H environments in each Pyr₁₃ cation (from the various CH₂ and CH₃ groups), which each give rise to in- and ex-pore resonances, with the different in-pore resonances not being resolved here. ¹⁹F and ¹H MAS NMR spectra of YP50F soaked with a second ionic liquid, EMITFSI, show similar features (Figure 6.1c and 6.1d). In the ¹⁹F spectrum, the Δδ value (−6.3 ppm) is similar to that observed for Pyr₁₃TFSI (−6.6 ppm), suggesting that the local magnetic environment of the in-pore TFSI anions is essentially identical for the two ionic liquids, despite the presence of different cations. Interestingly, the in-pore resonances observed here are considerably broader than those observed for experiments on YP50F carbon soaked with organic electrolyte (Section 4.3.1). This is presumably associated with the lower mobility of the in-pore ions here. Further studies of the in-pore ion dynamics are carried out in the next chapter.

The observation of in-pore resonances for anions and cations confirms that both ionic liquids spontaneously wet the carbon micropores of this carbon, consistent with MD simulations carried out on a model porous carbon.⁶⁸ On the basis of fits of the ¹⁹F and ¹H NMR spectra in Figure 6.1a and b, it is calculated that there are 1.6 mmol of in-pore anions per gram of YP50F for Pyr₁₃TFSI, with the same number obtained for in-pore cations. Thus, there are equal numbers of anions and cations in the carbon micropores in the absence of an applied potential. Taking the volumes of TFSI[−] and Pyr₁₃⁺ to be 148 and 152 Å³, respectively (calculated using the Molinspiration Property Calculation Service¹⁶⁸), the volume of in-pore ionic liquid is calculated to be 0.28 cm³ per gram of carbon. Comparing this to the carbon pore volume measured by N₂ gas sorption (0.71 cm³·g^{−1})¹⁴⁰ only 40 % of the pore volume accessible to N₂ is occupied by ionic liquid. Similar analysis for EMITFSI shows that there are 1.8 mmol of in-pore anions per gram of carbon. Taking the volume of EMI⁺ to be 118 Å³ (and assuming an equal number of anions and cations in the pores) there are then 0.29 cm³·g^{−1} of in-pore ions, again occupying 40 % of the carbon pore volume measured by N₂ gas adsorption. While the carbon micropores are significantly wetted in the absence of an applied potential and may be considered ionophilic, a considerable amount of pore volume measured by N₂ gas sorption is inaccessible to the ionic liquids studied here, presumably due to size and packing effects.

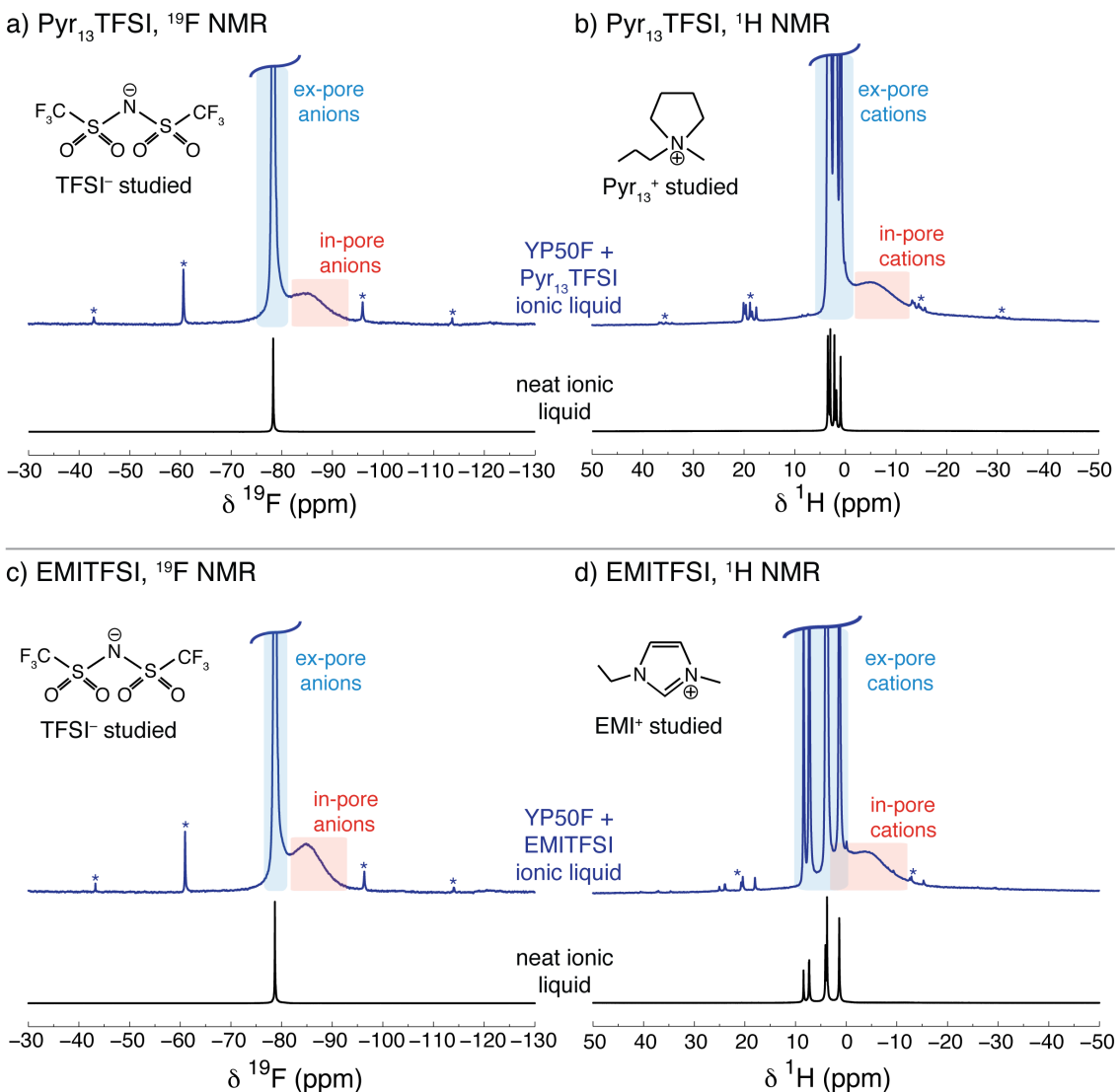


Figure 6.1 (a) ¹⁹F and (b) ¹H MAS NMR (7.1 T) spectra of YP50F carbon film soaked with Pyr₁₃TFSI ionic liquid. (c and d) Analogous spectra are shown with EMITFSI ionic liquid. Static spectra of the neat ionic liquids are displayed in each case for comparison. Asterisks mark spinning sidebands, which are observed for in- and ex-pore resonances, though the broad in-pore sidebands cannot be seen on this intensity scale. For both ionic liquids, the anions and cations wet the carbon micropores in the absence of an applied potential, giving rise to in-pore features in the spectra.

6.3.2 Experimental considerations for charging studies

There are two main approaches for studying supercapacitor charging mechanisms, *ex situ* and *in situ* studies. Generally, it is preferable to carry out *in situ* NMR experiments on a working supercapacitor device as it is charged and discharged. While *ex situ* NMR experiments can benefit from the resolution enhancements afforded by magic angle spinning, one must ensure that self-discharge processes (or relaxation of meta-stable phases and states) do not affect the results.

Figure 6.2 shows *ex situ* ¹⁹F NMR spectra of electrodes extracted from supercapacitor cells (YP50F carbon and Pyr₁₃TFSI ionic liquid) that had been charged to different

fixed voltages. Both static and MAS (5 kHz) NMR spectra are shown for the positive electrodes of cells charged to voltages of 0, 1 and 2.5 V. In the MAS experiments, in-pore and ex-pore anion features can be distinguished for all three samples. However, in the static experiments, the in-pore feature can only be seen as a broad shoulder for the 0 V sample. This suggests that the *in situ* approach (where samples must be static) will be challenging for ionic liquid-based supercapacitors, and so here the *ex situ* approach is pursued.

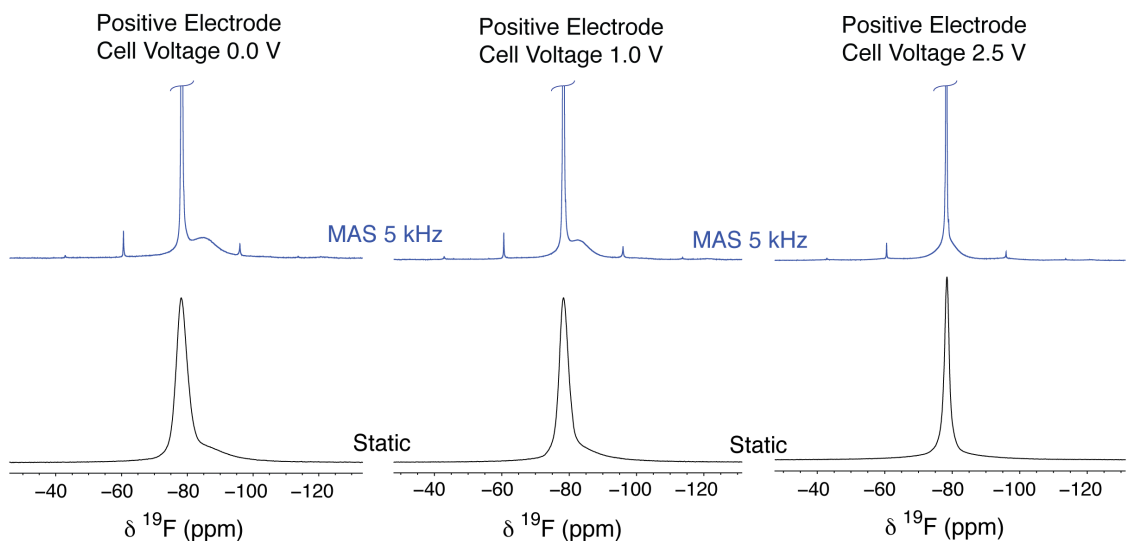


Figure 6.2 ^{19}F NMR (7.1 T) spectra for positive electrodes extracted from disassembled coin cell supercapacitors (YP50F carbon, $\text{Pyr}_{13}\text{TFSI}$ ionic liquid) with different states of charge. Static and MAS (5 kHz) spectra are shown for each sample.

In the *ex situ* NMR experiments, supercapacitor cells are charged to a given voltage and quickly transferred to an argon glovebox where they are disassembled. In the (approximately) five minute time period before disassembly, a small amount of self-discharge¹⁶⁹ can occur. However, this was only found to be significant for the highest studied cell voltages of 2.5 V. Here, the cell voltage had dropped to 2.48 V prior to disassembly. It is also possible that some self-discharge could occur following cell disassembly, though NMR spectra did not show significant changes on a timescale of 18 hours (while the NMR experiments only take a couple of minutes to acquire), suggesting that any self discharge of the electrodes is insignificant following their separation (Figure 6.3). Indeed, this principle is utilised in electrochemical flow capacitors,¹⁷⁰ whereby two carbon slurries are charged (one positively and one negatively) as they pass over electrodes before being physically stored in tanks. The slurries are then recombined at a later time when energy is required. Finally, it is noted

that unlike typical organic electrolytes, ionic liquids have very low volatility,¹⁶⁵ meaning there is negligible evaporation of liquid during cell disassembly.

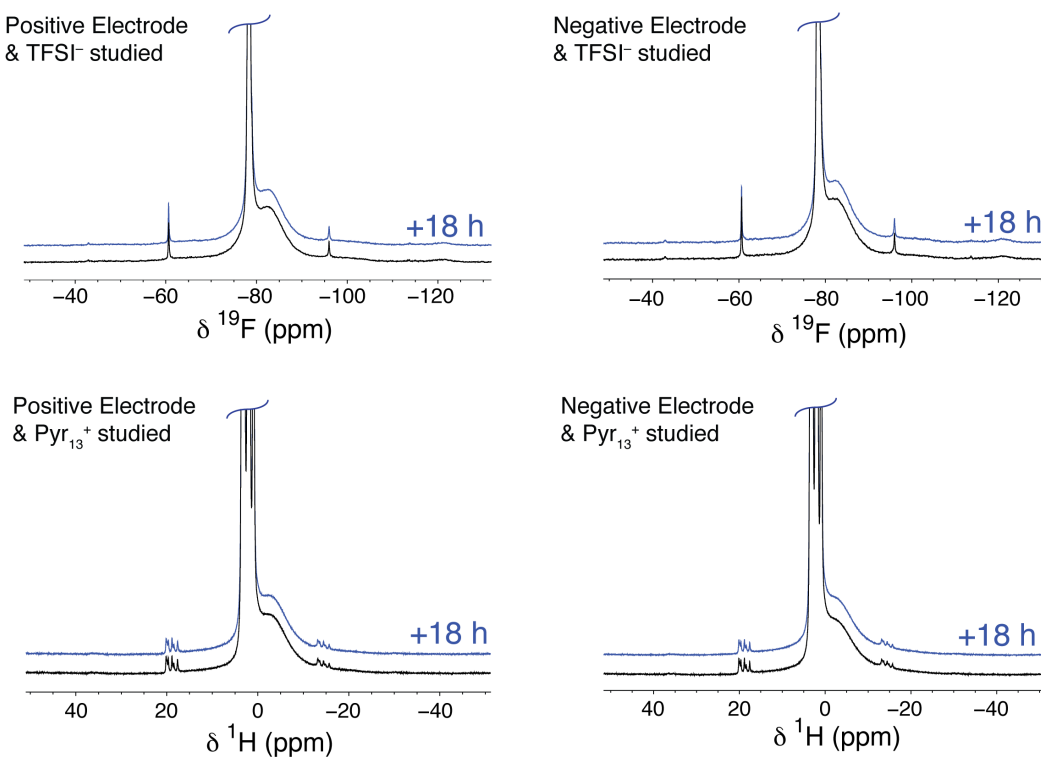


Figure 6.3 ^{19}F and ^1H NMR (7.1 T) spectra of electrodes extracted from a coin cell comprising YP50F carbon and $\text{Pyr}_{13}\text{TFSI}$ ionic liquid charged to a cell voltage of 1 V. Spectra are shown shortly after samples were packed (black) and \sim 18 hours after sample packing (blue). Spectra are offset for clarity (when plotted without an offset, the overlap of the lines is exact within the noise level of the spectra).

6.3.3 *Ex situ* NMR studies of $\text{Pyr}_{13}\text{TFSI}/\text{YP50F}$ supercapacitors

The ^{19}F NMR spectra (Figure 6.4a) of the positive and negative electrodes of a cell at a voltage of 0 V are similar to that observed in Figure 6.1a, with the in-pore resonance at -84.9 ppm in each spectrum. As the cell voltage is increased, the in-pore resonance shifts to higher frequency in both electrodes, while the ex-pore resonance does not show any change in frequency. Changes in the intensity of the in-pore resonance are also observed as the voltage is increased, though these are not immediately apparent by direct inspection of the spectra, which is in part due to changes in the intensity of the spinning sidebands, as discussed below. For ^1H spectra of the same samples (Figure 6.4b) the in-pore resonances again shift to higher frequency as the cell voltage is increased.

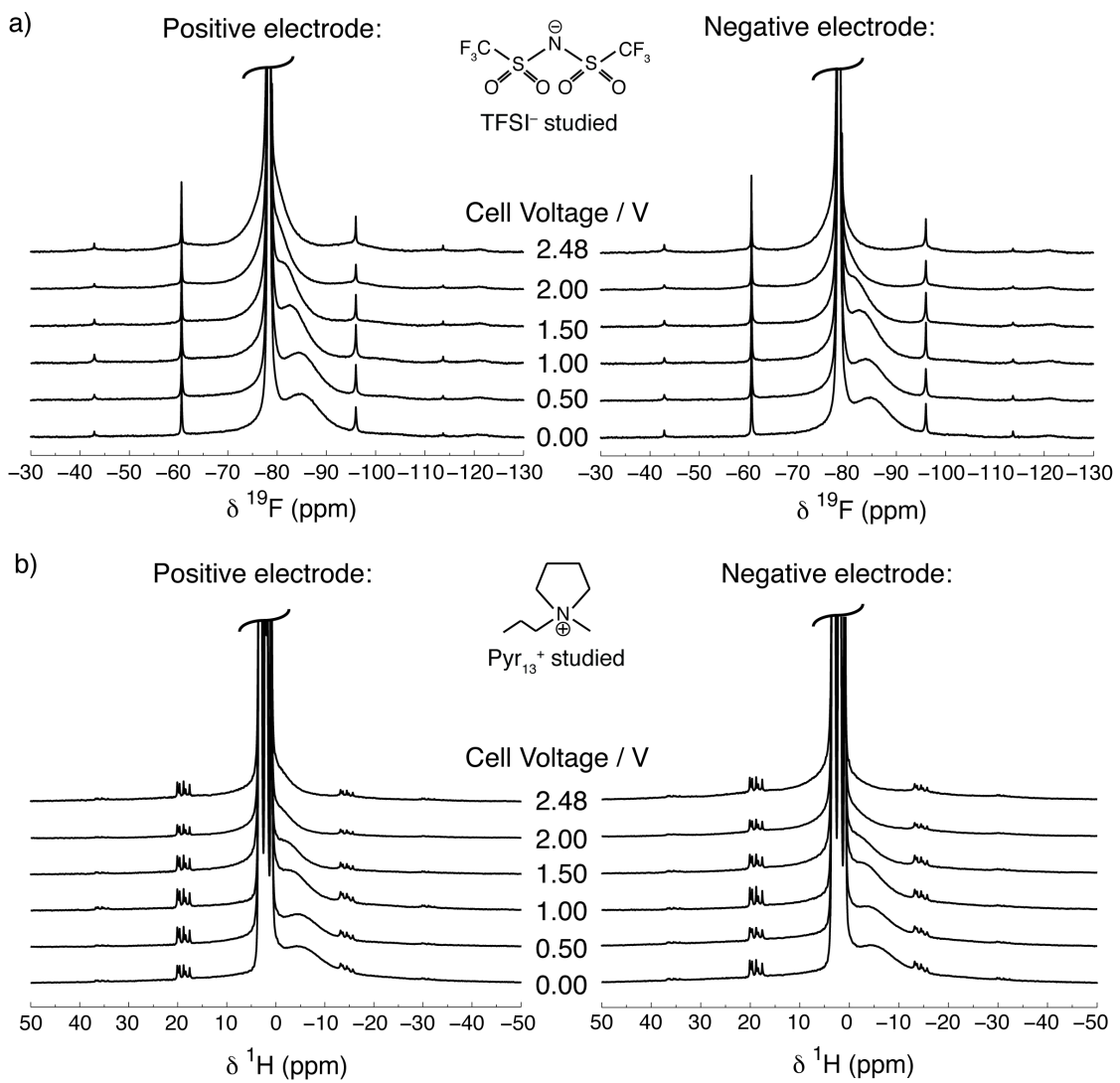


Figure 6.4 (a) ¹⁹F and (b) ¹H MAS NMR (7.1 T) spectra of electrodes extracted from disassembled supercapacitors (YP50F carbon and Pyr₁₃TFSI ionic liquid) charged to a range of different cell voltages. In-pore resonances show noticeable increases in chemical shift as the voltage is increased.

To obtain more detailed insight into the charge storage process, spectral fits were performed to extract the integrated intensities of the in-pore resonances, which are directly proportional to the number of ions in the carbon micropores. In the positive electrode, a clear general increase in the number of in-pore anions is observed as the cell voltage is increased (Figure 6.5a). At 2.48 V, a 46 % increase in the number of in-pore anions as compared to 0 V is observed. Taking the number of in-pore anions with no applied potential as 1.6 mmol·g⁻¹ (Figure 6.1a), the corresponding number at 2.48 V is 2.3 mmol·g⁻¹. Meanwhile, in the negative electrode, a general decrease in the number of in-pore anions is observed as the cell voltage is increased, the number of in-pore anions dropping by 29 % from 0–2.48 V, corresponding to a value of 1.1 mmol of anions per gram of carbon at 2.48 V. The relative intensities obtained from fits of the ¹H

spectra are shown in Figure 6.5b. In the positive electrode there are small decreases in the number of in-pore cations, while in the negative electrode there are small increases. Further inspection of the spectral fits reveals increases in the width of the spinning sideband manifold (*i.e.*, increases in anisotropy) for the in-pore ions as the cell voltage is increased. Indeed, this can be seen in Figure 6.4a as an increase in the intensity of the in-pore spinning sidebands upon charging (the in-pore sidebands are seen as broad features at \sim 60 and -95 ppm at 2.48 V in the ^{19}F spectra). These increases were observed for anions in both electrodes (Figure 6.6), suggesting that charging restricts the motion of in-pore ions regardless of the electrode polarisation. These changes of the width of the spinning sideband pattern make direct inspection of the intensity changes in Figure 6.4 difficult, necessitating a full deconvolution that accounts for the spinning sidebands, as was carried out here.

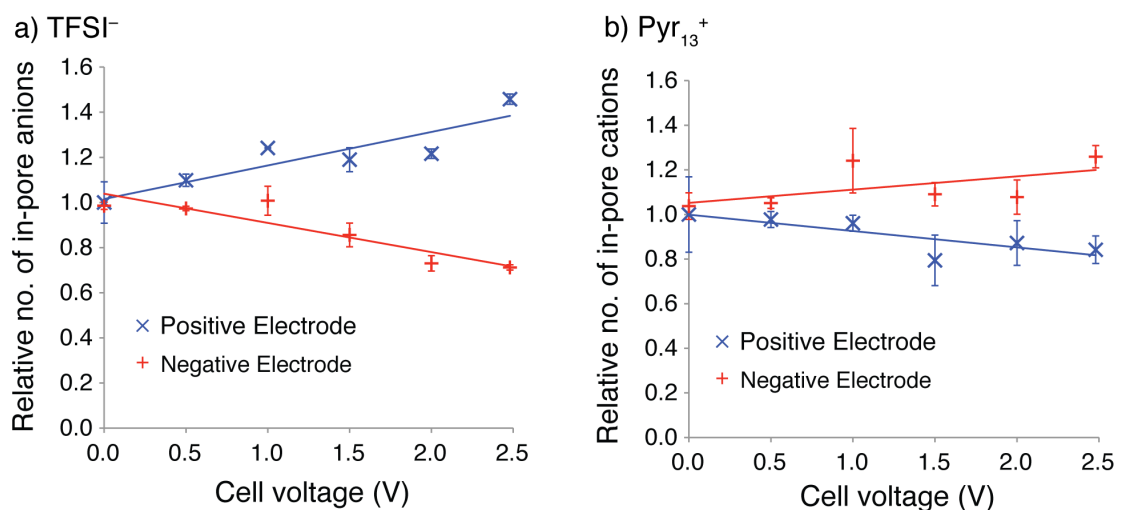


Figure 6.5 Number of in-pore ions for cells (YP50F, $\text{Pyr}_{13}\text{TFSI}$ ionic liquid) at different cell voltages relative to 0 V; (a and b) show normalised populations for anions and cations, respectively. Straight lines are shown to guide the eye. Data points represent the average of two measurements made on separate cells, with error bars representing the standard deviation in this average. Anions enter the carbon micropores in the positive electrode and leave the carbon micropores in the negative electrode upon charging. At the same time, a smaller number of cations enter the pores of the negative electrode and leave the pores of the positive electrode.

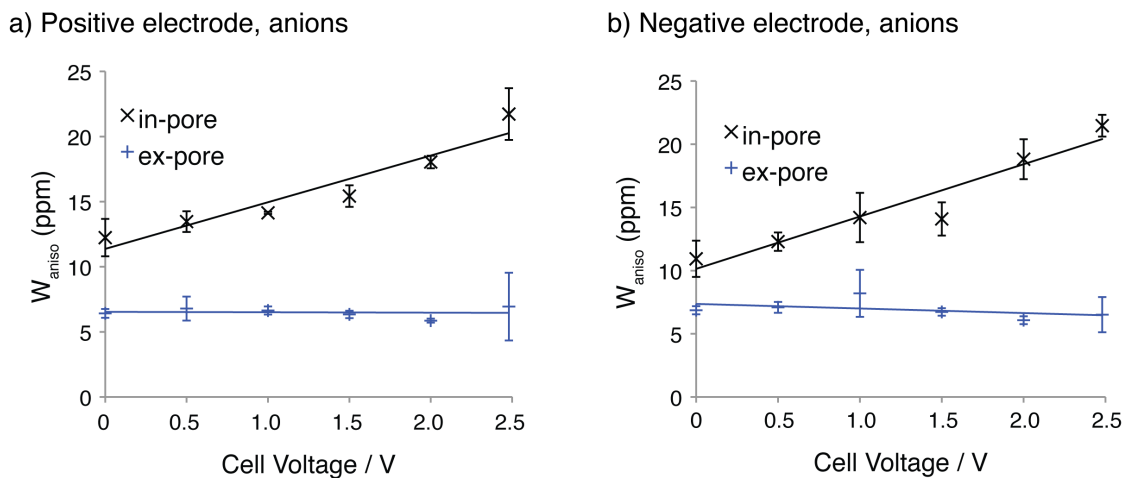


Figure 6.6 Variations of the width of the spinning sideband pattern obtained from fitting of ^{19}F *ex situ* NMR spectra. The parameter W_{aniso} gives a measure of the width of the spinning sideband pattern and is analogous to δ_{aniso} , the chemical shift anisotropy (see Section 3.2.1)

Overall, the charge storage mechanism is summarised as follows (see Figure 6.7a for a schematic). The pores are initially wetted with ionic liquid, with 1.6 mmol of in-pore ionic liquid per gram of material and an equal number of in-pore anions and cations. Charge storage then occurs by adsorption of counter-ions and desorption of co-ions, with TFSI^- adsorption dominating charge storage in the positive electrode and TFSI^- desorption dominating charge storage in the negative electrode. At the same time a smaller number of Pyr_{13}^+ are adsorbed in the negative electrode and desorbed in the positive electrode during charging. At this stage it is not thought that the difference in the behaviour of anions and cations is a kinetic effect, as supercapacitor cells were held at the studied voltages for relatively long times (1 h) compared to the time needed for current equilibration (at most 10 min). The volume of the ions is similar, suggesting that the origin of this phenomenon is not due to simple packing arguments. There are a number of possible causes of this effect, which include the following: (i) differences in the distribution of charge on the ions, (ii) steric effects due to differences in the shapes of the ions, and (iii) differences in the binding energies to the carbon. Further theoretical work and experiments must be done to explore these effects.

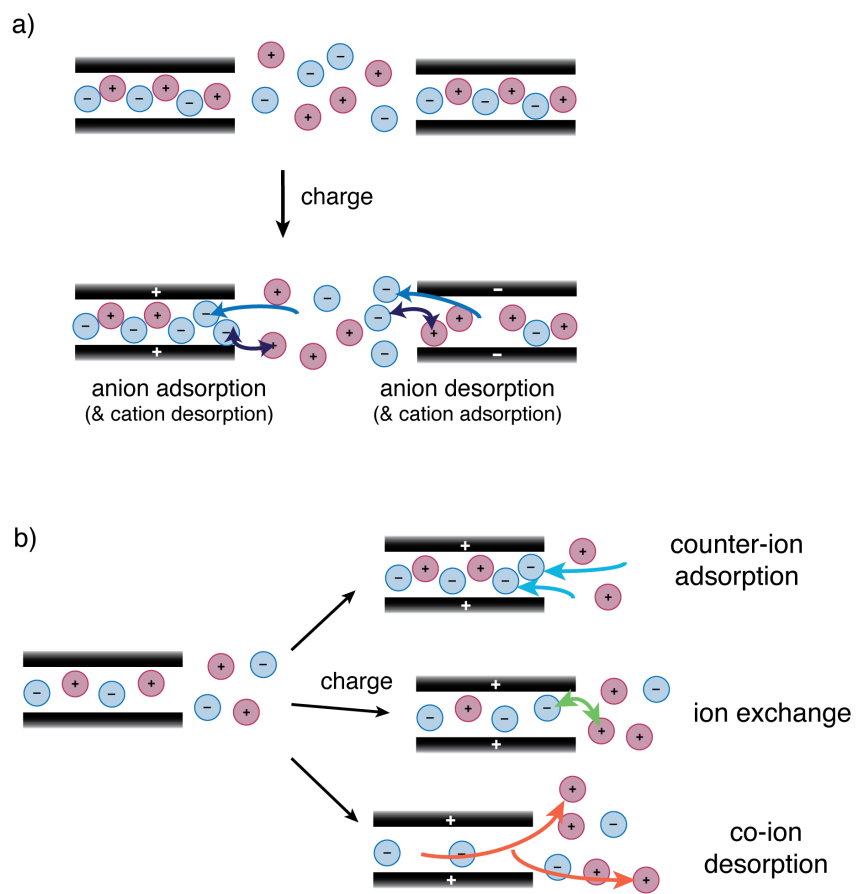


Figure 6.7 (a) Schematic illustrating the charge storage mechanism for the $\text{Pyr}_{13}\text{TFSI}/\text{YP50F}$ supercapacitor system. (b) Possible charging mechanisms for a carbon pore. Charge storage can take place by counter-ion adsorption, ion exchange or co-ion desorption. In reality a combination of these mechanisms will generally take place, as shown in (a).

Crucially, both counter-ions and co-ions are involved in the charge storage process, and charging is not driven simply by counter-ion adsorption as it often assumed in the literature. In principle a number of different charging mechanisms can take place involving different migrations of the counter-ions and co-ions, depicted in Figure 6.7b. Counter-ion adsorption, ion exchange (exchange of counter- and co-ions) and co-ion desorption can all result in an excess ionic charge in the carbon pores and charging of the electrode.

The findings from the NMR measurements presented here agree qualitatively with predictions from a MD study of 1-butyl-3-methylimidazolium hexafluorophosphate ionic liquid in model porous carbon electrodes, where charge storage was shown to proceed with both counter-ion adsorption and co-ion desorption from initially filled pores.⁶⁸ More recent theoretical work using mean-field theories^{74,76} and lattice models¹⁶⁷ revealed similar pictures of charge storage. However, none of these theoretical studies

have shown such significant differences between the behaviours of anions and cations. A small number of recent experimental studies have also studied the charge storage mechanism of ionic liquid-based supercapacitors. IR spectroscopy studies have suggested that charge storage proceeds via ion exchange in KOH-treated carbon nanofibres with EMITFSI ionic liquid.⁸² In contrast, analogous IR experiments on untreated nanofibres⁸² as well as CDC nanoparticles⁸¹ suggested that both anions and cations enter the carbon micropores during charging. A recent EQCM study of CDC with EMITFSI ionic liquid revealed that charge storage is generally dominated by adsorption of counter-ions into the carbon micropores, while ion exchange also takes place at low electrode potentials in the positively polarised electrode.⁸⁵ However, it is not straightforward to compare the results from *ex situ* NMR experiments here to those in the aforementioned IR and EQCM studies as they were performed under dynamic charging conditions (whereas the NMR measurements probe equilibrium states) and different materials were studied. Moreover, it is noted that the IR measurements probe the surface or near surface of carbon particles, while in EQCM it is unclear how ions in pores and voids of different sizes contribute to the measured mass changes. It is stressed that in contrast to other characterisation methods, NMR allows the in-pore ions to be studied separately from ex-pore ions, allowing more definitive conclusions to be made.

6.3.4 Chemical shift changes observed during charging

In addition to the changes of in-pore peak intensity during charging, marked chemical shift changes are also observed for in-pore ions (Figure 6.4). The in-pore chemical shifts obtained from the spectral fittings are shown in Figure 6.8. Clear increases are observed for both anions (Figure 6.8a) and cations (Figure 6.8b) in both electrodes, with the change in chemical shift with voltage appearing to depend on the polarisation of the electrode (positive or negative) rather than on the type of ion studied (anion or cation). In the negative electrode, the total increase of the in-pore chemical shift is 6.7 ± 0.1 ppm ($2.7 \text{ ppm} \cdot \text{V}^{-1}$) for the anions and 6.8 ± 0.2 ppm ($2.7 \text{ ppm} \cdot \text{V}^{-1}$) for the cations, with the changes being identical within error. For the positive electrode, smaller increases of 5.7 ± 0.4 ($2.3 \text{ ppm} \cdot \text{V}^{-1}$) and 5.2 ± 0.5 ppm ($2.1 \text{ ppm} \cdot \text{V}^{-1}$) were observed for the anions and cations, respectively, again similar within error. In the negative electrode at 2.5 V, the in-pore resonances are more deshielded than the ex-pore resonances, suggesting that an additional chemical shift mechanism may be operating for the charged carbons that is absent for uncharged carbons (Figure 6.8). Summarising the results here, the chemical shift changes observed during charging are nucleus-independent, though they do depend

on the polarisation of the electrode (positive or negative). The first *in situ* NMR studies of activated carbon supercapacitors revealed similar chemical shift changes, though only the anions were studied in that work (^{11}B NMR of BF_4^-).¹⁷ In-pore chemical shift changes were also observed by Deschamps *et al.* in ^{13}C and ^{11}B *ex situ* NMR studies of NEt_4^+ and BF_4^- in two different types of activated carbon electrodes.¹⁸ In that study, the chemical shift changes were on the order of $1 \text{ ppm} \cdot \text{V}^{-1}$, with the changes greater in the positive electrode than in the negative electrode.

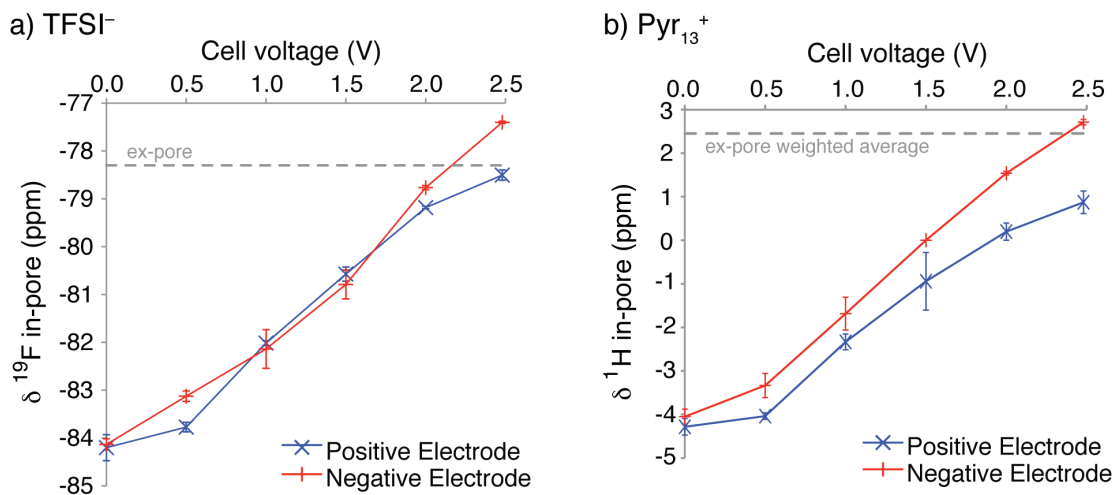


Figure 6.8 In-pore chemical shifts (YP50F, $\text{Pyr}_{13}\text{TFSI}$ ionic liquid) as a function of cell voltage. (a and b) Data for ^{19}F and ^1H spectra, respectively. Data points represent the average of two measurements made on separate cells, with error bars representing the standard deviation in this average. Clear increases in chemical shift are seen for both ions in both electrodes. The shifts depend primarily on the polarisation of the electrode (positive or negative) rather than the charge of the ion. Positions of the ex-pore resonances are also shown (the weighted average is shown for the cations (^1H NMR), as there are several resonances).

The apparent nucleus-independence of the in-pore chemical shift changes suggests that they arise from changes of the carbon ring current effects. There are at least three possible contributions to such changes:

1. The carbon structure may change during charging. The ring current shifts observed for in-pore ions are highly sensitive to the local carbon structures (see Chapter 5), and changes of the carbon pore size, for example, could modify the in-pore chemical shifts.
2. The carbon-ion distances may vary during charging due to coulombic interactions. As charge builds up, cations are expected to become more strongly associated with the negative electrode surface, while anions are expected to become less strongly associated with the negative electrode surface (and *vice versa* at the positive electrode). The

resulting increases or decreases in carbon-ion distances may change the observed chemical shifts, given the strong distance dependence of the ring current shifts (see Chapter 5).

3. Changes of the electronic structure of the carbon during charging may modify the ring current effects.

Considering contribution 1., it is not straightforward to probe changes of carbon structures on the nanoscale by conventional characterisation techniques, though macroscopic changes of electrode heights have been observed during charging. *In situ* electrochemical dilatometry and atomic force microscopy experiments have revealed small reversible height changes of porous carbon electrode films during charging and discharging.^{171–174} If these height changes arise from dilation of the carbon micropores as proposed, the distances between in-pore nuclei and carbon surfaces may be modified during charging. However, the height changes measured for YP17 activated carbon electrodes (similar to the YP50F activated carbon studied here) with NEt₄BF₄/ACN electrolyte were just +1.1 % and +0.5 % for the positive and negative electrodes, respectively.¹⁷² Such small changes are unlikely to have a large effect on the resonance frequencies observed for in-pore ions, as the small distance changes would result in a negligible change in the NICS. For example, a pore with a diameter of 10 Å could expand to 10.1 Å at most, giving rise to a change of the NICS on the order of ~0.1 ppm (see NICS calculations in Chapter 5).

Moving on to contribution 2., in the positive electrode, cations may move further from the carbon surfaces during charging due to coulombic repulsion. In principle, this could explain the increase of in-pore chemical shift observed in the ¹H spectra of the cations, as the longer ion-carbon distances would reduce the ring current shielding (Chapter 5). However, the anions in the positive electrode would be expected to show the opposite effect, moving closer to the electrode during charging, and with the in-pore resonance becoming more shielded. This is contrary to what is observed experimentally, where the resonance frequencies of the in-pore species increase during charging, regardless of the electrode or ion studied. It is therefore unlikely that changes of ion-carbon distances dominate the observed in-pore chemical shift changes. This is further substantiated by noting that a MD study of a supercapacitor comprising porous carbon electrodes showed only small changes of ion-carbon distances (about 0.2 Å) upon charging to a cell voltage of 1 V, although in this case an ionic liquid electrolyte was studied.⁶⁸

Finally, considering contribution 3., the electronic structure of the carbon will change during charging, and this could affect the ring current shifts. To explore the effect of charging on the NICS, calculations were performed on charged coronene molecules. Figure 6.9 shows NICS plots as a function of distance above the coronene ring plane for three different positions in the xy plane (A, B, and C). NICS calculations were performed for optimised coronene molecules with charges of $+1e$ (Figure 6.9a) and $-1e$ (Figure 6.9b), where e is the electronic charge.

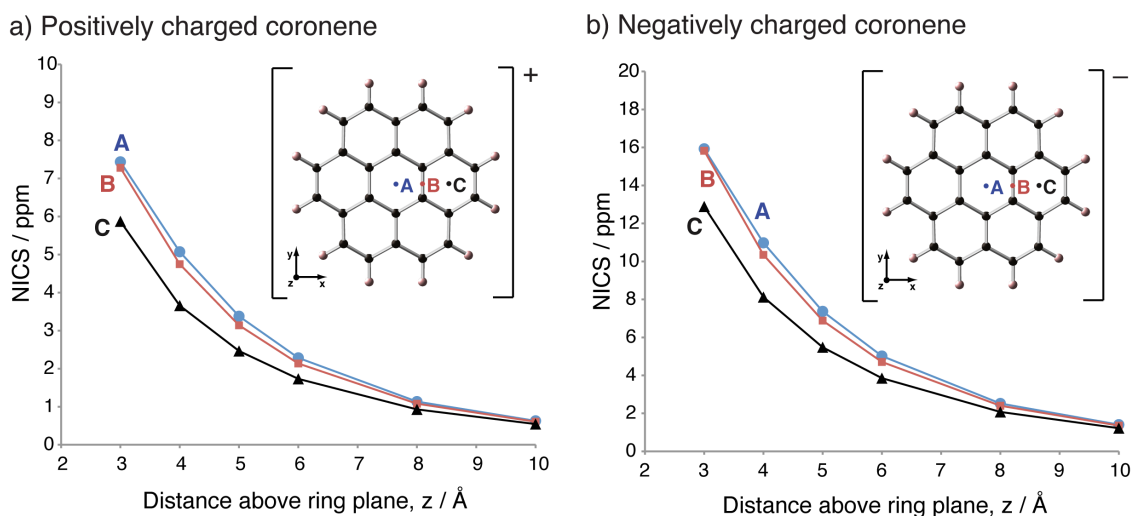


Figure 6.9 Calculated NICS values above (a) positively and (b) negatively charged coronene. Charging has a marked effect on the calculated NICS values.

For both the positively and negatively charged coronene molecules, positive NICS values were calculated for all positions considered above the carbon surface. This is in stark contrast to the calculations on neutral coronene (Chapter 5) where negative NICS values were calculated for the same positions. As discussed in Section 3.6, diatropic (diamagnetic) ring current effects¹¹² cause shielding fields above the planes of aromatic rings, while paratropic (paramagnetic) ring current effects¹¹⁶ cause deshielding fields above the planes of antiaromatic rings.¹¹⁵ Here, the calculated NICS values for charged coronenes are consistent with paratropic ring current effects. The calculated increase in resonance frequency for both positively and negatively charged coronene (compared to neutral coronene) qualitatively agrees with the NMR results, whereby the in-pore resonance shifts to higher frequencies upon charging in both the positive and negative electrodes, for both the anions and the cations. Indeed, in the negative electrode at 2.5 V, the experimental in-pore resonances are *deshielded* relative to the ex-pore resonances, consistent with paratropic ring currents. The differences in the magnitudes of the calculated NICSs close to the carbon surface may explain why slightly different

changes in resonance frequency are observed in the positive and negative electrodes experimentally. Interestingly, the in-pore chemical shift changes observed here are analogous to the chemical shifts observed in an experimental study on [18]annulene.¹¹³ Following two-electron reduction, the ¹H chemical shifts of the interior protons changed from −3.0 ppm to 28.1 ppm, explained as arising from the introduction of paratropic ring currents.

It is stressed that the magnitudes of the shifts predicted by the DFT calculations are significantly larger than what is observed experimentally (Figures 6.8 and 6.9). It is again noted here that the coronene model is a considerable oversimplification of the real activated carbon structure, and so quantitative agreement between the calculated and experimental results is not expected. Moreover, for the coronene calculations the electronic charge per carbon (on average) is 0.04 e, which is greater than the charge per carbon atom for the highest cell voltage studied experimentally here (2.5 V), which is estimated to be 0.015 e, using a capacitance value of 97.5 F·g^{−1} (see below for capacitance measurement) and with the assumption that the activated carbon is entirely composed of carbon. More NICS calculations should be carried out on a variety of larger charged carbon fragments in future work to better understand the effects of charging on the NICS. In principle, the in-pore chemical shift changes offer information about the electronic structure of the carbon. Indeed, the changes observed here are larger in magnitude than those observed in the study of Deschamps *et al.*,¹⁸ suggesting that the electronic structure of the studied carbons differ. The differences observed between the in-pore chemical shifts in the positive and negative electrodes may also offer some information about the electronic structure of the carbon, and the differences between the bonding and anti-bonding states.

In summary, it appears that the changes of the carbon electronic structure dominate the observed variation of the in-pore chemical shifts during charging, while changes of both the carbon structure and the carbon-ion distances have minor effects.

6.3.5 Studies of ionic liquids and CDCs

NMR experiments were carried out on TiC-CDCs soaked with Pyr₁₃TFSI ionic liquid to investigate the effects of carbon porosity on pore wetting (Figure 6.10a). For TiC-CDC-1000, the spectrum is similar to that observed for YP50F (reproduced from Figure 6.1 here for comparison) with a clear in-pore resonance observed. Fitting of the spectrum reveals that there are 1.9 mmol of in-pore anions per gram of TiC-CDC-1000 here, similar to the number of 1.6 mmol·g^{−1} obtained for YP50F. For TiC-CDC-600 on the

other hand, it is difficult to resolve an in-pore resonance, suggesting that there are few in-pore anions for this carbon. This is most probably due to the carbon pore size distribution, with fewer pores accessible to the ions here than for TiC-CDC-1000 (Figure 6.10b). The largest dimension of the ions studied here is on the order of 8 Å, and the pore size distributions show that TiC-CDC-1000 has a greater pore volume for pore diameters greater than this value. Previous electrochemical studies of a very similar ionic liquid to that studied here ($\text{Pyr}_{14}\text{TFSI}$) suggested that only pores with a diameter greater than 1 nm could be accessed by the ions.¹⁷⁵

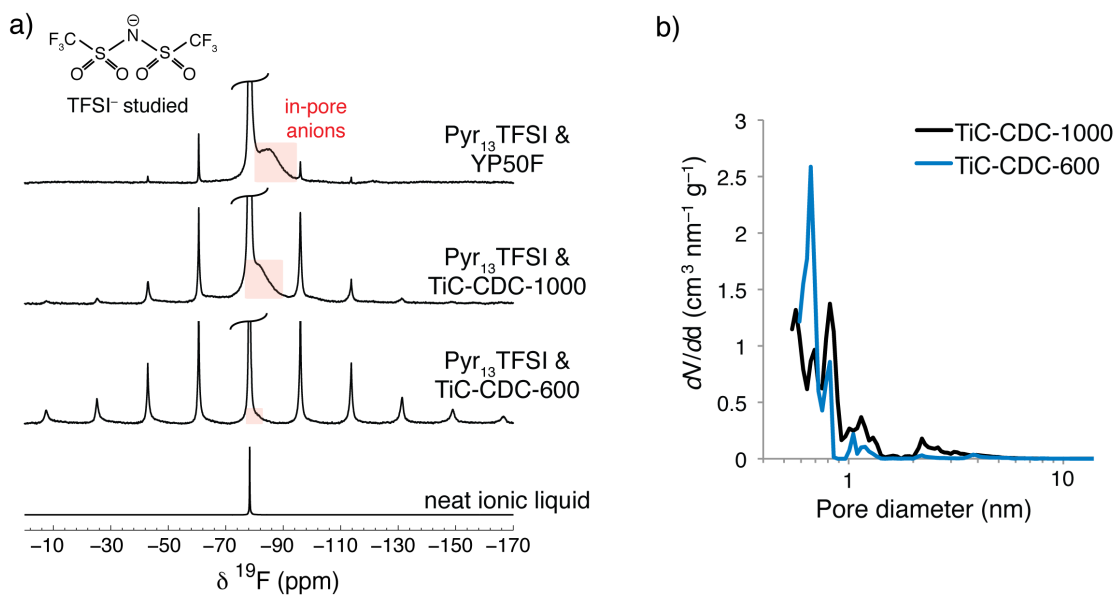


Figure 6.10 (a) ^{19}F MAS NMR (7.1 T) spectra of TiC-CDCs soaked with $\text{Pyr}_{13}\text{TFSI}$ ionic liquid. The corresponding spectrum for YP50F is also shown for comparison, as well as the spectrum of neat ionic liquid. (b) Pore size distributions extracted from N_2 sorption isotherms for TiC-CDC-600 and TiC-CDC-1000. The spectrum of TiC-CDC-600 shows few in-pore anions in the absence of an applied potential compared to TiC-CDC-1000, which can be rationalised by considering the pore size distributions.

Returning to Figure 6.10a, for TiC-CDC-600 the spinning sideband profile of the ex-pore resonance is very broad, spanning over 100 kHz. This is likely associated with a BMS effect arising from paramagnetism in the carbon,¹⁴⁶ arising from radicals on carbon atoms (often referred to as dangling bonds). Such radicals have been observed with electron paramagnetic resonance (EPR) spectroscopy for various activated carbons,^{176–179} with the unpaired spin electron density being as high as $8 \cdot 10^{19}$ spins per gram of carbon (~ 1 unpaired electron spin per 600 carbon atoms).¹⁷⁶ It is hypothesised here that the more defective TiC-CDC-600 has a higher density of radicals and thus has a broader spinning sideband pattern than TiC-CDC-1000. EPR experiments on these carbons could help to further explore these ideas.

Electrochemical characterisations were carried out on supercapacitor cells comprising YP50F, TiC-CDC-1000 and TiC-CDC-600 electrodes with $\text{Pyr}_{13}\text{TFSI}$ ionic liquid as the electrolyte. Cyclic voltammograms show a good capacitive signature for TiC-CDC-1000 with a near rectangular shape, similar to that observed for YP50F (Figure 6.11). TiC-CDC-600, on the other hand, shows a narrow and distorted voltammogram indicative of a poor capacitive performance. This is corroborated by capacitance measurements carried out using the galvanostatic charge-discharge method (Table 6.1), which reveal a capacitance of 57.1 F g^{-1} for TiC-CDC-1000, compared to just 2.7 F g^{-1} for TiC-CDC-600. The low capacitance of TiC-CDC-600 arises from the lack of accessible porosity for charge storage, as shown by the NMR measurements in Figure 6.10a. Electrochemistry studies of ionic liquid supercapacitors in the literature have revealed similar effects when the ions are unable to access the carbon porosity due to their sizes.^{57,175} For TiC-CDC-1000, where a significant number of ions can access the carbon pores (Figure 6.10a), the capacitance is considerably higher. Interestingly, the capacitance of YP50F is higher still than TiC-CDC-1000, despite the slightly better wetting of the carbon pores (at zero applied potential) in TiC-CDC-1000. This suggests that other effects, such as pore-size/ion-size matching⁵⁷ are also important here. *Ex situ* NMR measurements on these carbons could offer an effective strategy to further elucidate the differing performances of these carbons.

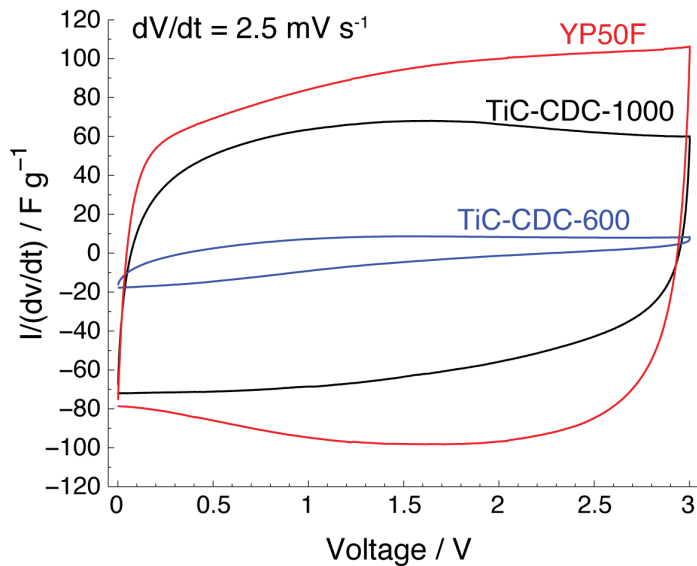


Figure 6.11 Cyclic voltammograms for supercapacitors comprising different carbon electrodes, all with $\text{Pyr}_{13}\text{TFSI}$ ionic liquid electrolyte. TiC-CDC-600 shows poor performance compared to TiC-CDC-1000, with YP50F outperforming both TiC-CDCs.

Table 6.1 Capacitance values measured by galvanostatic charge-discharge measurements.

Carbon	I / A g ⁻¹	C / F g ⁻¹
YP50F	0.055	97.5
TiC-CDC-1000	0.050	57.1
TiC-CDC-600	0.009	2.7

6.4 Summary and Outlook

This chapter has demonstrated the application of NMR methods for studying ionic liquid-based supercapacitors. In the absence of an applied potential, the measurements show that there are a considerable number of ions adsorbed inside the carbon pores, with an equal number of cations and anions observed. *Ex situ* NMR measurements have then been shown to be a powerful technique for probing the charging mechanisms of ionic liquid supercapacitors. Changes of the in-pore peak intensities relate to changes of the in-pore populations during charging. For the Pyr₁₃TFSI/YP50F system, charging was found to be dominated by the migration of anions in and out of the carbon pores, with the migration of cations playing a minor role. Crucially, charging is not driven simply by the adsorption of counter-ions as is commonly assumed, and the adsorption/desorption of the co-ions also plays an important role. The causes of the different behaviour of the anions and cations in this system are at this point unclear and theoretical studies should be carried out to investigate the packing of ions inside carbon pores and to probe the carbon-ion interactions. Further NMR experiments on a range of different electrolytes and carbons may also help to elucidate the factors that dictate the type of charge storage mechanism that operates. In principle, the methods presented here can be directly applied to other carbon and electrolyte systems, provided that the ions contain suitable NMR nuclei and that the in- and ex-pore resonances can be resolved.

The *ex situ* NMR measurements presented here provide new information regarding the charge storage mechanism, though at this point charging dynamics have not been considered. Given the knowledge that migration of ions in and out of the carbon pores brings about charge storage, studies of the in-pore ion dynamics should help with the understanding of the rates at which supercapacitors can store charge. This is the topic of Chapter 7. Ideally, *in situ* NMR measurements (Chapter 8) should be developed for the study of ionic liquid supercapacitors, to allow the study of working devices as they are charged and discharged.

In addition to the variations of in-pore peak intensity, changes of the in-pore chemical shifts are observed upon charging. These changes are nucleus-independent, though depend on the polarisation of the electrode. NICS calculations have shown that the chemical shifts expected for ions nearby carbon surfaces can be drastically modified by carbon charging, and suggest that the introduction of paratropic ring current effects dominate the observed chemical shift changes. In principle, these chemical shift changes can be related to the electronic structure of the carbon, though first more theoretical work must be done to better understand the effects of charging on the ring current shifts.

Finally, measurements on TiC-CDCs soaked with ionic liquid show that the accessibility of pores to ions can readily be probed with the NMR technique. This helps to explain the poor capacitive performance of TiC-CDC-600 with Pyr₁₃TFSI, where few ions can access the carbon pores. In principle the NMR method could be used to screen new porous carbon and electrolyte combinations, and identify suitable combinations to test in supercapacitors.

Chapter 7

Dynamics of Ions Confined in Carbon Pores

7.1 Context and Scope

Supercapacitors store a relatively small amount of energy when compared to batteries, but have the advantage of being able to charge and discharge much more rapidly. Much of current supercapacitor research seeks to increase the energy density of devices without sacrificing their characteristic high power densities. Tailoring of the pore size distribution of the microporous carbon electrodes has been shown to be an effective approach to increase the capacitance,^{31,57,58} though experiments and simulations have revealed that as the pore size is decreased towards the sizes of the ions the power performance can suffer.^{31,69} Another strategy to increase the energy density of supercapacitors is to use ionic liquids as an alternative to traditional organic electrolytes (see Chapter 6).^{12,24} While these allow higher operating voltages and the storage of more energy, low ionic conductivities are detrimental to device power performances.¹⁶⁵ Charge storage in ionic liquid supercapacitors takes place via the migration of anions and cations in and out of the carbon pores, as shown by the NMR measurements in the previous chapter and MD simulations.⁶⁸ The migration of ions through the tortuous carbon pores will then be the rate-limiting step for supercapacitor charging. New experimental methods must be developed to study in-pore ion dynamics so that the power performance of supercapacitors can be understood.

NMR spectroscopy is a powerful probe of dynamic processes on a range of timescales.⁹⁴ As was shown in Chapter 4, 2D EXSY experiments can probe chemical exchange between the in-pore and ex-pore environments, revealing in-pore – ex-pore exchange on a ms timescale. Such EXSY experiments only allow studies of exchange

for spectrally resolved sites, so are less well suited to probe dynamics of the ions within the carbon pores. In principle, lineshape measurements can give complementary dynamic information on ms or μ s timescales.¹⁰⁹ In Chapter 6, the in-pore resonance observed for ionic liquid-soaked carbons was found to be considerably broader than in analogous experiments with organic electrolytes (Chapter 4) suggesting that this linewidth is sensitive to dynamics. In-pore linewidths also showed variations when different carbons were studied (Chapter 5). Studies in the literature have shown similar variations of in-pore linewidth for different carbon materials, which have been suggested to arise from differences in ion dynamics in some cases,¹⁴¹ and from structural differences between the carbons in others.¹⁴⁴

The main aim of this chapter is to study the dynamics of the in-pore ions and how they are affected by temperature, the presence of solvent molecules and the structure of the carbon. Variable temperature NMR measurements on ionic liquid-soaked porous carbons show that the linewidths observed for in-pore ions are sensitive to the rate of their diffusive motion. For YP50F carbon, it is shown that in-pore TFSI⁻ has faster ionic diffusion in EMITFSI than in Pyr₁₃TFSI ionic liquid, while addition of acetonitrile (the standard organic solvent used in supercapacitor electrolytes) greatly increases the rate of in-pore diffusion in both cases. Simulations of the chemical exchange processes within the carbon pores allow an estimation of the timescale and energy barrier associated with in-pore diffusion, and the results allow a rationalisation of the differing charging dynamics measured for supercapacitors with different electrolytes. Finally, the effects of carbon porosity on ion dynamics are discussed, which is shown to be an interesting direction for new research in this area.

7.2 Experimental Details

7.2.1 Materials

The studied carbon materials and ionic liquids are described in Sections 6.2.1 and 6.2.2. For NMR experiments with acetonitrile, deuterated acetonitrile, ²H₃CCN (99.80 %, Eurisotop, referred to as dACN) was used.

7.2.2 Sample preparation for NMR experiments

For carbon samples soaked with ionic liquids, the sample preparation is described in Section 6.2.3. For samples containing an ionic liquid diluted with deuterated acetonitrile, a sample was first prepared as described in Section 6.2.3. The volume of deuterated acetonitrile required to dilute the ionic liquid to 1.8 M was then calculated

and added to the sample by microsyringe before quickly capping the rotor. Since some solvent may be lost by evaporation during syringing, the rotor was then reweighed to determine the actual amount of acetonitrile added. The concentration of the resulting organic electrolyte was then determined from the volumes of ionic liquid and solvent in the sample.

7.2.3 NMR experiments

NMR experiments were carried out as described in Section 6.2.4. For variable-temperature NMR measurements, temperature calibrations were performed by ^{207}Pb NMR experiments on lead nitrate.^{180,181} Experiments on lead nitrate with different MAS rates showed that the frictional heating effect at 5 kHz MAS is less than 1 °C.

7.2.4 Lineshape simulations

A program was written in Matlab software to probe the timescale of the exchange processes discussed in Section 7.3.1. In the model, a number of different resonance frequencies are first defined, which represent the range of possible frequencies that may be experienced by ions inside the porous carbon structure. In the simulations, the trajectories of different nuclear spins are computed as their resonance frequencies hop between the different possible values at an exchange rate, k_{ex} . Each time a frequency hop occurs, the new frequency of the spin is chosen at random from the possible values, *i.e.*, the spatial arrangement of the sites is not taken into account. The signals arising from an ensemble of 60 000 spins are summed and the resulting FID is Fourier transformed to give the simulated NMR spectrum. The simulated linewidth can then be measured by fitting in dmfit software.¹³⁷ No nuclear spin relaxation is taken into account in the simulations.

7.2.5 Electrochemical characterisations

Electrochemical tests were carried out on coin cell devices, fabricated as described in Section 6.2.5, with galvanostatic charge-discharge capacitance measurements carried out as detailed in Section 6.2.7.

7.3 Results and Discussion

7.3.1 Variable temperature NMR measurements

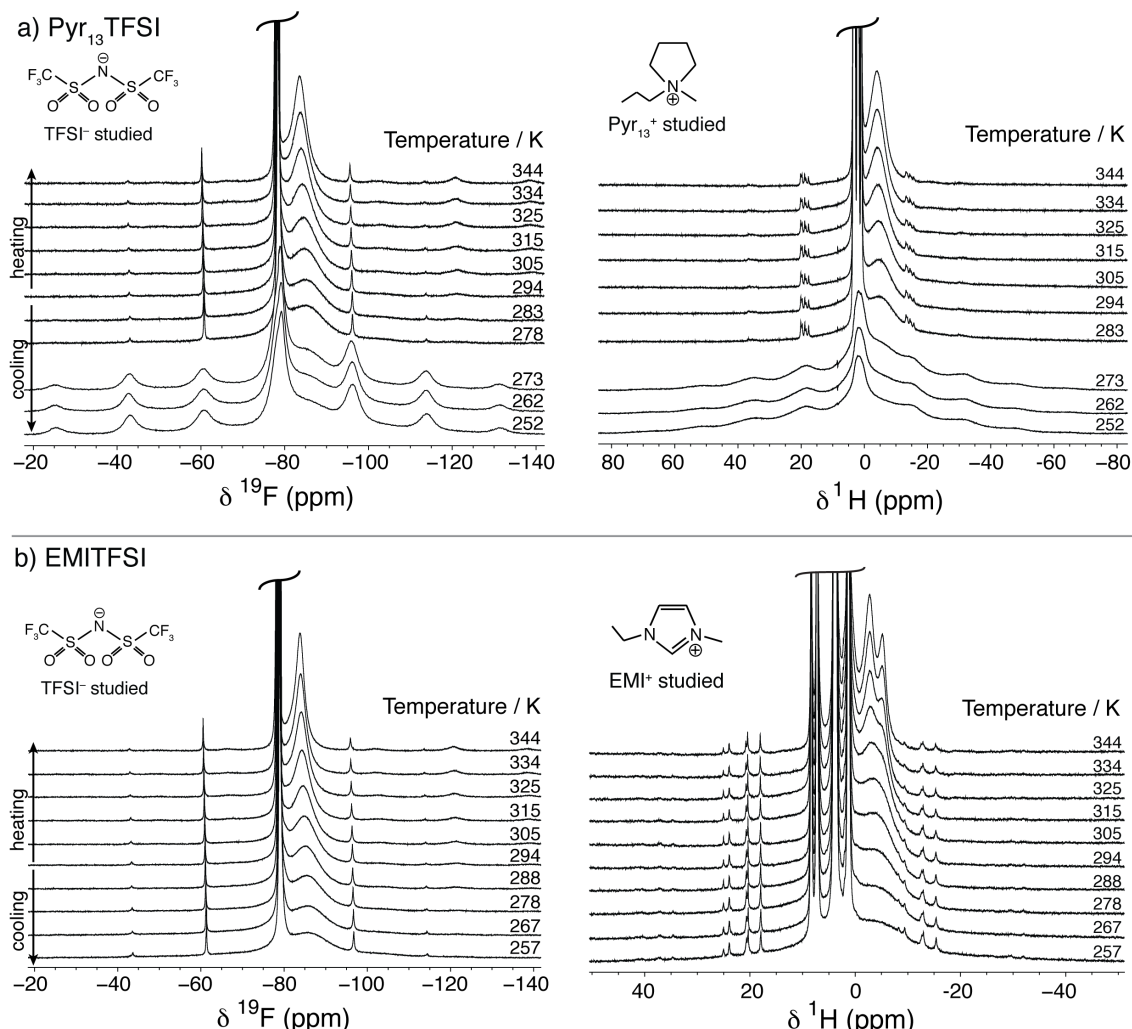


Figure 7.1 ^{19}F and ^1H MAS NMR (7.1 T) spectra of YP50F carbon film soaked with (a) Pyr₁₃TFSI and (b) EMITFSI at different temperatures. Clear reductions in the in-pore linewidth are observed as the temperature is increased, reflecting the increase in the mobility of the anions in the carbon micropores.

Variable temperature MAS NMR measurements were carried out on YP50F carbon samples soaked with ionic liquids to investigate the effects of dynamics (Figure 7.1). On cooling YP50F soaked with Pyr₁₃TFSI to 273 K (Figure 7.1a), the ex-pore ionic liquid displays a dramatic change in lineshape, with considerable broadening and a large increase in the width and intensity of the spinning sideband manifold in both the ¹⁹F and ¹H NMR spectra. Below 273 K this lineshape persists and does not show any further changes. This behaviour is consistent with the ex-pore ionic liquid freezing upon cooling from 278 to 273 K. Indeed, the freezing point of Pyr₁₃TFSI mixed with BP2000 (Cabot Corp.) porous carbon was recently reported to be 275 K, though the distinction was not made between in- and ex-pore liquid in that study.¹⁸² Despite the freezing of ex-

pore ionic liquid, the in-pore environment shows continual changes in linewidth throughout the low-temperature regime, with no evidence of a freezing event observed. The freezing point of the in-pore ionic liquid is therefore suppressed relative to the ex-pore, presumably because confinement in the carbon micropores hinders the formation of an ordered solid phase. Xu *et al.* recently observed a similar phenomenon in a ^1H NMR study of a mesoporous carbon, where in-pore water remained liquid at temperatures as low as 223 K.¹⁴² Returning to Figure 7.1a, at temperatures of 278 K and above, the ex-pore resonance does not show any significant linewidth changes, while the in-pore linewidth steadily decreases as the temperature is increased, with the changes similar in the ^{19}F and ^1H spectra. The ^{19}F and ^1H MAS NMR spectra of YP50F soaked with EMITFSI (Figure 7.1b) again show clear decreases of the in-pore linewidth as the sample temperature is increased. Here, there is no evidence of freezing over the studied temperature range, though this is not surprising given that the freezing point of EMITFSI is 223 K.¹⁸³

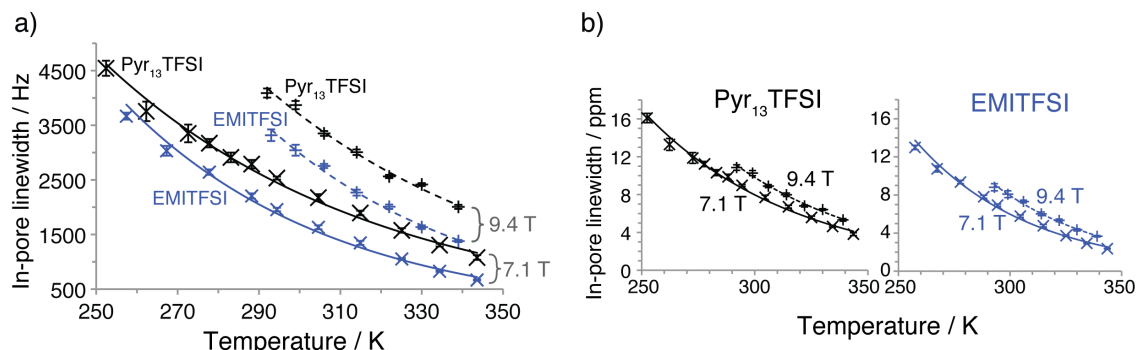


Figure 7.2 Measured ^{19}F in-pore linewidths (full linewidth at half-maximum peak intensity) from ^{19}F spectra in Figure 7.1 (at 7.1 T), with additional measurements at 9.4 T also shown. Measurements are given in (a) Hz, (b) ppm. Curved lines were added to the plots simply to guide the eye. Decreases in the in-pore linewidths are observed as the temperature is increased, with the linewidths larger in ppm at higher magnetic field strength.

Focussing on the ^{19}F variable temperature NMR data, the measured in-pore linewidths are plotted in Figure 7.2 and show clear decreases as the sample temperatures are increased. The ^{19}F in-pore linewidth is consistently smaller for EMITFSI than Pyr₁₃TFSI over the studied temperature range. In addition to the measurements shown in Figure 7.1 (recorded at 7.1 T), spectra were also recorded at a higher magnetic field strength of 9.4 T. The in-pore linewidths at 9.4 T were found to be greater in both Hz and ppm than those recorded at 7.1 T (Figure 7.2). In principle, the in-pore linewidth could arise from a number of different mechanisms. First, the porous carbon studied here has a highly disordered structure such that the ions will occupy a range of different

adsorption sites in the carbon micropores.⁷³ As shown in Chapter 5, sites inside pores with different sizes, different graphene-like domain sizes, and different amounts of curvature will give rise to different ring current effects and thus a distribution of different chemical shifts. In the absence of any motion, each ion will contribute separately to the spectrum and the lineshape will represent the weighted distribution of the different chemical shifts in the system. In this case the linewidth should scale linearly (in Hz) with the magnetic field strength, yielding identical linewidths on the ppm scale. However, diffusion (chemical exchange) of the ions between the different sites leads to lineshape perturbations.^{94,102} When the rate of diffusive motion exceeds the frequency width of the distribution of chemical shifts, a single coalesced resonance is observed which is narrower than the overall distribution of shifts (see Section 3.5). In the so-called “fast-intermediate” exchange regime, where the exchange rate is comparable to (but still greater than) the width of the distribution of chemical shifts, increases in the rate of motion lead to a reduction of the peak linewidth, referred to as motional narrowing (Section 3.5). In this regime increases in linewidth (in ppm) are observed when the magnetic field is increased, as observed here (Figure 7.2b). This arises because at a higher magnetic field strength the distribution of chemical shifts spans a wider range of frequencies, and hence, faster motion is required for line narrowing. Second, the in-pore linewidth may also have a contribution from residual dipole-dipole couplings between the studied nuclear spins; however, a linewidth dominated by such interactions should remain constant (in Hz) at different magnetic field strengths. The observations in Figure 7.2a, that the linewidths show a significant increase at a stronger magnetic field, rule out dipole-dipole interactions as the dominant source of the linewidth.

The findings point toward the distribution of different adsorption sites in the carbon as the dominant source of the in-pore linewidth. This is further corroborated by the temperature dependence of the NMR spectra. As the temperature is increased, the ions become increasingly mobile inside the carbon micropores and diffuse more quickly between the different sites. This leads to motional narrowing of the in-pore resonance, confirming that ionic motion is in the fast-intermediate regime.⁹⁴ While ¹H in-pore linewidths are less easily extracted (than ¹⁹F linewidths) due to the different chemical environments in the cations, the variation of the ¹H and ¹⁹F in-pore linewidths with temperature is qualitatively similar (Figure 7.1), suggesting that the rate of in-pore diffusive motion of the anions and cations is not drastically different.

In principle, the observed linewidth changes can be directly correlated with the rate of motion. Extraction of accurate exchange rates, however, requires: (i) an estimate of the lineshape in the absence of ionic motion, and (ii) a model for ionic motion in the highly heterogeneous carbon pore structure. While NICS calculations on model carbon fragments (Chapter 5) can be used to estimate the range of possible shifts for adsorbed ions, the treatment of (ii) is not trivial since the distances and pathways between sites with different chemical shifts are not known. In the absence of an accurate model for the micro- and macroscopic structure of this activated carbon, a simple multi-site exchange model was developed to investigate the time scales required to reproduce the experimental linewidths and obtain order-of-magnitude estimates for the rate of motion.

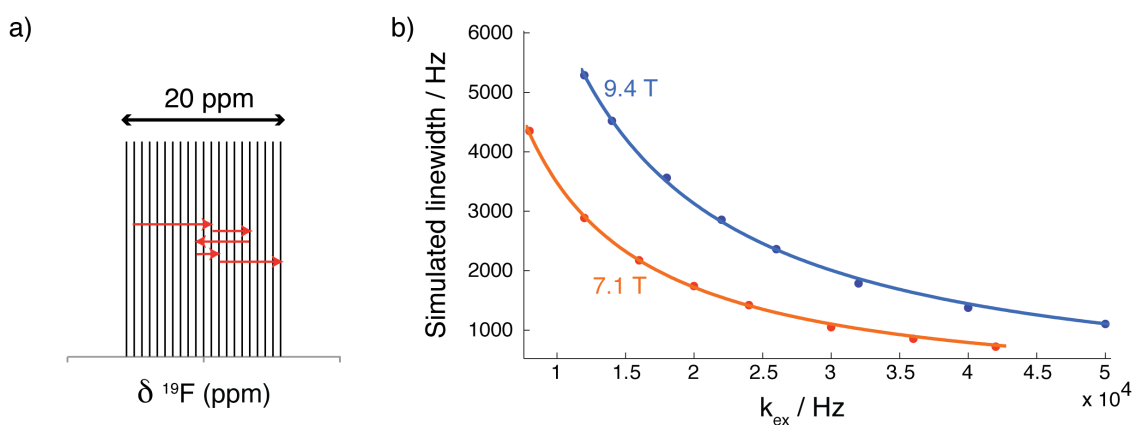


Figure 7.3 (a) Distribution of chemical shift sites studied in the multi-site exchange model. The red arrows show the first five steps of a possible trajectory. Simulated linewidths are shown in (b) for a range of different exchange rates and at two different magnetic field strengths. Stretched exponential fits of the simulated data are also shown.

In the model, a number of different resonance frequencies are first defined (Figure 7.3a), which are intended to represent the range of possible resonance frequencies that in-pore ions may have. While it is difficult to know the exact form of this distribution, its width can be estimated of the basis of NICS calculations on model carbon fragments. Such calculations (Chapter 5) suggest that values can vary from large negative values of ~ -16 ppm inside carbon slit-pores, to small positive values of $\sim +2$ ppm at the edge of planar carbon fragments,¹⁴² giving a range of possible shifts for adsorbed ions on the order of 20 ppm. As such, in the first instance a uniform distribution of frequencies spanning 20 ppm was studied (Figure 7.3a). Spectra were then simulated for an ensemble of spins hopping randomly between the different sites at an exchange rate, k_{ex} (see Section 7.2.4 for more details).

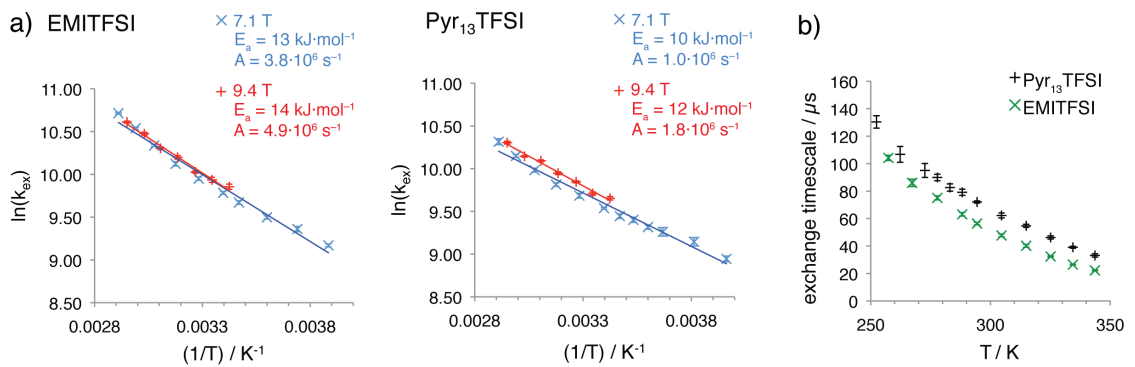


Figure 7.4 (a) Natural logarithms of extracted exchange rates against inverse temperature. For an Arrhenius-type thermally activated process, $\ln(k_{\text{ex}}) = \ln(A) - (E_a/k_B T)$, where A is a constant, E_a is the activation energy associated with the process, and k_B is Boltzmann's constant. Extracted E_a and A parameters for the 7.1 T data are shown in (a). In (b), exchange timescales (which are the inverse of the extracted exchange rates for the 7.1 T data) are plotted against temperature.

A number of simulations were run with different k_{ex} values to study the effect of chemical exchange on the spectral lineshape. Simulated linewidths (full-linewidth at half-maximum peak intensity) are shown in Figure 7.3b for simulations carried out at two different magnetic field strengths, with the simulated data fitted well using stretched exponential functions. The fitted functions were then used to extract k_{ex} values from the experimental linewidth data for in-pore anions (Figure 7.4a). In principle, exchange rates extracted from spectra at the two different field strengths should be identical. For EMITFSI, this is the case within error, and for Pyr₁₃TFSI the agreement is also reasonable, giving confidence in the approach. The simulations suggest that the diffusive motion of in-pore TFSI⁻ between different adsorption sites in the carbon pores is a thermally activated Arrhenius-type process, with an activation barrier on the order of 10 kJ·mol⁻¹. The calculated time scales for this motion (*i.e.*, for random hops between the sites that give rise to the broadened lineshape) vary on the order of ~20–130 μs depending on the temperature (344–252 K) and the ionic liquid studied (Figure 7.4b). At all temperatures studied, the time scale for in-pore TFSI⁻ motion is faster for EMITFSI than for Pyr₁₃TFSI. For example, at 294 K the calculated time scales are 72 and 56 μs for Pyr₁₃TFSI and EMITFSI, respectively, meaning that diffusion of in-pore TFSI⁻ is 1.3 times faster for EMITFSI than Pyr₁₃TFSI at this temperature. Previous pulsed field gradient (PFG) NMR measurements on neat ionic liquids showed that TFSI⁻ has faster self-diffusion in EMITFSI than Pyr₁₃TFSI, by a factor of 1.6 at 294 K.^{184,185} The measurements here demonstrate that this general difference is retained under confinement, though the difference becomes smaller.

It is interesting to explore the length scale associated with the exchange process. Assuming that the self-diffusion coefficient, D , for TFSI in neat Pyr₁₃TFSI at 292 K remains unchanged from that measured for free ionic liquid at $0.13 \cdot 10^{-10} \text{ m}^2 \cdot \text{s}^{-1}$,¹⁸⁶ and considering a diffusion time, t , of 72 μs (the simulated timescale for exchange for Pyr₁₃TFSI at 292 K above) this yields a diffusion distance of $(6Dt)^{0.5} = 75 \text{ nm}$ for the TFSI anions. This relatively large value of 0.075 μm may be compared to the typical carbon primary particle sizes that are on the order of 1 - 10 μm . In reality the diffusion value is likely greatly reduced inside the tortuous network of the carbon micropores. For example, a two orders of magnitude reduction in the self-diffusion coefficient would reduce the estimated diffusion distance to 7.5 nm, *i.e.*, approaching the same order of magnitude of the size of the carbon fragments studied in the NICS calculations. Confinement may also reduce the dimensionality of diffusion (*e.g.*, two-dimensional diffusion for a slit-shaped pore), which would further reduce the calculated diffusion distance. Ideally, PFG NMR measurements¹⁸⁷ would be carried out to extract the in-pore ionic self-diffusion coefficients directly. This will form a part of future work.

Crucially, the in-pore linewidth gives a measure of how quickly the ions diffuse through the carbon pores, allowing one to compare the mobility of different electrolytes under confinement; the faster the diffusion is, the narrower the in-pore resonance. The finding that the TFSI anions diffuse more rapidly through the carbon micropores for EMITFSI than for Pyr₁₃TFSI has important implications for the power performances of these ionic liquids as supercapacitor electrolytes (discussed in Section 7.3.3). It is stressed that the results obtained from the multi-site exchange simulations depend on the initial choice of the distribution of resonance frequencies. Other chemical shift distributions with different widths were investigated and it was found that while the exact values of the extracted exchange rates and activation energies depend on the model used, the orders of magnitude of these quantities remain unchanged. Ideally, chemical shift distributions would be calculated for model carbon structures such as those of Palmer *et al.*⁴⁷ Furthermore, the lack of treatment of the complex spatial arrangement of adsorption sites in the carbon micropores will have a large effect on the results obtained in the simulations. More sophisticated spectral simulations, which take into account the connectivity of different sites in the heterogeneous carbon pore structures will provide more detailed insight into the exchange process observed here.

7.3.2 Effects of addition of acetonitrile solvent

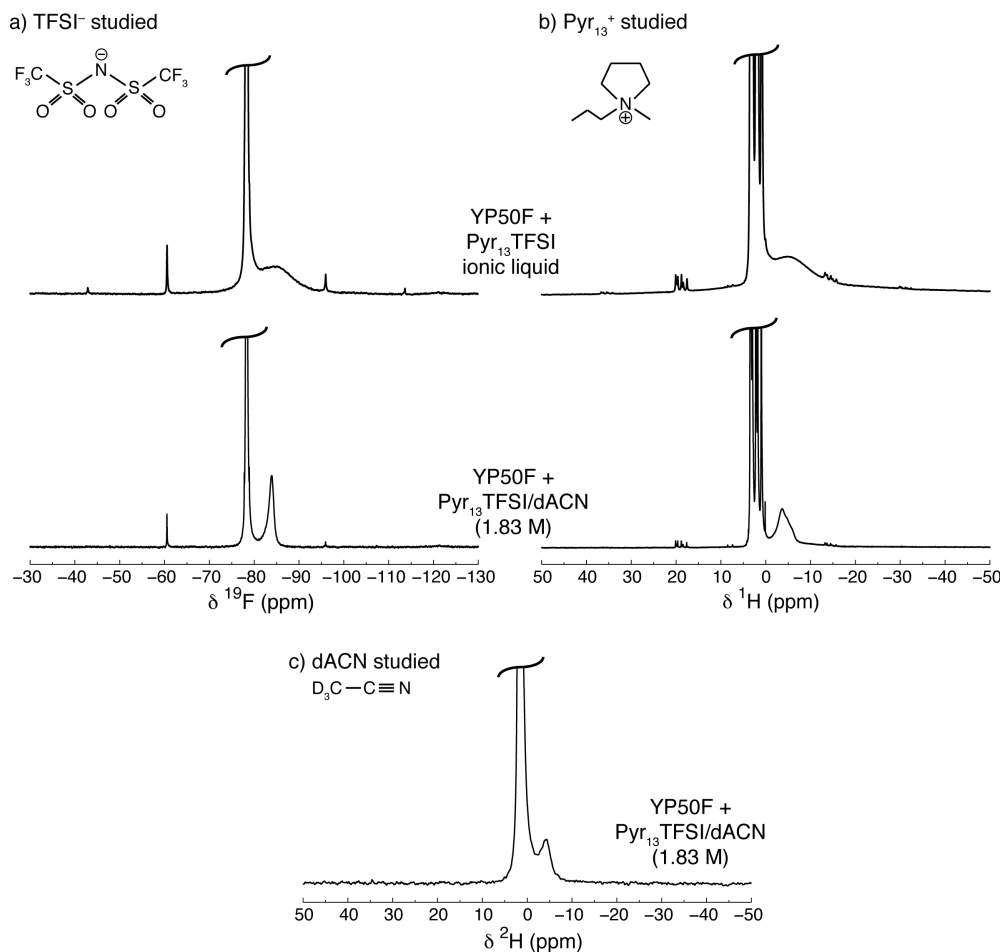


Figure 7.5 MAS NMR (7.1 T) spectra of YP50F film soaked with Pyr₁₃TFSI/dACN (1.8 M). ¹⁹F, ¹H, and ²H spectra are shown in (a), (b), and (c), allowing study of the anions, cations, and solvent, respectively. Spectra of YP50F soaked with neat Pyr₁₃TFSI are shown for comparison. Spectra show that the addition of an organic solvent significantly increases the mobility of the in-pore ions.

Acetonitrile was added to a sample of YP50F and Pyr₁₃TFSI to study the effect of an organic solvent on the structure and dynamics of the carbon-electrolyte interface. Deuterated acetonitrile (D₃CCN or dACN) was used to allow the separate study of the solvent and Pyr₁₃ cations, with the resulting 1.8 M electrolyte being referred to as Pyr₁₃TFSI/dACN. Comparison of the ¹⁹F and ¹H spectra before and after the addition of acetonitrile shows that the linewidths of the in-pore resonances are dramatically decreased following the addition of the solvent (Figure 7.5). For example, the linewidth of the in-pore ¹⁹F resonance drops from 2530 to 340 Hz (Figure 7.5a). The observation of an in-pore resonance in the ²H spectrum (Figure 7.5c) confirms the presence of acetonitrile in the carbon micropores. The broader resonances observed in the ²H spectra (compared to the ¹⁹F and ¹H spectra) may arise from chemical exchange of solvent molecules between the in-pore and the ex-pore environments.

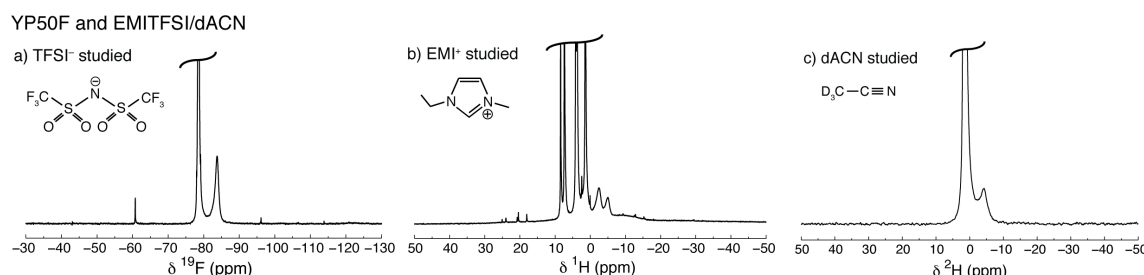


Figure 7.6 MAS NMR (7.1 T) spectra of YP50F films soaked with EMITFSI/dACN (1.87 M). (a) ^{19}F , (b) ^1H and (c) ^2H spectrum. Additional of acetonitrile again significantly narrows the in-pore resonances.

Spectra were also recorded for a sample containing YP50F and EMITFSI/dACN (Figure 7.6), with the in-pore resonances again significantly narrowed compared to the sample without solvent. The large reductions of the in-pore linewidths for anions and cations following the addition of acetonitrile show that its presence in the micropores greatly speeds up in-pore ionic diffusion. On the basis of the multi-site exchange simulations (see above), a time scale of 13 μs for motion of in-pore TFSI is estimated for Pyr₁₃TFSI/dACN, that is, in-pore diffusion of TFSI⁻ is 5.5 times faster following the addition of acetonitrile, representing a dramatic increase. For EMITFSI/dACN an identical time scale of 13 μs for in-pore TFSI is estimated, suggesting that the motion of in-pore anions is not significantly affected by different cations in the solvated electrolytes. It is noted that the difference between the ^{19}F chemical shifts of the in- and ex-pore resonances decreases slightly after adding solvent (*e.g.*, from 6.6 to 5.7 ppm for Pyr₁₃TFSI). This may be because the presence of acetonitrile slightly lengthens the average carbon-ion distances, giving rise to weaker ring current effects. This may be due to the partial solvation of the ions, though the increased exchange between the in-pore and the ex-pore environments may also have an effect.

Table 7.1 Comparison of number of moles of in-pore anions and electrolyte volumes before and after adding acetonitrile. Electrolyte volumes are calculated using the ion volumes given in Section 6.3.1. For solvated ionic liquids, the volume of acetonitrile (46 Å per molecule)¹⁶⁸ is included, with the moles of in-pore acetonitrile determined from fitting of the ^2H spectra. The % pore volume occupied is calculated by comparing the electrolyte volume to the carbon pore volume measured by N₂ gas sorption (0.71 cm³·g⁻¹).¹⁴⁰ Finally, calculated ratios of in-pore solvent to ion pairs are given, assuming equal numbers of anions and cations in the pores.

electrolyte	moles TFSI ⁻ in-pore / mmol·g ⁻¹	electrolyte volume in-pore / cm ³ ·g ⁻¹	% pore volume occupied	solvent:ions in-pore
Pyr ₁₃ TFSI	1.6	0.28	40%	-
Pyr ₁₃ TFSI/dACN (1.83 M)	1.1	0.34	48%	4.6
EMITFSI	1.8	0.29	40%	-
EMITFSI/dACN (1.87 M)	1.2	0.30	42%	3.5

Table 7.1 summarises the populations of in-pore anions and the corresponding volumes of in-pore electrolyte for neat and solvated ionic liquids. For both ionic liquids, the number of in-pore anions decreases following the addition of acetonitrile, yet the total volume of in-pore electrolyte increases slightly. These two findings suggest that acetonitrile displaces some ions from the carbon micropores while at the same time occupying some previously empty pores that are inaccessible to the ions. This latter finding is consistent with MD simulations of 1-butyl-3-methylimidazolium hexafluorophosphate/ACN in a model porous carbon, which showed that acetonitrile is able to occupy the smaller carbon pores with tubular and pocket-like geometries, while ions tend to occupy less confined sites.⁷³ Going further, ratios of solvent molecules to ion pairs in the pores are calculated, which represent average solvation numbers. For both electrolytes, the in-pore solvation number is reduced compared to that for the overall electrolyte (calculated as 5.0 in both cases). This shows that in the absence of an applied potential, solvation numbers are decreased in the carbon micropores, with the effect being more significant for EMITFSI than Pyr₁₃TFSI. This is presumably as the ions have stronger non-covalent interactions with the carbon than the solvent. The increased in-pore ion desolvation of the EMI⁺-based electrolyte could arise from stronger carbon-ion interactions for EMI⁺ (compared to Pyr₁₃⁺), though there may also be a contribution from differences in the ion desolvation energies. It is noted that EMI⁺ has an aromatic π system that may permit π - π interactions with carbon surfaces. While greater in-pore populations are observed for EMITFSI than Pyr₁₃TFSI (with or without a solvent), there are not, however, significant differences in the ring current shifts for the two cations. This suggests that the desolvation energies of the ions are also important in determining the in-pore solvation numbers.

7.3.3 Rationalising the rate performance of supercapacitors

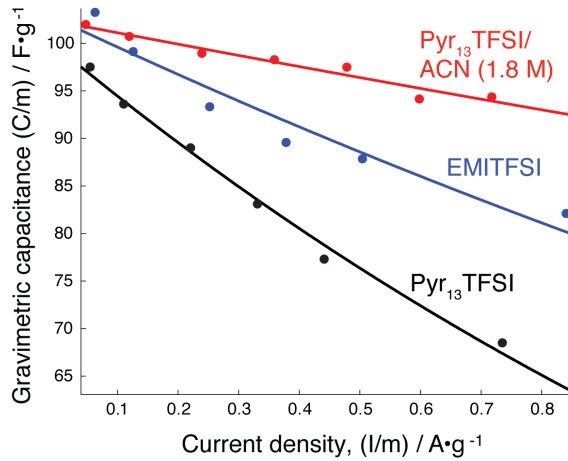


Figure 7.7 Gravimetric capacitance measurements for coin cells with YP50F activated carbon electrodes and different electrolytes. Capacitances were measured for a series of different current densities at ambient temperature. Exponential fits are shown, with R^2 values varying from 0.99 to 0.92 to 0.94 for Pyr₁₃TFSI, EMITFSI, and Pyr₁₃TFSI/ACN, respectively. The results show that these three electrolytes have very different power handling capabilities.

The *ex situ* NMR measurements presented in the previous chapter showed that supercapacitor charging involves both adsorption of counter-ions and desorption of co-ions, with the adsorption and desorption of anions playing a more dominant role than that of cations, while here, in-pore linewidths have been correlated with the rate at which ionic species diffuse through the carbon micropores. Together these findings offer a new opportunity to rationalise the power performances of supercapacitors. Figure 7.7 shows measurements of the gravimetric capacitance of three supercapacitor cells comprising YP50F electrodes with different electrolytes. At low current densities the gravimetric capacitances of the three cells are similar, with the capacitance of the EMITFSI-based cell being slightly larger than that of the Pyr₁₃TFSI and Pyr₁₃TFSI/ACN cells. As the applied current is increased, all cells show a decrease in capacitance, though the EMITFSI-based cell shows better performance at high currents than the Pyr₁₃TFSI cell, while the Pyr₁₃TFSI/ACN cell outperforms both cells with neat ionic liquids. This is quantified by exponential fits of the form:

$$\frac{C}{m} = \frac{C_0}{m} \exp\left(-\frac{I/m}{i/m}\right) \quad [7.1]$$

where m is the electrode mass, C_0/m is the gravimetric capacitance in the limit of $I \rightarrow 0$, and i/m is a characteristic current density at which the capacitance, C , has decayed to C_0/e . The larger the value of i/m , the better the capacitance retention with increasing

current density. The obtained i/m values are 1.9, 3.4, and 8.4 A·g⁻¹ for Pyr₁₃TFSI, EMITFSI, and Pyr₁₃TFSI/ACN (1.8 M), respectively, giving a ratio of 1:1.8:4.4.

In Section 7.3.1 it was shown that for EMITFSI, the in-pore anions are more mobile than for Pyr₁₃TFSI, while addition of acetonitrile greatly increases the mobility of the anions and cations in the carbon micropores (Section 7.3.2). The linewidth measurements and simulations allowed an estimation of the ratio of in-pore anionic diffusion rates as 1:1.3:5.5 for Pyr₁₃TFSI, EMITFSI, and Pyr₁₃TFSI/ACN (1.8 M), respectively, at ambient temperature. Interestingly, these values appear to show some correlation with the i/m values above, and may help to explain the observed electrochemical rate performance. The faster the in-pore ionic diffusion, the better the capacitance retention at high current rates. Overall, the findings show that the development of new ionic liquids with faster in-pore ionic diffusion is crucial if these devices are to compete with conventional organic electrolytes in terms of power performance. However, it is noted that the diffusion information obtained from the NMR experiments is for samples in equilibrium states with no applied voltage. Any changes of ionic mobility that might occur during charging are not considered. This is in contrast to the capacitance measurements that probe dynamic processes where the voltage continuously varies. Future studies should be carried out to probe ionic diffusion under dynamic charging conditions. One particularly interesting technique in this regard is electrophoretic NMR, where ionic mobilities can be measured with the application of an applied electric field.^{188,189}

7.3.4 Effects of carbon porosity on dynamics

In principle, NMR spectra of different carbons soaked with electrolytes should provide information about differences in the ion dynamics in these carbons. Indeed, NMR spectra for electrolyte-soaked TiC-CDCs and activated carbons in Chapters 4 and 5, showed marked variations of the in-pore linewidth. Importantly, this linewidth depends on both the distribution of possible chemical shifts for in-pore species, and the rate at which ions diffuse between the different sites. Thus, when comparing in-pore linewidths between different samples, differences in both the distribution of possible chemical shifts and in-pore diffusion need to be taken into account.

For the TiC-CDC carbons studied in Chapter 4, both the carbon pore size distribution and carbon ordering varied across the series. This means the distribution of chemical shift sites for in-pore ions is markedly different for these carbons, and differences of the in-pore linewidths cannot straightforwardly be correlated to differences in diffusion.

However, the vacuum-annealed TiC-CDCs studied in Chapter 5 offer a more controlled series here, as the carbon ordering (which dominates the ring current shift) was shown to be similar for this series of carbons, while small differences in the carbon pore size remained. For these carbons, the in-pore linewidths decrease as annealed carbons with higher chlorine-treatment temperatures are studied (Figure 7.8a). This is despite a broadening of the pore size distribution for these samples that would be expected to slightly broaden the distribution of chemical shift sites (Figure 7.8b). These findings point towards faster in-pore diffusion for the carbons prepared at higher chlorine-treatment temperature, giving rise to the narrower in-pore linewidths. Going from TiC-CDC-400-VAC to TiC-CDC-600-VAC, there is a clear increase in the average pore size, which likely gives rise to the faster in-pore diffusion, and the narrower in-pore linewidth. The differences between TiC-CDC-600-VAC and TiC-CDC-800-VAC are more subtle, with the mode pore size distribution shifting to lower values for TiC-CDC-800-VAC, but at the same time additional pore volume is introduced above diameters of 1 nm. These larger pores appear to dominate the behaviour here, giving rise to faster in-pore ionic diffusion. The hypotheses here agree well with results from pulsed-field gradient NMR measurements, which showed that the self-diffusion coefficients of water and methanol adsorbed in activated carbons increase with the average pore size of the carbon.¹⁸⁷ These pore size effects are important for the power performances of supercapacitors, and are likely responsible for the poorer power performance observed for TiC-CDCs with smaller pores.^{31,69}

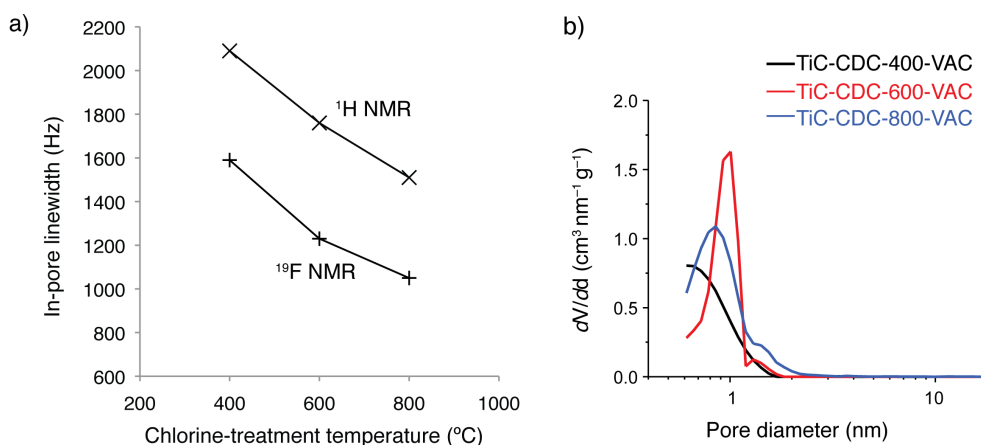


Figure 7.8 (a) Variation of the ¹⁹F and ¹H in-pore linewidths for vacuum-annealed carbons soaked with $\text{NEt}_4\text{BF}_4/\text{dACN}$ (1.5 M). Linewidths are consistently larger for ¹H due to the presence of the unresolved CH_2 and CH_3 groups in the NEt_4 cations. (b) Pore size distributions of the carbons extracted from N_2 gas sorption isotherms. Decreases of the in-pore linewidths arise from increases of the rate of in-pore diffusion.

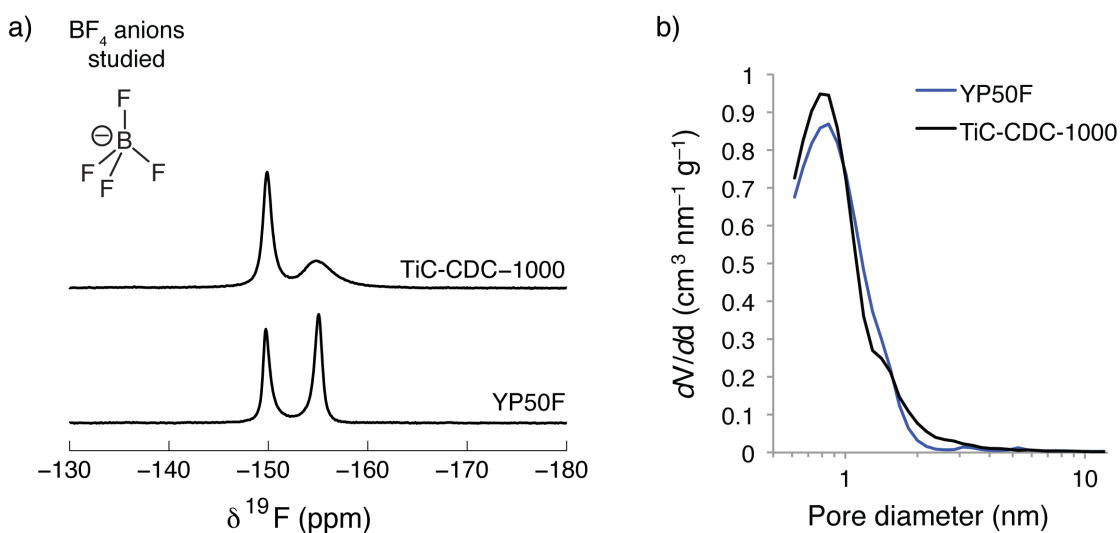


Figure 7.9 (a) ${}^{19}\text{F}$ MAS NMR (9.4 T) spectra of TiC-CDC-1000 and YP50F carbon samples soaked with $\text{NEt}_4\text{BF}_4/\text{dACN}$ (1.5 M). Spectra are reproduced from Chapter 4 for convenience. (b) Pore size distributions of the carbons. The in-pore lineshapes are markedly different despite the similar pore distributions and structural ordering of these carbons.

A further interesting comparison is that between TiC-CDC-1000 and YP50F. NMR spectra for these carbons show large differences in the in-pore lineshape with a considerably broader resonance observed for TiC-CDC-1000 (Figure 7.9a). This is despite the very similar pore size distributions (Figure 7.9b) and the very similar local structural ordering of these carbons (Chapter 5). Therefore, it is expected that the distribution of chemical shift sites for in-pore ions in these two carbons should be similar. The differences in the in-pore linewidths therefore arise from dynamic effects, and suggest that in-pore ionic motion is faster for YP50F than TiC-CDC-1000. The faster ion dynamics in this carbon could arise from a number of different factors. Firstly, while the overall pore size distributions of these carbons are very similar, the connectivity and arrangement of the pores in space may be different, which could lead to differences in tortuosity and therefore the self-diffusion. For example, if pores of different sizes are arranged in a hierarchical fashion, the diffusion may be faster than if the arrangement of pores were random. Secondly, the local pore geometries may differ for these carbons, with differing degrees of pore curvature for example. Lastly, the surface chemistry of these carbons may be different. Porous carbons are known to have a number of functional groups on the carbon surfaces, which may interact with the ions and mediate the diffusion processes. These effects need to be investigated in more detail, and more advanced spectral simulations must be developed to understand the interplay between carbon pore structures and the observed dynamics and NMR spectra. These findings could then complement diffusion measurements from MD

simulations^{190–192} and pulsed-field gradient NMR measurements.¹⁸⁷ It is envisaged that a better understanding of in-pore ion dynamics will aid the design of new electrode materials for supercapacitors with both high energy and power densities.

7.4 Summary and Outlook

The transport of electrolyte ions through the pores of carbon electrodes is a key factor for determining the power performance of supercapacitors. In light of this, the effects of translational dynamics on the NMR lineshapes observed for in-pore ions have been investigated. A range of different adsorption sites, with different chemical shifts, exist for ions in the carbon pores, which gives rise to the in-pore linewidth observed in the NMR spectra. The exact linewidth is sensitive to the rate of in-pore ionic diffusion, such that information on this motion can be extracted from the NMR spectra.

Specifically, the diffusion of TFSI anions through the carbon pores of YP50F activated carbon soaked with EMITFSI and Pyr₁₃TFSI ionic liquids was investigated. In-pore TFSI⁻ diffusion was found to be faster for EMITFSI than Pyr₁₃TFSI, with the ratio of diffusion constants estimated as 1.3 at 294 K on the basis of multi-site exchange simulations. Upon the addition of acetonitrile solvent, some ions are displaced from the carbon pores, and the rate of in-pore ionic diffusion is significantly increased (the estimated increase is by a factor of 5.5 for Pyr₁₃TFSI diluted to ~1.8 M). The in-pore ions are also observed to be desolvated in the absence of an applied potential. The findings from the NMR measurements then help to rationalise the different rate performances of different electrolytes in supercapacitors, with the extracted rates of in-pore diffusion showing some correlation with the rate at which supercapacitor devices can store charge. New ionic liquids with faster in-pore ionic diffusion must be developed if they are to compete with the power performance of organic electrolytes. Measurements of in-pore linewidths in NMR experiments represent an interesting new method to probe the rate of in-pore diffusion and should facilitate the testing of new carbon-electrolyte combinations for application in supercapacitors. However, more work (such as electrophoretic NMR measurements) must be done to explore how in-pore diffusion is affected by the application of an applied potential.

As well as changes of the electrolyte, the carbon structure has been shown to affect the in-pore diffusion rates. Vacuum-annealed TiC-CDC samples with larger pores give rise to faster in-pore ionic diffusion and narrower linewidths in the NMR spectra. Carbons with nearly identical pore size distributions can also give rise to drastically different in-

pore linewidths, likely due to differences between the spatial arrangement and geometry of the pores. More sophisticated spectral simulation methods must be developed to take into account (i) the connectivity of the different adsorption sites and pores, (ii) adsorption thermodynamics, and (iii) the dependence of the NICS on the local carbon structure. The development of lattice simulation methods is ongoing here,¹⁶⁴ whereby a lattice grid is used to represent realistic carbon structures, with the free energies and chemical shifts of the different sites obtained by MD and DFT calculations. The first results have highlighted how the lineshapes observed for ions diffusing between pores in a carbon particle are sensitive to the spatial arrangement of the pores.¹⁶⁴ When combined with experiments, these simulations should allow an understanding of the effects of the carbon and electrolyte structures on ion dynamics.

Chapter 8

In situ NMR Studies of Supercapacitors

8.1 Context and Scope

Recent applications of molecular modelling and the development of new characterisation methods have greatly enhanced our understanding of how supercapacitors work (see Chapter 2). Together these approaches have revealed that processes such as ion adsorption and ion exchange can both contribute to supercapacitor charging. However, a full quantification of the charging mechanism remains illusive, and more advanced characterisation methods must be developed to give detailed insights into the molecular mechanisms of the supercapacitance phenomenon.

A number of studies have recently highlighted the development of NMR spectroscopy as a new tool to study supercapacitor charging mechanisms.^{17,18,93} Most of these studies have been carried out *ex situ*, with the disassembly of charged supercapacitor devices and the subsequent characterisation of the electrodes by NMR.^{18,93,145} These experiments can benefit from the resolution enhancements of magic angle spinning, and have revealed changes of the in-pore ion populations during charging, as well as changes of the in-pore chemical shifts (as demonstrated in Chapter 6 for ionic liquid-based supercapacitors). However, the *ex situ* approach is limited to the study of equilibrium states and there are concerns that electrolyte evaporation during cell disassembly could affect the composition of the carbon pores when volatile solvents such as acetonitrile are used. In principle, the *in situ* NMR approach has many advantages including: (i) spectra are acquired directly on working devices so that any problems associated with cell disassembly are avoided, (ii) dynamic processes and non-equilibrium states can be probed, and (iii) it is time efficient as a single supercapacitor

cell is studied.¹²⁵ However, in these measurements static samples must be studied which can reduce spectral resolution compared to *ex situ* experiments. The *in situ* approach was recently applied to supercapacitors for the first time by Wang *et al.*¹⁷ ¹¹B NMR experiments were used to probe the behaviour of BF₄⁻ anions as bag cell supercapacitors (activated carbon electrodes, and NEt₄BF₄/ACN electrolyte) were charged to different voltages. It was shown that the adsorption processes occurring at each electrode could be studied separately by introducing a long supercapacitor design where the electrodes were shifted laterally from one another. However, the electrochemical properties of the long supercapacitor cell were not fully explored, and while clear changes in both the local environments and populations of the adsorbed anions were observed, the links between these and the supercapacitor charging mechanism were not studied in detail.

The main aim of this chapter is to further develop the *in situ* NMR approach for the study of supercapacitors, such that quantitative-level information about the charging mechanism can be obtained. The *in situ* methodology is first optimised by investigating the electrochemical performance of supercapacitors with different designs, as well as the effects of sample orientation on the NMR spectra. *In situ* ¹⁹F NMR spectra are then presented for a YP50F supercapacitor with the organic electrolyte NEt₄BF₄/ACN (1.5 M), with the variations of the in-pore BF₄⁻ peak intensity allowing the migration of the anions to be probed and different charging regimes to be identified. Experiments with simultaneous electrochemical cycling then show a continuous variation of the in-pore chemical shift that is correlated to the charge state of the carbon. In a follow up study, ³¹P and ¹⁹F NMR experiments on a new PEt₄BF₄/ACN electrolyte allow the study of both the cations and the anions offering a more complete quantification of the charge storage mechanism. Here, charging is shown to proceed by ion exchange in the positive electrode, and by ion adsorption in the negative electrode. Finally, the application of the *in situ* NMR technique to TiC-CDC electrode materials is discussed, with the first results suggesting that differences between carbon structures can have an effect on the charging mechanism that operates.

8.2 Experimental Details

8.2.1 Materials

YP50F (Kuraray, Japan) and TiC-CDC-1000 carbon films were used as electrodes (see Section 4.2.1 for details of synthesis of TiC-CDC-1000, and the film preparation method). In initial electrochemical tests of different cell designs, the electrolyte used

was 1.5 M NEt₄BF₄/ACN (see Section 4.2.2). The same electrolyte was used for *in situ* NMR experiments, except that the solvent was replaced by deuterated acetonitrile, D₃CCN (Euriso-top, 99.96 %), the resulting electrolyte is referred to as NEt₄BF₄/dACN. A second electrolyte used for *in situ* NMR experiments was 1.5 M tetraethylphosphonium tetrafluoroborate (Tokyo Chemical Industries, >98 %) in acetonitrile, referred to as PEt₄BF₄/ACN.

8.2.2 Sample preparation

All sample preparation was carried out in an argon glovebox. Model electrodes were prepared for preliminary (and calibration) experiments by hermetically sealing a carbon film piece inside a plastic bag (3M packaging film) with the chosen volume of NEt₄BF₄/dACN electrolyte, which was added using a microsyringe. Samples for experiments on the different cell components (current collector, separator) were prepared in a similar fashion.

Supercapacitors were made in plastic bags. Two pieces of carbon film were adhered to carbon-coated aluminium mesh, and a Cellgard 2500 (monolayer polypropylene, 25 µm thickness) separator was placed between them. These components were placed inside a plastic bag, which was hermetically sealed on three sides. The cell was then saturated with electrolyte before a final seal was made to close the bag. For NMR measurements, the supercapacitor bag cells were held between two plastic inserts in order to provide rigidity and to allow better control over the cell orientation inside the NMR coil.

8.2.3 Electrochemistry

All cells were tested on a Bio-logic cycler or an Arbin Instruments battery cycler with a two-electrode configuration. Cyclic voltammetry was used both to test the performance of different cells and to run *in situ* NMR experiments with simultaneous electrochemical cycling. Fixed voltage *in situ* NMR experiments were performed using chronoamperometry experiments (see Section 2.2.3), whereby a fixed cell voltage was applied to the cell and the decay of the current towards 0 A was measured. Sufficient time (typically on the order of 40 min) was allowed for equilibration of the cell before acquiring *in situ* NMR data.

8.2.4 NMR details

All NMR experiments were performed using a Bruker Avance spectrometer operating at a magnetic field strength of 7.1 T, corresponding to a ¹⁹F Larmor frequency of 284.2 MHz, with a Bruker HX double resonance static probe using a 6.8 mm inner diameter

solenoid coil. ^{19}F NMR spectra were referenced relative to neat hexafluorobenzene (C_6F_6) at -164.9 ppm, while ^{31}P spectra were referenced to 85 wt. % H_3PO_4 (aq.) at 0 ppm. The “depth” pulse sequence¹⁰⁴ was used to acquire all *in situ* NMR spectra in order to reduce the background signals (*e.g.*, from the PTFE parts in the probe). The total delay between excitation and detection of the signal was 60 μs in all experiments, except for those on the YP50F/PEt₄BF₄ system, where this delay was 90 μs . Spectral fitting was carried out using dmfit software.¹³⁷ In each case a single peak was used for the in-pore environment, while at least three resonances were typically needed to fit the ex-pore/free electrolyte features due to the different features arising from BMS shifts. For each electrode, the spectrum obtained at 0 V was fitted first, as this showed the best resolution of the in-pore resonance. The obtained peak positions and intensities were then used as a starting point to fit the spectrum at the next highest voltage.

8.2.5 *In situ* NMR experiments

Bag cell supercapacitors were positioned inside the solenoid coil, with electrochemistry cables running down the bore of the magnet (from the top) to the cell where they were connected to the current collectors. Slightly different procedures were employed for experiments on the NEt₄BF₄ and PEt₄BF₄ cells. For the YP50F/NEt₄BF₄ system, the cell was cycled between 0 and 2.3 V five times by cyclic voltammetry at a sweep rate of 0.5 $\text{mV}\cdot\text{s}^{-1}$, prior to performing NMR experiments. The positively charged electrode was first positioned inside the coil for detection, and afterwards the cell was physically shifted to position the negatively charged electrode inside the NMR detection region. For the PEt₄BF₄ cells, no electrochemical cycling was carried out before the *in situ* NMR measurements. Here, the same electrode was also studied in all experiments. The cell was first charged to positive voltages, with the working (positive) electrode situated in the NMR detection region. Afterwards, the cell voltage was then reversed to negative values to allow the study of a negatively charged electrode. In all fixed voltage experiments, recycle delays were adjusted to give quantitative spectra. For experiments with simultaneous cyclic voltammetry, 94 NMR spectra were obtained per full cycle (0 V \rightarrow 2.3 V \rightarrow 0 V) with a recycle interval of 3 s, unless otherwise stated. While this does not yield fully quantitative spectra, it reduces the time required to obtain each spectrum, enabling more spectra to be acquired during each cycle.

8.3 Results and Discussion

8.3.1 Cell designs for *in situ* NMR

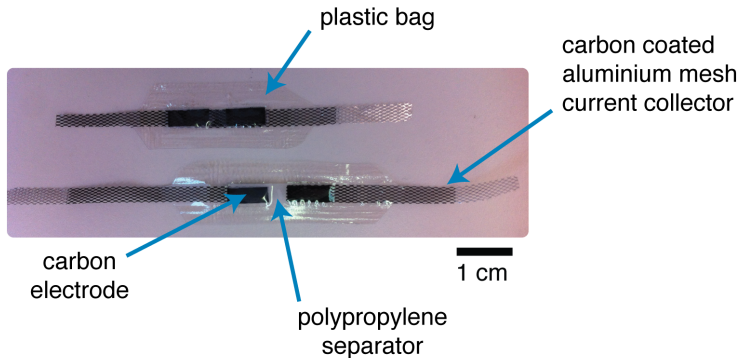


Figure 8.1 Photograph of bag cell supercapacitors; top “overlaid” design, bottom “long” design.

In situ NMR experiments typically use cells sealed inside plastic bags (Figure 8.1), which are transparent to radio frequency pulses, and can be fabricated with the desired shapes and sizes to fit into a solenoid coil used in static NMR probes.¹²⁵ Three different bag cell supercapacitor designs were tested to compare their electrochemical performances. The “conventional” cell design (Figure 8.2a) represents a typical supercapacitor, with the two electrodes situated directly on top of each other. Here, both electrodes must be placed inside the NMR coil during *in situ* NMR experiments, making it difficult to separate processes occurring at each electrode.¹⁷ In the “long” cell design (Figure 8.1, 8.2b), the electrodes are shifted laterally with respect to each other so that a single electrode can be placed in the NMR detection region. In the previous work of Wang *et al.*, this allowed the anion environments to be tracked separately in the positive and negative electrodes, although long times were needed to charge and discharge the device.¹⁷ The “overlaid” cell design introduced here (Figure 8.1, 8.2c) also allows a single electrode to be placed in the NMR detection region, but the current collector of the opposite electrode is situated closer to the electrode under study.

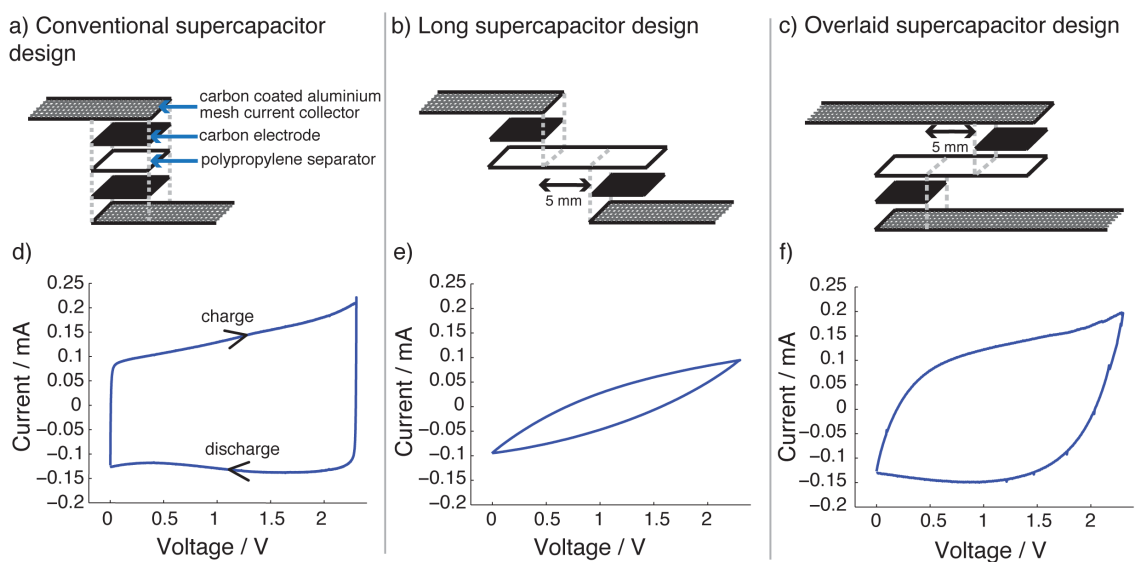


Figure 8.2 Supercapacitor cell designs (a-c) and their cyclic voltammograms at $0.5 \text{ mV}\cdot\text{s}^{-1}$ (d-f). In each case the cyclic voltammogram of the fourth cycle is shown. The overlaid cell design allows each electrode to be studied separately in the NMR experiments while maintaining reasonable electrochemical performance.

Cyclic voltammograms for conventional, long, and overlaid supercapacitors, each cycled at $0.5 \text{ mV}\cdot\text{s}^{-1}$ between 0 and 2.3 V, are shown in parts d, e, and f of Figure 8.2, respectively. Distortion from the rectangular shape arises from resistive contributions (see Section 2.2.1). A characteristic near-rectangular shape is observed for the conventional supercapacitor (Figure 8.2d), whereas the long cell design displays a far from ideal voltammogram (Figure 8.2e), with a plateau indicative of pure capacitive behaviour not observed. However, a considerable improvement is achieved by switching to the overlaid design, where the observed voltammogram is much closer to the ideal case (Figure 8.2f). This is presumably due to the stronger electric field generated for the overlaid cell design. It is also noted that the estimated capacitance of YP50F (calculated from the discharge current at 1 V) is $99 \text{ F}\cdot\text{g}^{-1}$, which is in good agreement with the literature value of $95 \text{ F}\cdot\text{g}^{-1}$.¹⁹³ Importantly, the overlaid design introduced here allows a single electrode to be placed inside the NMR detection region, while maintaining good electrochemical performance. This design was therefore used for all *in situ* NMR experiments that follow here.

8.3.2 Effects of sample orientation and supercapacitor components on spectral resolution

Prior to carrying out NMR experiments on working supercapacitor devices, control experiments were performed to systematically investigate the resonances that arise from electrolyte confined in the various cell components (Figure 8.3). Samples were prepared

by injecting NEt_4BF_4 /dACN (1.5 M) electrolyte onto the different cell components (a model carbon electrode, a piece of current collector and a piece of separator, approximate dimensions 4×8 mm) and sealing them inside plastic bags. NMR experiments were then carried out in a static NMR probe with a solenoid coil, whereby the samples were studied in two different orientations; “vertical” and “horizontal” which refer to the orientation of the short edge of the rectangular-shaped samples relative to the applied magnetic field (see Figure 8.3).

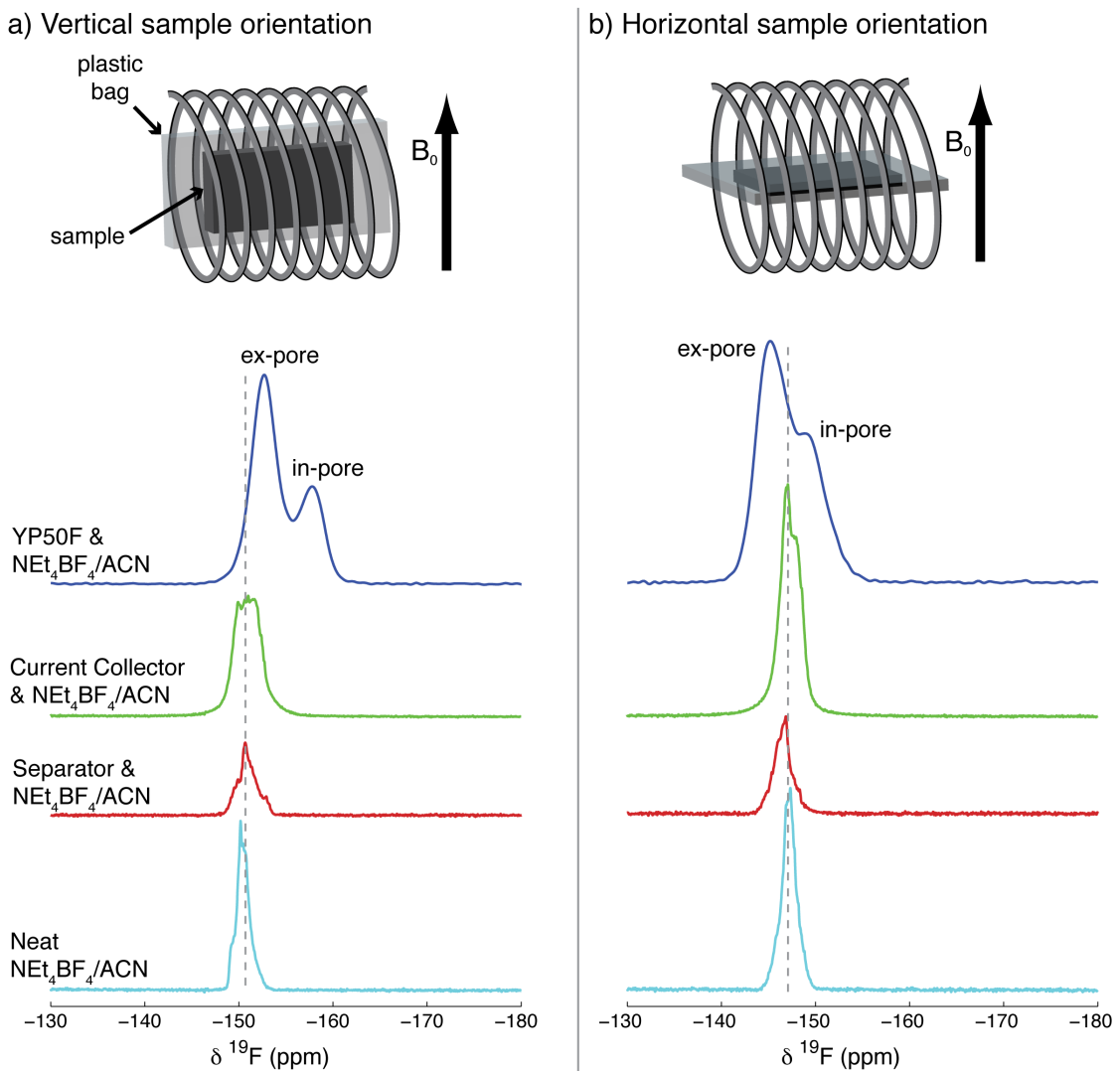


Figure 8.3 Static NMR (7.1 T) experiments carried out on supercapacitor cell components soaked with electrolyte. Experiments were carried out for two different sample orientations; (a) vertical and (b) horizontal.

In the vertical orientation, in- and ex-pore resonances can be observed for the BF_4^- anions in the model electrode sample, as expected (Figure 8.3a). The respective chemical shifts, -157.6 and -152.6 ppm, differ from those observed in experiments on carbons packed inside rotors oriented at the magic angle (-155.1 and -149.8 ppm, see

Chapter 4). For samples of electrolyte-soaked current collector and separator, features are observed at \sim 151 ppm, similar to the spectrum observed for neat electrolyte sealed inside a plastic bag. Importantly, the introduction of these additional components does not cause any additional shifts that could complicate the NMR spectrum of a supercapacitor cell. The different in- and ex-pore chemical shifts observed for the model carbon electrode here, compared to those for a sample oriented at the magic angle (Chapter 4), arise from BMS effects associated with the highly anisotropic shape (near planar) of the samples studied here. These effects are also the cause of the several small sharp features that can be observed for electrolyte in different regions of the current collector, separator and neat electrolyte samples. Such BMS effects have been shown to be significant in previous studies of lithium-ion battery electrodes,^{146,147} and biological membranes confined between rectangular glass slides.^{98,101}

Experiments carried out with the samples in the horizontal orientation allow a further investigation of the BMS effects (Figure 8.3b). For the model carbon electrode, the in-pore resonance is no longer well resolved and appears as a shoulder at \sim 149.4 ppm, with the ex-pore resonance at $-$ 145.3 ppm. Both of these resonances appear at higher frequency than in the spectrum recorded in the horizontal orientation (\sim 8 ppm higher for the in-pore, and \sim 7 ppm for the ex-pore), highlighting the effect of the sample orientation on the BMS effects here. The current collector, separator and neat electrolyte samples also display resonances that are shifted relative to the spectra recorded in the horizontal orientation, with resonances at \sim 147 ppm (with a \sim 4 ppm shift from the horizontal orientation). These resonances now fall at an intermediate position between the in- and ex-pore resonances, and will reduce in-pore – ex-pore resolution for spectra acquired on working supercapacitors. This is in contrast to the vertical orientation where these resonances appear at higher frequency than both the in- and ex-pore resonances. In light of this, the vertical orientation was chosen for all further NMR experiments, as this allows the best resolution of the in-pore resonance.

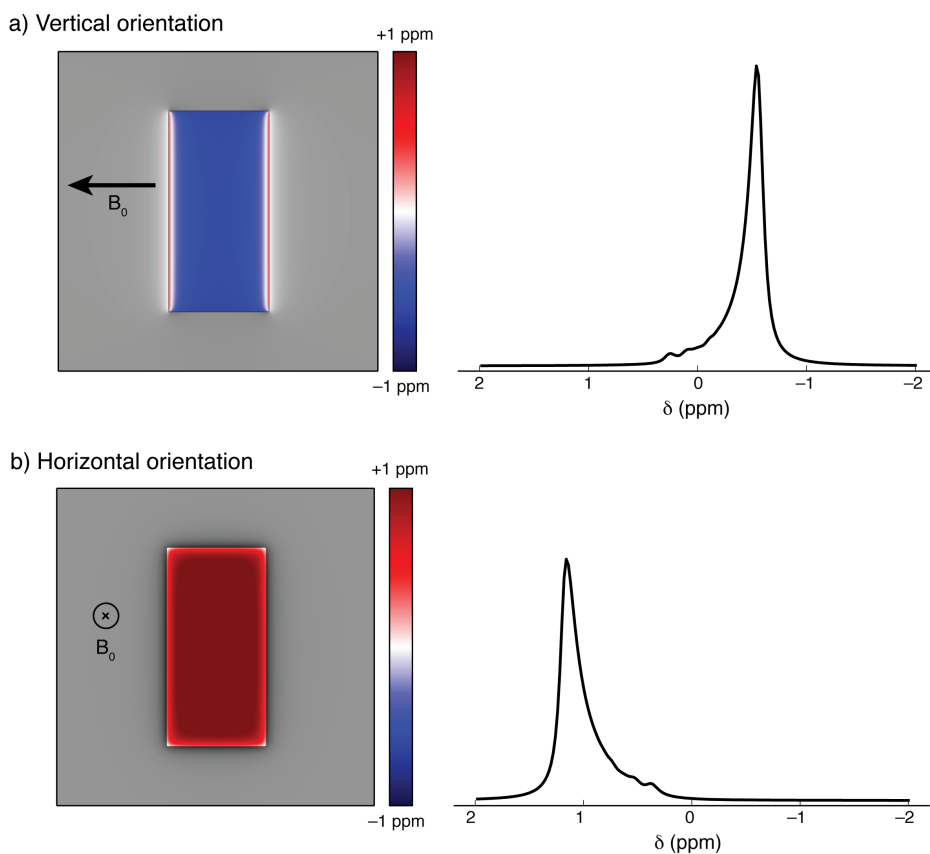


Figure 8.4 Calculations of the magnetic field inhomogeneity arising from BMS effects for a homogeneous cuboid of dimensions 1:10:20 and with a diamagnetic susceptibility of -2 ppm (corresponding to an SI volume susceptibility of $-2 \cdot 10^{-6}$). (a) Vertical orientation, and (b) horizontal orientation.

Calculations of the inhomogeneous broadening for a model diamagnetic electrode are shown in Figure 8.4, and help to visualise and explain the BMS effects observed in Figure 8.3. Calculations were performed by Dr. Andrew Ilott using the approach of Salomir *et al.*⁹⁹ The calculated spectra show qualitative agreement with the effects observed experimentally, with a change of shift of the main resonance of $\sim 1.5 \text{ ppm}$ observed upon sample rotation, on the order of the magnitude of the susceptibility value (2 ppm) used in the calculation. This suggests that the diamagnetic susceptibility of the electrolyte-soaked YP50F carbon studied above (Figure 8.3) is on the order of $\sim 10 \text{ ppm}$, which is in qualitative agreement with measurements on similar porous carbons,¹⁴³ while the susceptibility is smaller for the neat electrolyte, as expected.

8.3.3 NMR spectrum of a supercapacitor at 0 V

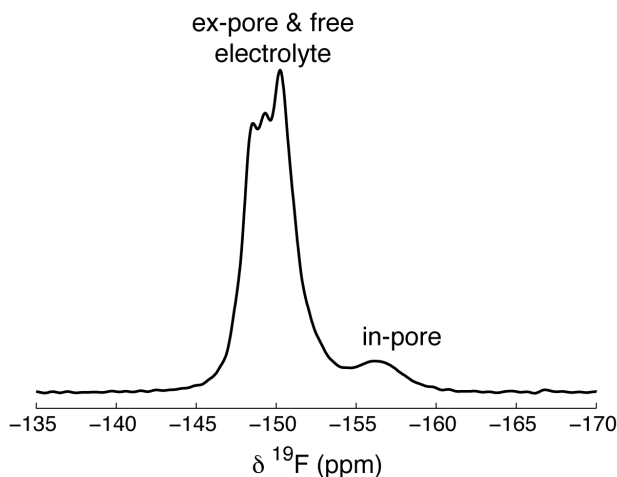


Figure 8.5 ${}^{19}\text{F}$ NMR spectrum of an overlaid supercapacitor cell (YP50F, 1.5 M NEt_4BF_4 /dACN) in the vertical orientation, with a cell voltage of 0 V. The in-pore BF_4^- resonance can be observed, despite the presence of a large amount of free electrolyte in the cell.

Figure 8.5 shows the NMR spectrum of an overlaid supercapacitor cell held at a cell voltage of 0 V, with a single electrode placed inside the NMR detection region, and with the cell in the vertical orientation. The in-pore anion resonance can be observed here, appearing at -156.2 ppm, as well as several more intense features arising from the large amount of ex-pore electrolyte and free electrolyte external to the carbon electrode. The ex-pore/free electrolyte signal appears to comprise at least three superimposed components, which is attributed to BMS effects owing to the irregular shape of the sample, indeed, similar features were observed above for neat electrolyte sealed inside a plastic bag (Figure 8.3). The in-pore resonance is shifted to higher frequency by approximately 1.4 ppm relative to its position in the spectrum for the model carbon electrode above (Figure 8.3a). This discrepancy is likely due to small differences in the BMS effects arising from the supercapacitor cell, possibly due to its imperfect alignment and orientation in the NMR coil. Importantly, despite the intense features arising from the large amount of free electrolyte in the plastic bag cell, the spectrum shows that the in-pore resonance can be resolved for an overlaid supercapacitor at zero potential. Thus, with this cell design and orientation, changes in the anion environments may be tracked as a function of applied potential. It is noted that the in-pore resolution here is improved compared to previous experiments where the horizontal orientation was used.¹⁷

8.3.4 In situ ^{19}F NMR spectroscopy at fixed voltages

a) Positive electrode studied

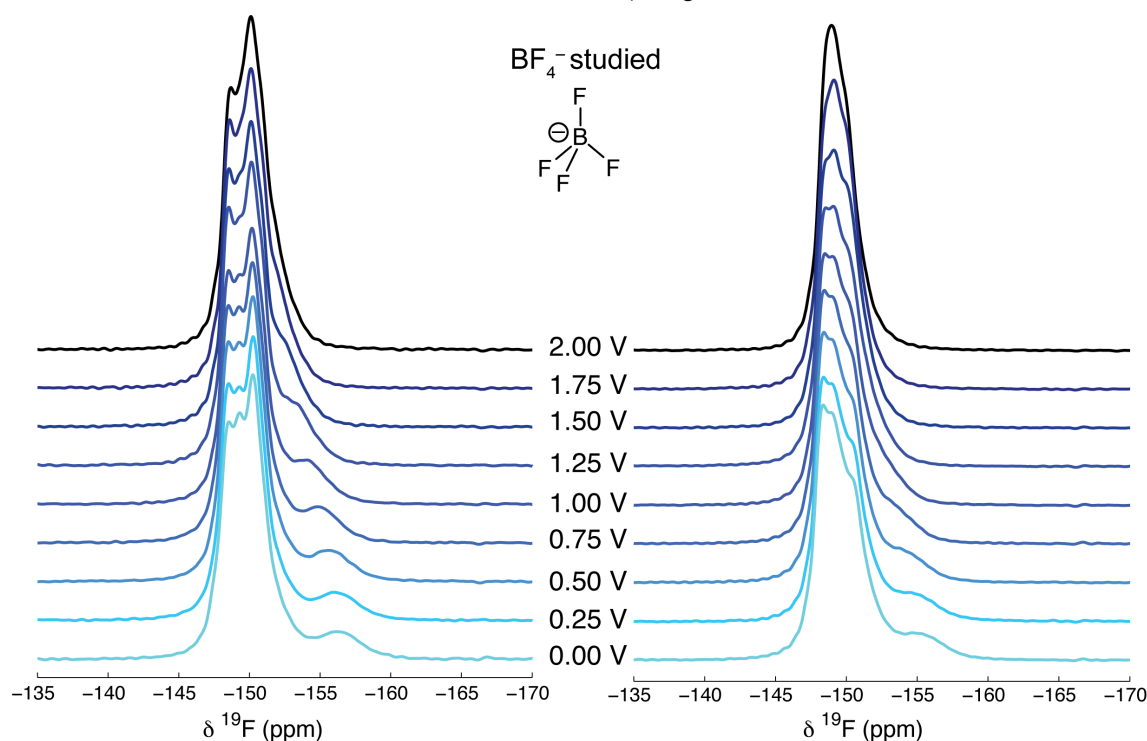


Figure 8.6 ^{19}F NMR (7.1 T) spectra of an overlaid supercapacitor cell (YP50F, 1.5 M NEt_4BF_4 /dACN); (a) positively charged electrode, and (b) negatively charged electrode. Changes of the in-pore chemical shift and intensity are seen during charging.

To investigate changes of the BF_4^- anion environments as a function of applied potential, ^{19}F NMR spectra of a single supercapacitor electrode were acquired while the cell was held at different voltages. For the positive electrode (Figure 8.6a) the in-pore feature shows gradual increases in resonance frequency with the cell voltage, while the ex-pore/free electrolyte features do not display significant changes in resonance frequency. The in-pore feature also appears to show changes in intensity with voltage. After the positive electrode was studied, the supercapacitor cell was physically shifted so that the negatively charged electrode was situated in the NMR detection region, and the ^{19}F NMR spectra at various applied cell voltages are shown in Figure 8.6b. At 0 V, a spectrum similar to that in Figure 8.6a is observed, with the in-pore feature visible at -154.9 ppm. This feature is approximately 1.5 ppm higher in frequency than what was observed for the positive electrode at 0 V. This is most probably due to BMS effects, since different electrodes (with slightly different sizes and orientations relative to the applied magnetic field) are investigated. As the voltage is increased from 0 to 2 V, the in-pore feature shifts to higher frequency, as was observed in the positive electrode. However, here changes in the intensity of the in-pore feature appear to be less

pronounced. It is noted that while ^1H NMR is an attractive option to study the NEt_4^+ cations in this system, the large number of plastic components used in the bag cell results in a broad and intense background ^1H signal that precludes the observation of the relatively low intensity electrolyte resonances.

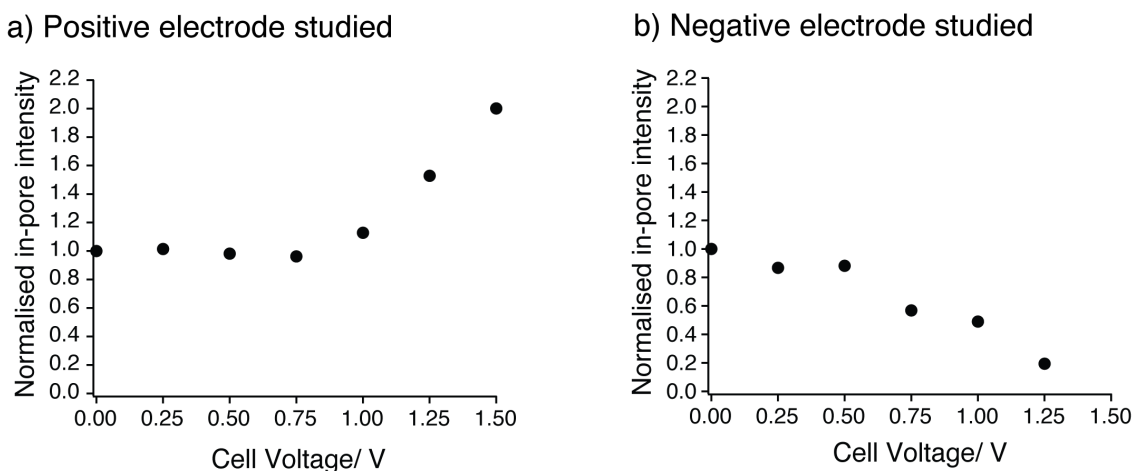


Figure 8.7 In-pore anion intensities obtained from fits of the data in Figure 8.6, for (a) the positive electrode, and (b) the negative electrode. Intensities are normalised to the values at 0 V. While gradual decreases of in-pore intensity are observed in the negative electrode, there appears to be two regimes with different behaviour in the positive electrode.

To aid with the interpretation of the results shown in Figure 8.6, spectra were fitted to quantify the position and intensity of the in-pore resonance at each voltage. Spectral fits were carried out by Dr. Hao Wang (University of Cambridge), with details given in Section 8.2.4. Good fits could not be obtained for spectra acquired above 1.5 V (positive electrode) and 1.25 V (negative electrode), due to the significant overlap of the resonances. Figure 8.7 shows the fitted intensities of the in-pore resonance for the positive and negative electrodes, which in each case are normalised to the intensity measured for each electrode at 0 V. For the positive electrode, at cell potentials between 0 and 0.75 V, the intensity of the in-pore resonance does not change significantly. However, between 0.75 and 1.5 V a relatively sharp increase in intensity is observed. For the negative electrode, the intensity of the in-pore resonance appears to decrease steadily over the studied voltage range.

The quantification of in-pore anions offers insight into the charge storage mechanism of the system. For the positive electrode, two distinct charging regimes can be identified. At voltages lower than 0.75 V, the almost constant intensity of the in-pore feature indicates that the charge storage process does not involve significant changes in the number of in-pore anions. This suggests that the mechanism of charge storage in this

low-voltage regime is dominated by the ejection of NEt₄ cations from the carbon micropores. At voltages above 0.75 V, the abrupt increase in intensity of the in-pore feature shows that BF₄ anions migrate into the micropores and that the anions play a more significant role in the charge storage process in this regime. For the negative electrode, the intensity of the in-pore feature decreases steadily with voltage. In principle, the loss of BF₄ anions from the micropores should leave an excess of cations within the micropores to counteract the negative charge developed in the electrode.

The observation of different charge storage mechanisms depending on the cell voltage shows some qualitative agreement with findings from EQCM measurements on similar systems to those studied here. A study of an activated carbon with NEt₄BF₄/propylene carbonate (0.1 M) electrolyte, showed that for small charge densities, anion-cation mixing (exchange) occurred within the carbon micropores, with co-ion ejection playing a significant role in the charge storage process.⁸⁴ At higher charge densities, the charging mechanism was then dominated by counter-ion adsorption. A more recent EQCM study on CDC electrodes with EMITFSI/ACN (2 M) electrolyte revealed similar effects in the positive electrode.⁸⁵ The observation of an apparent “threshold” voltage of 0.75 V, whereby an abrupt increase in the in-pore resonance intensity is observed, may be related to the different charging regimes identified by EQCM experiments.

Interestingly, the charge storage mechanism elucidated here differs from that observed with Pyr₁₃TFSI ionic liquid and the same activated carbon in the *ex situ* NMR measurements in Chapter 6. This suggests that the exact nature of the ions studied affects the charge storage mechanism that operates. Factors such as the ion size/shape, the electronic structure of the ions, and differences in the ion-carbon interactions may dictate which charge storage mechanism operates here. More theoretical work must be done to investigate these effects.

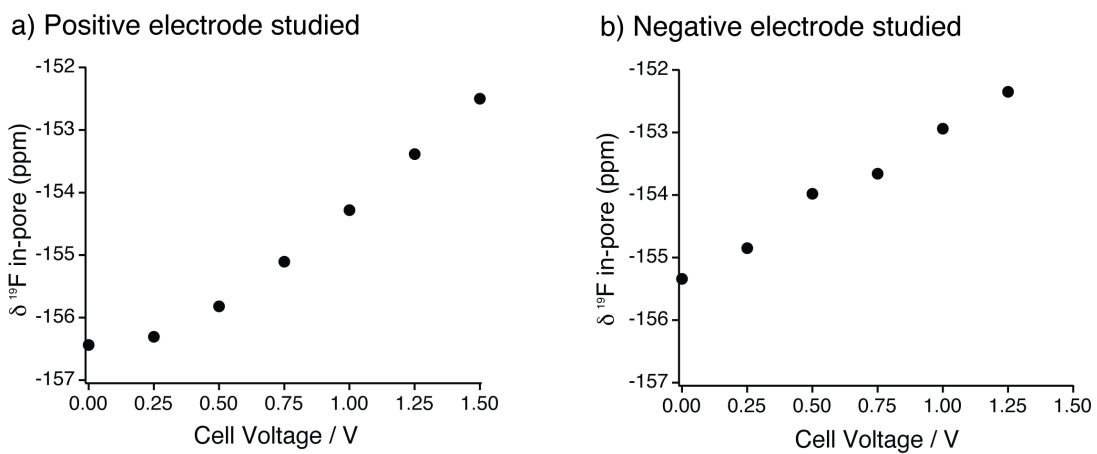


Figure 8.8 In-pore chemical shifts obtained from fits of the data in Figure 8.6, for (a) the positive electrode, and (b) the negative electrode. Increases in the chemical shift are observed in both electrodes.

Clear increases in chemical shift are observed with voltage for the in-pore anions in both electrodes (Figure 8.8). In the positive electrode, only a small increase is observed between 0 and 0.5 V, with larger, approximately linear, increases observed at higher voltages (Figure 8.8a). As the cell voltage is increased from 0 to 1.5 V, a total increase in chemical shift of 3.9 ppm is measured. At voltages above 1.5 V, the in-pore resonance appears to shift to higher frequencies still (Figure 8.6a), although this prevents reliable fitting of the spectra because of increased overlap of spectral features. In the negative electrode the chemical shift of the in-pore resonance appears to vary in a linear fashion for the entirety of the studied voltage range (Figure 8.8b). As the voltage is increased from 0 to 1.25 V, the chemical shift increases from -155.3 to -152.4 ppm, representing a total increase of 2.9 ppm. Similar chemical shifts were observed in the first ^{11}B *in situ* NMR studies of a very similar activated carbon supercapacitor,¹⁷ though the changes were not quantified in that study.

The chemical shift variations with voltage reported here are very similar to those reported in Chapter 6 for *ex situ* NMR measurements on the same activated carbon with Pyr₁₃TFSI ionic liquid electrolyte. For example, in the positive electrode, the in-pore chemical shift change for TFSI anions was +3.6 ppm on charging from 0 to 1.5 V, compared to +3.9 ppm for the positive electrode for BF₄⁻ anions here over the same voltage range. In the negative electrode, for TFSI the in-pore shift increased by 2.7 ppm on charging from 0 to 1.25 V, again very similar to the increase observed for BF₄⁻ here of 2.9 ppm. The deviation from linearity was also observed in both studies for the positive electrode for cell voltage changes between 0 and 0.5 V. The findings of very similar shift variations for two drastically different electrolytes (Pyr₁₃TFSI ionic liquid

and 1.5 M NEt₄BF₄/dACN) further corroborate the idea that the in-pore chemical shift changes arise from changes of the carbon electronic structure that occur during charging (Chapter 6).

8.3.5 *In situ* NMR spectroscopy with dynamic cycling

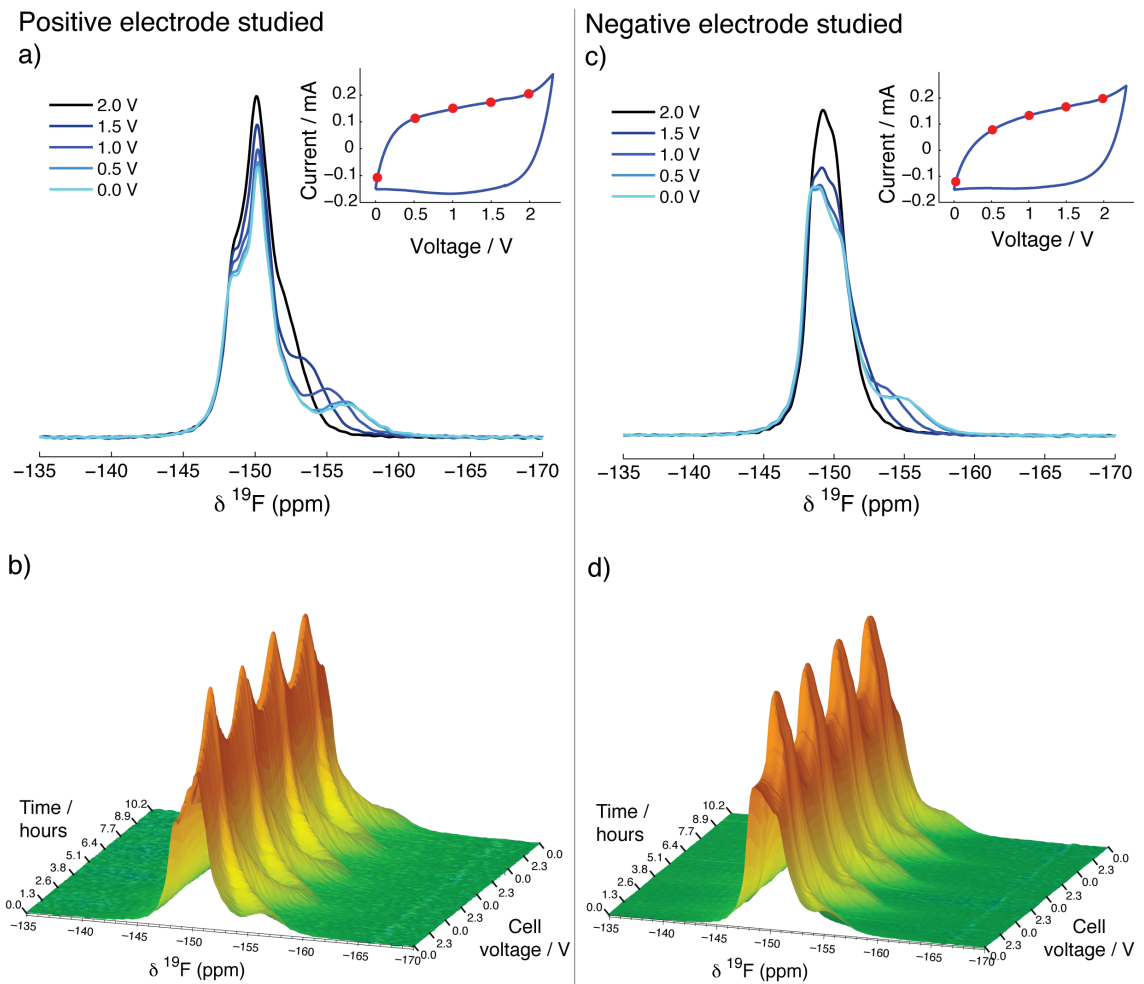


Figure 8.9 (a) Selected ¹⁹F NMR spectra of the positive electrode of an overlaid supercapacitor cycled by cyclic voltammetry. Spectra are extracted from the charge during the second cycle. (b) Successive NMR spectra from four full cycles are shown back to back. (c, d) Analogous results for the negative electrode of the supercapacitor cell are shown. The results show that the variation of the in-pore chemical shift with voltage is highly periodic.

With the improved electrochemical response of the overlaid cell design, it is possible to record *in situ* NMR spectra for an overlaid supercapacitor undergoing simultaneous cyclic voltammetry. ¹⁹F NMR spectra were collected while a cell was cycled between 0 and 2.3 V at a rate of 0.5 mV·s⁻¹, with spectra acquired for four full electrochemical cycles. Since the cell voltage is changed continuously, small changes of ~0.05 V occur during the acquisition of one NMR spectrum. Since this change is small (~2 %)

compared to the full cycling window of 2.3 V, the voltage may be approximated to be constant during the acquisition of one NMR spectrum. Figure 8.9a shows selected ^{19}F NMR spectra of the positive electrode extracted at different points from the cyclic voltammogram of the second cycle, shown as an inset. Spectra corresponding to voltages of 0, 0.5, 1, 1.5, and 2 V are shown. The spectrum acquired at 0 V shows a form very similar to the spectrum of the positive electrode for a fixed (static) voltage of 0 V shown in Figure 8.5, with the in-pore resonance observed at -156.3 ppm. For spectra obtained at later stages in the charging cycle, the in-pore feature is observed to shift to higher frequencies, in good agreement with the fixed voltage behaviour shown in Figure 8.6a. The NMR spectra shown in Figure 8.9a represent a small selection of the total acquired NMR data. In Figure 8.9b, NMR spectra for all four electrochemical cycles are shown in a three-dimensional plot. This plot reveals a highly periodic variation of the in-pore resonance, the frequency of which varies in almost perfect correlation with the applied voltage. NMR spectra of the negative electrode (Figure 8.9c) again resemble those acquired at fixed voltages (Figure 8.6b). In Figure 8.9d, the periodic shifting of the in-pore resonance is observed, as in the positive electrode.

Further insight into this phenomenon can be obtained by comparing *in situ* NMR spectra acquired at different electrochemical cycling rates. At the relatively slow rate of $0.5 \text{ mV}\cdot\text{s}^{-1}$ (Figure 8.10a), the variation of the in-pore chemical shift (seen to the right-hand side of the contour plot) is well synchronized with the applied voltage. Moreover, a capacitive electrochemical signature with a near rectangular cyclic voltammogram is observed. However, when the cycling rate is increased to $5 \text{ mV}\cdot\text{s}^{-1}$ (Figure 8.10b), a considerable lag between the periodic variation of the in-pore chemical shift and the applied voltage is observed. Indeed, close inspection of the spectra (see inset) shows that between voltages of 0.64 V on charge and 1.66 V on the following discharge, the shift of the in-pore resonance is found to increase. On the other hand, between voltages of 1.66 V on discharge and 0.64 V on the next charge cycle, the shift of the in-pore resonance decreases. This differs from the behaviour observed at the lower cycling rate of $0.5 \text{ mV}\cdot\text{s}^{-1}$, where the shift of the in-pore resonance does not show significant lags behind the applied voltage. Inspection of the electrochemistry helps explain this behaviour. At the faster cycling rate of $5 \text{ mV}\cdot\text{s}^{-1}$, the cyclic voltammogram is far from ideal, with a non-rectangular shape observed. Importantly, positive currents flow between 0.67 V on the charge and 1.64 V on the next discharge, and during this time the magnitude of the charge stored in each electrode increases. However, between voltages of 1.64 V on discharge and 0.67 V on the next charge, a negative current flows and the

magnitude of the charge stored in each electrode decreases. The voltages at which the direction of the current reverses agree well with the voltages at which the direction of the in-pore shift variation reverses in the NMR spectra. This confirms that the changes of the in-pore shift are directly correlated with the magnitude of the charge stored in the electrodes and not the potential difference applied to the cell. Overall, the *in situ* NMR spectra obtained with simultaneous cycling further support the ideas developed in Chapter 6, that the in-pore chemical shift arises from changes of the electronic structure of the carbon during charging, which modify the carbon ring current effects. In principle, in-pore intensities could also be extracted from these experiments to investigate the charging mechanism, though here the recycle delay used in the experiments was insufficient for complete longitudinal relaxation of the spins, preventing quantification.

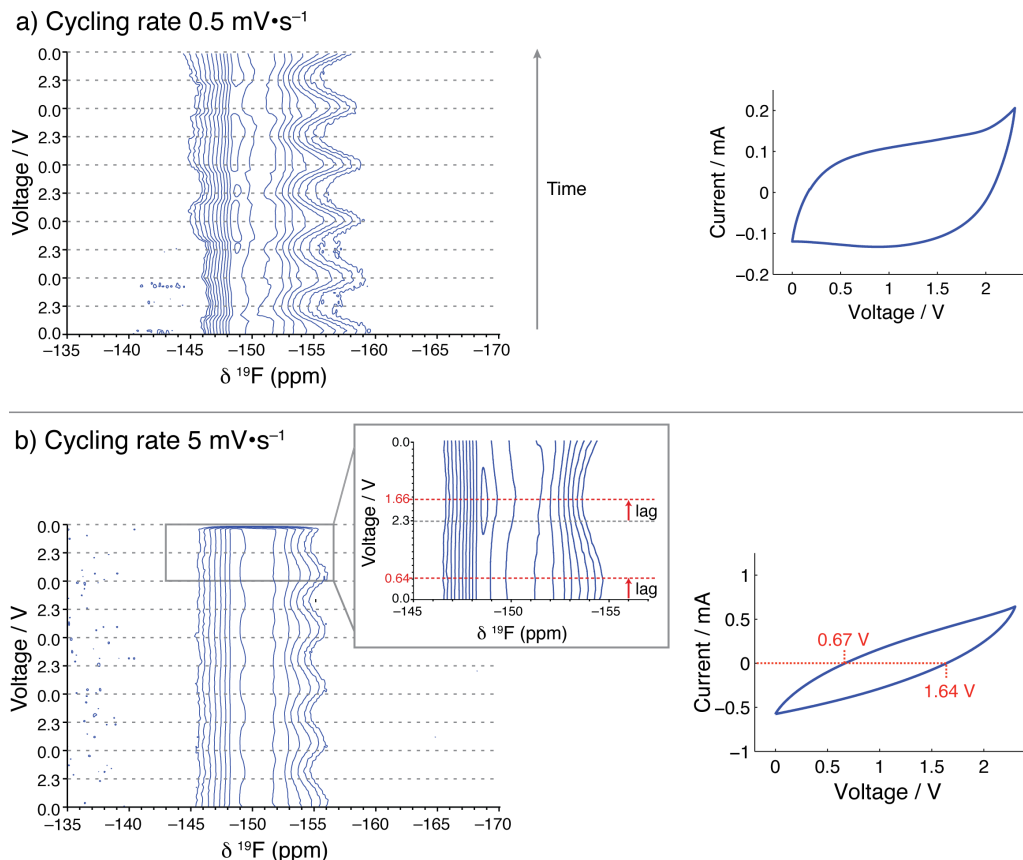


Figure 8.10 Contour plots of successive *in situ* ^{19}F NMR spectra of the negative electrode of an overlaid supercapacitor cell with simultaneous electrochemical cycling. Representative cyclic voltammograms are shown beside the spectra. Data is shown for cycling rates of (a) $0.5 \text{ mV}\cdot\text{s}^{-1}$ and (b) $5 \text{ mV}\cdot\text{s}^{-1}$. In part (b), enlarged spectra are shown for the fifth cycle as an inset. For each two-dimensional spectrum, 18 slices were recorded per charging cycle, with recycle delays of (a) 30 s and (b) 3 s.

8.3.6 Further studies of the charging mechanism

Spectra presented in this chapter so far have focussed on the BF_4^- anions (^{19}F NMR), as ^1H NMR studies of the NEt_4^+ cations are complicated by large background signals arising from the plastic components of the bag cells. In principle, ^{15}N NMR experiments ($I = \frac{1}{2}$) could be carried out, but the low natural abundance and low gyromagnetic ratio of this nucleus make measurements impractical without isotopic enrichment. A much more feasible strategy is to replace the cation with one that has more favourable NMR nuclei. In a follow on study, the NEt_4BF_4 electrolyte salt was swapped with PEt_4BF_4 to allow ^{31}P NMR ($I = \frac{1}{2}$) studies of the cation environments. Sample preparation, NMR experiments and data analysis were all carried out by Dr. John Griffin (University of Cambridge), with some of the main results discussed here.

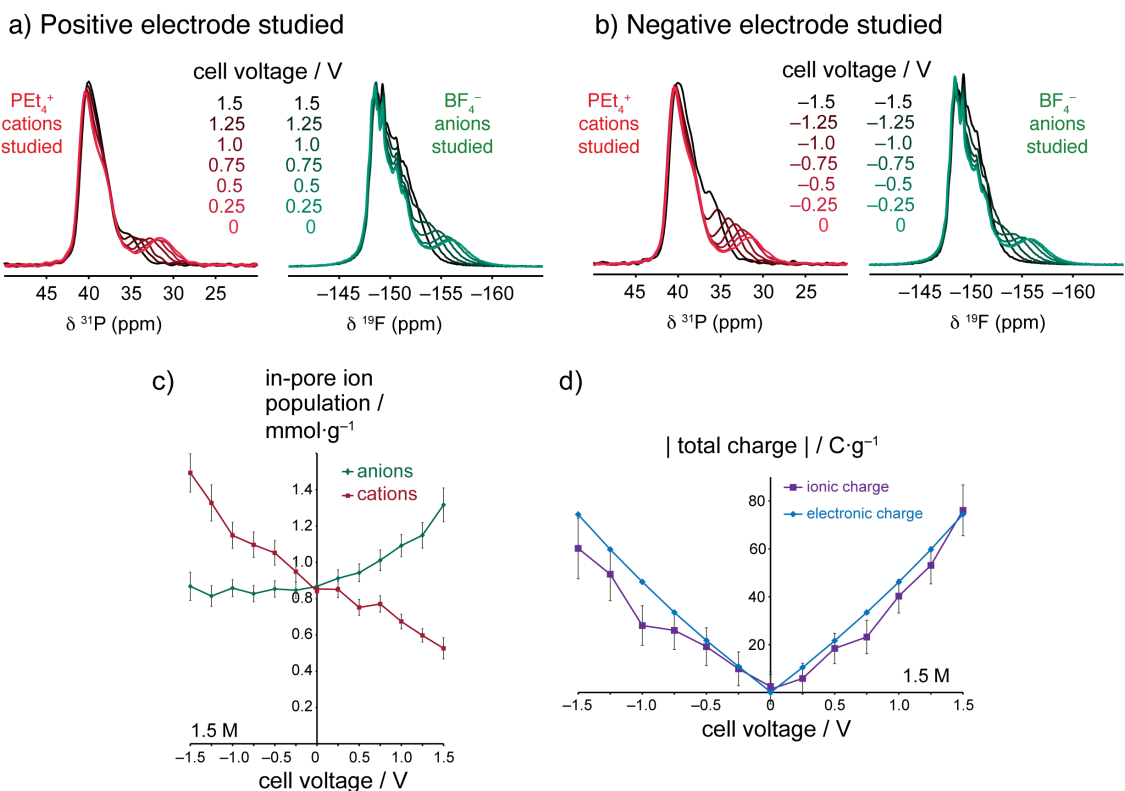


Figure 8.11 ^{19}F and ^{31}P *in situ* NMR spectra acquired on a YP50F supercapacitor with $\text{PEt}_4\text{BF}_4/\text{ACN}$ (1.5 M) electrolyte, for (a) positive electrode polarisations, (b) negative electrode polarisations. (c) In-pore ion populations for the different electrode polarisations, positive cell voltages correspond to experiments in which the positive electrode was studied, while for negative cell voltages the negative electrode was studied. (d) Magnitudes of the in-pore ionic charge, from the data in (c), and the electronic charge, obtained from electrochemical data. Different charging mechanisms operate in the two electrodes, but in both cases the in-pore ionic charge is balanced by the electronic charge of the carbon.

Figure 8.11 shows ^{19}F and ^{31}P *in situ* NMR spectra of an overlaid YP50F supercapacitor with $\text{PEt}_4\text{BF}_4/\text{ACN}$ (1.5 M) electrolyte at different fixed applied voltages, with the

NMR spectra qualitatively similar to those presented above for the NEt_4BF_4 system (Figure 8.6). The in-pore resonances again shift to higher frequencies during charging, with changes of intensity also observed. Fits of the in-pore resonance intensity were compared with calibration samples to obtain an absolute quantification of the in-pore population at each cell voltage (Figure 8.11c). In the positive electrode, charging takes place by the simultaneous adsorption of anions and desorption of cations, representing an ion exchange process. In the negative electrode on the other hand, the anion population remains approximately constant during charging, with adsorption of the cations then dominating the charge storage mechanism. In both electrodes the excess ionic charge developed in the carbon pores is balanced by the electronic charge stored in the carbon (Figure 8.11d), obtained by integrating the current response measured during the constant voltage measurements.

The finding of such different charging mechanisms in the positive and negative electrodes further suggests that differences in the interactions between the charged carbon surfaces and the ions may dictate which mechanism operates. The charge storage mechanism elucidated here should also be contrasted to that observed above for the $\text{NEt}_4\text{BF}_4/\text{YP50F}$ system, where anion desorption processes were observed in the negative electrode, and a ‘jump’ in the in-pore anion population was observed above 0.75 V in the positive electrode. This suggests that even a change of the electrolyte as subtle as NEt_4^+ to PEt_4^+ can affect the charge storage mechanism. However, it should also be noted that the cell studied here was not cycled by cyclic voltammetry prior to carrying out NMR measurements (in contrast to the $\text{NEt}_4\text{BF}_4/\text{ACN}$ study above where the cell was cycled five times by cyclic voltammetry), so differences may also arise from changes of the charge storage mechanism that occur in the first few charge-discharge cycles. More experiments and theoretical work must be done to study these phenomena.

8.3.7 *The application of in situ NMR methods to other carbon materials*

In principle, the *in situ* NMR approach is readily applicable to any given carbon electrode material, though resolution of the in-pore environments will depend on the $\Delta\delta$ values and in-pore linewidths. TiC-CDC-1000 was selected for a further *in situ* NMR study as the measured $\Delta\delta$ value (-5.4 ppm) is comparable to that for YP50F (-5.7 ppm). *In situ* NMR spectra recorded at fixed voltages for a TiC-CDC-1000 overlaid cell with $\text{PEt}_4\text{BF}_4/\text{ACN}$ (1.5 M) electrolyte are shown in Figure 8.12. In the ^{19}F NMR spectra, the in-pore anion resonance is observed as a broad shoulder at ~ 156 ppm (Figure 8.12a).

On charging to 1.5 V, this resonance visibly increases in intensity in the positive electrode, clearly showing the role of anion adsorption processes in the positive electrode. Such an increase in in-pore anion intensity is not observed in the negative electrode, where intensity appears to be lost during charging. In both electrodes, general shifts of the in-pore resonance to higher frequency are observed, similar to in the studies of YP50F. However, small positive chemical shift changes are observed in the positive electrode for cell voltages between 0 and 0.5 V, which was not observed for YP50F. This suggests that differences between the carbon structures can affect the ring current shifts upon charging. ^{31}P NMR spectra (Figure 8.12b) also exhibit broad in-pore shoulders at 0 V (\sim 32 ppm), though the changes of intensity upon charging are less apparent. This is partly due to the lower signal to noise ratio of these spectra, but it may also indicate that the changes of the ^{31}P spectra with voltage here are also less pronounced than those in the ^{19}F spectra.

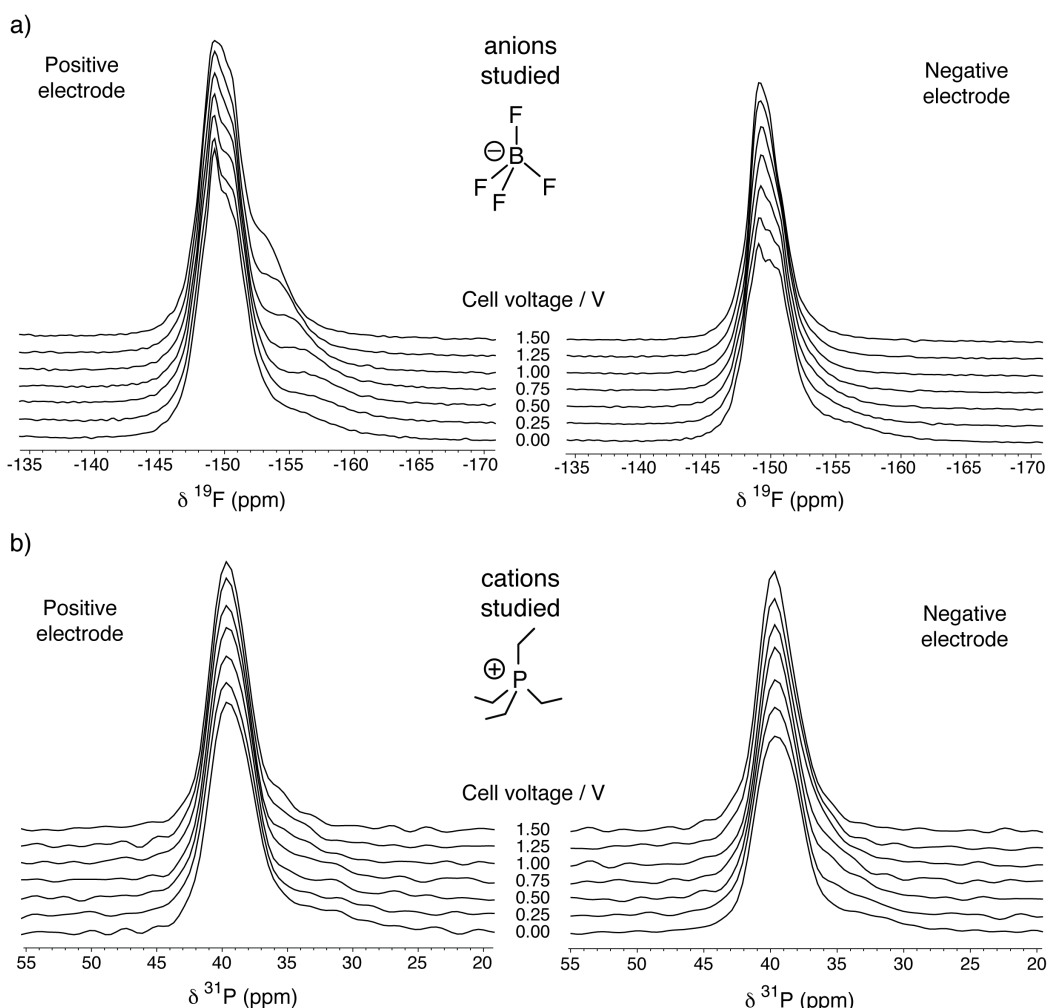


Figure 8.12 (a) ^{19}F , and (b) ^{31}P *in situ* NMR spectra of a TiC-CDC-1000 overlaid supercapacitor cell with $\text{PET}_4\text{BF}_4/\text{ACN}$ (1.5 M) electrolyte. Clear changes can be observed in the ^{19}F spectra during charging, though changes in the ^{31}P spectra are unclear.

For the majority of the spectra shown in Figure 8.12 it was not possible to obtain a unique spectral fit, due to the poor resolution of the in-pore resonance. However, changes of the total integrated signal intensity of the spectra can still offer some information about the charging process. The integrated intensity changes were converted to changes of moles by performing calibration experiments (Figure 8.13a,b). Here, model carbon electrodes soaked with different volumes of electrolyte were sealed inside plastic bags and NMR spectra were acquired. This allowed spectral intensities to be correlated with electrolyte-volumes, and therefore moles of ions. The extracted changes of the number of moles for the positive and negative charging regimes are then shown in Figure 8.13c, with changes given relative to the 0 V spectra. Clear increases in signal intensity are observed for the anions during charging of the positive electrode, in agreement with the observed increase of in-pore intensity in the spectra. In the negative electrode, a decrease of the number of anions is observed, suggesting that anion desorption processes take place. For the cations, only small changes are seen in the positive electrode up to \sim 1 V at which point there appears to be some desorption of cations. In the negative electrode on the other hand, steady increases in the number of moles of detected cations are observed. It is stressed that the distinction between in-pore and ex-pore/free electrolyte resonances has not been made here. To a first approximation, the changes observed in Figure 8.13c will arise from changes of the in-pore populations, though ideally further experimental evidence would be obtained to verify the charging mechanism. Given the poor spectral resolution here, alternative NMR methods must be developed in future work to resolve the behaviour of the in- and ex-pore resonances.

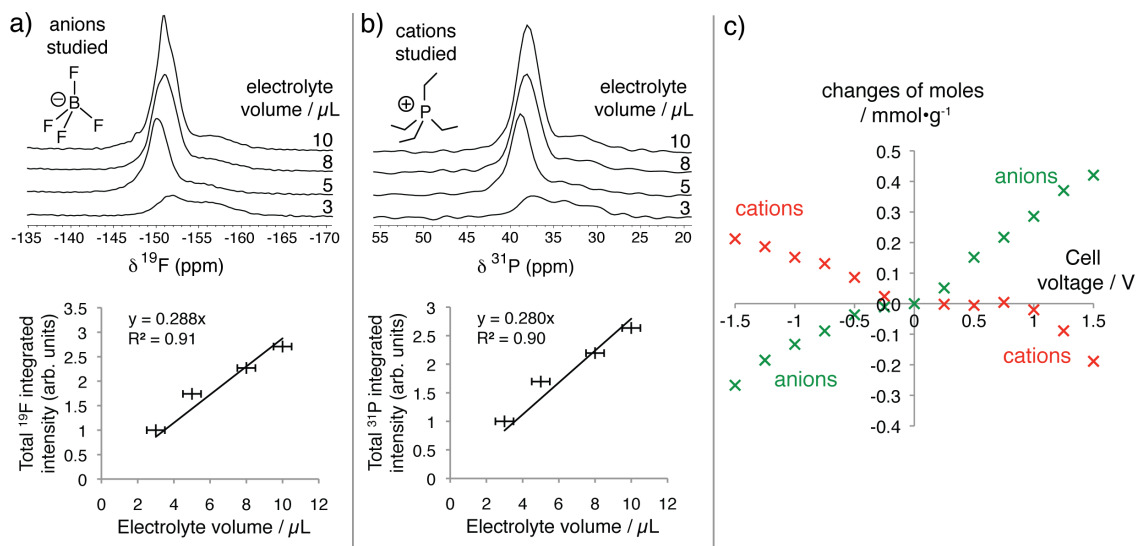


Figure 8.13 (a) ^{19}F and (b) ^{31}P calibration NMR experiments on model TiC-CDC-1000 electrodes soaked with $\text{PEt}_4\text{BF}_4/\text{ACN}$ (1.5 M) electrolyte. The integrated intensities are plotted for each sample, which allows a calibration curve to be obtained which correlates spectral intensity to electrolyte volume (and therefore moles). (c) Extracted changes of moles (relative to 0 V) from the *in situ* NMR spectra. The results give insights into the charge storage mechanism of the system.

The preliminary results here may be contrasted with the results for the same electrolyte with YP50F carbon (Section 8.3.6). For YP50F, ion exchange processes occurred in the positive electrode, while charging in the negative electrode was dominated by counter-ion adsorption. In contrast, for TiC-CDC-1000 charging appears to be dominated by counter-ion adsorption in the positive electrode, while in the negative electrode an ion exchange mechanism appears to be operating. This interesting result suggests that differences in the carbon structure bring about differences in the mechanism of charge storage in supercapacitors. This may be related to differences of surface chemistry, and further experiments and theoretical work must be done to investigate these phenomena.

8.4 Summary and Outlook

In this chapter, the development and application of *in situ* NMR spectroscopy to supercapacitors has been presented. Practical aspects of the *in situ* methodology have been investigated, such as the influence of the cell design on electrochemical performance. The overlaid cell design used here has the advantages of allowing the separate study of the two electrodes in the NMR measurements, while maintaining reasonable electrochemical performance. The orientation of the samples in the NMR coil has been shown to have a significant effect on the spectral resolution that can be obtained, with the vertical cell orientation preferred over the horizontal orientation.

In situ NMR experiments have been carried out on the YP50F - NEt₄BF₄/ACN system. By tracking the in-pore anion peak intensities, the charging mechanism was probed whereby anion desorption takes place in the negative electrode, and anion adsorption takes place in the positive electrode, but only once a threshold cell voltage of 0.75 V is reached. Meanwhile, the in-pore chemical shift changes show good agreement with those measured on the YP50F - Pyr₁₃TFSI ionic liquid system (Chapter 6), confirming the idea that these shifts are associated with changes of the carbon electronic structure that occur during charging. Experiments with simultaneous cyclic voltammetry further confirm these ideas, showing that the periodic shifting of the in-pore resonance is synchronised with the magnitude of the electronic charge stored in the electrodes.

PEt₄BF₄ has been introduced as a new electrolyte salt that allows the study of the PEt₄ cations via ³¹P NMR experiments. *In situ* NMR experiments on YP50F then allow the quantification of the in-pore populations of anions and cations, and show that the charging mechanism depends on the polarisation of the electrode. In the positive electrode, charging takes place via ion exchange, while in the negative electrode charging is dominated by counter-ion adsorption. This mechanism differs from that observed for TiC-CDC-1000, where nearly the exact reverse behaviour is observed in the two electrodes. The wealth of data presented in this Chapter, and in Chapter 6, highlight the sensitivity of the charging mechanism to both the electrolyte and the carbon studied. Understanding these factors is an important next step if one is to fully unravel the molecular mechanisms of the supercapacitance phenomenon. Ultimately, it is envisaged that such an understanding will aid with the development of new carbon materials and electrolytes that show superior performance.

Experiments on TiC-CDC-1000 demonstrate that the applicability of the *in situ* NMR approach is limited by the spectral resolution of the in-pore resonance from the intense ex-pore/free electrolyte features. New *in situ* NMR methods must be developed to study the full range of carbon materials and electrolytes, including systems that show broad in-pore resonances (*e.g.*, ionic liquid devices) and systems that show small $\Delta\delta$ values (*e.g.*, TiC-CDC-600 devices). One possible approach is to filter the NMR spectra so that the in-pore resonance is favoured over the other resonances. This may be possible on the basis of their different nuclear relaxation times as is often done in relaxometry measurements in studies of porous media.¹⁹⁴ Another possibility, explored in the next chapter, is to filter spectra based on the spatial proximity of the ions to carbon surfaces.

Chapter 9

Selecting Adsorbed Species with Cross Polarisation

9.1 Context and Scope

NMR spectroscopy has been demonstrated as a powerful method for studying supercapacitors. However, the NMR approach relies on the spectral resolution of the in- and ex-pore resonances, which can be a problem for systems with viscous electrolytes such as ionic liquids (see Chapter 6), and for carbon electrodes that give rise to small ring current shifts and/or broad resonances (as in the *in situ* NMR studies of TiC-CDC-1000 in Chapter 8). When charged electrodes are studied, the shift of the in-pore resonances towards the ex-pore resonances can further impede resolution. The development of advanced NMR methods that improve spectral resolution is therefore necessary if a wide range of electrolytes and carbon materials are to be studied.

One particularly useful technique in NMR is cross polarisation (CP), where magnetisation is transferred from one nucleus to another by a heteronuclear dipolar coupling mechanism (Section 3.4.3). While this method is typically used to enhance the signal obtained for dilute or insensitive nuclei,¹⁰³ it may also be used for spectral editing, whereby the spectrum is biased on the basis of the spatial proximity of the detected spins to the heteronuclei. This approach has been used to study molecules adsorbed on zeolites,^{106,107} and to study the structure of biominerals.^{195,196} A characteristic feature of CP experiments is that the signal intensity depends on the contact time (the time during which magnetisation transfer takes place) used in the experiments. An understanding of the build-up and decay of this signal intensity with the contact time, or the “CP kinetics” is important, as it allows the experiments to be

optimised to give the most intense signals possible, while also offering dynamical and structural information.¹⁰⁸

The main aim of this chapter is to apply the CP technique to supercapacitors. It is shown that it is possible to transfer magnetisation from the ¹³C nuclear spins in isotopically enriched CDC electrodes to the nearby ¹H or ¹⁹F nuclear spins of the in-pore cations and anions of Pyr₁₃TFSI ionic liquid. In contrast to in-pore ions, ex-pore ions are not detected in the CP experiments due to the much longer distances between these ions and the carbon surfaces. Studies of the CP kinetics in charged electrodes show that the dipolar couplings between the carbon electrode and the cations become stronger in both electrodes following charging, suggesting that charging slows down the motion of the in-pore cations, irrespective of the electrode polarisation.

9.2 Experimental Details

9.2.1 Materials

Full details of the synthesis of ¹³C enriched TiC-CDC samples are given in Section 5.2.2. All experiments used Pyr₁₃TFSI ionic liquid (see Section 6.2.2).

9.2.2 NMR details

NMR experiments were performed using a Bruker Avance spectrometer operating at a magnetic field strength of 7.1 T, corresponding to a ¹H Larmor frequency of 300.2 MHz. A Bruker 2.5 mm double resonance probe was used. Unless otherwise indicated, NMR experiments were performed at an MAS rate of 5 kHz. ¹⁹F NMR spectra were referenced relative to neat hexafluorobenzene (C₆F₆) at -164.9 ppm, ¹H NMR spectra were referenced relative to tetramethylsilane using the CH₃ resonance of liquid ethanol at 1.2 ppm as a secondary reference, and ¹³C NMR spectra were referenced to the resonance of the tertiary carbon atom in adamantane at 38.5 ppm. For direct excitation experiments, recycle delays were adjusted to give quantitative spectra for all nuclei. For CP experiments the recycle delay was 3 s in all cases.

The standard pulse sequence for CP¹⁰³ was modified by adding an initial “saturation train” of $\pi/2$ pulses on the channel on which data was acquired. This was done to suppress artefacts arising from direct excitation, such that only signal generated by cross polarisation was observed. Unless otherwise stated, a train of 20 $\pi/2$ pulses was used, with the pulses separated by delays of 20 ms. The contact times for CP experiments are given in the figure captions. For CP experiments on Ti¹³C-CDC-1000 samples, contact

pulse powers of ~75 and ~70 kHz were used for ^1H and ^{13}C , respectively, with no power ramping applied to either channel. The same pulse powers were used for the spin-locking periods in the measurements of $T_{1\rho}$. For CP experiments on the Ti ^{13}C -CDC-800 sample, contact pulses were ~60 kHz and ~50 kHz, for ^{13}C and ^{19}F respectively for the $^{13}\text{C} \rightarrow ^1\text{H}$ experiments, while for $^{13}\text{C} \rightarrow ^1\text{H}$, respective contact pulse powers were ~65 and ~50 kHz. Excitation pulse powers were between 95 and 122 kHz in all experiments. Spectral fits were carried using the Sola package in Topspin software using a chemical shift anisotropy model. A single peak was used to fit the in-pore resonance, and a single peak was used for each ex-pore resonance.

For NMR experiments on carbons soaked with ionic liquids, the samples were prepared as described in Section 6.2.3.

9.2.3 *Ex situ* NMR experiments

The procedure for the fabrication of coin cell supercapacitors and subsequent *ex situ* NMR experiments was identical to that outlined in Sections 6.2.5 and 6.2.6. A single cell voltage of 1.5 V was studied, with a value of 1.44 V measured immediately before cell disassembly.

9.3 Results and Discussion

9.3.1 Selecting the in-pore ions with cross polarisation

CP MAS NMR experiments were carried out on Ti ^{13}C -CDC-800 soaked with Pyr₁₃TFSI ionic liquid to investigate the utility of the CP method for the study of adsorption in porous carbons. The direct excitation experiment (*i.e.*, the normal NMR experiment) reveals both in- and ex-pore resonances for the TFSI anions (Figure 9.1a), with the spectrum similar to that observed for TiC-CDC-1000 soaked with the same ionic liquid shown in Chapter 6. The $^{13}\text{C} \rightarrow ^{19}\text{F}$ CP experiment, on the other hand, reveals solely an in-pore resonance, with the chemical shift and lineshape correlating well with that seen in the direct excitation experiment. Spectra with ^1H detection (Figure 9.1b) reveal similar effects for the Pyr₁₃ cations, with the $^{13}\text{C} \rightarrow ^1\text{H}$ CP experiment showing only the in-pore cation resonances.

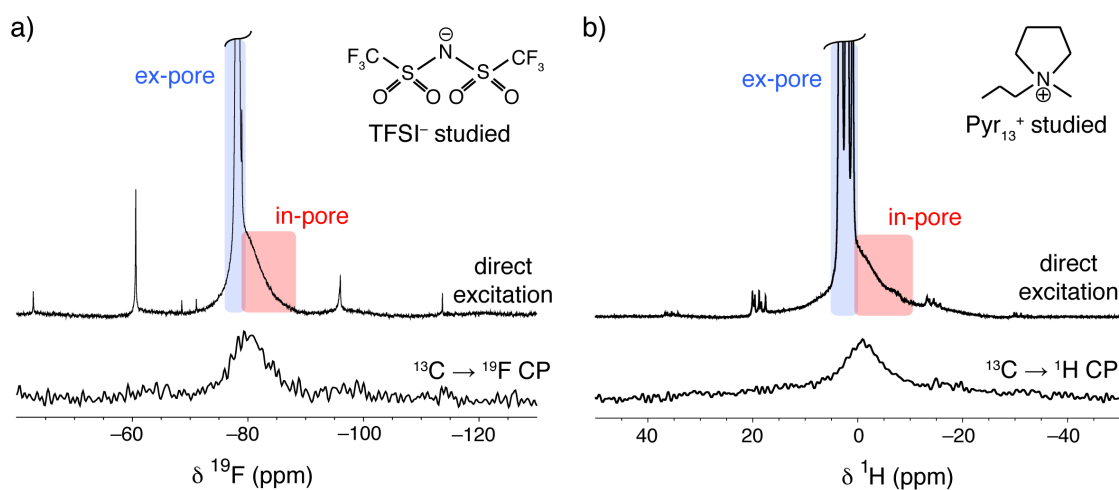


Figure 9.1 ¹⁹F (a) and ¹H (b) MAS NMR (7.1 T) spectra for Ti¹³C-CDC-800 soaked with Pyr₁₃TFSI ionic liquid. In each case spectra from direct excitation and CP experiments (4 ms contact time) are shown. The CP experiments reveal solely the in-pore features. The signal to noise ratio is higher in the ¹H detected CP experiment than the ¹⁹F detected experiment, despite the shorter experiment time for the former (~15 minutes vs. ~2 hours). The CP experiments take considerably longer than the direct excitation experiments, for which the total experiment time is on the order of 1 minute in each case.

These effects may be rationalised, since magnetisation transfer in the CP experiment occurs via heteronuclear dipolar couplings, the strength of which are proportional to r^{-3} , where r is the distance between the coupled nuclei (Section 3.2.2).¹⁰⁵ Thus, only spins separated by a few ångstroms are detected in CP experiments, explaining why only in-pore ions are detected when signal is transferred from the ¹³C nuclei here. The CP experiments provide further validation of the spectral assignments, and confirm that the ex-pore ions are remote from the carbon surfaces compared to the in-pore ions. The experiments provide a new method to edit the spectra. It is noted, however, that the CP experiments take considerably longer than direct excitation experiments, with the ¹⁹F and ¹H detected CP experiments in Figure 9.1 taking ~2 hours and ~15 minutes to acquire, respectively, compared to experiment times of ~1 minute for each of the direct excitation experiments.

The CP transfer is performed in reverse to the conventional sense here. Typically CP is used to enhance signal intensity for insensitive nuclei (e.g., ¹³C), by transferring magnetisation from sensitive nuclei (such as ¹H or ¹⁹F), with the maximum theoretical enhancement given by the ratio of the gyromagnetic ratios of the nuclei (e.g., a maximum enhancement of ~4 for ¹H → ¹³C).¹⁰⁵ Here, however, by transferring from an insensitive nucleus (¹³C) to a sensitive nucleus (such as ¹H), a signal diminishment by a factor of ~4 is expected. The more sensitive nuclei usually have the added benefit of

shorter longitudinal relaxation times (T_1) allowing a faster repetition of the pulse sequence when carrying out the CP transfer in the conventional direction. The success of the reverse approach carried out here relies on the isotopic enrichment of the carbon electrode (99 % ^{13}C), which provides more magnetisation to transfer, while also giving rise to relatively short T_1 s for ^{13}C in the solid state. For example, the T_1 value of Ti ^{13}C -CDC-1000 was measured as 0.9 s by the saturation recovery method.

Preliminary CP experiments using standard pulse programs revealed some artefacts associated with “breakthrough” of ex-pore magnetisation (Figure 9.2a). This is thought to arise from transverse magnetisation generated directly by the contact pulse on the ^{19}F channel (rather than by cross polarisation). This hypothesis is confirmed by experiments with an initial saturation train on the ^{19}F channel (Figure 9.2b), which destroys any ^{19}F magnetisation prior to cross polarisation, such that the formation of artefacts associated with direct excitation is no longer possible. All CP experiments in this Chapter (for both ^1H and ^{19}F detection) therefore used the pulse sequence shown in Figure 9.2b.

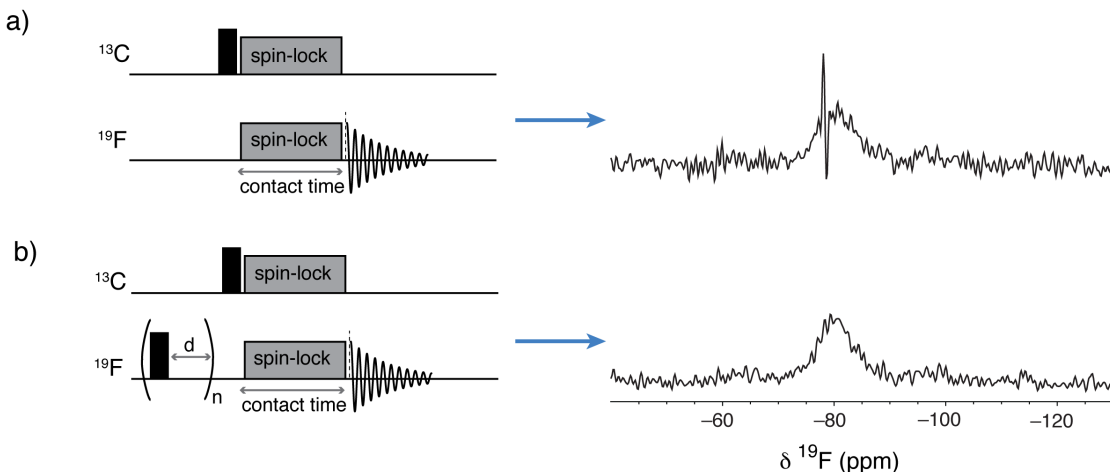


Figure 9.2 (a) Conventional pulse sequence for cross polarisation from ^{13}C to ^{19}F , and $^{13}\text{C} \rightarrow ^{19}\text{F}$ CP MAS NMR (7.1 T) spectrum obtained for Ti ^{13}C -CDC-800 soaked with Pyr $_{13}\text{TFSI}$ ionic liquid. Here an artefact is observed at ~ 78 ppm. (b) Modified pulse sequence with an initial saturation train on the ^{19}F channel, and CP MAS NMR (7.1 T) spectrum acquired with $n = 20$, and $d = 50$ ms. The contact time was 4 ms in each case. The modified pulse sequence suppresses the formation of artefacts.

^1H NMR spectra for Ti ^{13}C -CDC-1000 soaked with Pyr $_{13}\text{TFSI}$ ionic liquid reveal similar effects to those for Ti ^{13}C -CDC-800 (Figure 9.3a), with the CP spectra shown for two different MAS rates here. The 2D HETCOR experiment shown in Figure 9.3b confirms the idea that the in-pore cation resonance (-1.1 ppm) is correlated with the porous carbon (124 ppm) in the CP experiment. No correlations are seen for the directly bonded ^{13}C - ^1H pairs in the Pyr $_{13}^+$ cations. This is largely because the carbon nuclei in

the cations have the natural abundance of ^{13}C spins ($\sim 1\%$), such that there are very few ^{13}C nuclei to transfer magnetisation from. Moreover, rotation of the in-pore cations will average the orientation of the ^{13}C - ^1H inter-nuclear vectors (with respect to the applied magnetic field direction), which will average the intramolecular dipole-dipole couplings to zero in the limit of isotropic rotation. The remaining ^{13}C - ^1H dipolar couplings are between the ^{13}C spins in the porous carbon and the ^1H spins in the cations (the positions of which are averaged by rotation). These couplings will be reduced by the translational motion of the cations, as such motion will vary the orientations of the ^{13}C - ^1H inter-nuclear vectors.

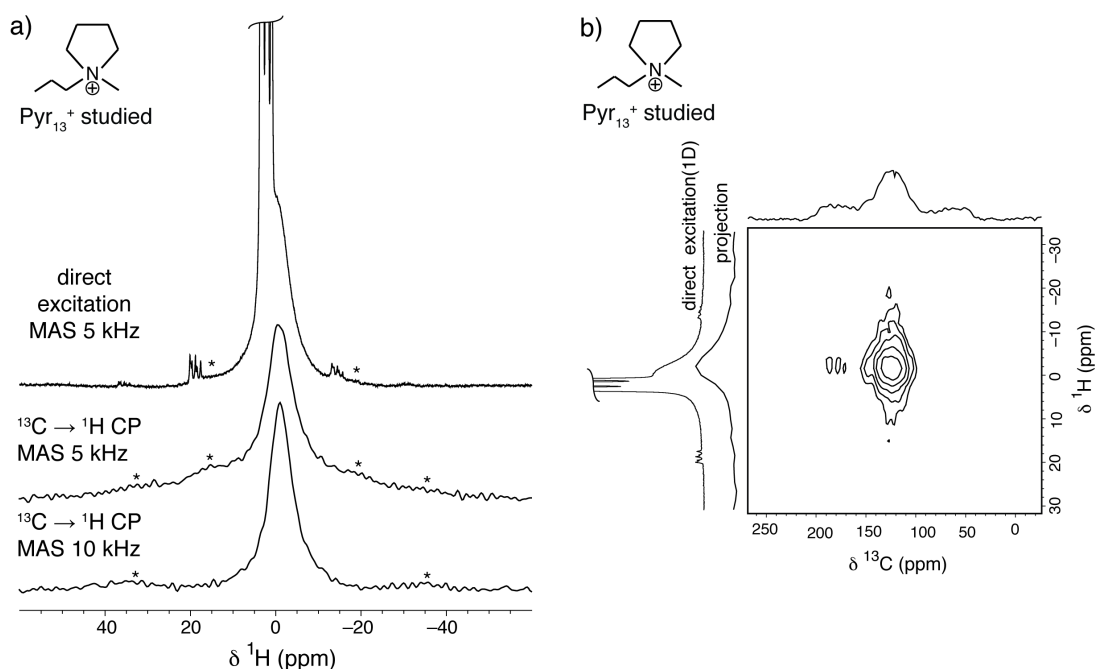


Figure 9.3 NMR (7.1 T) spectra for Ti^{13}C -CDC-1000 soaked with $\text{Pyr}_{13}\text{TFSI}$ ionic liquid. (a) ^1H NMR direct excitation and CP experiments, with the sample spinning speeds indicated on the figure, and in-pore spinning sidebands marked with asterisks. (b) $^{13}\text{C} \rightarrow ^1\text{H}$ 2D HETCOR experiment (5 kHz MAS). The contact time for CP was 6 ms in all cases.

Interestingly the CP spectra (Figure 9.3a) show more intense in-pore spinning sidebands than the direct excitation spectrum, where these sidebands are barely visible. This was quantified by spectral fits (Sola program in Topspin) that give a measure of the width, W_{aniso} , of the spinning sideband pattern (The W_{aniso} parameter is analogous to a chemical shift anisotropy parameter, δ_{aniso} , see Section 3.2.1). For the in-pore resonance here, W_{aniso} was found to be 5, 20 and 24 ppm for the direct excitation, CP (MAS 5 kHz) and CP (MAS 10 kHz) experiments, respectively, with the values for the two CP spectra agreeing within the estimated error associated with the fits (~ 2 or 3 ppm). The spectral fits also reveal that the linewidth of the isotropic in-pore resonance is larger in the CP

(MAS 5 kHz) spectrum than in the direct excitation spectrum, with FWHMs of 2500 and 2000 Hz, respectively. Together these findings suggest that the CP experiments detect a subset of the in-pore ions with slower dynamics. It is hypothesised that the CP experiments favour the most confined ions that are undergoing the slowest translational and rotational motion and therefore have the largest dipolar couplings. However, it is unclear what the dominant anisotropic NMR interaction is here though (dipolar couplings, BMS effects, chemical shift anisotropy *etc.*).

9.3.2 CP kinetics for $Ti^{13}C$ -CDC-1000 soaked with $Pyr_{13}TFSI$

The $^{13}C \rightarrow ^1H$ CP kinetics for measurements on $Ti^{13}C$ -CDC-1000 soaked with $Pyr_{13}TFSI$ are shown in Figure 9.4a. The signal intensity builds up as the contact time is increased to about 6 ms, after which slight decreases in signal intensity are observed. Thus, if the signal to noise ratio is to be maximised for this sample, contact times of ~6 ms should be used. Following the approach reviewed by Kolodziejski and Klinowski (see Section 3.4.3),¹⁰⁸ the build-up of the signal can be fit according to Equation 9.1:

$$I(t) = A \left[\exp\left(\frac{-t}{T_{1\rho}(^{13}C)}\right) - \exp\left(-t\left(\frac{1}{T_{CP}} + \frac{1}{T_{1\rho}(^1H)}\right)\right) \right] \quad [9.1]$$

Where t is the contact time, T_{CP} is a time constant associated with the magnetisation transfer from 1H to ^{13}C , $T_{1\rho}(^{13}C)$ and $T_{1\rho}(^1H)$ are longitudinal relaxation times in the rotating frame, and A is a constant given by:

$$A = I_0 \left(1 + \frac{T_{CP}}{T_{1\rho}(^1H)} - \frac{T_{CP}}{T_{1\rho}(^{13}C)} \right)^{-1} \quad [9.2]$$

Where I_0 is a constant that is proportional to the intensity that would be obtained in a direct excitation experiment for the species that undergo cross polarisation.¹⁰⁸

The relaxation times $T_{1\rho}(^{13}C)$ and $T_{1\rho}(^1H)$ were measured by carrying out spin-locking experiments (see Section 3.4.3). In these experiments, magnetisation obtained by CP was spin-locked for a range of different times, and $T_{1\rho}$ values were extracted by fitting the decay of the signal intensity to Equation 3.24. The values obtained for $T_{1\rho}(^1H)$ and $T_{1\rho}(^{13}C)$ were 2.5 and 67 ms, respectively. These parameters were then fixed in the fit of the CP kinetics to Equation 9.1 (Figure 9.4a), where a value of 3.0 ms was obtained for T_{CP} . While the fit is generally good, there is some deviation between the fitted function and the experimental data at contact times above 3 ms (Figure 9.4a). This may be

because there is a distribution of different in-pore environments, each with slightly different T_{CP} and $T_{1\rho}$ values.

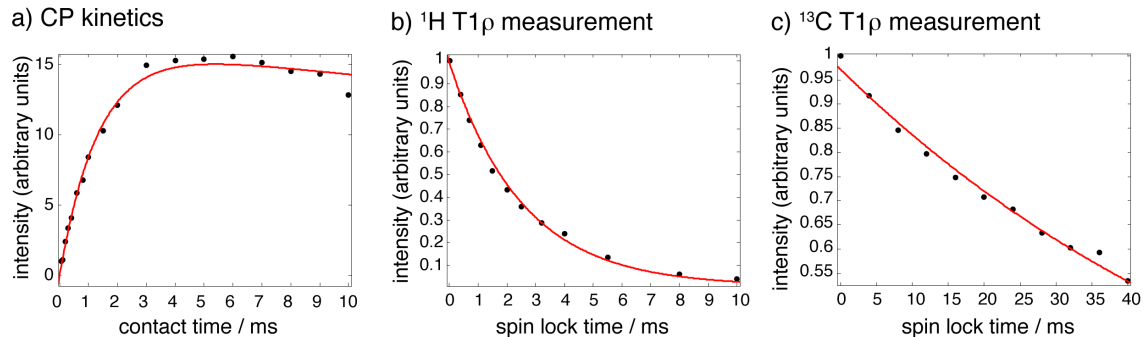


Figure 9.4 (a) $^{13}\text{C} \rightarrow ^1\text{H}$ CP kinetics for Ti^{13}C -CDC-1000 soaked with $\text{Pyr}_{13}\text{TFSI}$ ionic liquid, with a fit to Equation 9.1 shown in red. In (b) and (c) $T_{1\rho}$ measurements are shown for ^1H and ^{13}C , respectively, with the signal generated by cross polarisation (contact time of 4 ms) from the other nucleus in each case. Here, red lines show fits to Equation 3.24.

The T_{CP} value depends on the strength of the dipolar couplings, with shorter values corresponding to stronger dipolar couplings. The T_{CP} value therefore depends on both; the distances between the coupling spins, and the presence of any motion of these spins relative to each other. These effects are best understood by considering some examples from the literature. $^1\text{H} \rightarrow ^{13}\text{C}$ measurements on β -carotene showed that one-bond magnetisation transfers in CH_2 groups were characterised by T_{CP} values of between 0.7 – 0.8 ms.¹⁹⁷ Longer T_{CP} values of between 1.5 – 1.7 ms were recorded for the CH_3 groups, due to their considerable rotational motion, while a typical quaternary carbon group (with no attached protons) also showed a longer value of T_{CP} of, ~1.7 ms, in this case due to the larger distances between the ^{13}C and ^1H nuclei.¹⁹⁷ For systems with both considerable dynamics and large ^{13}C - ^1H distances, such as the fullerene-toluene mixture studied by Kolodziejksi *et al.*, long T_{CP} values have been measured (T_{CP} was measured as 13 ms for magnetisation transfer from the fullerenes to protons in toluene solvent).¹⁹⁸ Solid adamantane represents another interesting case, as here the rapid molecular motion of the adamantane molecules on the crystal lattice averages out all intramolecular dipole-dipole couplings with magnetisation transfer then occurring via intermolecular couplings (with T_{CP} then measured at ~2.3 ms).^{199,200} The relatively large T_{CP} value of 3.0 ms obtained here for the Ti^{13}C -CDC-1000/ $\text{Pyr}_{13}\text{TFSI}$ system appears consistent with an intermolecular interaction between the carbon and the protons on the Pyr_{13} cations. Further work is required to study the significance of the T_{CP} value and to simulate the CP build-up for model spin systems. It may even be possible to calculate

dipolar couplings from MD trajectories of model carbon systems soaked with ionic liquid.

9.3.3 CP measurements on charged electrodes

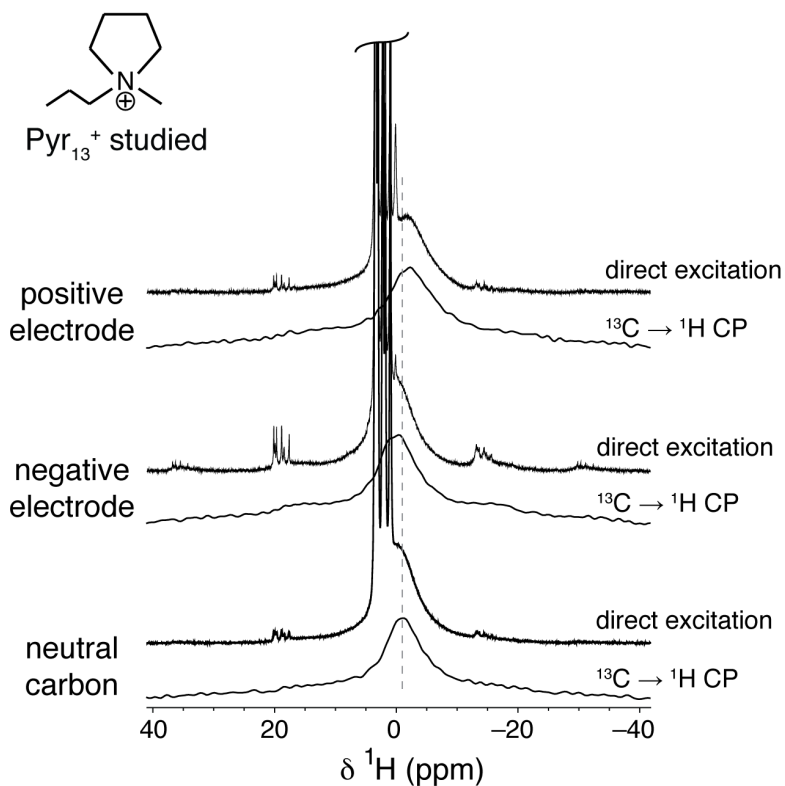


Figure 9.5 NMR (7.1 T) spectra for a piece of neutral carbon soaked with $\text{Pyr}_{13}\text{TFSI}$ ionic liquid, as well as for the positively and negatively charged electrodes extracted from a supercapacitor cell ($\text{Ti}^{13}\text{C}-\text{CDC}-1000$ with $\text{Pyr}_{13}\text{TFSI}$ ionic liquid) with a cell voltage of 1.44 V. Direct excitation and $^{13}\text{C} \rightarrow ^1\text{H}$ CP (4 ms contact time) experiments are shown in each case. The direct excitation spectra are normalised by the amount of carbon in each sample, while the CP spectra are scaled arbitrarily for ease of comparison with the direct excitation spectra.

$^1\text{H} \rightarrow ^{13}\text{C}$ CP experiments were carried out on electrodes extracted from a charged supercapacitor cell to investigate the effects of charging on the CP kinetics. *Ex situ* NMR experiments were carried out on a cell ($\text{Ti}^{13}\text{C}-\text{CDC}-1000$ with $\text{Pyr}_{13}\text{TFSI}$ ionic liquid) with a measured cell voltage of 1.44 V immediately before cell disassembly, and a capacitance of $\sim 25 \text{ F}\cdot\text{g}^{-1}$. The in-pore resonance shows some small shifts upon charging (Figure 9.5), with the $^{13}\text{C} \rightarrow ^1\text{H}$ CP experiments filtering the spectrum effectively in each case and revealing solely an in-pore environment. These experiments reveal that the in-pore resonance shifts from -0.9 ppm (neutral sample) to -0.5 ppm in the negative electrode and -1.5 ppm in the positive electrode. This negative chemical shift change in the positive electrode contrasts to the positive shift changes observed

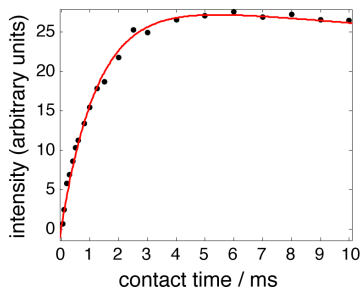
elsewhere in this thesis for YP50F activated carbon and other activated carbons in the literature.^{17,18,93} It is, however, reminiscent of the small positive shifts observed in the *in situ* ¹⁹F NMR spectra of BF₄⁻ in the TiC-CDC-1000 - PEt₄BF₄/ACN system at low cell potentials (see Section 8.3.7). These findings suggest that the structure of the carbon can influence the chemical shift mechanism during charging. Given the observation of similar effects for cations (here) and anions (in Section 8.3.7), both in the positive electrode, the effect seems to be associated with the electronic structure of the carbon. Clearly, more work must be done to understand the differences between the electronic structures of YP50F and TiC-CDC-1000, and to understand the resulting effects on the observed chemical shifts.

The CP kinetics were investigated in each electrode (Figure 9.6), following the approach detailed for the neutral sample above, with a summary of the fitted parameters given in Table 9.1. For the charged electrodes the measured T_{CP} values are shorter, consistent with stronger dipolar couplings between the ¹³C nuclei in the carbon electrodes and the ¹H nuclei in the Pyr₁₃ cations. This could arise from a combination of shorter carbon-cation distances and a reduction in the mobility of the in-pore cations. However, it is not expected that the carbon-cation distances should decrease in both electrodes upon charging due to coulombic interactions. Indeed, MD simulations on model CDC electrodes suggested that the cation density near the carbon surface increases in the negative electrode, but decreases slightly in the positive electrode.⁶⁸ Instead, this suggests that changes of the ion-dynamics dominate the observed variations of T_{CP} here, with a slowing down of the translation and rotation of the cations in both the charged electrodes. The longer $T_{1\rho}({}^1H)$ values for ¹H in both electrodes also suggest that charging brings about a change in the cation dynamics on a μ s timescale. Interestingly, the I_0 values obtained from the fits of the CP kinetics show increases in both electrodes following charging, despite the relatively small changes of the in-pore cation populations determined from direct excitation experiments (Table 9.1). This suggests that the sub-set of in-pore cations selected by CP has increased following charging, again consistent with a slowing down of the dynamics of the cations in both electrodes. Here the effect is more pronounced in the negative electrode, where the attractive interactions of the cations with the carbon surfaces may have an effect. Overall, the CP kinetics measurements show that the motion of the in-pore cations is slowed down in both electrodes by the application of a potential. This supports the findings of the *ex situ* NMR measurements of the YP50F - Pyr₁₃TFSI system in Section 6.3.3, where increases in the W_{aniso} parameter were observed with voltage for in-pore

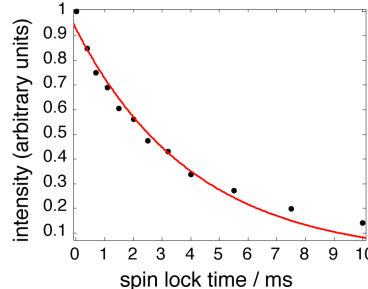
ions in both electrodes. Importantly, this slowing down of in-pore ionic motion will be detrimental to the power performance of supercapacitors (Chapter 7).

Positive electrode studied

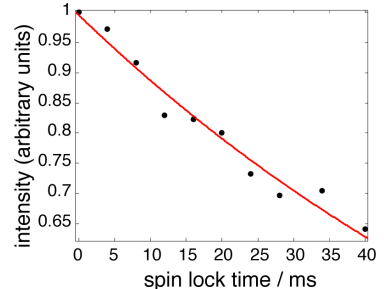
a) CP kinetics



b) $T_{1\rho}(^1\text{H})$ measurement

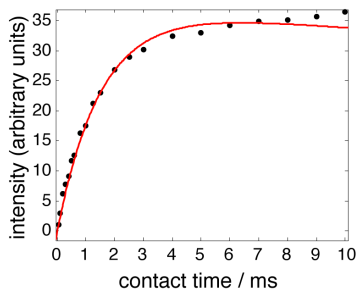


c) $T_{1\rho}(^{13}\text{C})$ measurement

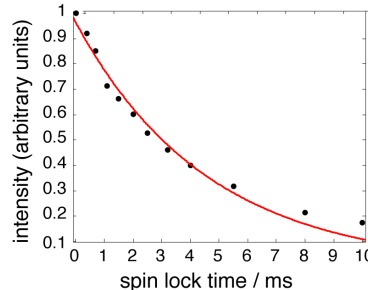


Negative electrode studied

d) CP kinetics



e) $T_{1\rho}(^1\text{H})$ measurement



f) $T_{1\rho}(^{13}\text{C})$ measurement

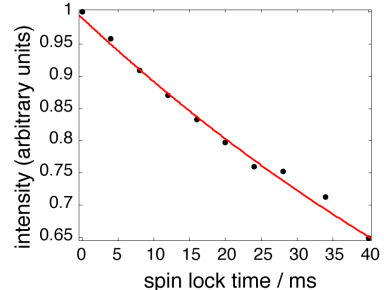


Figure 9.6 (a) $^{13}\text{C} \rightarrow ^1\text{H}$ CP kinetics for the positive electrode extracted from a coin cell supercapacitor (Ti^{13}C -CDC-1000 with $\text{Pyr}_{13}\text{TFSI}$ ionic liquid) with a cell voltage of 1.44 V. In (b) and (c) $T_{1\rho}$ measurements are shown for ^1H and ^{13}C , respectively, with the signal generated by cross polarisation (contact time of 4 ms) from the other nucleus in each case. In (d), (e) and (f) analogous data is shown for the negative electrode of the same cell. Fits to Equation 9.1 are shown in red in (a) and (d), while fits to Equation 3.24 are shown in (b), (c), (e) and (f). The signal intensity in the CP kinetics experiments is scaled by the amount of carbon electrode in each sample.

Table 9.1 Parameters obtained from fits of the CP kinetics data shown in Figures 9.4 and 9.6. The $T_{1\rho}$ values were measured independently, and their values were fixed in the CP kinetics fits. Upper and lower values at 95 % confidence bounds are given in brackets. I_0 (CP) is obtained from Equation 9.2, and is proportional to the intensity that would be obtained in a direct excitation experiment for the species that undergo CP. The I_0 (direct excitation) ratio was measured by performing one-pulse ^1H NMR experiments on each sample, with spectral fitting carried out to obtain the in-pore intensity for each sample.

sample	$T_{\text{cp}} / \text{ms}$	$T_{1\rho}(^1\text{H}) / \text{ms}$	$T_{1\rho}(^{13}\text{C}) / \text{ms}$	$I_0(\text{CP})$	$I_0(\text{CP})$ ratio	$I_0(\text{direct excitation})$ ratio
neutral	3.0 (2.3, 3.6)	2.5 (2.4, 2.7)	67 (61, 72)	36 (35, 37)	1.0	1.0
positive electrode	1.8 (1.7, 2.0)	4.1 (3.5, 4.7)	87 (74, 100)	41 (41, 43)	1.2	1.0
negative electrode	2.3 (2.0, 2.5)	4.6 (4.0, 5.2)	96 (89, 103)	56 (54, 58)	1.6	1.1

9.4 Summary and Outlook

This chapter has demonstrated the application of CP NMR experiments as a method to selectively observe in-pore ions in supercapacitor electrodes. When magnetisation is transferred from ^{13}C enriched CDCs to nuclei in the cations (^1H) or anions (^{19}F), only the in-pore resonances are observed. This unambiguously confirms that in-pore ions are located within ångstrom distances of the carbon surfaces, while ex-pore ions are more remote. In practice, the CP experiments select a subset of the in-pore ions, with only the most confined ions observed.

Ex situ NMR experiments carried on the Ti ^{13}C -CDC-1000 - Pyr $_{13}\text{TFSI}$ system show that the $^{13}\text{C} \rightarrow ^1\text{H}$ CP kinetics are sensitive to charging. These measurements suggest that the translational and rotational dynamics of the cations slow down upon charging, regardless of the electrode polarisation. This has important implications for supercapacitor charging, and indicates that the charging rates will decrease for higher applied potentials.

More work must be done to understand the observed CP kinetics, which depend together on the distances between the pairs of coupling nuclei and the complex translational and rotational motion of the ions through the porous network of the carbon. One possibility may be to calculate dipolar couplings from MD trajectories on realistic model electrodes soaked with ionic liquid, and study how these are affected by charging. Depending on the timescale of the processes, lower level calculations may be more appropriate however.

While the CP NMR technique offers new insights into the structure and dynamics of the electrode-electrolyte interface in supercapacitors, it relies on the fabrication of isotopically enriched electrodes, and the time for the acquisition of data is somewhat longer than that for direct excitation NMR experiments. Further techniques should be developed to distinguish between the in- and ex-pore ions, perhaps based on differences in their nuclear-spin relaxation or self-diffusion properties.

Chapter 10

Conclusions and Further Work

NMR spectroscopy has been shown to be a powerful technique for studying supercapacitors. NMR spectra of the electrolyte confined inside the electrodes are a rich source of information about the composition and dynamics of the electrode-electrolyte interface, and the changes that occur upon charging. This thesis has developed a detailed understanding of the factors that influence the form of the NMR spectra, and the resulting information that can be obtained.

The success of the NMR approach stems from the unique ability to separately observe in-pore species, which are confined inside the carbon pores. DFT calculations on model carbon fragments show that these species are subject to ring current effects, which indiscriminately shield the resonances arising from electrolyte cations, anions and solvent molecules. The calculations show that the observed chemical shifts are sensitive to the local carbon structure, with both smaller carbon pores and larger ordered carbon domains giving rise to greater chemical shielding effects. These findings explain the variations seen in the experimental chemical shifts for a range of electrolyte-soaked carbide-derived carbons with different structures. Having developed this understanding, information about the structures of the carbons can be extracted from the NMR spectra, with the sizes of the ordered carbon domains found to increase with the temperature used in the synthesis. If the potential of this new structural characterisation method is to be fully realised, advanced computational methods must be developed to simulate the NMR spectra for electrolyte species confined in realistic porous carbon structures.

The *in situ* NMR methodology has been systematically developed to allow the study of working supercapacitors, while *ex situ* experiments offer an attractive alternative when spectral resolution is poor. The changes of the in-pore resonance intensity that occur during supercapacitor charging allow the migration of electrolyte ions in and out of the carbon pores to be quantified. Given the significant number of ions residing in the

carbon pores in the absence of an applied potential, a range of charging mechanisms can operate when a potential is applied, involving different amounts of counter-ion adsorption and co-ion desorption. Experiments on the same activated carbon with different electrolytes have shown that the charging mechanism depends on both the polarisation of the electrode, and the choice of electrolyte ions. Importantly, charging is not generally driven by counter-ion adsorption alone, as is assumed in many studies. The NMR measurements also suggest that different carbon structures give rise to different charging mechanisms, though more experiments must be done to explore these effects. Further theoretical studies should also help to explore the factors that determine the charging mechanism that operates.

The NMR spectra of electrolyte-soaked carbons are also sensitive to dynamic effects, with the linewidth of the in-pore resonance giving a measure of the diffusion rate. When the linewidth measurements are combined with multi-site simulations of the chemical exchange processes inside the carbon pores, the in-pore mobility of different electrolytes can be contrasted, and the charging performances of devices can be rationalised. The slower in-pore ionic diffusion observed for ionic liquids explains the poorer power performances compared to devices using organic electrolytes. Linewidth measurements on different carbons confirm that larger pores result in faster diffusion, while also suggesting that more subtle factors such as pore connectivity and tortuosity can have an effect. Further experiments should be carried out to directly measure the in-pore diffusion rates in supercapacitor electrodes. In particular, PFG NMR measurements on a range of electrolytes and electrode materials will help to establish the key parameters that influence diffusion. Ideally, such measurements would be carried out in the presence of an electric field during the charging and discharging of working supercapacitors. Advanced molecular simulations of ion dynamics will also provide complementary information and can guide the formulation and interpretation of experiments.

During supercapacitor charging, marked changes of the in-pore chemical shifts are observed, arising from changes of the electronic structure of the carbon and the introduction of paratropic ring currents. In principle, the observed shift changes offer information about the electronic structure, but first the theory detailing the link between this structure and the chemical shift must be developed. These shift changes can hinder the resolution of the in-pore environment, especially for carbons that give rise to broader in-pore resonances. To make the NMR approach more widely applicable,

techniques must be developed to improve the resolution of the in-pore environment. One approach has been demonstrated here whereby magnetisation is transferred from isotopically enriched carbon electrodes solely to the in-pore ions by cross polarisation. These experiments also offer information about the ion dynamics and suggest that the in-pore ions move more slowly following the application of a potential. However, this method is relatively time consuming and more general approaches, potentially based on the different relaxation or diffusion properties of the ions, should be developed to resolve the behaviours of the in- and ex-pore ions when spectral resolution is poor.

The NMR method has offered new insights into the molecular mechanisms of charge storage in supercapacitors. The challenging but crucial next step is to use this new information to design and develop innovative materials with improved performances. Beyond the field of supercapacitors, it is envisaged that the methods and ideas developed here will be applicable to studies of porous carbons for gas storage, water treatment and catalysis.

Bibliography

- (1) Kempton, W.; Tomić, J. *J. Power Sources* **2005**, *144*, 280.
- (2) Winter, M.; Brodd, R. *Chem. Rev.* **2004**, *104*, 4245.
- (3) Tarascon, J. M.; Armand, M. *Nature* **2001**, *414*, 359.
- (4) Castelvecchi, D. *Nature* **2015**, DOI:10.1038/nature.2015.17469.
- (5) Simon, P.; Gogotsi, Y. *Nat. Mater.* **2008**, *7*, 845.
- (6) Miller, J. R.; Burke, A. *Electrochim. Soc. Interface* **2008**, *17*, 53.
- (7) Kötz, R. *Electrochim. Acta* **2000**, *45*, 2483.
- (8) Miller, J. R.; Simon, P. *Science* **2008**, *321*, 651.
- (9) Ruan, D. *at the 4th International Symposium on Enhanced Electrochemical Capacitors*; 2015.
- (10) Burke, A. *Electrochim. Acta* **2007**, *53*, 1083.
- (11) Simon, P.; Gogotsi, Y. *Acc. Chem. Res.* **2013**, *46*, 1094.
- (12) Béguin, F.; Presser, V.; Balducci, A.; Frackowiak, E. *Adv. Mater.* **2014**, *26*, 1.
- (13) Burt, R.; Birkett, G.; Zhao, X. S. *Phys. Chem. Chem. Phys.* **2014**.
- (14) Merlet, C.; Rotenberg, B.; Madden, P. A.; Salanne, M. *Phys. Chem. Chem. Phys.* **2013**, *15*, 15781.
- (15) Bhattacharyya, R.; Key, B.; Chen, H.; Best, A. S.; Hollenkamp, A. F.; Grey, C. P. *Nat. Mater.* **2010**, *9*, 504.
- (16) Key, B.; Bhattacharyya, R.; Morcrette, M.; Seznéc, V.; Tarascon, J.-M.; Grey, C. P. *J. Am. Chem. Soc.* **2009**, *131*, 9239.
- (17) Wang, H.; Köster, T. K.-J.; Trease, N. M.; Ségalini, J.; Taberna, P.-L.; Simon, P.; Gogotsi, Y.; Grey, C. P. *J. Am. Chem. Soc.* **2011**, *133*, 19270.
- (18) Deschamps, M.; Gilbert, E.; Azais, P.; Raymundo-Piñero, E.; Ammar, M. R.; Simon, P.; Massiot, D.; Béguin, F. *Nat. Mater.* **2013**, *12*, 351.
- (19) Bard, A. J.; Faulkner, L. R. *Electrochemical Methods: Fundamentals and Applications*; Wiley, 2001.
- (20) Augustyn, V.; Simon, P.; Dunn, B. *Energy Environ. Sci.* **2014**, *7*, 1597.
- (21) Taberna, P.-L.; Simon, P.; Fauvarque, J. F. *J. Electrochem. Soc.* **2003**, *150*, A292.
- (22) Stoller, M. D.; Ruoff, R. S. *Energy Environ. Sci.* **2010**, *3*, 1294.
- (23) Lewandowski, A.; Olejniczak, A.; Galinski, M.; Stepniak, I. *J. Power Sources* **2010**, *195*, 5814.
- (24) Armand, M.; Endres, F.; Macfarlane, D.; Ohno, H.; Scrosati, B. *Nat. Mater.* **2009**, *8*, 621.
- (25) Lin, R.; Taberna, P.-L.; Presser, V.; Pérez, C. R.; Malbosc, F.; Rupesinghe, N. L.; Teo, K. B. K.; Gogotsi, Y.; Simon, P. *J. Phys. Chem. Lett.* **2011**, *2*, 2396.
- (26) Tsai, W.-Y.; Lin, R.; Murali, S.; Li Zhang, L.; McDonough, J. K.; Ruoff, R. S.; Taberna, P.-L.; Gogotsi, Y.; Simon, P. *Nano Energy* **2013**, *2*, 403.
- (27) Zhai, Y.; Dou, Y.; Zhao, D.; Fulvio, P. F.; Mayes, R. T.; Dai, S. *Adv. Mater.* **2011**, *23*, 4828.
- (28) Marsh, H.; Rodriguez-Reinoso, F. *Activated Carbon*; 1st ed.; Elsevier Sci. Ltd., 2006.
- (29) Pandolfo, A. G.; Hollenkamp, A. F. *J. Power Sources* **2006**, *157*, 11.
- (30) Gogotsi, Y.; Nikitin, A.; Ye, H.; Zhou, W.; Fischer, J. E.; Yi, B.; Foley, H. C.; Barsoum, M. W. *Nat. Mater.* **2003**, *2*, 591.

- (31) Chmiola, J.; Yushin, G.; Gogotsi, Y.; Portet, C.; Simon, P.; Taberna, P.-L. *Science* **2006**, *313*, 1760.
- (32) Presser, V.; Heon, M.; Gogotsi, Y. *Adv. Funct. Mater.* **2011**, *21*, 810.
- (33) Dash, R.; Chmiola, J.; Yushin, G.; Gogotsi, Y.; Laudisio, G.; Singer, J.; Fischer, J.; Kucheyev, S. *Carbon* **2006**, *44*, 2489.
- (34) Harris, P. *Crit. Rev. Solid State Mater. Sci.* **2005**, *30*, 235.
- (35) Harris, P. *J. Mater. Sci.* **2013**, *48*, 565.
- (36) Franklin, R. E. *Acta Cryst.* **1951**, *4*, 253.
- (37) Franklin, R. E. *Proc. R. Soc. A* **1951**, *209*, 196.
- (38) Billinge, S.; Thorpe, M. *Local Structure from Diffraction*; Plenum New York, 1998.
- (39) Kane, M. S.; Goellner, J. F.; Foley, H. C.; Difrancesco, R.; Billinge, S. J. L.; Lansing, E.; Allard, L. F. *Chem. Mater.* **1996**, *8*, 2159.
- (40) Petkov, V.; Difrancesco, R. G.; Billinge, S. J. L.; Acharya, M.; Foley, H. C. *Phil. Mag. B* **1999**, *79*, 1519.
- (41) Acharya, M.; Strano, M. S.; Mathews, J. P.; Billinge, S. J. L.; Petkov, V.; Subramoney, S.; Foley, H. C. *Phil. Mag. B* **1999**, *79*, 1499.
- (42) Harris, P. J. F.; Liu, Z.; Suenaga, K. *J. Phys. Condens. Matter* **2008**, *20*, 362201.
- (43) Kumar, A.; Lobo, R.; Wagner, N. *Carbon* **2005**, *43*, 3099.
- (44) Jain, S. K.; Pellenq, R. J.; Pikunic, J. P.; Gubbins, K. E. *Langmuir* **2006**, *24*, 9942.
- (45) Palmer, J.; Jain, S. *Characterisation Porous Solids VIII* **2009**, *318*, 56.
- (46) Shi, Y. *J. Chem. Phys.* **2008**, *128*, 234707.
- (47) Palmer, J. C.; Llobet, A.; Yeon, S.-H.; Fischer, J. E.; Shi, Y.; Gogotsi, Y.; Gubbins, K. E. *Carbon* **2010**, *48*, 1116.
- (48) Tuinstra, F.; Koenig, J. L. *J. Chem. Phys.* **1970**, *53*, 1126.
- (49) Pimenta, M. A.; Dresselhaus, G.; Dresselhaus, M. S.; Cançado, L. G.; Jorio, A.; Saito, R. *Phys. Chem. Chem. Phys.* **2007**, *9*, 1276.
- (50) Kaneko, K. *J. Membr. Sci.* **1994**, *96*, 59.
- (51) Lastoskie, C.; Gubbins, K. E.; Quirkert, N. *J. Phys. Chem.* **1993**, *97*, 4786.
- (52) Dombrowski, R. J.; Hyduke, D. R.; Lastoskie, C. M. *Langmuir* **2000**, *16*, 5041.
- (53) Neimark, A. V.; Lin, Y.; Ravikovitch, P. I.; Thommes, M. *Carbon* **2009**, *47*, 1617.
- (54) Gamby, J.; Taberna, P.-L.; Simon, P.; Fauvarque, J. F.; Chesneau, M. *J. Power Sources* **2001**, *101*, 109.
- (55) Kim, Y.-J.; Masutzwawa, Y.; Ozaki, S.; Endo, M.; Dresselhaus, M. S. *J. Electrochem. Soc.* **2004**, *151*, E199.
- (56) Chmiola, J.; Largeot, C.; Taberna, P.-L.; Simon, P.; Gogotsi, Y. *Angew. Chem. Int. Ed. Engl.* **2008**, *47*, 3392.
- (57) Largeot, C.; Portet, C.; Chmiola, J.; Taberna, P.-L.; Gogotsi, Y.; Simon, P. *J. Am. Chem. Soc.* **2008**, *130*, 2730.
- (58) Raymundo-Piñero, E.; Kierzek, K.; Machnikowski, J.; Béguin, F. *Carbon* **2006**, *44*, 2498.
- (59) Centeno, T. A.; Sereda, O.; Stoeckli, F. *Phys. Chem. Chem. Phys.* **2011**, *13*, 12403.
- (60) Garcia-Gomez, A.; Moreno-Fernandez, G.; Lobato, B.; Centeno, T. A. *Phys. Chem. Chem. Phys.* **2015**, *17*, 15687.
- (61) Fedorov, M. V.; Kornyshev, A. A. *Electrochim. Acta* **2008**, *53*, 6835.
- (62) Merlet, C.; Salanne, M.; Rotenberg, B.; Madden, P. A. *J. Phys. Chem. C* **2011**, *115*, 16613.
- (63) Merlet, C.; Salanne, M.; Rotenberg, B.; Madden, P. A. *Electrochim. Acta* **2013**, *101*, 262.

- (64) Feng, G.; Cummings, P. T. *J. Phys. Chem. Lett.* **2011**, *2*, 2859.
- (65) Jiang, D.; Jin, Z.; Wu, J. *Nano Lett.* **2011**, *11*, 5373.
- (66) Kondrat, S.; Kornyshev, A. *J. Phys. Condens. Matter* **2011**, *23*, 022201.
- (67) Kondrat, S.; Georgi, N.; Fedorov, M. V.; Kornyshev, A. A. *Phys. Chem. Chem. Phys.* **2011**, *13*, 11359.
- (68) Merlet, C.; Rotenberg, B.; Madden, P. A.; Taberna, P.-L.; Simon, P.; Gogotsi, Y.; Salanne, M. *Nat. Mater.* **2012**, *11*, 306.
- (69) Péan, C.; Merlet, C.; Rotenberg, B.; Madden, P. A.; Taberna, P.-L.; Daffos, B.; Salanne, M.; Simon, P. *ACS Nano* **2014**, *8*, 1576.
- (70) Soolo, E.; Brandell, D.; Liivat, A. *J. Mol. Model* **2012**, *18*, 1541.
- (71) Xing, L.; Vatamanu, J.; Smith, G. D.; Bedrov, D. *J. Phys. Chem. Lett.* **2012**, *3*, 1124.
- (72) Vatamanu, J.; Hu, Z.; Bedrov, D.; Perez, C.; Gogotsi, Y. *J. Phys. Chem. Lett.* **2013**, *4*, 2829.
- (73) Merlet, C.; Péan, C.; Rotenberg, B.; Madden, P. A.; Daffos, B.; Taberna, P.-L.; Simon, P.; Salanne, M. *Nat. Comm.* **2013**, *4*, 2701.
- (74) Kondrat, S.; Kornyshev, A. *J. Phys. Chem. C* **2013**, *117*, 12399.
- (75) Lee, A. A.; Kondrat, S.; Oshanin, G.; Kornyshev, A. A. *Nanotechnology* **2014**, *25*, 315401.
- (76) Kondrat, S.; Wu, P.; Qiao, R.; Kornyshev, A. A. *Nat. Mater.* **2014**, *13*, 387.
- (77) Perkin, S.; Crowhurst, L.; Niedermeyer, H.; Welton, T.; Smith, A. M.; Gosvami, N. N. *Chem. Commun.* **2011**, *47*, 6572.
- (78) Perkin, S.; Klein, J. *Phys. Chem. Chem. Phys.* **2010**, *12*, 1243.
- (79) Li, H.; Wood, R. J.; Endres, F.; Atkin, R. *J. Phys. Condens. Matter* **2014**, *26*, 284115.
- (80) Carstens, T.; Gustus, R.; Ho, O.; Borisenko, N.; Endres, F.; Li, H.; Wood, R. J.; Page, A. J.; Atkin, R. *J. Phys. Chem. C* **2014**, *118*, 10833.
- (81) Richey, F. W.; Dyatkin, B.; Gogotsi, Y.; Elabd, Y. A. *J. Am. Chem. Soc.* **2013**, *135*, 12818.
- (82) Richey, F. W.; Tran, C.; Kalra, V.; Elabd, Y. A. *J. Phys. Chem. C* **2014**, *118*, 21846.
- (83) Levi, M. D.; Salitra, G.; Levy, N.; Aurbach, D.; Maier, J. *Nat. Mater.* **2009**, *8*, 872.
- (84) Levi, M. D.; Levy, N.; Sigalov, S.; Salitra, G.; Aurbach, D.; Maier, J. *J. Am. Chem. Soc.* **2010**, *132*, 13220.
- (85) Tsai, W.-Y.; Taberna, P.-L.; Simon, P. *J. Am. Chem. Soc.* **2014**, *136*, 8722.
- (86) Levi, M. D.; Sigalov, S.; Salitra, G.; Elazari, R.; Aurbach, D. *J. Phys. Chem. Lett.* **2011**, *2*, 120.
- (87) Boukhalfa, S.; He, L.; Melnichenko, Y. B.; Yushin, G. *Angew. Chem. Int. Ed.* **2013**, *52*, 1.
- (88) Boukhalfa, S.; Gordon, D.; He, L.; Melnichenko, Y. B.; Nitta, N.; Magasinski, A.; Yushin, G. *ACS Nano* **2014**, *8*, 2495.
- (89) Prehal, C.; Weingarth, D.; Perre, E.; Lechner, R. T.; Amenitsch, H.; Paris, O.; Presser, V. *Energy Environ. Sci.* **2015**, *8*, 1725.
- (90) Grey, C. P.; Dupré, N. *Chem. Rev.* **2004**, *104*, 4493.
- (91) Chevallier, F.; Letellier, M.; Morcrette, M.; Tarascon, J.-M.; Frackowiak, E.; Rouzaud, J.-N.; Be'guin, F. *Electrochem. Solid State Lett.* **2003**, *6*, A225.
- (92) Letellier, M.; Chevallier, F.; Morcrette, M. *Carbon* **2007**, *45*, 1025.
- (93) Lee, S.-I.; Saito, K.; Kanehashi, K.; Hatakeyama, M.; Mitani, S.; Yoon, S.-H.; Korai, Y.; Mochida, I. *Carbon* **2006**, *44*, 2578.
- (94) Levitt, M. *Spin Dynamics: Basics of Nuclear Magnetic Resonance (2nd Edition)*; 2008.

- (95) Ashbrook, S. E.; Dawson, D.; Griffin, J. M. *Local Structural Characterisation: Inorganic Materials Series*; Wiley, 2013.
- (96) Schenk, J. F. *Med. Phys.* **1996**, 23, 815.
- (97) Levitt, M. H. *Conc. Magn. Res.* **1995**, 8, 77.
- (98) Ulrich, R.; Glaser, R. W.; Ulrich, A. S. *J. Magn. Reson.* **2003**, 164, 115.
- (99) Salomir, R.; De Senneville, B. D.; Moonen, C. T. *Conc. Magn. Res.* **2003**, 19B, 26.
- (100) Manning, A. P.; Giese, M.; Terpstra, A. S.; MacLachlan, M. J.; Hamad, W. Y.; Dong, R. Y.; Michal, C. A. *Magn. Reson. Chem.* **2014**, 52, 532.
- (101) Glaser, R. W.; Ulrich, A. S. *J. Magn. Reson.* **2003**, 164, 104.
- (102) Keeler, J. *Understanding NMR Spectroscopy (2nd Edition)*; Wiley, 2010.
- (103) Apperley, D. C.; Harris, R. K.; Paul Hodgkinson. *Solid-state NMR Basic Principles and Practice*; 2012.
- (104) Cory, D. G.; Ritchey, W. M. *J. Magn. Reson.* **1988**, 80, 128.
- (105) Burum, D. P. *Encycl. Nucl. Magn. Reson.* **1996**, 3, 1535.
- (106) Lim, K. H.; Grey, C. P. *Chem. Commun.* **2000**, 13, 2257.
- (107) White, J. L.; Beck, L. W.; Haw, J. F. *J. Am. Chem. Soc.* **1992**, 114, 6182.
- (108) Kolodziejksi, W.; Klinowski, J. *Chem. Rev.* **2002**, 102, 613.
- (109) Bain, A. D. *Prog. Nucl. Magn. Reson. Spectrosc.* **2003**, 43, 63.
- (110) Harris, R. K.; Thompson, T. V.; Norman, P. R.; Pottage, C. *Carbon* **1999**, 37, 1425.
- (111) Jonathan, C.; Greeves, N.; Warren, S.; Wothers, P. *Organic Chemistry*; OUP Oxford, 2001.
- (112) Pople, J. A. *J. Chem. Phys.* **1956**, 24, 1111.
- (113) Oth, J. F. M.; Woo, E. P.; Sondheimer, F. *J. Am. Chem. Soc.* **1973**, 6259, 7337.
- (114) Schleyer, P. v. R.; Maerker, C.; Dransfeld, A.; Jiao, H.; Hommes, N. J. R. V. E. *J. Am. Chem. Soc.* **1996**, 7863, 6317.
- (115) Chen, Z.; Wannere, C. S.; Corminboeuf, C.; Puchta, R.; Schleyer, P. v. R. *Chem. Rev.* **2005**, 105, 3842.
- (116) Pople, J. A. *J. Am. Chem. Soc.* **1966**, 88, 4811.
- (117) Atkins, P. W.; Friedman, R. *Molecular Quantum Mechanics*; OUP Oxford, 2005.
- (118) Hohenberg, P.; Kohn, W. *Phys. Rev.* **1964**, 136, 864.
- (119) Kohn, W.; Sham, L. J. *Phys. Rev.* **1965**, 140, 1133.
- (120) Foresman, J. B.; Frisch, A. *Exploring Chemistry With Electronic Structure Methods: A Guide to Using Gaussian*; Gaussian, 1996.
- (121) Becke, A. D. *J. Chem. Phys.* **1993**, 98, 5648.
- (122) Cheeseman, J. R.; Trucks, G. W.; Keith, T. A.; Frisch, M. J. *J. Chem. Phys.* **1996**, 104, 5497.
- (123) Kibalchenko, M.; Payne, M. C.; Yates, J. R. *ACS Nano* **2011**, 5, 537.
- (124) Kondrat, S.; Pérez, C. R.; Presser, V.; Gogotsi, Y.; Kornyshev, A. A. *Energy Environ. Sci.* **2012**, 5, 6474.
- (125) Blanc, F.; Leskes, M.; Grey, C. P. *Acc. Chem. Res.* **2013**, 46, 1952.
- (126) Harris, R. K.; Thompson, T. V.; Norman, P. R.; Pottage, C.; Trethewey, A. N. *J. Chem. Soc., Faraday Trans.* **1995**, 91, 1795.
- (127) Harris, R. K.; Thompson, T. V.; Forshaw, P.; Foley, N.; Thomas, K. M.; Norman, P. R.; Pottage, C. *Carbon* **1996**, 34, 1275.
- (128) Harris, R. K.; Thompson, T. V.; Norman, P. R.; Pottage, C. *J. Chem. Soc. Faraday Trans.* **1996**, 92, 2615.
- (129) Shaw, J. A.; Harris, R. K.; Norman, P. R. *Langmuir* **1998**, 14, 6716.
- (130) Dickinson, L. M.; Harris, R. K.; Shaw, J. A.; Chinn, M.; Norman, P. R. *Magn. Reson. Chem.* **2000**, 38, 918.

- (131) Liu, X.; Pan, X.; Shen, W.; Ren, P.; Han, X.; Bao, X. *J. Phys. Chem. C* **2012**, *116*, 7803.
- (132) Chen, Q.; Herberg, J. L.; Mogilevsky, G.; Wang, H.-J.; Stadermann, M.; Holt, J. K.; Wu, Y. *Nano Lett.* **2008**, *8*, 1902.
- (133) Sekhaneh, W.; Koteka, M.; Dettlaff-Weglikowska, U.; Veeman, W. S. *Chem. Phys. Lett.* **2006**, *428*, 143.
- (134) Shen, K.; Pietrass, T. *J. Phys. Chem. B* **2004**, *108*, 9937.
- (135) Anderson, R. J.; McNicholas, T. P.; Kleinhammes, A.; Wang, A.; Liu, J.; Wu, Y. *J. Am. Chem. Soc.* **2010**, *132*, 8618.
- (136) McNicholas, T. P.; Wang, A.; Neill, K. O.; Anderson, R. J.; Stadie, N. P.; Kleinhammes, A.; Parilla, P.; Simpson, L.; Ahn, C. C.; Wang, Y.; Wu, Y.; Liu, J. *J. Phys. Chem. C* **2010**, *114*, 13902.
- (137) Massiot, D.; Fayon, F.; Capron, M.; King, I.; Le Calvé, S.; Alonso, B.; Durand, J.-O.; Bujoli, B.; Gan, Z.; Hoatson, G. *Magn. Reson. Chem.* **2002**, *40*, 70.
- (138) Lazzaretti, P. *Prog. Nucl. Magn. Reson. Spectrosc.* **2000**, *36*, 1.
- (139) Facelli, J. C. *Magn. Reson. Chem.* **2006**, *44*, 401.
- (140) Porada, S.; Weingarth, D.; Hamelers, H. V. M.; Bryjak, M.; Presser, V.; Biesheuvel, P. M. *J. Mater. Chem. A* **2014**, *2*, 9313.
- (141) Borchardt, L.; Oschatz, M.; Paasch, S.; Kaskel, S.; Brunner, E. *Phys. Chem. Chem. Phys.* **2013**, *15*, 15177.
- (142) Xu, Y.; Watermann, T.; Limbach, H.-H.; Gutmann, T.; Sebastiani, D.; Bunkowsky, G. *Phys. Chem. Chem. Phys.* **2014**, *16*, 9327.
- (143) Vora, P.; Gopu, P.; Rosario-Canales, M.; Pérez, C.; Gogotsi, Y.; Santiago-Avilés, J.; Kikkawa, J. *Phys. Rev. B* **2011**, *84*, 155114.
- (144) Xing, Y.-Z.; Luo, Z.-X.; Kleinhammes, A.; Wu, Y. *Carbon* **2014**, *77*, 1132.
- (145) Kim, T.; Ideta, K.; Jung, D.; Saito, K.; Park, J.; Rhee, C. K.; Miyawaki, J.; Mochida, I.; Yoon, S.-H. *RSC Adv.* **2014**, *4*, 16726.
- (146) Zhou, L.; Leskes, M.; Ilott, A. J.; Trease, N. M.; Grey, C. P. *J. Magn. Reson.* **2013**, *234*, 44.
- (147) Trease, N. M.; Zhou, L.; Chang, H. J.; Zhu, B. Y.; Grey, C. P. *Solid State Nucl. Magn. Reson.* **2012**, *42*, 62.
- (148) Sebastiani, D. *Chem. Phys. Chem.* **2006**, *7*, 164.
- (149) Ren, P.; Zheng, A.; Pan, X.; Han, X.; Bao, X. *J. Phys. Chem. C* **2013**, *117*, 23418.
- (150) Bühl, M. *Chem. Eur. J.* **1998**, *4*, 734.
- (151) Jusélius, J.; Sundholm, D.; Gauss, J. *J. Chem. Phys.* **2004**, *121*, 3952.
- (152) Fliegl, H.; Taubert, S.; Lehtonen, O.; Sundholm, D. *Phys. Chem. Chem. Phys.* **2011**, *13*, 20500.
- (153) Johansson, M. P.; Jusélius, J.; Sundholm, D. *Angew. Chem. Int. Ed.* **2005**, *44*, 1843.
- (154) Moran, D.; Stahl, F.; Bettinger, H. F.; Scaefer III, H. F.; Schleyer, P. v. R. *J. Am. Chem. Soc.* **2003**, *125*, 6746.
- (155) Vähäkangas, J.; Ikäläinen, S.; Lantto, P.; Vaara, J. *Phys. Chem. Chem. Phys.* **2013**, *15*, 4634.
- (156) M. J. Frisch, G. W. Trucks, H. B. Schlegel, G. E. S., M. A. Robb, J. R. Cheeseman, J. A. Montgomery, Jr., T. V., K. N. Kudin, J. C. Burant, J. M. Millam, S. S. Iyengar, J. T., V. Barone, B. Mennucci, M. Cossi, G. Scalmani, N. R.; G. A. Petersson, H. Nakatsuji, M. Hada, M. Ehara, K. T.; R. Fukuda, J. Hasegawa, M. Ishida, T. Nakajima, Y. Honda, O. K.; H. Nakai, M. Klene, X. Li, J. E. Knox, H. P. Hratchian, J. B. C.; V. Bakken, C. Adamo, J. Jaramillo, R. Gomperts, R. E. S.; O. Yazayev, A. J. Austin, R. Cammi, C. Pomelli, J. W. O.; P. Y. Ayala, K. Morokuma, G. A. Voth, P. Salvador, J. J. D.; V. G. Zakrzewski, S.

- Dapprich, A. D. Daniels, M. C. S.; O. Farkas, D. K. Malick, A. D. Rabuck, K. R.; J. B. Foresman, J. V. Ortiz, Q. Cui, A. G. Baboul, S. C.; J. Cioslowski, B. B. Stefanov, G. Liu, A. Liashenko, P. P.; I. Komaromi, R. L. Martin, D. J. Fox, T. Keith, M. A. A.-L.; C. Y. Peng, A. Nanayakkara, M. Challacombe, P. M. W. G.; B. Johnson, W. Chen, M. W. Wong, C. Gonzalez, and J. A. P. Gaussian 03, Revision E.01.
- (157) Bondi, A. *J. Phys. Chem.* **1965**, *68*, 441.
- (158) Zickler, G. A.; Smarsly, B.; Gierlinger, N.; Peterlik, H.; Paris, O. *Carbon* **2006**, *44*, 3239.
- (159) Ma, Z.; Halling, M. D.; Solum, M. S.; Harper, J. K.; Orendt, A. M.; Facelli, J. C.; Pugmire, R. J.; Grant, D. M.; Amick, A. W.; Scott, L. T. *J. Phys. Chem. A* **2007**, *111*, 2020.
- (160) Kawasumi, K.; Zhang, Q.; Segawa, Y.; Scott, L. T.; Itami, K. *Nat. Chem.* **2013**, *5*, 739.
- (161) Panich, A. M.; Shames, A. I.; Sergeev, N. A.; Olszewski, M.; McDonough, J. K.; Mochalin, V. N.; Gogotsi, Y. *J. Phys. Condens. Matter* **2013**, *25*, 245303.
- (162) Osswald, S.; Chmiola, J.; Gogotsi, Y. *Carbon* **2012**, *50*, 4880.
- (163) Dyatkin, B.; Gogotsi, Y. *Faraday Discuss.* **2014**, *172*, 139.
- (164) Merlet, C.; Forse, A. C.; Griffin, J. M.; Frenkel, D.; Grey, C. P. *J. Chem. Phys.* **2015**, *142*, 094701.
- (165) Brandt, A.; Pohlmann, S.; Varzi, A.; Balducci, A.; Passerini, S. *MRS Bull.* **2013**, *38*, 554.
- (166) Largeot, C.; Taberna, P.-L.; Gogotsi, Y.; Simon, P. *Electrochem. Solid-State Lett.* **2011**, *14*, A174.
- (167) Lee, A. A.; Kondrat, S.; Kornyshev, A. A. *Phys. Rev. Lett.* **2014**, *113*, 048701.
- (168) Molinspiration Property Calculation Service,
<http://www.molinspiration.com/services/volume.html>.
- (169) Lewandowski, A.; Jakobczyk, P.; Galinski, M.; Biegun, M. *Phys. Chem. Chem. Phys.* **2013**, *15*, 8692.
- (170) Presser, V.; Dennison, C. R.; Campos, J.; Knehr, K. W.; Kumbur, E. C.; Gogotsi, Y. *Adv. Energy Mater.* **2012**, *2*, 895.
- (171) Hahn, M.; Barbieri, O.; Gallay, R.; Kötz, R. *Carbon* **2006**, *44*, 2523.
- (172) Ruch, P. W.; Kötz, R.; Wokaun, A. *Electrochim. Acta* **2009**, *54*, 4451.
- (173) Hantel, M. M.; Presser, V.; Kötz, R.; Gogotsi, Y. *Electrochem. Commun.* **2011**, *13*, 1221.
- (174) Arruda, T. M.; Heon, M.; Presser, V.; Hillesheim, P. C.; Dai, S.; Gogotsi, Y.; Kalinin, S. V.; Balke, N. *Energy Environ. Sci.* **2013**, *6*, 225.
- (175) Lazzari, M.; Mastragostino, M.; Pandolfo, A. G.; Ruiz, V.; Soavi, F. *J. Electrochem. Soc.* **2011**, *158*, A22.
- (176) Manivannan, A.; Chirila, M.; Giles, N. C.; Seehra, M. S. *Carbon* **1999**, *37*, 1741.
- (177) Zhecheva, E.; Stoyanova, R.; Jiménez-Mateos, J. M.; Alcantra, R.; Lavela, P.; Tirado, J. L. *Carbon* **2002**, *40*, 2301.
- (178) Watanabe, A.; Ishikawa, H.; Mori, K. *Carbon* **1989**, *27*, 863.
- (179) Miyagawa, I.; Sogabe, K.; Ohuchi, M.; Hukao, K. *Chem. Phys. Lett.* **1994**, *225*, 364.
- (180) Bielecki, A.; Burum, D. P. *J. Magn. Reson.* **1995**, *116*, 215.
- (181) Beckmann, P. A.; Dybowski, C. *J. Magn. Reson.* **2000**, *146*, 379.
- (182) Weingarth, D.; Drumm, R.; Foelske-Schmitz, A.; Kotz, R.; Presser, V. *Phys. Chem. Chem. Phys.* **2014**, *16*, 21219.
- (183) McEwen, A. B.; Ngo, H. L.; Lecompte, K.; Goldman, J. L. *J. Electrochem. Soc.* **1999**, *146*, 1687.

- (184) Borodin, O.; Gorecki, W.; Smith, G. D.; Armand, M. *J. Phys. Chem. B* **2010**, *114*, 6786.
- (185) Bayley, P. M.; Best, A. S.; Macfarlane, D. R.; Forsyth, M. *Phys. Chem. Chem. Phys.* **2011**, *13*, 4632.
- (186) Hayamizu, K.; Tsuzuki, S.; Seki, S.; Fujii, K.; Suenaga, M.; Umebayashi, Y. *J. Chem. Phys.* **2010**, *133*, 194505.
- (187) Dubinin, M. M.; Vartapetian, R. S.; Voloshchuk, A. M.; Karger, J.; Pfeifer, H. *Carbon* **1988**, *26*, 515.
- (188) Hayamizu, K.; Aihara, Y. *J. Phys. Chem. Lett.* **2010**, *1*, 2055.
- (189) Zhang, Z.; Madsen, L. A. *J. Chem. Phys.* **2014**, *140*, 084204.
- (190) Liu, Y.-C.; Moore, J. D.; Roussel, T. J.; Gubbins, K. E. *Phys. Chem. Chem. Phys.* **2010**, *12*, 6632.
- (191) Palmer, J. C.; Moore, J. D.; Brennan, J. K.; Gubbins, K. E. *Adsorption* **2010**, *17*, 189.
- (192) Nicolaï, A.; Monti, J.; Daniels, C.; Meunier, V. *J. Phys. Chem. C* **2015**, *119*, 2896.
- (193) Francke, R.; Cericola, D.; Kötz, R.; Weingarth, D.; Waldvogel, S. R. *Electrochim. Acta* **2012**, *62*, 372.
- (194) Chen, J. J.; Kong, X.; Sumida, K.; Manumpil, M. A.; Long, J. R.; Reimer, J. A. *Angew. Chem. Int. Ed.* **2013**, *52*, 12043.
- (195) Kolmas, J.; Kolodziejski, W. *Chem. Commun.* **2007**, *21*, 4390.
- (196) Kolmas, J.; Kolodziejski, W. *Chem. Phys. Lett.* **2012**, *554*, 128.
- (197) Kolodziejski, W.; Kasprzycka-Gutman, T. *Solid State Nucl. Magn. Reson.* **1998**, *11*, 177.
- (198) Kolodziejski, W.; Corma, A.; Wozniak, K.; Klinowski, J. *J. Phys. Chem.* **1996**, *100*, 7345.
- (199) Pines, A.; Gibby, M. G.; Waugh, J. S. *J. Chem. Phys.* **1973**, *59*, 569.
- (200) Rethwisch, D. G.; Jacintha, M. A.; Dybowski, C. R. *Anal. Chim. Acta* **1993**, *283*, 1033.